

NO-ALOG 969

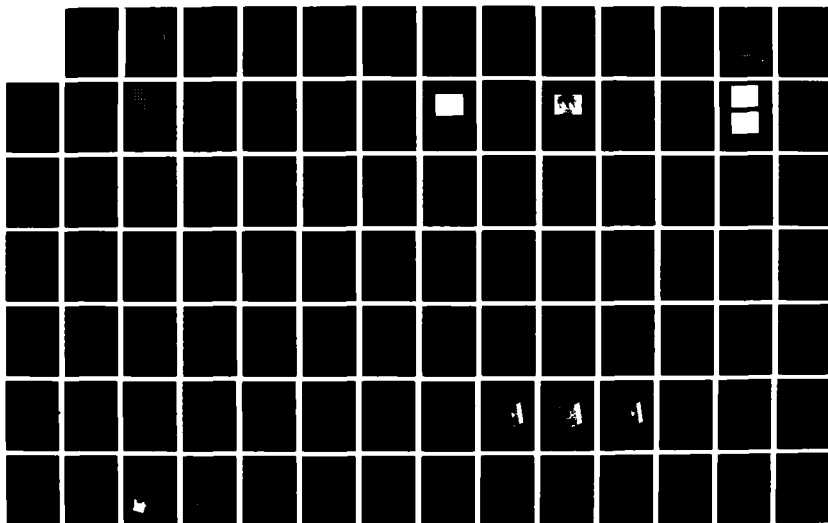
MANOELECTRONICS(U) TEXAS INSTRUMENTS INC DALLAS
R T BATE ET AL 14 AUG 87 TI-88-87-50 ARO-21243.11-EL
DARG29-84-C-0009

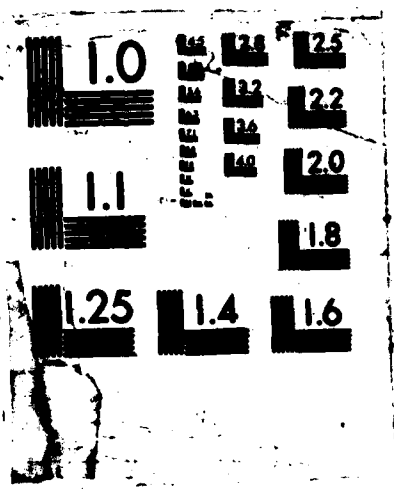
1/3

UNCLASSIFIED

F/G 28/10

NL





DTIC FILE COPY

ARO 21243.11-EL

2

AD-A186 969

NANOELECTRONICS

FINAL TECHNICAL REPORT

R. T. BATE, M. A. REED, AND W. R. FRENSLEY

U.S. ARMY RESEARCH OFFICE

DAAG29-84-C-0009

DTIC
ELECTE
OCT 29 1987
S D
D

18 AUGUST 1987

Texas Instruments Incorporated
P.O. Box 665936, M/S 154
Dallas, TX 75265-5936

APPROVED FOR PUBLIC RELEASE;
DISTRIBUTION UNLIMITED

224

THE VIEW, OPINIONS, AND/OR FINDINGS CONTAINED IN THIS REPORT ARE THOSE OF THE AUTHOR(S) AND SHOULD NOT BE CONSTRUED AS AN OFFICIAL DEPARTMENT OF THE ARMY POSITION, POLICY, OR DECISION, UNLESS SO DESIGNATED BY OTHER DOCUMENTATION.

UNCLASSIFIED

SECURITY CLASSIFICATION OF THIS PAGE (When Data Entered)

ADA186969

REPORT DOCUMENTATION PAGE

1a. REPORT SECURITY CLASSIFICATION Unclassified		1b. RESTRICTIVE MARKINGS	
2a. SECURITY CLASSIFICATION AUTHORITY		3. DISTRIBUTION/AVAILABILITY OF REPORT Approved for public release; distribution unlimited.	
2b. DECLASSIFICATION/DOWNGRADING SCHEDULE			
4. PERFORMING ORGANIZATION REPORT NUMBER(S) 08-87-50		5. MONITORING ORGANIZATION REPORT NUMBER(S) ARO 21243.11-EL	
6a. NAME OF PERFORMING ORGANIZATION Texas Instruments Incorporated		7a. NAME OF MONITORING ORGANIZATION U.S. Army Research Office	
6b. ADDRESS (City, State, and Zip Code) P.O. Box 655936 Dallas, Texas 75265		7b. ADDRESS (City, State, and Zip Code) Post Office Box 12211 Research Triangle Park, NC 27709-2211	
8a. NAME OF FUNDING/SPONSORING ORG. U.S. Army Research Office	8b. OFFICE SYMBOL (If applicable)	9. PROCUREMENT INSTRUMENT IDENTIFICATION NUMBER DAAG29-84-C-0009	
8c. ADDRESS (City, State, and Zip Code) Post Office Box 12211 Research Triangle Park, NC 27709-2211		10. SOURCE OF FUNDING NUMBERS	
		PROGRAM ELEMENT NO.	PROJECT NO.
		TASK NO.	WORK UNIT ACCESSION NO.
11. TITLE (Include Security Classification) Nanoelectronics (Unclassified)			
12. PERSONAL AUTHOR(S) R. T. Bate, M. A. Reed, W. R. Frensley			
13a. TYPE OF REPORT Final Technical	13b. TIME COVERED 15 June 1984 - 14 June 1987	14. DATE OF REPORT (Year, Month, Day) 1987 August 14	15. PAGE COUNT 141
16. SUPPLEMENTARY NOTATION The views, opinions, and/or findings contained in this report are those of the author(s) and should not be construed as an official Department of the Army position, policy, or decision, unless so designated by other documentation.			
17. COSATI CODES		18. SUBJECT TERMS (Continue on reverse if necessary and identify by block number)	
FIELD	GROUP	Resonant Tunneling, Quantum Size Effects, Quantum Dots, Quantum-Coupled Devices, Molecular Beam Epitaxy, Electron Beam Lithography	
19. ABSTRACT (Continue on reverse side if necessary and identify by block number) Results of theoretical and experimental research on resonant tunneling diodes are reported. Of particular interest were the effects of restriction of the lateral dimensions of the device to achieve quantum confinement of electrons in all three dimensions. The theoretical efforts within this program were devoted to applying a quantum-transport approach to understanding the behavior of the resonant-tunneling diode. When this program began, there had been no demonstration of total spatial quantization in a fabricated semiconductor system. We pioneered work in this field by investigating the photoluminescence of laterally			
20. DISTRIBUTION/AVAILABILITY OF ABSTRACT <input type="checkbox"/> UNCLASSIFIED/UNLIMITED <input type="checkbox"/> SAME AS RPT. <input type="checkbox"/> DTIC USERS		21. ABSTRACT SECURITY CLASSIFICATION UNCLASSIFIED	
22a. NAME OF RESPONSIBLE INDIVIDUAL Dr. Michael Stroschio		22b. TELEPHONE (Include Area Code) (919) 549-0641	22c. OFFICE SYMBOL

UNCLASSIFIED

SECURITY CLASSIFICATION OF THIS PAGE (When Data Entered)

19. ABSTRACT (Continued)

confined multiple quantum wells, known as "quantum dots." The results gave the first evidence for spatial quantization in a fabricated system and have stimulated considerable activity in the creation of microfabricated quantum structures. We undertook an extensive study of resonant tunneling in GaAs structures as a baseline approach. We investigated excited state resonant tunneling and were the first to show clear negative differential resistance because of resonant tunneling through excited states. We fabricated and electrically characterized quantum dot resonant tunneling structures. Effort was also expended on fabrication and characterization of silicon tunneling structures.



UNCLASSIFIED

SECURITY CLASSIFICATION OF THIS PAGE (When Data Entered)

TABLE OF CONTENTS

<u>SECTION</u>		<u>PAGE</u>
I.	FOREWORD.	1
II.	THEORY.	2
III.	GaAs STRUCTURES	3
	A. TEST STRUCTURES FOR LATERAL QUANTIZATION.	3
	B. TEST STRUCTURES FOR VERTICAL TRANSPORT.	3
	C. LATERALLY QUANTIZED RESONANT TUNNELING STRUCTURES . . .	3
	1. Microfabrication Approach	4
	2. E-Beam Lithography.	4
	3. Reactive Ion Etching.	13
	4. Contacting Quantum Dots	17
	5. Electrical Transport Data	18
IV.	SILICON STRUCTURES.	29
V.	RECOMMENDATIONS FOR FURTHER WORK.	31
	A. FABRICATION	31
	1. Molecular Beam Epitaxy.	31
	2. Patterning.	31
	3. Anisotropic Etching	33
	B. THEORY/EXPERIMENT	33
	REFERENCES.	35
	PARTICIPATING PERSONNEL	37
	LIST OF APPENDICES.	37



Accession For	
NTIS CRA&I	<input checked="" type="checkbox"/>
DTIC TAB	<input type="checkbox"/>
Unannounced	<input type="checkbox"/>
Justification	
By	
Distribution/	
Availability Codes	
Dist	Avail and/or Special
A-1	

LIST OF ILLUSTRATIONS

<u>FIGURE</u>		<u>PAGE</u>
1.	Schematic of fabrication sequence of quantum dot devices. .	5
2.	Schematic of MBE grown resonant tunneling diode structure (not to scale).	6
3.	Pattern used for focusing and aligning e-beam exposures . .	7
4.	E-beam exposed test pattern referred to as "multidot" . . .	9
5.	The 12 different patterns used for e-beam writing of quantum dots.	10
6.	Schematic of undercut profile obtained with e-beam exposure of PMMA bilayer resist structure.	12
7.	Scanning electron micrograph of lifted-off metal dots showing effects of distributed evaporation sources	14
8.	Scanning electron micrograph of RIE columns containing quantum dots.	16
9.	Scanning electron micrographs taken during polyimide etch- back process: (a) metal contacts of quantum dot devices appearing above polyimide layer. (b) partial clearing of polyimide from multidot pattern.	19
10.	Pattern used to contact quantum dots, including alignment level	20
11.	I-V trace at 300 K of a $4 \mu\text{m}^2$ resonant tunneling large area device.	21
12.	I-V trace at 300 K of a single quantum dot of the 2 x 2 pixel dimension	22
13.	I-V trace at 100 K of a single quantum dot of the 2 x 2 pixel dimension	24
14.	I-V trace at 4.2 K of a single quantum dot of the 2 x 2 pixel dimension	25
15.	Time-dependent current fluctuations at a fixed bias of 0.71 V of the single quantum dot of the 2 x 2 pixel dimension	26
16.	Time-dependent current fluctuations at a fixed bias of 0.875 V of the single quantum dot of the 2 x 2 pixel dimension	27

NANOELECTRONICS
FINAL TECHNICAL REPORT FOR
CONTRACT NO. DAAG29-84-C-0009

I. FOREWORD

The program that was originally called "Ultrasmall Electronics" and is now called "Nanoelectronics" originated at Texas Instruments in mid-1982. Its initiation was based on the realization that the anticipated attainment of integrated circuit device and interconnect scaling limits in the mid-1990s would end the historical trend of exponentially increasing functional density, and that revolutionary devices and architectures would be required to resume the historical trend.¹

Shortly after the program began, a new class of resonant tunneling devices employing lateral quantization effects was conceived at TI. These devices, called "Quantum-Coupled Devices,"² were described in a White Paper sent to DoD in late 1982. Subsequently, GaAs embodiments and fabrication processes were conceived for these devices, and one patent on a fabrication process for the GaAs embodiment has been issued.³ Proposals to fabricate and test these embodiments were submitted to ARO and to ONR. In response to these proposals, TI was awarded two contracts, DAAG29-84-C-0009, "Ultrasmall Electronics"; and N00014-84-C-0125, "Research on GaAs Quantum-Coupled Structures That Can Be Used as Electron Devices," to explore two different approaches to the realization of these devices. The thrust of the ARO contract was to explore the feasibility of a vertical tunneling structure with lateral quantization. This report summarizes the results of that effort.

Many of the results obtained under the contract have been published or submitted for publication in scientific journals. In these cases, brief descriptions of the effort are given, and reference is made to reprints or preprints that appear as appendices. To limit the size of this report, papers already published in readily available journals are represented here only with abstracts. In other cases, where complete descriptions of the work have not been submitted or published, more extensive discussions are included.

II. THEORY

Theoretical efforts in this program were devoted to applying a quantum-transport approach, which was initially developed at Texas Instruments under Contract No. N00014-84-C-0125, to understand resonant-tunneling diode behavior.

In the quantum-transport approach the internal state of the device is represented by the Wigner distribution function, which is an operator, rather than by a set of wavefunctions. This representation is necessary if one is to include both coherent and incoherent effects. The major incoherent effects in quantum devices arise from the effects of the electrical contacts and from stochastic processes within the device itself (such as scattering of electrons by phonons). The contacts to the device are modeled by the boundary conditions on the Wigner function, and these introduce time-irreversibility into the model. Appendix A gives details of this approach.

The quantum-transport approach was applied to several problems in the theory of resonant-tunneling devices. One was the dependence of the current density and transient response time on the barrier layer width, as described in Appendix B. A second problem concerned the small-signal ac response of the device. The treatment of this problem is described in Appendix C.

Finally, a very preliminary effort was made to incorporate phonon scattering processes into the model of the resonant-tunneling diode. This was done at the level of a classical Boltzmann collision term. The results of this work are discussed in Appendix D.

III. GaAs STRUCTURES

A. TEST STRUCTURES FOR LATERAL QUANTIZATION

The goal of this program is to demonstrate vertical electronic transport through laterally quantized structures. When this program began, there had been no demonstration of total spatial quantization in a fabricated semiconductor system. We pioneered work in this field by investigating the photoluminescence of laterally confined multiple quantum wells, known as "quantum dots." The fabrication and results of this work are detailed in Appendix E. The results gave the first evidence for spatial quantization in a fabricated system and have stimulated considerable activity in the creation of microfabricated quantum structures.⁴⁻⁶

B. TEST STRUCTURES FOR VERTICAL TRANSPORT

A necessary condition for studying the proposed vertical, laterally quantized coupled tunneling structures is a demonstrated expertise in resonant tunneling structures. We undertook an extensive study of resonant tunneling in GaAs structures as a baseline approach. We were quickly able to achieve world-record peak-to-valley ratios at room temperature with MBE grown structures exhibiting excellent quantum well and tunnel barrier uniformity (Appendix F). We then investigated excited state resonant tunneling and were the first to show clear negative differential resistance due to resonant tunneling through excited states (Appendix G). An outgrowth of this work was the concern that incoherent tunneling (so-called "sequential" tunneling) was occurring in these structures, so a set of samples utilizing tailorable superlattice barriers was investigated (Appendices H through J). The results, given in Appendix J, demonstrate that coherent resonant tunneling does indeed occur.

Appendices K through M list some review articles and talks by our group concerning this work.

C. LATERALLY QUANTIZED RESONANT TUNNELING STRUCTURES

After completing the initial phases of the work described above, we began fabricating laterally quantized resonant tunneling structures. Because of the central nature of this work, the fabrication, methods, and results are

described in detail in the following subsections. This work was presented at the 31st International Symposium on Electron, Ion, and Photon Beams, and details are given in Appendix N.

1. Microfabrication Approach

To study electron transport through quantum dots, we have adopted a microfabrication approach, which is summarized in Figure 1. After molecular beam epitaxy (MBE) growth of a resonant tunneling diode structure and formation of a backside ohmic contact, an e-beam lithography step is used to define an ensemble of quantum dots. A lift-off process will leave metal dots that will serve both as an etch mask and as a topside ohmic contact. A highly anisotropic reactive ion etching (RIE) process will proceed through the quantum well structure, producing the desired lateral confinement of the GaAs dots. A planarizing layer of dielectric material will be deposited and then etched-back to uncover the topside dot contacts. Finally, a gold layer will connect the quantum dots with a bond pad. Details of these steps are given in the following sections.

The MBE-grown resonant tunneling structure used for the fabrication was similar to that detailed in Appendix F: a 50 Å undoped GaAs spacer layer/50 Å $\text{Al}_{0.27}\text{Ga}_{0.73}\text{As}$ barrier/50 Å undoped GaAs quantum well structure, clad by thick ($\sim 0.5 \mu\text{m}$) n^+ GaAs contacts.

2. E-Beam Lithography

An initial patterned metal layer (AuGe/Ni/Au ohmic metallization) was defined on the GaAs wafers by contact optical lithography. This pattern was used primarily to facilitate the positioning of the e-beam exposed quantum dot structures and to allow careful focusing of the e-beam instrument to permit the finest possible dots to be exposed. The pattern defined 16 exposure sites per die with focusing structures near each exposure site. This pattern is shown in Figure 3.

To expose features on the order of $0.1 \mu\text{m}$ we used a JEOL scanning electron microscope that was modified to achieve a microlithography capability. The TI e-beam lithography instruments were not designed for ultra-high resolution work, and other high resolution electron microscopes at

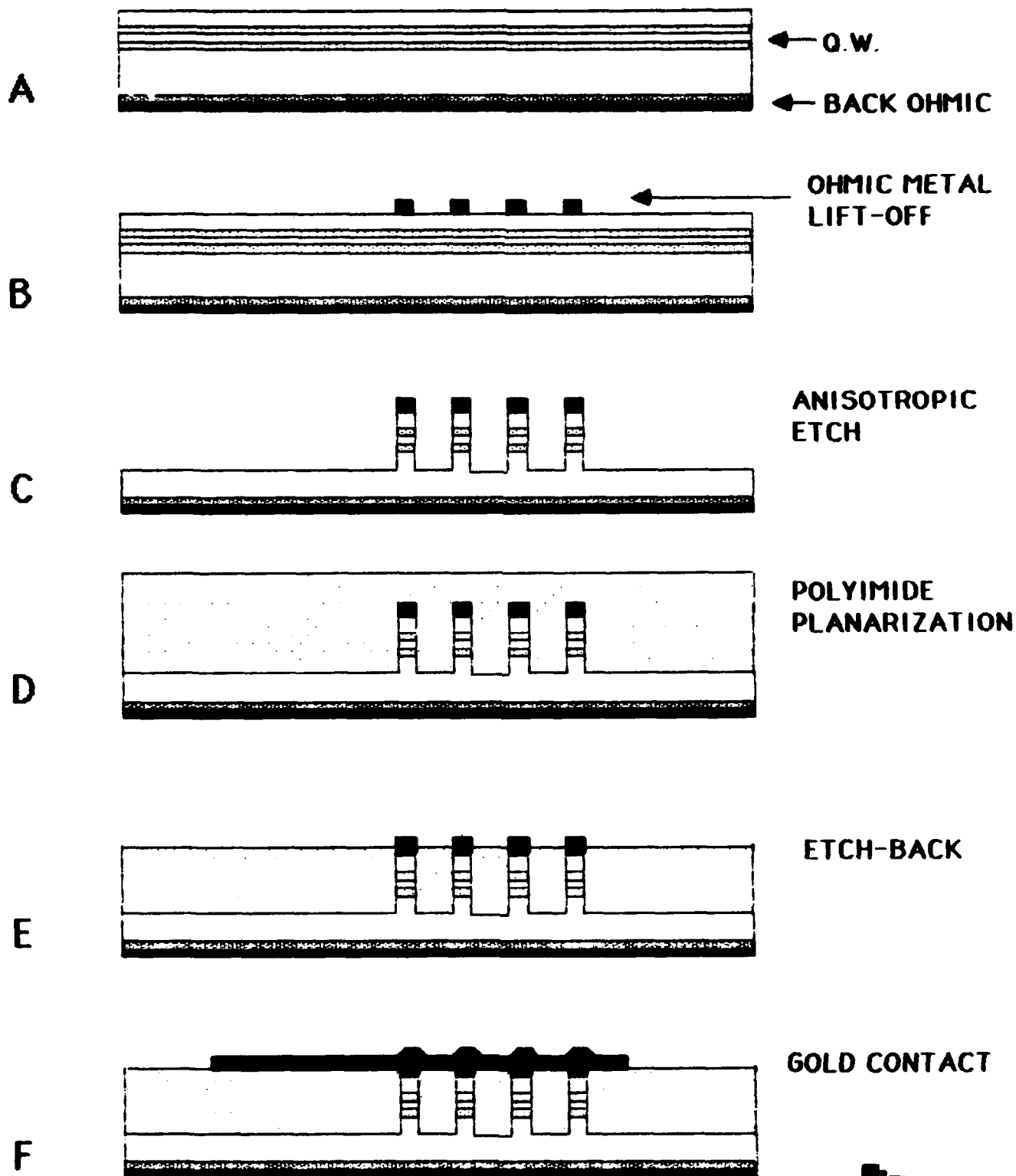


Figure 1. Schematic of fabrication sequence of quantum dot devices.

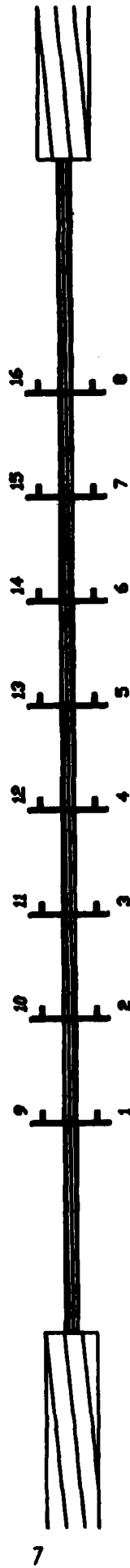


Figure 3. Pattern used for focusing and aligning e-beam exposures.

TI have no real lithography features at present. A Tracor Northern image and x-ray analysis unit attached to the JEOL SEM was used in conjunction with a Tracor Northern program to provide rudimentary patterning abilities.⁷ The beam scanning and blanking were computer controlled, as was the stage movement.

This system has some significant limitations as a lithographic tool. The stage motion is accomplished by stepper motors as an open loop system. The software attempts to reduce errors by overdriving and always approaching from one direction, but absolute positioning accuracy is no better than 2 to 3 μm . The design tool allows only a 256 x 256 pixel pattern; however, the DACs that control the beam allow a beam address of 1024 x 512 pixels (although the program addresses 512 x 512). Fortunately, the positioning accuracy and limited design capabilities are not serious limitations for this work. However, the discrepancy in the pattern design grid and beam address does create limitations in this case. The minimum feature, which is a single pixel, is exposed as four separate (spatially as well as temporally) beam flashes. This obviously limits the minimum dot size attainable with this system.

In spite of these limitations, we were able to expose some features that were 1000 \AA and slightly smaller. Other processing problems (see discussion on evaporation) limited our minimum dot size to approximately 1000 \AA .

Exposures on a single die included 13 different patterns, each written using a 10 μm wide field size. Therefore, each pixel is (ideally) a 393 \AA square. One of these patterns was a test pattern including square dots that ranged in size from as large as 9 x 9 pixels down to 1 x 1 pixels, all placed on 1 μm center spacings, as shown in Figure 4. This multidot pattern was used in the early stages of this work for process evaluation. It was also used as a development end-point indicator that was visible in an optical microscope.

Figure 5 shows the other 12 patterns that were used. The 3 x 3 pixel dots were exposed as 16, 9, and 4 dot arrays on 1 μm center spacing.

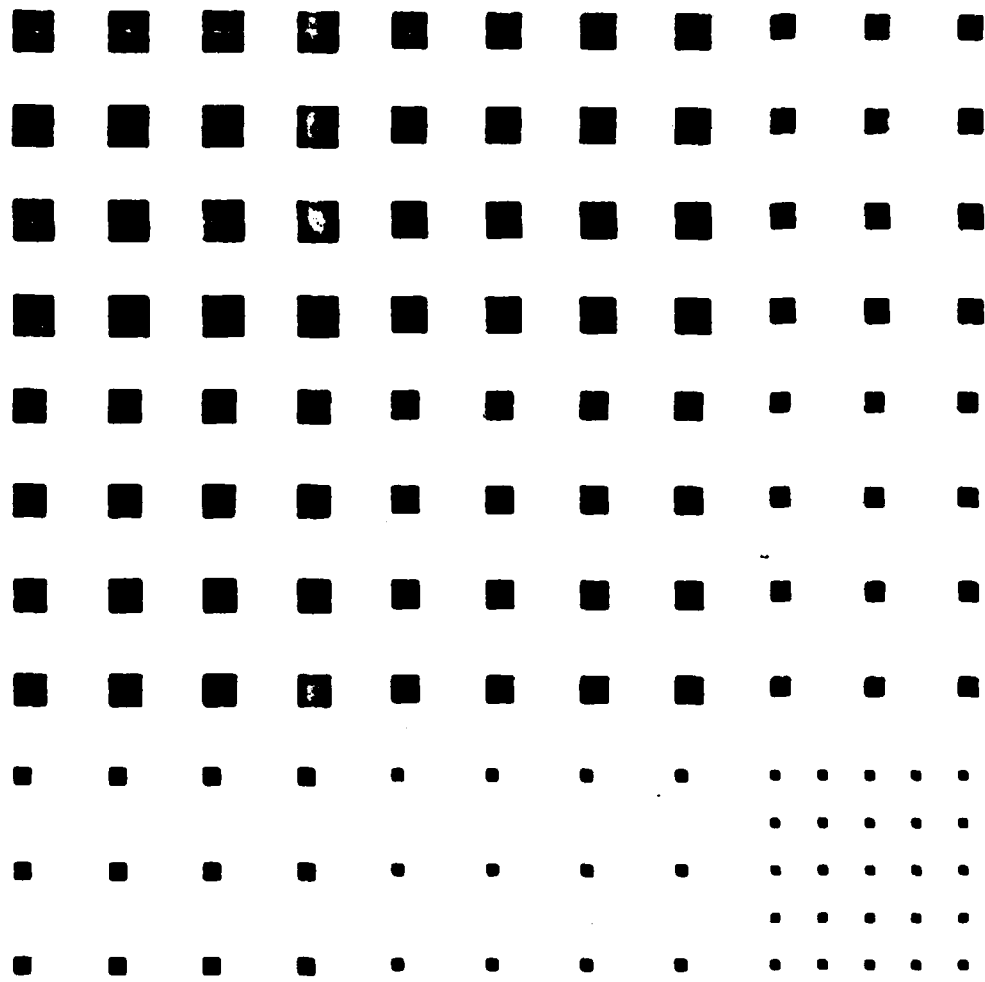


Figure 4. E-beam exposed test pattern referred to as "multidot".

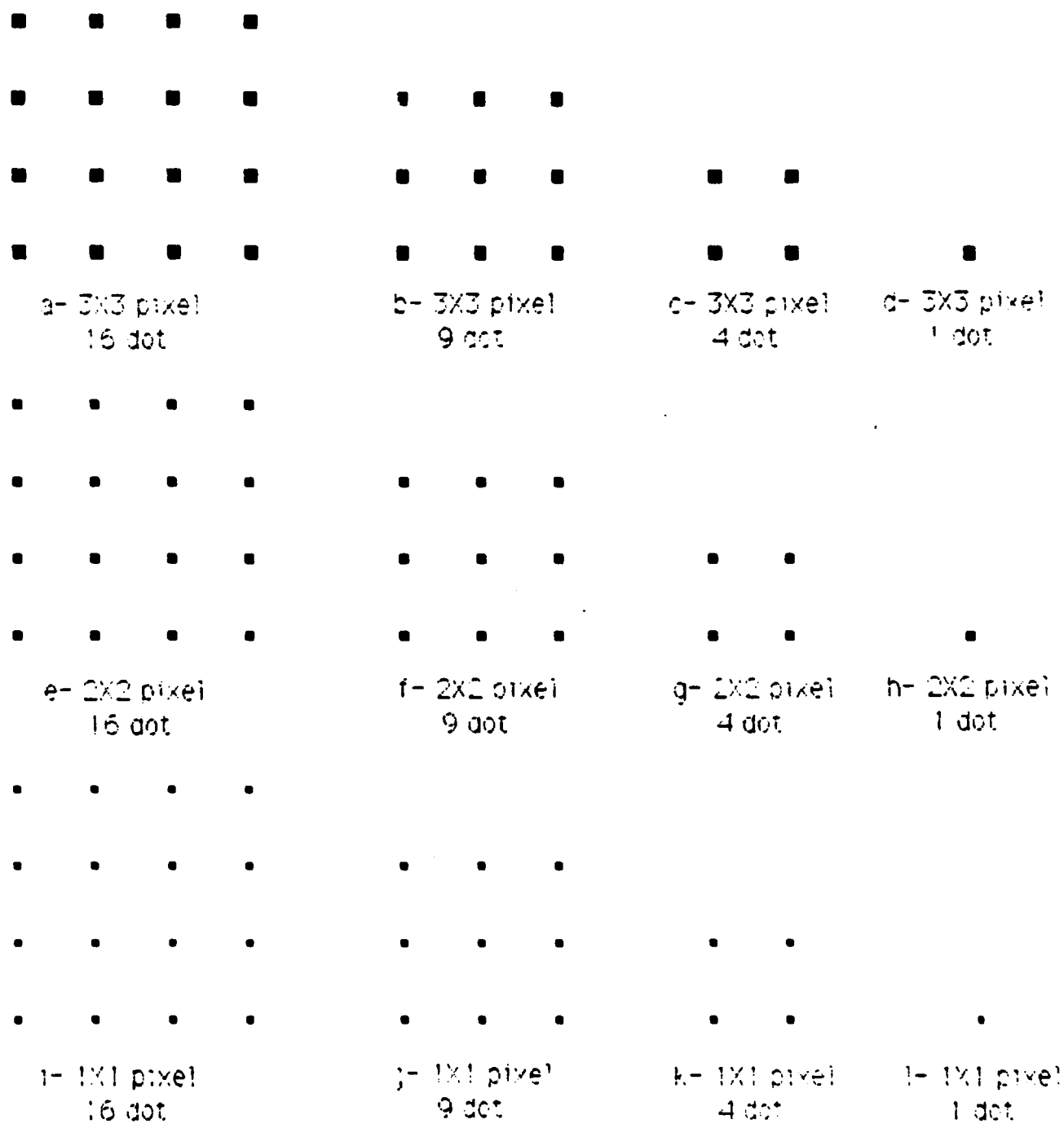


Figure 5. The 12 different patterns used for e-beam writing of quantum dots.

and as single dots. The 2 x 2 and 1 x 1 pixel dots were also exposed as arrays of 16, 9, and 4 and as single dots. The 16 exposure positions on a single die consisted of four multidot patterns, where one was exposed before and after each series of 1 x 1, 2 x 2, and 3 x 3 pixel dots.

The exposures were made with a 3 pA beam with 39 keV accelerating potential. At this small beam current the secondary electron signal from the gold pattern under the resist was not particularly strong. Therefore, significant care had to be taken to focus and stigmatize the beam while viewing the predefined focusing pattern on the sample. Even so, it was difficult to obtain a completely astigmatic beam for each exposure. We have no direct measurement of the spot size for these conditions, but from image resolution we estimate it to be 100 Å or less.

To successfully write all patterns, the dwell time for each e-beam flash (four per pixel) had to be set at 0.6, 0.9, and 1.8 ms for the 3 x 3, 2 x 2, and 1 x 1 pixel patterns, respectively. These conditions produced dots that had nominal diameters of 0.25, 0.15, and 0.1 µm. The progressively higher doses in terms of µC/cm² may be at least partially understood by the proximity effect inherent in electron beam exposures. Recent studies have shown that there is some anomalous energy deposition at 200 to 2000 Å radial distance from the beam center that does not fit the standard double Gaussian approximation and is not predicted by Monte Carlo modeling of electron beam interaction.^{8,9} We believe that this short-range proximity effect plays an important role in our exposures.

A bilayer resist scheme was used to aid the lift-off of the metal dots.¹⁰ The resist system consisted of a lower layer of 3000 Å thick, 450,000 molecular weight (MW) polymethylmethacrylate (PMMA) and a top layer of 1000 Å thick, 950,000 MW PMMA. The lower layer is more sensitive because of its lower MW and is expected to develop faster, producing an undercut profile as depicted in Figure 6. The 950,000 MW PMMA is in a xylene solution instead of the standard chlorobenzene, so that the top layer may be spun on with a minimum of mixing with the lower layer.

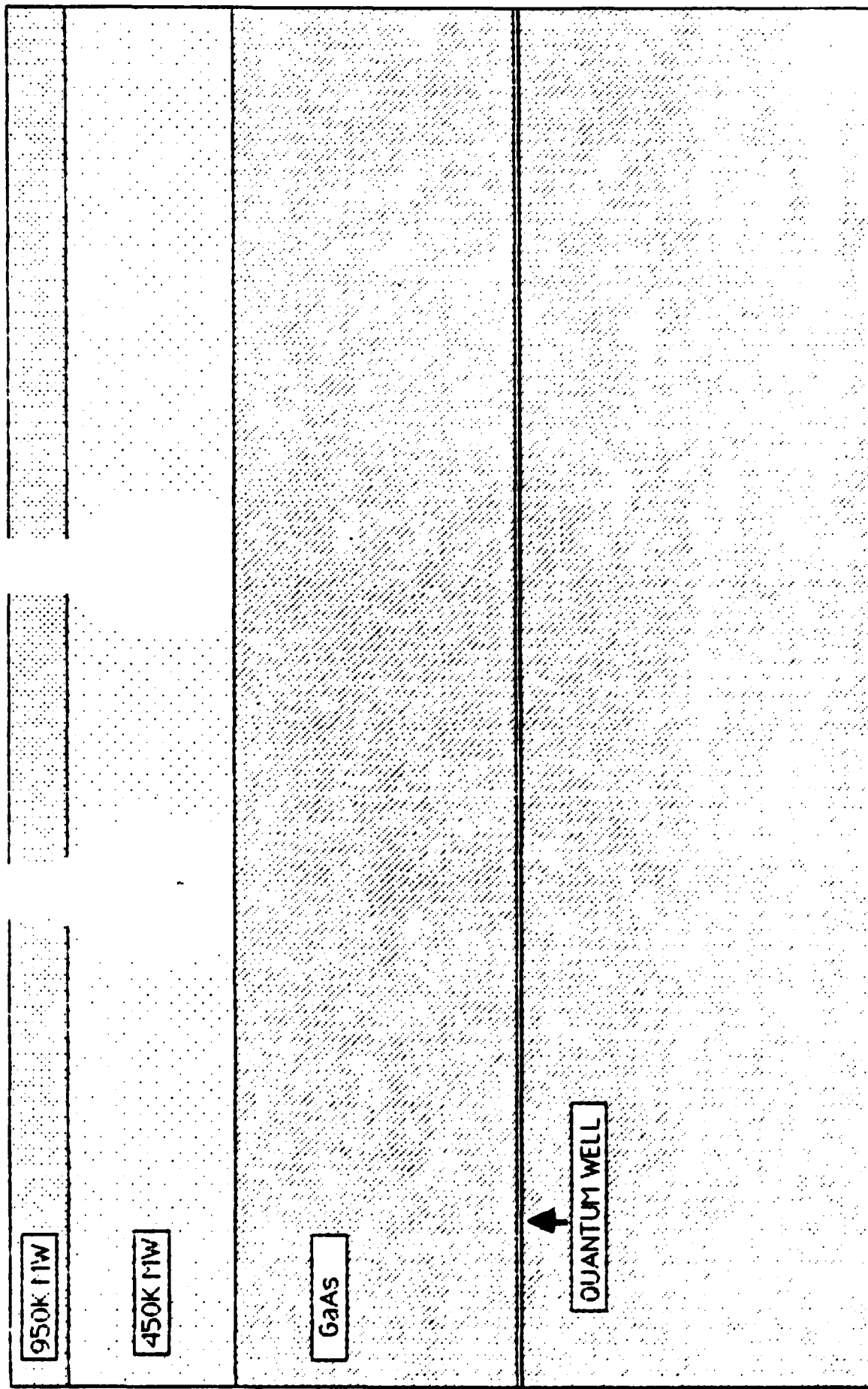


Figure 6. Schematic of undercut profile obtained with e-beam exposure of PNMA bilayer resist structure.

The metal dots that are lifted off must serve as both etch mask and ohmic contact. They are formed from three sequential evaporations: 500 Å of Au/Ge alloy (12% Ge), 150 Å Ni, and a top layer of 600 Å of Au.

The lift-off of features that are similar in size to the thickness of the layer to be lifted has significant limitations that are related to evaporator geometry. Metal atoms arriving at the sample with abnormal incidence may be deposited on the resist sidewalls rather than on top of the resist or at the bottom of the resist hole. This sidewall deposition reduces the opening so much that the hole can become completely closed. In this case the deposited dots become cone-shaped. The angular spread of the metal atoms impinging on the samples is determined by the evaporation source size and the source-to-sample distance. These two parameters are not easily adjustable in a given evaporator.

Because this deposition requires three metal layers and is accomplished in a resistively heated evaporator where there are three distinct evaporation sources, an additional effect occurs in the form of a lateral misalignment or displacement of the three layers. For the evaporator that was used, this amounts to a shift of 300 Å, which is significant when trying to create 1000 Å devices. The distributed source also exacerbates the metal deposition on the resist sidewalls. Figure 7 is an SEM of evaporated dots that clearly shows this misalignment of metal layers, as well as the conical shape due to the closing of the resist opening.

An ohmic contact was also formed on the backside of the Si doped GaAs wafer. This was accomplished by evaporating 500 Å AuGe, 150 Å Ni, and 1500 Å Au on the back of the wafer. This contact serves as a common ground for all the devices.

3. Reactive Ion Etching

The reactive ion etching (RIE) process used to etch down through the quantum well structure was developed to meet several criteria: excellent anisotropy, smooth etched surfaces, and a good high GaAs-to-Au etch ratio. It is also desirable to minimize etching induced damage. While no attempt was made to quantify etch damage, preference was given to etch conditions

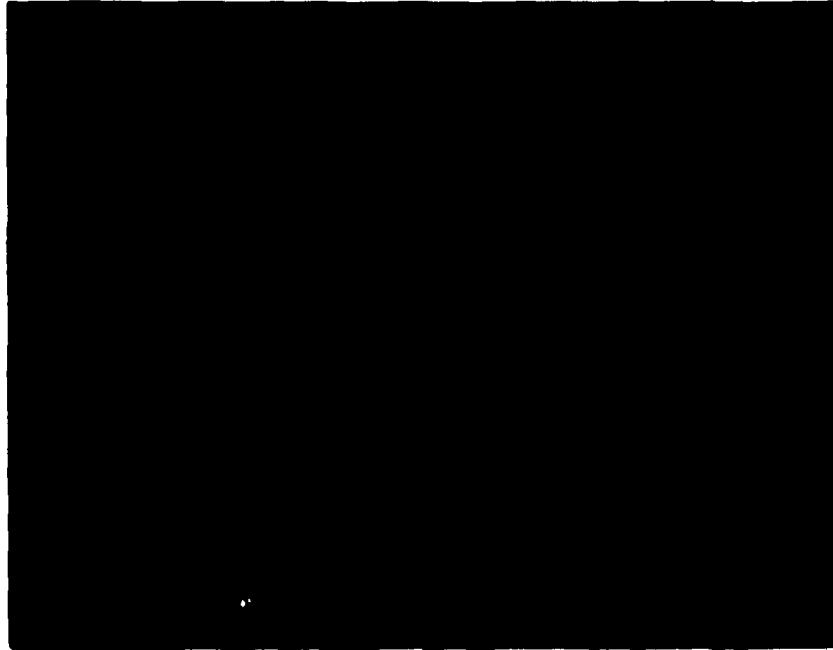


Figure 7. Scanning electron micrograph of lifted-off metal dots showing effects of distributed evaporation sources.

that provided lower ion energies. Some data suggest that lower ion energy results in less damage.⁸

Boron trichloride (BCl_3) was used as the etch gas, primarily because we have a significant amount of experience with its use. In addition, BCl_3 etches GaAs and AlGaAs at similar rates, which is desirable in this instance.

A large parameter space was explored by varying the pressure and flow (independently) of the etch gas, the self bias potential, and the electrode material. The following conditions were selected: a pressure of 30 millitorr, a flow of 30 SCCM, rf power to develop 300 V self bias potential, and a silicon electrode surface. These conditions provided a 300 Å/min GaAs etch rate, a 20 Å/min Au etch rate, excellent anisotropy, and reasonably smooth etched surfaces. There was some variability in the etch rates, and the above values are nominal.

For the quantum dot devices, we etched to a depth of at least 6000 Å to assure that the quantum well area (at a depth of 5000 Å) was completely isolated. It may be sufficient to etch down to the quantum well area, but not through it, and expect surface depletion to effectively isolate the quantum wells.⁹ However, by etching completely through the quantum well, we achieved unambiguous isolation, a known physical size, and an estimate of the extent of the surface depletion layer on the column surface. Figure 8 is an SEM that shows several quantum dot devices successfully reactive ion etched.

While we were successful in fabricating some quantum dot devices that exhibited NDR and fully ohmic contact behavior, other devices that were fabricated exhibited no ohmic contact behavior. The AuGe-Ni-Au ohmic contact is known to form an inhomogeneous interface with GaAs. Grains of different alloys are formed at this interface, and it is known that the conduction path of the ohmic contact is formed only in certain areas. When the size of the contact area is commensurate with the size of these grains, it is reasonable to expect that ohmic formation may be erratic. Nevertheless, in at least one case we produced a set of devices (a single die) in which all ohmic contacts

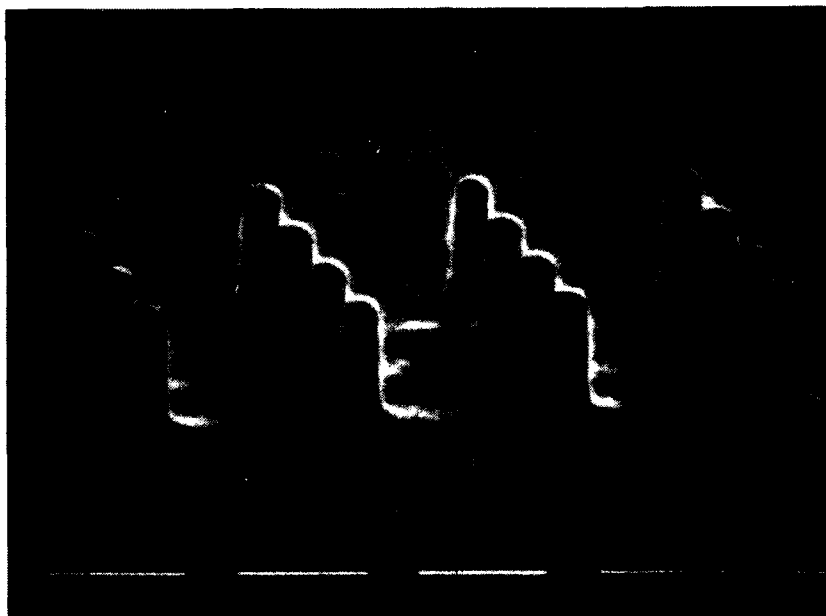


Figure 8. Scanning electron micrograph of RIE columns containing quantum dots.

were good. While the inhomogeneity of the ohmic contacts may explain our results, we also offer as speculation the following view.

We believe that the RIE GaAs/Au etch ratio was marginal for this process. We know that even when some of the top layer of Au is etched away, ohmic behavior will still be preserved. We speculate that when all the top layer of Au is removed and the etch proceeds into the AuGe/Ni region, the ohmic quality of the contact may be severely degraded. In our process the etching of 6000 Å of GaAs also removed 400 Å of Au from the top of the metal dots. If we had had the full thickness of the evaporated metal layers, this would have left 200 Å of the top Au layer. However, as mentioned above, misalignment of the ohmic metal layers and the closing of the resist openings yielded less than ideal metal layers in the lifted dots.

In our experiments the quantum dot devices were processed on small portions of wafers with only one or two chips at a time. When good ohmic contacts were formed, nearly all devices worked. When the quantum dot devices did not form good ohmic contacts, larger diodes in the multidot patterns (which are less sensitive to the metal layer misalignment and resist hole closing and should have full metal thicknesses) demonstrated good ohmic behavior. This observation is in agreement with our hypothesis of marginal etch ratio.

At some stage the metal dots were alloyed for 2.5 minutes at 430°C. In some cases the alloying was done prior to the RIE step and in other cases, after. We looked for evidence of migration of the metal when alloying was carried out after the RIE step and observed none. While we were more successful with samples that were alloyed after RIE, the data are insufficient to determine if this is a significant factor.

4. Contacting Quantum Dots

To make electrical contact to the ohmic contacts at the top of the isolated quantum dot diodes, a planarizing layer of polyimide was spun on the wafer. The polyimide was etched with O₂ RIE until the metal contacts on the quantum dot devices were uncovered. In this way direct electrical contact could be made to the devices.

The polyimide layer did not effectively planarize the optically defined pattern. However, planarization in the area of the quantum dot devices was quite good when a layer approximately $1.4 \mu\text{m}$ thick was spun on and allowed to settle for two hours prior to curing.

The reactive ion etching of the polyimide was carried out in short stages while we were monitoring the thickness of the polyimide in the relevant regions by diffraction color and inspecting the sample in an SEM. In some SEM viewing conditions the dielectric polyimide will charge positively and will therefore appear very dark when imaged using secondary electrons. This permits very easy determination of the emergence of the metal contacts of the quantum dot devices that are conductive and provide a strong secondary electron image. Figure 9(a) is an SEM of a group of devices that have had the polyimide etched just enough to uncover the ohmic contacts. Figure 9(b) shows a multidot group of devices in which imperfect planarization has led to exposure of some of the contacts, while others are still covered by a thin layer of polyimide.

The fabrication is completed by patterning a metal layer that contacts the devices. The pattern is shown in Figure 10. The metal layer consists of 100 \AA of Ti for adhesion and 2000 \AA of Au. The 16 pads are used for probing and wire bonding when the chips are mounted in a 16-pin DIP.

5. Electrical Transport Data

To determine the effects of lateral quantization on transport, we fabricated and measured large lateral area devices as well as quantum dot devices. Figure 11 shows the room temperature I-V characteristic of a large area ($2 \mu\text{m}^2$) resonant tunneling diode fabricated by chemical mesa etching from the MBE material discussed above. The structure exhibits a 1.6:1 peak-to-valley tunnel current ratio and a current density at resonance of $1.6 \times 10^4 \text{ A/cm}^2$.

We then examined transport through the quantum dot structures. Figure 12 shows a similar I-V characteristic of a single quantum dot resonant tunneling structure at 300 K. The structure clearly shows negative



Figure 9. Scanning electron micrographs taken during polyimide etch-back process: (a) metal contacts of quantum dot devices appearing above polyimide layer. (b) partial clearing of polyimide from multidot pattern.

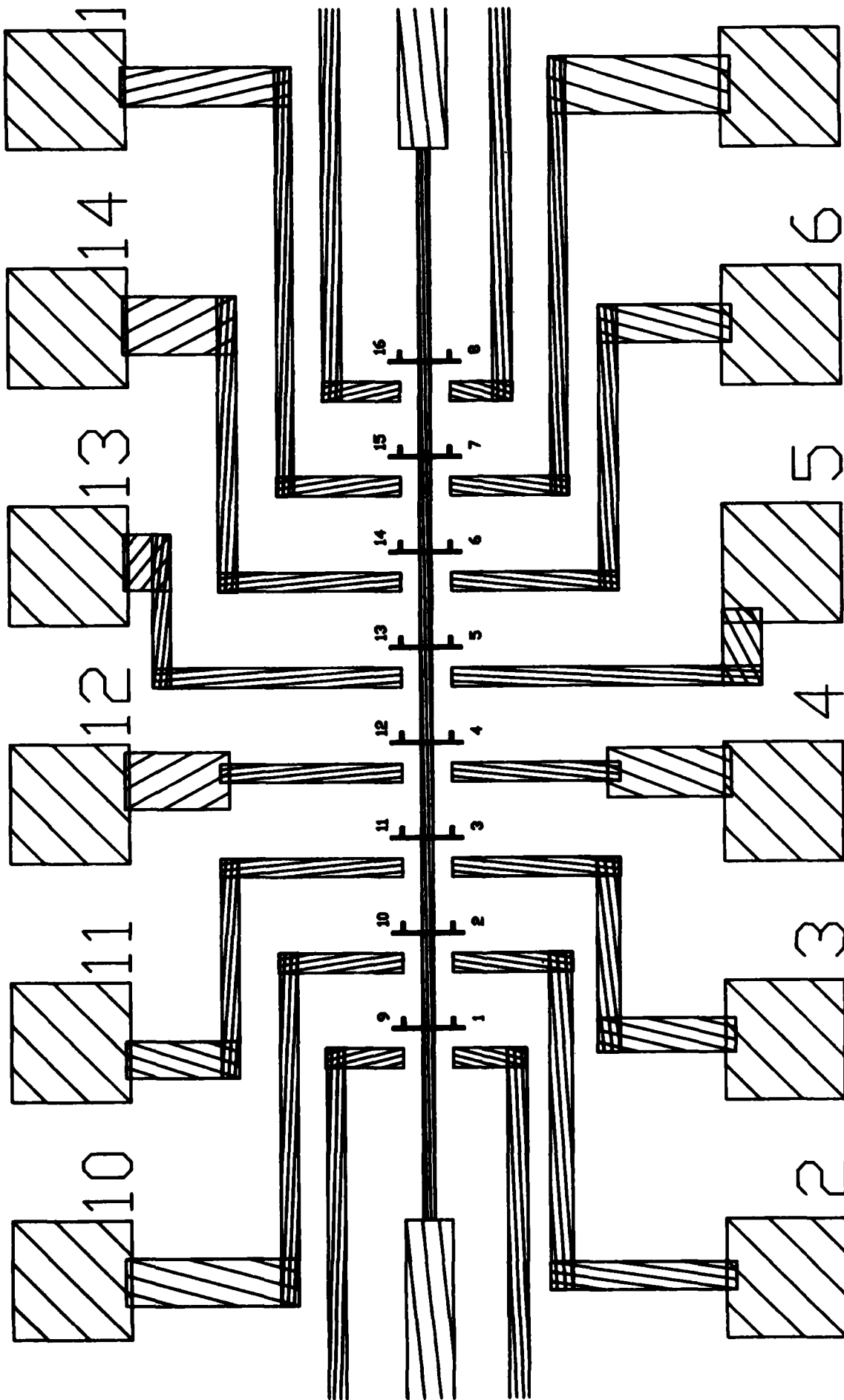


Figure 10. Pattern used to contact quantum dots, including alignment level.

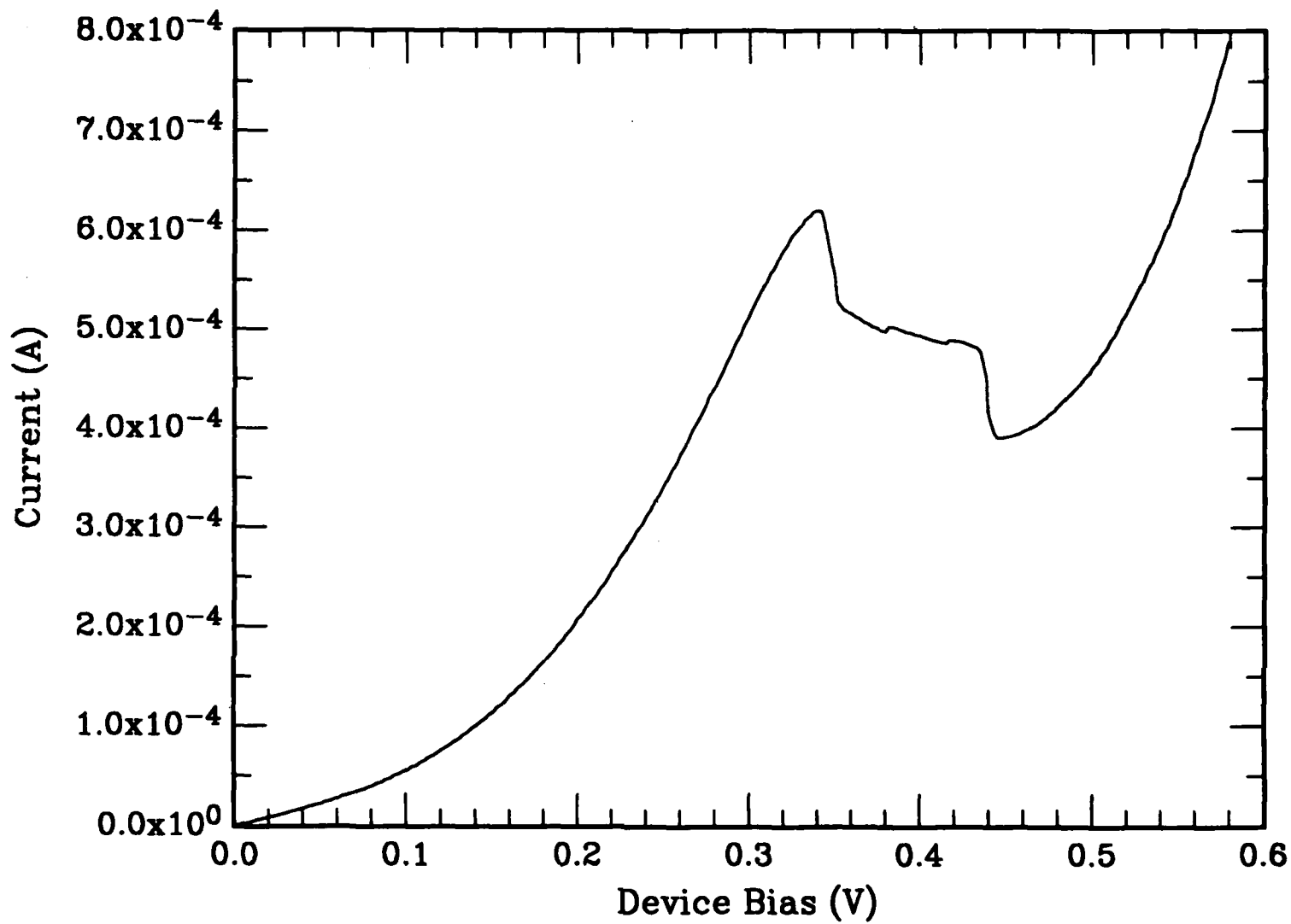


Figure 11. I-V trace at 300 K of a $4 \mu\text{m}^2$ resonant tunneling large area device.

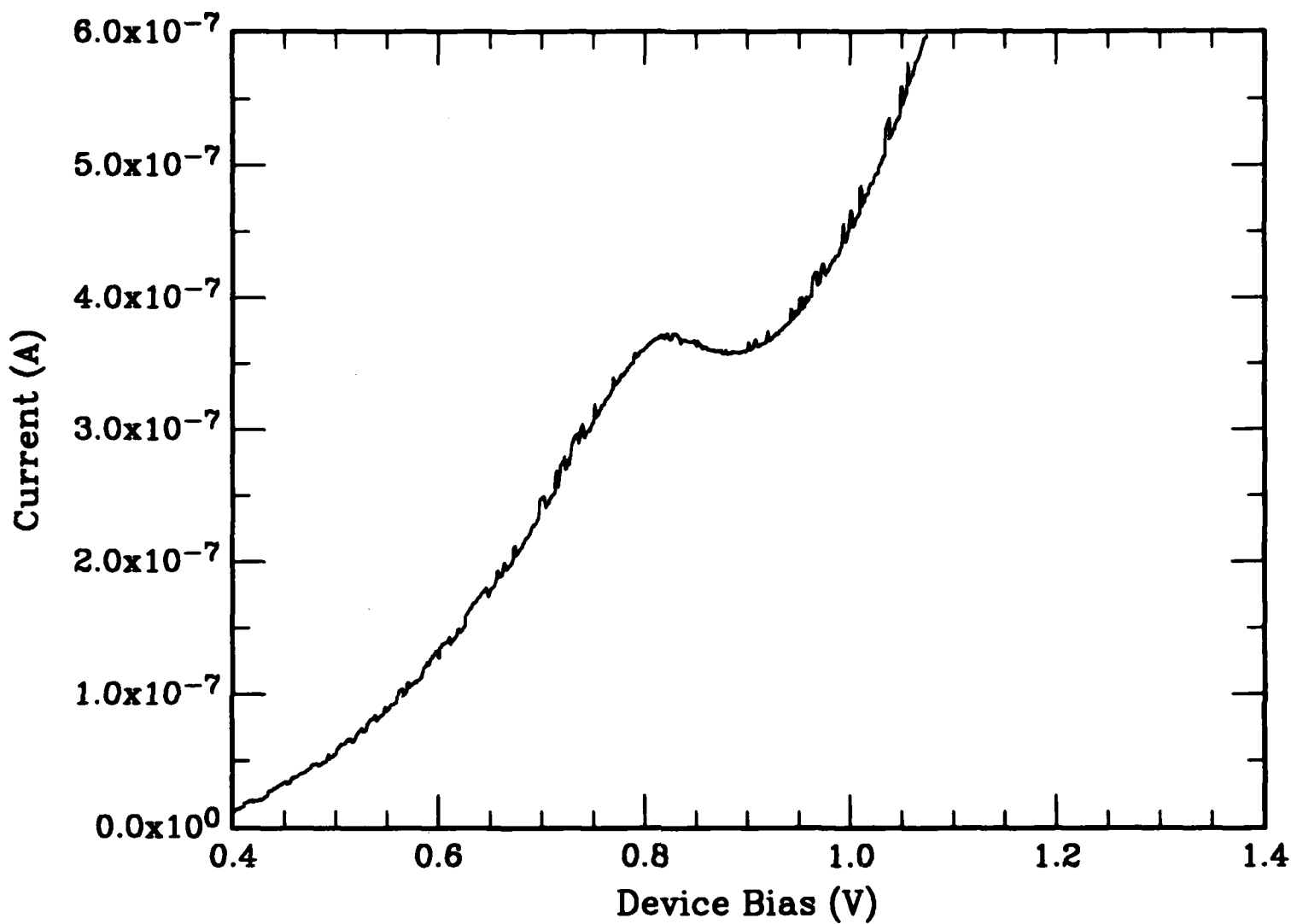


Figure 12. I-V trace at 300 K of a single quantum dot of the 2 x 2 pixel dimension (approximately $0.25 \times 0.15 \mu\text{m}$).

differential resistance (NDR), though the peak-to-valley ratio is degraded from that of the large area structure, probably because of process damage. The I-V characteristic clearly exhibits a "noise" that is far above the system background noise. The origin of this noise is the so-called "single electron switching" phenomenon¹³ that has been observed in narrow Si MOSFET wires. Traps in or near the narrow conduction channel and/or near the Fermi level can emit or capture electrons with a temperature-dependent characteristic time. This can be seen in Figure 13, where the switching is better defined at 100 K than at 300 K. Since the switching rate is thermally activated, there will be a temperature range (a priori expected to be rather random for the different traps) over which the effect is observable. These traps can be "frozen out," as we see in Figure 14, where the temperature has been lowered to 4.2 K.

The trap switching rate is not only temperature dependent, but also naturally dependent on the position of the Fermi level relative to the trap, i.e., the device bias. The lowering of specific traps through the Fermi level is clearly evident (at 0.6 V, 0.8 V to 0.85 V, and 1.0 V to 1.1 V).

Figures 15 and 16 show a time-dependent trace of the current through this device at fixed bias voltage, at $T = 84$ K. Figure 15 shows clear switching between two discrete resistance states at $V = 0.71$ V, implying the trapping and detrapping of single electrons onto the same trap. At higher device bias (0.875 V), the switching due to a number of traps is evident.

We also examined the larger 3×3 single dot structure (the 1×1 was inoperative) and other multiple dot patterns and found results similar to those presented here.

We attempted to determine the activation energy of one of the traps shown here, but experienced sudden device failure at low temperature before these data could be completed. The mechanism for this failure is unknown.

The relatively large size of the device (let us consider in detail the 2×2 device) makes the observation of such an effect a little suspect.

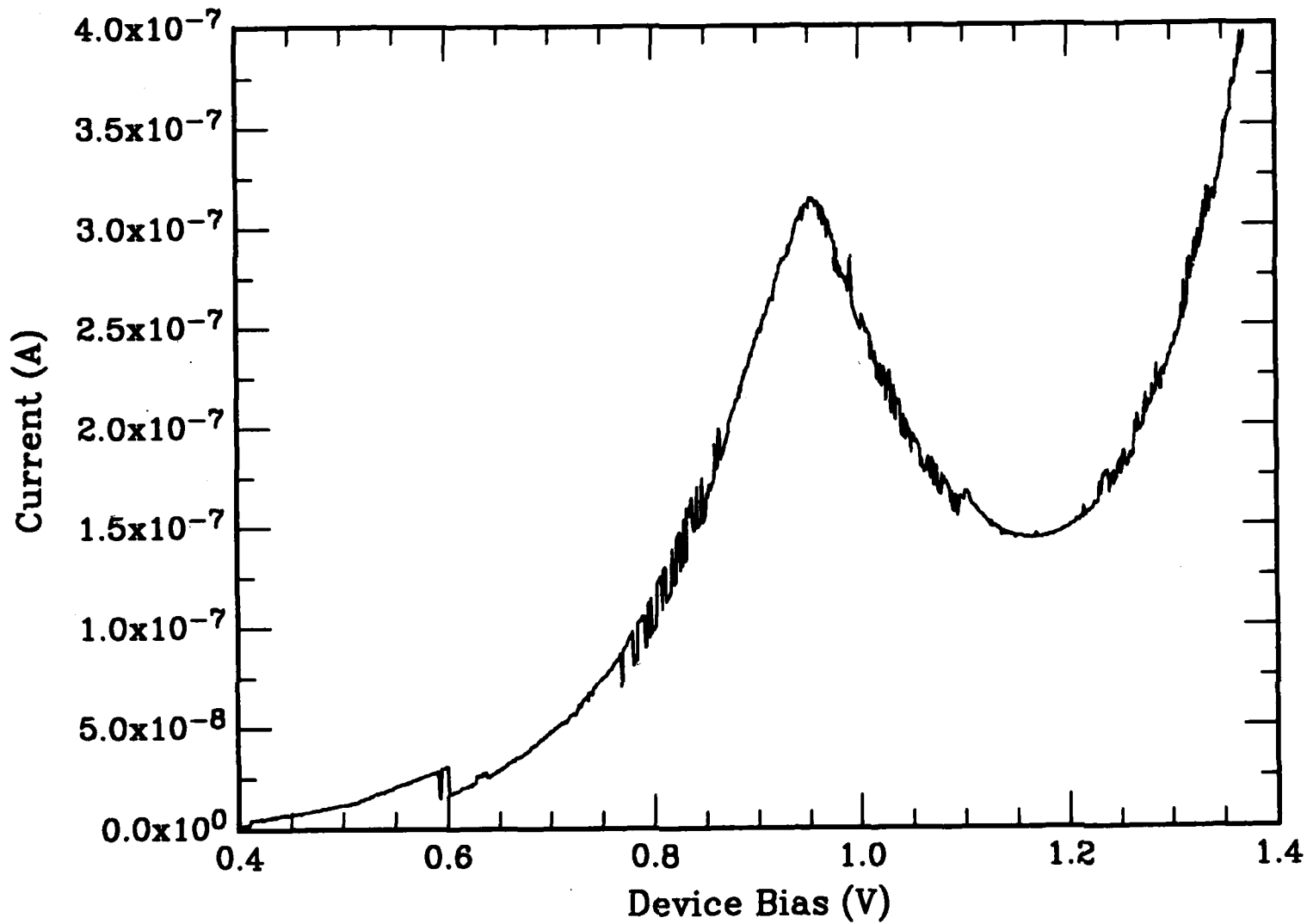


Figure 13. I-V trace at 100 K of a single quantum dot of the 2 x 2 pixel dimension (approximately $0.25 \times 0.15 \mu\text{m}$).

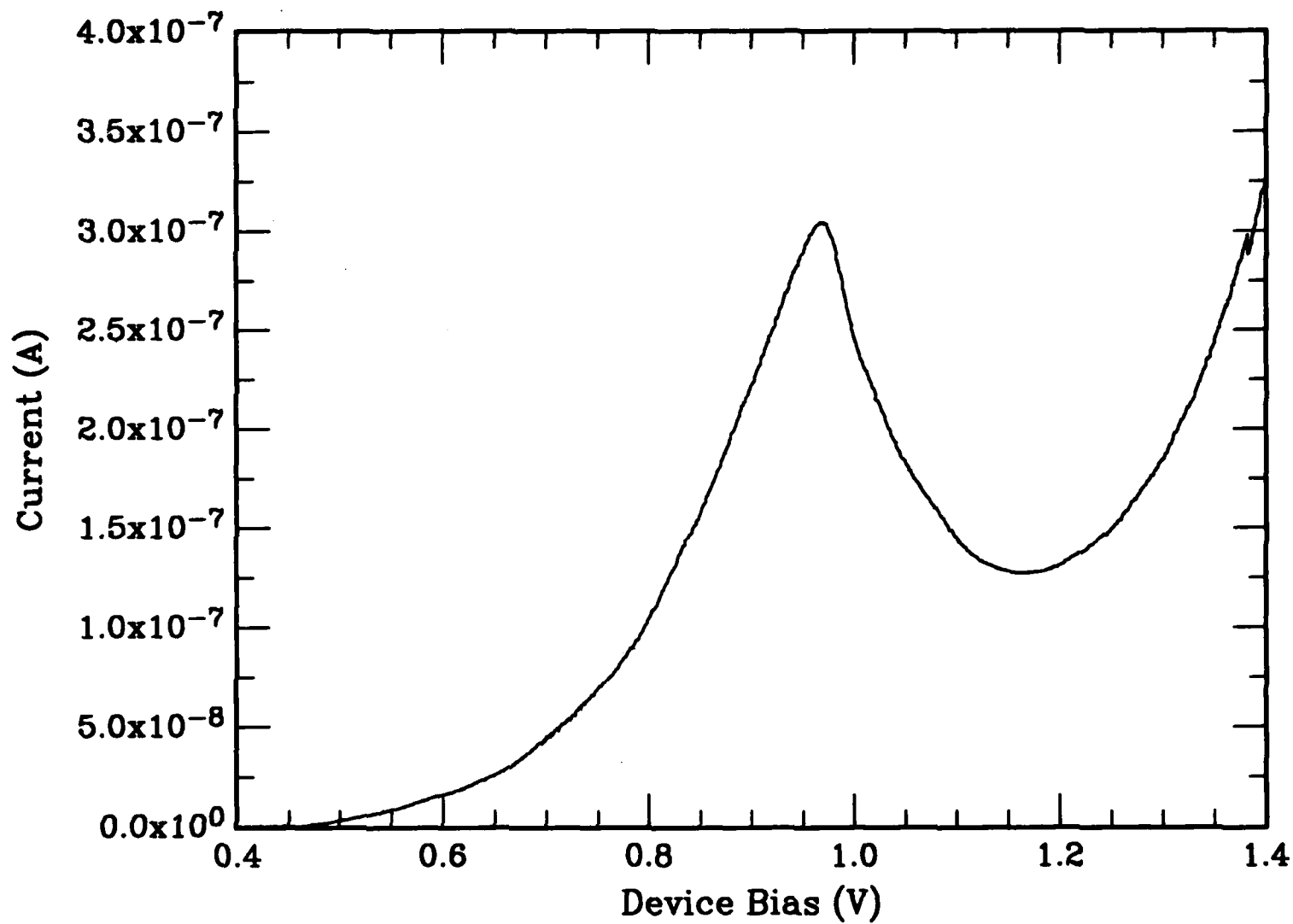


Figure 14. I-V trace at 4.2 K of a single quantum dot of the 2 x 2 pixel dimension (approximately $0.25 \times 0.15 \mu\text{m}$).

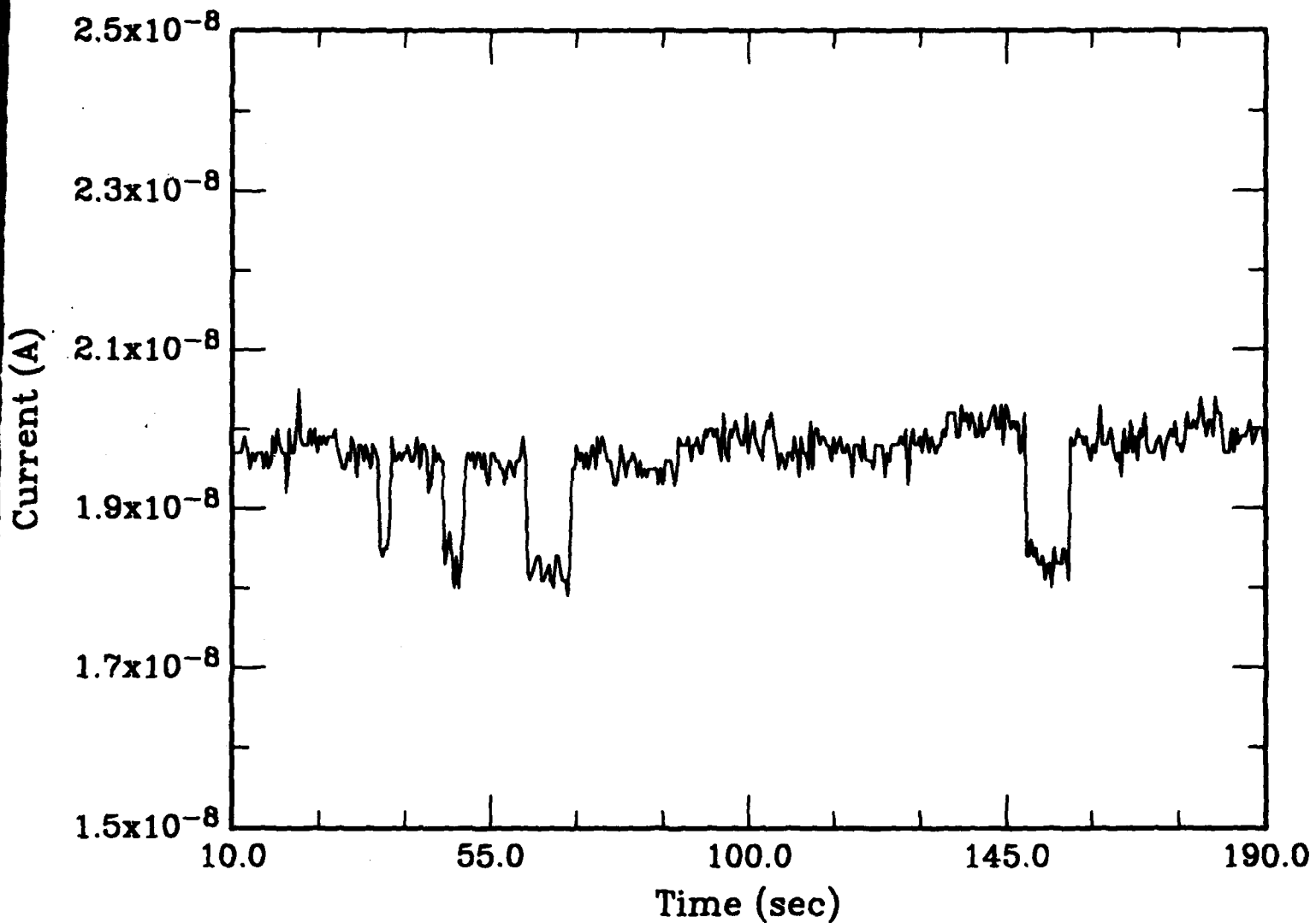


Figure 15. Time-dependent current fluctuations at a fixed bias of 0.71 V of the single quantum dot of the 2 x 2 pixel dimension (approximately $0.25 \times 0.15 \mu\text{m}$). $T = 84 \text{ K}$.

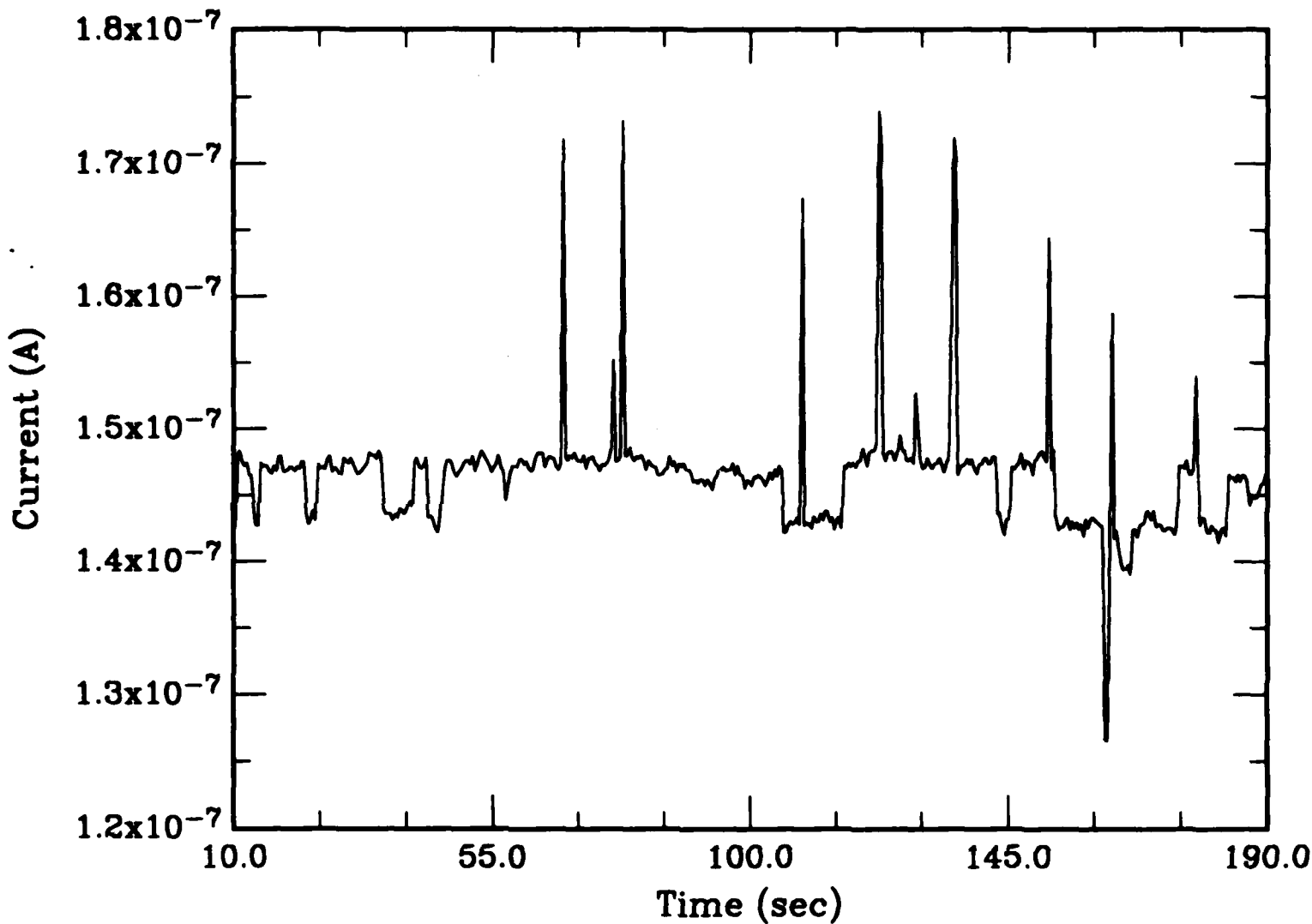


Figure 16. Time-dependent current fluctuations at a fixed bias of 0.875 V of the single quantum dot of the 2 x 2 pixel dimension (approximately 0.25 x 0.15 μm). T = 84 K.

However, the effects of depletion at the etched mesa surfaces have not been taken into account. Taking the observed current at resonance and assuming that the current density must be the same as in the large area device, we calculate that the effective (circular) conduction path diameter is $\sim 500 \text{ \AA}$, consistent with the observation of the switching phenomena. This implies a depletion layer of approximately 1000 \AA .

At these lateral dimensions, splitting of the quantum well resonance due to lateral size quantization should be observable. High resolution scans have been performed at 4.2 K and 1.2 K (similar to Figure 14) around the NDR peak, but no definite indications of lateral quantization have been observed.

IV. SILICON STRUCTURES

During the first half of the contract, we fabricated and characterized silicon tunneling structures. A brief account of this work is given here. A more extensive report is given in Appendix P.

Conduction at high fields in thin layer stacks of materials commonly used in silicon integrated circuit processing has been examined. These results show that Fowler-Nordheim tunneling is the dominant conduction process in metal-oxide-silicon single- and multiple-dielectric systems. When included in these structures, intrinsic (undoped) polycrystalline silicon is essentially depleted of carriers and acts as a second dielectric. Correction of the field strength in the oxides in these stacks to account for the bias dropped across the polysilicon results in a single set of parameters characterizing the tunneling process, which shows a rapid onset in the vicinity of 5 MV/cm. Conduction in series combinations of polycrystalline silicon and extremely thin oxides is dominated by Schottky barrier tunneling at aluminum-polysilicon interfaces, probably caused by defective thin oxides.

Four lots of test devices were studied. In all cases the test devices consisted of capacitors ranging from 5.63×10^{-4} to 2.1×10^{-2} cm². Best results were obtained on the 5.63×10^{-4} cm² capacitors. In general, the vertical structure consisted of a thermal oxide on silicon, undoped polycrystalline silicon of various thicknesses, and an aluminum contact layer. All oxides were grown at 900°C in dry oxygen. All poly layers were deposited at 600°C in a hydrogen ambient.

All oxide thicknesses were measured by ellipsometry immediately after growth. Although in some cases reliable thickness measurements on the thinner oxides was difficult, it was possible to get repeatable figures on all slices. Following metal patterning, the high frequency capacitance versus voltage characteristic was obtained. In the case of MOS stacks this provided an independent measurement of oxide thickness, and where possible, was a reliable measure of poly thickness in stacks containing one or more poly layers. Slow sweep I-V characteristics were obtained on all devices, to breakdown on at least two devices on each slice.

The slow sweep I-V characteristics were replotted as $\ln (J/E_{ox}^2)$ vs $1/E_{ox}$, and a linear region was found. Fowler-Nordheim parameters that were in reasonable agreement with published figures from similar structures were obtained from the devices in two of the three lots characterized electrically. The third lot showed evidence of a lack of continuity in both oxide and poly layers for layer thicknesses less than 50 Å. In the first two lots, Fowler-Nordheim tunnelling was the dominant conduction mechanism. In the third lot, conduction was controlled by an Al-silicon Schottky barrier, due to the lack of integrity in the oxide and poly layers. Some structures in the third lot had considerably thicker polysilicon layers, and these devices showed a resistive behavior attributed to the undoped polysilicon.

The biggest problem encountered in this part of the program was control of process variables. It was not possible to obtain the desired structures reproducibly. The same oxide growth parameters that resulted in 80 Å films in one lot produced 160 Å oxides in the next. Poly deposition parameters that produced 80 Å poly layers in one lot produced 1300 Å layers in the next. While it is true that extensive experience in silicon processing technology can benefit a quantum coupled structure program, it is clear that these structures cannot be fabricated in a production front-end. Parameters required for the thin layers in quantum coupled structures are sufficiently different from those used in present devices to require recalibration of the apparatus used. This is not desirable in a production front-end.

Two items are particularly striking in this program: one is the extraordinary progress made in quantum coupled devices fabricated in GaAs; the other is the difficulty encountered in adapting current silicon technology to approach ultrasmall dimensions. It seems clear that fabrication facilities dedicated to nanometer range films will be required to obtain quantum coupled structures in silicon.

V. RECOMMENDATIONS FOR FURTHER WORK

A. FABRICATION

The significant progress made in the fabrication of quantum dot diodes is extremely encouraging. The fact that reasonable operation of the devices was obtained with the relatively simple processing techniques employed suggests that a number of modifications in the processing could produce superior results. Processing improvements could be made in several areas, as discussed below.

1. Molecular Beam Epitaxy

A significant advantage of the nonalloyed ohmic contacts would be the ability to reduce the thickness of the GaAs contact layer. This would reduce the demands on the anisotropic etching of the material and would allow the use of a shorter and potentially less damaging etch process. In addition, eliminating the requirement for the multimetal lift-off would eliminate many of the complications mentioned in the fabrication section. The ability to lift off a single metal that has better dry etching resistance than Au would permit a thinner layer (in part due to the reduced GaAs contact thickness), which would facilitate lift-off of smaller dots and would be a simpler, more reliable process.

A possible solution would be the use of an InAs top layer. The pinning of the Fermi level in the gap for InAs allows a nonalloyed contact to be formed for nearly any metal chosen and would eliminate the angular resolution problem of multiple evaporated sources. TI has a demonstrated capability in the MBE growth of In compounds, not only for "bulk" applications, but also for complex strained-layer resonant tunneling structures (Appendix O).

2. Patterning

The lithographic technique used to pattern the dots is obviously a critical stage of the fabrication. Several facets of the method used thus far could be improved, such as resolution, placement accuracy, dimensional control, and induced damage.

We have ordered a state-of-the-art e-beam lithography tool that would provide superior resolution and placement accuracy. Considerable research is also needed on the details of high resolution e-beam patterning, which could aid in the understanding of this process. Advances in e-beam patterning capabilities will be required for quantum effect devices to be practical. However, the most significant benefit could be obtained by using an entirely different lithographic technique.

Masked ion beam lithography (MIBL) is capable of short exposure times, has demonstrated 400 Å resolution, and is capable of printing features down to approximately 100 Å.^{14,15} The major advantage of MIBL for this work is its unparalleled linewidth control.¹⁶ When lithography is performed with e-beam instruments near the limits of their resolution, the feature sizes are a strong function of the particular beam size and shape. While it is entirely possible to write sub-1000 Å dots with e-beam lithography, it is extremely difficult to carefully control the size of the features. With MIBL it is possible to reliably obtain sub-1000 Å features with very tight control of size.

High resolution e-beam lithography is still required, of course, to fabricate MIBL masks, and one cannot be assured that any one mask patterned by e-beam will have dots of exactly the size desired. However, once the mask is fabricated, MIBL will permit the patterning of dots with excellent feature size control time after time. There is added advantage in the possibility of doing e-beam patterning when the masks are thin membranes, thus reducing the backscattering effect and possibly improving resolution.¹⁷

MIBL also offers the potential of eliminating damage induced by the lithography step. The range of protons in solids is relatively short, approximately 1 μm/100 keV. By adopting a simple bilayer resist approach and adjusting the energy of the exposing protons, it is possible to avoid any deposition of energy in the semiconductor substrate. This is not possible with e-beam lithography.

Texas Instruments has a collaborative program with the University of Houston to develop and use MIBL. Dr. J. C. Wolfe will soon have a 200 keV

proton exposure tool and currently has all the required experience and facilities to produce high resolution MIBL masks. Through this association we should be able to capitalize on the capability of MIBL to produce large quantities of uniform dot patterns with no process-induced damage.

3. Anisotropic Etching

As discussed in the fabrication section, the RIE technique was marginal with respect to etch ratio and is probably responsible for some degree of semiconductor damage. Several possibilities could improve both situations: (1) a systematic investigation of etch-induced damage could be accomplished; (2) other etch gases could be explored; and (3) improvements could be made to the RIE apparatus, such as incorporating a load lock mechanism. Optimization of the RIE process step will result in improved electrical performance of the quantum dot devices.

While reactive ion etching is a powerful and effective anisotropic dry etching technique, other alternatives also look promising. Ion beam assisted etching¹⁸ and hot jet etching¹⁹ have proved viable for etching GaAs and have potential advantages over RIE in terms of cleanliness, selectivity, and damage control. One of these two techniques could be an extremely effective method of fabricating quantum dot devices. Hot jet etching may be particularly effective in reducing damage, since no ion beam is used during etching. We believe it would be prudent to attempt to develop these techniques and compare them to RIE, and to each other, especially with regard to etch-induced damage.

B. THEORY/EXPERIMENT

The demonstration of a practical formulation of quantum transport theory under the present contract is a major accomplishment that should be extended in several directions. For instance, a more detailed description of the interaction between a device and its contacts must be developed. In addition, the treatment of incoherent processes within the device requires more careful consideration. For example, is it correct to use the same sort of collision operator for random elastic scattering (as from impurities or alloy variations) as that used for inelastic (phonon) scattering? Finally, the structure of the theory itself needs more thorough examination. The

importance of the eigenvalues of the Liouville operator is pointed out in Appendix C, but what is the significance of the associated eigenfunctions? A deeper understanding of such issues could lead to an intuitive understanding of the workings of quantum devices that will permit their technological development to be pursued more effectively.

To provide a theoretical basis for the understanding of experimental data on laterally quantized structures, a means for extending quantum transport theory to such structures must be developed. This is more difficult than we believed at the inception of this contract, and it will certainly require much greater computer power than does the one-dimensional problem.

The observation of single electron trapping phenomena in quantum dot tunneling demonstrates that we have confined the transport to dimensions necessary for lateral quantization. It is also encouraging that only a small number of traps are present. Measurements of the activation energies, the magnitude of the switching, etc., would allow a study of the types of traps generated as a function of process variables to determine the least degrading fabrication processes. This could also be correlated to the sudden failure of devices that we have observed.

The absence of fine structure in the characteristics due to lateral quantization is puzzling. Is the "roughness" of the depletion layer responsible? Is a different (contact) electron distribution necessary, and would this be the same for ground and excited states? Can the application of a magnetic field (parallel to the current direction) minimize edge effects? We recommend a further effort to determine the cause for the absence of the fine structure in these devices.

REFERENCES

1. R. T. Bate, presented at Fourth Workshop on the Physics of Submicron Structures, Champaign, Illinois, (1983); R. T. Bate, presented at 1984 Device Research Conference, Santa Barbara, California; G. H. Heilmeier, Proceedings of the 1984 IEDM, Section 1.1, p.2.
2. Texas Instruments Proposal No. 25-R83 (1983); National Research Council Report on Artificially Structured Materials pp.79-82, (1985).
3. M.A. Reed and R. T. Bate, "Process for Fabricating Quantum Well Devices" U.S. Patent No 4,575,424, issued March 18, 1986.
4. K. Kash, A. Scherer, J. M. Worlock, H. G. Craighead, and M. C. Tamargo, Appl. Phys. Lett. 49, 1043 (1986).
5. J. Cibert, P. M. Petroff, G. Dolan, D. J. Werder, S. J. Pearton, A. C. Gossard, and J. H. English, Appl. Phys. Lett. 49, 1275 (1986).
6. A. Scherer and H. G. Craighead, Appl. Phys. Lett. 49, 1284 (1986).
7. P. E. Russel, T. North, and T. M. Moore, Microbeam Analysis - 1986, A. D. Romig and W. F. Chambers eds. (San Francisco Press, San Francisco, CA, 1986), pp.663-666.
8. J. A. Oro, Ph.D. Thesis, Electrical Engineering Dept., University of Houston, 1987.
9. D. M. Tennant, G. E. Doran, and R. E. Howard, Presented at the 31st International Symposium on Electron, Ion, and Photon Beams, May 26-29, 1987, Woodland Hills CA.
10. M. J. Rooks, P. McEuen, S. Wind, and D. E. Prober, Mat. Res. Soc. Symp. Proc. 76, 55, (1987).

REFERENCES

(Continued)

11. S. W. Pang, G. A. Lincoln, R. W. McClelland, P. D. DeGraff, M. W. Geis, and W. J. Piacentini, *J. Vac. Sci. Technol.* B1, 1334 (1983).
12. S. Thoms, I. McIntyre, S. P. Beaumont, M. Al-Mudares, R. Cheung, and C. D. W. Wilkinson, Presented at the 31st International Symposium on Electron, Ion, and Photon Beams, May 26-29, 1987, Woodland Hills CA.
13. K. S. Raals, W. J. Skocpol, L. D. Jackel, R. E. Howard, L. A. Fetter, R. W. Epworth, and D. M. Tennant, *Phys. Rev. Lett.* 52, 228 (1984).
14. J. N. Randall, D. C. Flanders, N. P. Economou, J. P. Donnelly, and E. I. Bromley, *Appl. Phys. Lett.* 42, 457 (1983).
15. J. N. Randall, D. C. Flanders, N. P. Economou, J. P. Donnelly, and E. I. Bromley, *J. Vac. Sci. Technol.* B3, 58 (1985).
16. J. N. Randall, *J. Vac. Sci. Technol.* A4, 777 (1986).
17. C. D. W. Wilkinson and S. P. Beaumont in The Physics and Fabrication of Microstructures and Microdevices, M. J. Kelly and C. Weisbuch eds. (Springer-Verlag, 1986), pp. 36-50.
18. G. A. Lincoln, M. W. Geis, S. W. Pang, and N. N. Efremow, *J. Vac. Sci. Technol.* B1, 1043 (1983).
19. M. W. Geis, N. N. Efremow, S. W. Pang, and A. C. Anderson, *J. Vac. Sci. Technol.* B5, 363 (1987).

PARTICIPATING PERSONNEL

Robert T. Bate
William R. Frensley
Richard Gale
Russell Pinizotto
John N. Randall
Mark A. Reed

List of Appendices

- A. "Wigner Function Model of a Resonant-Tunneling Semiconductor Device," accepted for publication in Physical Review B.
- B. "Quantum Transport Simulation of the Resonant-Tunneling Diode," from Proceedings of the International Electron Devices Meeting, 7-10 December 1986, p. 571.
- C. "Quantum-Transport Calculation of the Small-Signal Response of a Resonant-Tunneling Diode," accepted for publication in Applied Physics Letters.
- D. "Quantum-Transport Modeling of Resonant-Tunneling Devices," presented at the Fifth International Conference on Hot Carriers in Semiconductors, Boston, MA, July 20-24, 1987.
- E. "Spatial Quantization in GaAs-AlGaAs Multiple Quantum Dots," M. A. Reed, R. T. Bate, K. Bradshaw, W. M. Duncan, W. R. Frensley, J. W. Lee, and H. D. Shih, J. Vac. Sci. Technol. B4, 358 (1986). (Abstract only.)
- F. "Investigation of Quantum Well and Tunnel Barrier Growth by Resonant Tunneling," M. A. Reed, J. W. Lee, R. K. Aldert, and A. E. Wetzel, J. Mat. Res. 1, 337 (1986).

- G. "Excited State Resonant Tunneling in GaAs-AlGaAs Double Barrier Heterostructures," M. A. Reed, Superlattices and Microstructures 2, 65 (1986). (Abstract only.)
- H. "Resonant Tunneling Through a Double GaAs/AlAs Superlattice Barrier, Single Quantum Well Heterostructure," M. A. Reed, J. W. Lee, and H.-L. Tsai, Appl. Phys. Lett. 49, 158 (1986). (Abstract only.)
- I. "Resonant Tunneling in a Double GaAs/AlAs Superlattice Barrier Heterostructure," M. A. Reed and J. W. Lee, presented at the 13th International Symposium on GaAs and Related Compounds, Las Vegas, NV, 1986, and published in Gallium Arsenide and Related Compounds 1986, Inst. Phys. Conf. Ser. No. 83, 545 (1987).
- J. "Resonant Tunneling in Double Superlattice Barrier Heterostructures," M. A. Reed and J. W. Lee, presented at the Second International Conference on Superlattices, Microstructures, and Microdevices, Goteborg, Sweden, 17-20 August 1986 and published in Superlattices and Microstructures 3, 111 (1987). (Abstract only.)
- K. "Resonant Tunneling in Double Barrier Heterostructures," M. A. Reed, R. T. Bate, and J. W. Lee, presented at the SPIE Conference on Quantum Well and Superlattice Physics, 22-27 March 1987, Bay Point, FL, and to be published in the SPIE Conference Proceedings, Vol. 792.
- L. "Semiconductor Heterojunction Resonant Tunneling Devices", M. A. Reed, invited talk at the Meeting of the American Physical Society, New York, NY, 16-20 March 1987 (Bull. Am. Phys. Soc. 32, 745 (1987)).
- M. "Quantum Semiconductor Devices," M. A. Reed, invited talk at the 3rd International Symposium on Molecular Devices, 6-8 October 1986, Washington, D.C.
- N. "Microstructure Fabrication and Transport Through Quantum Dots," J. N. Randall, M. A. Reed, T. M. Moore, R. J. Matyi, and J. W. Lee, to be published in J. Vac. Sci. Technol.

- O. "Resonant Tunneling in a GaAs/AlGaAs Barrier/InGaAs Quantum Well Heterostructure," M. A. Reed and J. W. Lee, Appl. Phys. Lett. 50, 845 (1987). (Abstract only.)

- P. "Conduction Processes in Thin Layer Stacks Composed of Al, Intrinsic Polycrystalline Si, and Thermal Silicon Dioxide on Silicon," Richard Gale.

APPENDIX A

**WIGNER FUNCTION MODE OF A RESONANT-TUNNELING
SEMICONDUCTOR DEVICE**

**Wigner function model of a resonant-tunneling
semiconductor device**

William R. Frensley

Central Research Laboratories

Texas Instruments Incorporated

Dallas, Texas 75265

ABSTRACT

A model of an open quantum system is presented in which irreversibility is introduced via boundary conditions on the single-particle Wigner distribution function. The Wigner function is calculated in a discrete approximation by solution of the Liouville equation in steady state, and the transient response is obtained by numerical integration of the Liouville equation. This model is applied to the quantum-well resonant-tunneling diode. The calculations reproduce the negative-resistance characteristic of the device, and indicate that the tunneling current approaches steady state within a few hundred femtoseconds of a sudden change in applied voltage.

This manuscript has been submitted to *Physical Review B*.

PACS numbers: 73.40.Lq, 05.60.+w, 73.40.Gk, 85.30.De

I. INTRODUCTION

The progress of semiconductor fabrication technology, particularly the hetero-epitaxial technology, has permitted the fabrication of structures¹ and devices^{2,3} whose behavior is dominated by quantum-interference effects. By providing a mechanism to control current flow through nanometer-scale semiconductor structures, such quantum interference effects might form the basis for a new generation of solid-state electronic technology.⁴ The successful development of such a technology will require a much more detailed understanding of the dynamic behavior of size-quantized systems than is presently available.

A key property of any device, which has not been adequately addressed in the case of quantum tunneling devices, is the transient response to changes in the externally applied voltage. The transient response determines the ultimate switching speed and frequency response of the device. Because a device is a physical system characterized by openness and irreversibility, the analysis of its behavior, and particularly the analysis of the transient response must be performed within the framework of statistical mechanics, rather than pure-state quantum mechanics. A preliminary report on the calculation of the transient response of a tunneling device has appeared.⁵ This paper describes the calculation in detail.

In the present work the quantum-well resonant-tunneling diode^{2,3,6} (RTD) has been taken to be the prototype quantum semiconductor device. This device consists of a single quantum well bounded by tunneling barriers, as shown in Fig. 1. As a bias voltage is applied to the device, the resonant state in the well is pulled down in energy with respect to the more negative electrode, and the tunneling current through this state depends on the density of occupied states in the electrode. When the resonant state is pulled below the conduction band edge of the electrode, the tunneling current decreases. The device thus shows negative differential resistance, which is attributable to quantum interference.

II. OPENNESS AND IRREVERSIBILITY OF THE DEVICE

An electron device is necessarily an open system; it is useless unless connected to an electrical circuit and able to exchange electrons with that circuit. If one wishes to study the behavior of the device apart from that of the circuit, it is convenient to

represent the effects of the external circuit by ideal electron reservoirs attached to the terminals of the device. The term "open system" is used here in a more restricted sense than is common in the statistical physics literature.⁷ For the present purposes, an open system is one which is connected to reservoirs of conserved particles, so that the interaction between the system and a reservoir necessarily involves a particle current through an interface (real or idealized) between the system and the reservoir. A concrete example is a semiconductor device (the system) to which a metal wire (the reservoir) is attached through an Ohmic contact (the interface). The body of literature of which Ref. 7 is representative is primarily concerned with a related problem which I will refer to as "damping." In the semiconductor device example, this is the interaction between the electrons and phonons (regarded as a heat bath) which leads to electrical resistance.

The dynamic behavior of a device must be time-irreversible. This is demonstrated by the existence of the current-voltage $I(V)$ curve that is conventionally used to characterize a device. Each point of the $I(V)$ curve represents a steady state, and all of the points except $V=0$ represent a non-equilibrium steady state. A time-reversible system cannot stably approach such a steady state.

Landauer⁸ has pointed out that if one considers conduction through a sample in which only elastic scattering occurs, the resulting finite conductivity requires that energy be dissipated in the reservoirs to which the sample is connected. The connection between openness and dissipation may be readily perceived in other physical systems, perhaps most clearly in the vacuum tube (or valve) of an earlier generation of electronic technology.⁹ The vacuum is certainly not a dissipative medium, but making electrical contact to it through metal electrodes results in a device which displays an $I(V)$ curve and which dissipates energy (generally in the anode). Thus openness and dissipation are related. What is perhaps less obvious is that dissipation or irreversibility is a *necessary* feature of any meaningful description of the interaction between an open system and the reservoirs to which it is connected. If the boundary conditions are reversible, then unstable solutions to the transient response are admitted. This will become apparent when we consider the effect of open-system boundary conditions on the eigenvalue spectrum of the Liouville super-operator.

The connection between open-system boundary conditions and the eigenvalue spectrum can be seen in the simpler case of the Hamiltonian. Consider the conventional demonstration of the Hermiticity of the single-particle Hamiltonian.¹⁰ This demonstration proceeds by invoking Green's identity to transpose the Laplace operator, which leaves a surface term. This term is conventionally taken to be zero, but it can be expressed as

$$H - H^\dagger = \frac{\hbar}{i} \int_S \mathbf{j} \cdot d\mathbf{s} \quad (1)$$

where \mathbf{j} is the current operator and S is the boundary of the domain in which the Hamiltonian is defined. One maintains the Hermiticity of the Hamiltonian by choosing wavefunctions for which the surface integral vanishes: states that are well localized within the domain, or stationary scattering states for which the incoming and outgoing flux cancel. Now, in general, there must be a net change in the electron density in a device as the device passes from one steady state to another. For example, the resonant state in the RTD shows a large electron density peak in the quantum well. Therefore, during the process of establishing this state, there must be a net inward current flow to "fill up" the well. However, according to (1), a set of basis states (on a finite spatial domain) that could describe such a process would result in a non-Hermitian Hamiltonian.

III. STATISTICAL MECHANICS

Irreversible quantum phenomena are properly treated at a statistical level.¹¹ That is, a level at which the state of the quantum system is represented by an operator (density matrix,¹² Wigner function,¹³ or Green's function,¹⁴ typically) rather than by a wavefunction. The statistical representation is required if one is to describe both the superposition of complex-valued amplitudes leading to interference effects, and the superposition of real-valued probabilities leading to incoherent phenomena. Let us briefly review the fundamental relations of quantum statistical mechanics, in order to define the terms and display the equations that will be invoked.

A statistically mixed quantum state is described by a density matrix¹² which, in a real-space basis, can be written as

$$\rho(x, x') = \sum_{|i\rangle} w_i \langle x|i\rangle \langle i|x'\rangle \quad (2)$$

where $|i\rangle$ represents a complete set of states and w_i is a probability. The time evolution of the density matrix is given by the quantum Liouville equation:

$$\begin{aligned} \partial\rho/\partial t &= (1/i\hbar)[H, \rho] \equiv (L/i\hbar)\rho \\ &= \frac{1}{i\hbar} \left\{ -\frac{\hbar^2}{2m} \left[\frac{\partial^2}{\partial x^2} - \frac{\partial^2}{\partial x'^2} \right] \rho + [v(x) - v(x')] \rho \right\}, \end{aligned} \quad (3)$$

where H is the Hamiltonian and L is the Liouville (super)operator. The potential v will include contributions from the device structure in the form of heterojunction band discontinuities and from the electrostatic (Hartree) potential due to mobile electrons, ionized impurities and externally applied fields. In the present work the independent-electron model will be assumed, so that only the single-electron reduced density matrix or distribution function is required.

The Wigner distribution function¹³ is obtained from the density matrix by changing the independent variables to $\chi = \frac{1}{2}(x+x')$ and $\xi = x-x'$. The classical position is then identified with χ and the Fourier transform of ξ is taken to obtain the classical momentum variable:

$$f(\chi, k) = \int_{-\infty}^{\infty} d\xi e^{-i k \xi} \rho(\chi + \frac{1}{2}\xi, \chi - \frac{1}{2}\xi). \quad (4)$$

This transformation of variables and its effect on the boundary conditions for finite systems is illustrated in Fig. 2. The Liouville equation for the Wigner function can then be written

$$\frac{\partial f}{\partial t} = -\frac{\hbar k}{m} \frac{\partial f}{\partial \chi} - \frac{1}{\hbar} \int_{-\infty}^{\infty} \frac{dk'}{2\pi} V(\chi, k'-k) f(\chi, k') \quad (5)$$

where the kernel of the potential operator is given by

$$V(\chi, k) = 2 \int_0^{\infty} d\xi \sin(k\xi) [v(\chi + \frac{1}{2}\xi) - v(\chi - \frac{1}{2}\xi)]. \quad (6)$$

The nonlocal potential is the means by which interference between alternative paths enters the Wigner function formalism.¹⁵

The density matrix and thus the Wigner function may be normalized so as to represent the particle density. Thus the electron density $n(x)$ (in units of particles per cm^3 , for example) can be found from

$$n(x) = \rho(x,x) = \int_{-\infty}^{\infty} \frac{dk}{2\pi} f(x,k). \quad (7)$$

The continuity equation can be derived from the Liouville equation (5) by integrating with respect to k . The contribution from the potential operator vanishes by antisymmetry and one obtains an expression for the current density:

$$j(x) = \int_{-\infty}^{\infty} \frac{dk}{2\pi} \frac{\hbar k}{m} f(x,k). \quad (8)$$

Now let us consider the effect of boundary conditions on the eigenvalue spectrum of the Liouville super-operator. The Hermiticity of L follows directly from that of the Hamiltonian H for a closed, conservative system. Such a system can only display oscillatory behavior. If we change the boundary conditions so as to allow particles to pass into or out of the system, we violate the Hermiticity of Liouville operator, because its Hermiticity depends upon a relation derived from (1). This introduces imaginary parts into at least some of the eigenvalues of L , or real parts into some of the eigenvalues of $(L/i\hbar)$, giving a real exponential character to the time-dependence of f . If the open-system boundary conditions are time-reversible, then the real parts of the eigenvalues of $(L/i\hbar)$ occur symmetrically. That is, there is a positive real part, corresponding to an unstable solution, for every negative real part.¹⁶ An example of such a boundary condition may be applied to the density matrix.¹⁷ It is $\partial\rho/\partial x = 0$, along boundaries parallel to the x and x' axes (shown as the long-dashed lines in Fig. 2). This is a plausible boundary condition for an open system, because it leads to a constant density at the boundary, approximating the effect of a fixed chemical potential at the boundary. Fixing the chemical potential is the usual way to represent an Ohmic contact in classical semiconductor device analyses.^{18,19} In the present case, however, its time-reversal symmetry leads to an unphysical exponentially growing solution of the Liouville equation.

One might expect that the unstable eigenvalues would be removed by the inclusion of the damping which results from coupling the system to a heat bath. (The damping in semiconductors is due to random scattering of electrons by phonons.²⁰) Within the simple models which I have studied,¹⁶ such is not the case. If one uses a simple Fokker-Planck operator²¹ to approximate the effects of phonon scattering, then damping coefficients which are appropriate to a high-mobility material such as GaAs are not sufficient to render the time-dependent behavior stable. Damping coefficients about an order of magnitude too large are required to remove the positive eigenvalues. Thus, the stability of a model of an open system should be guaranteed by the open-system boundary conditions themselves, and this means that these boundary conditions must be time-irreversible.

The required irreversibility can be obtained in a physically appealing way by assuming that the reservoirs to which the device is connected have properties analogous to those of a black body: the distribution of electrons emitted into the device from the reservoir is characterized by the thermal equilibrium distribution function of the reservoir, and all electrons impinging upon a reservoir from the device are absorbed by the reservoir without reflection. To implement this picture, we must be able to distinguish the sense of the velocity of an electron at the position of the boundary. Thus the Wigner function is the natural representation for an open system. Let the interface between the device and the left-hand reservoir occur at $x=0$, and the interface between the device and the right-hand reservoir occur at $x=l$. Then we may write the open-system boundary conditions as

$$\begin{aligned} f(0, k) &= f_l(k) \quad |k > 0 \\ f(l, k) &= f_r(k) \quad |k < 0 \end{aligned} \tag{9}$$

Note that these boundary conditions are appropriate for the Liouville equation in the form (5). The derivative is first order in x so one value of f must be specified for each k . The dependence on k is expressed as an integral, so no boundary conditions need be specified in the k -direction. The reservoirs are characterized by the chemical potential μ and reciprocal temperature β . The equilibrium distribution functions of the reservoirs can be written (after integrating over the transverse momenta) as

$$f_{l,r}(k) = (m/\pi\hbar^2\beta_{l,r}) \ln \{1 + \exp[-\beta_{l,r}(\hbar^2k^2/2m - \mu_{l,r})]\}. \tag{10}$$

The physical picture which underlies these boundary conditions is of course well known. It is invoked in most forms of transport calculation, including scattering analyses of conductance⁸ and tunneling²²⁻²⁴, and classical calculations such as those performed by Monte Carlo methods.^{25,26} The characteristic feature of such calculations, however, is that the interaction between the system and the reservoir is treated *implicitly* within an algorithmic procedure. The usefulness of this approach is inherently limited. We will see that the *explicit* statement of the boundary conditions (9) leads to new insights and calculational capabilities.

The most important insight is that the boundary conditions (9) assure the stability of the solutions of the Liouville equation. This may be demonstrated by proving that the real parts of the eigenvalues of $(L/i\hbar)$ are all non-positive. We may do so by evaluating the expectation value of the homogeneous part of $(L/i\hbar)$ for an arbitrary distribution function f . Note that because L is a super-operator, the expectation value is taken between operators (the distribution functions). If we define the inner product of distribution functions in the obvious way, the expectation value is readily evaluated. Again the contribution from the potential operator vanishes by antisymmetry and the gradient operator can be integrated to obtain:

$$\begin{aligned} \langle f, (L/i\hbar) f \rangle &= \int dx \int dk f (L/i\hbar) f = (\hbar/2m) \int dk k [f^2(0, k) - f^2(l, k)] \\ &= (\hbar/2m) \left[\int_{-\infty}^0 k f_s^2(0, k) dk + \int_0^{\infty} k f_l^2(0, k) dk - \int_{-\infty}^0 k f_r^2(l, k) dk - \int_0^{\infty} k f_s^2(l, k) dk \right]. \quad (11) \end{aligned}$$

Here I have used the notation f_s to denote the part of the distribution function that is a property of the system, that is, not specified by the boundary conditions. For the homogeneous case, $f_l = f_r = 0$. Then the terms containing these quantities vanish, and the two terms containing f_s are clearly non-positive. Therefore the real parts of the eigenvalues of $(L/i\hbar)$ must all be non-positive. The physical interpretation of this argument is that the electrons in an open system will eventually escape and the internal density will approach zero if there is no inward current flow from the reservoirs.

IV. DISCRETE MODEL

The problems which are of interest in studying the behavior of quantum devices do not fall into the domain of analytically soluble problems. The results of

the present model must therefore be evaluated numerically. This requires that the infinite number of mathematical operations implied by the continuum formulation of the problem must be reduced to a finite number. A natural way to do this is to replace the continuous domain of the problem by a mesh or lattice of discrete points in phase space.

The position coordinates x will be taken to be elements of a uniformly spaced set with mesh spacing Δ_x : $x \in \{0, \Delta_x, 2\Delta_x, \dots, l\}$. The number of mesh points in the x dimension is thus $N_x = l/\Delta_x + 1$. The underlying wavefunctions and the operators which act upon them are assumed to be defined only on a mesh point (although for the purpose of evaluating the potential operator (6) the mesh may be extended into the reservoirs). The definition of the Wigner distribution function (4) may be discretized as follows: The position argument χ takes discrete values from the set defined above. (Henceforth I will neglect the distinction between the position argument of the Wigner function χ and the position argument of the wavefunction x , and refer to both of these quantities as x .) The relative coordinate ξ , from which the momentum argument is obtained, must be treated more carefully. Because we have assumed that the potential is only defined at integral multiples of Δ_x and because ξ appears in (6) with a coefficient of $\frac{1}{2}$, we must constrain ξ to take only even multiples of Δ_x : $\xi \in \{0, 2\Delta_x, 4\Delta_x, \dots, l_\xi\}$. Then when we take the Fourier transform with respect to ξ as in (4) or (6), the resulting function is periodic in k with a period of π/Δ_x . The maximum value of ξ in this scheme, l_ξ , is not necessarily related to any of the previously defined quantities. It determines the maximum distance over which quantum correlations are taken into account, thus determining in some sense the number of alternative paths which are allowed to interfere.¹⁵ In the present calculations, l_ξ has been taken to be equal to l .

The domain is similarly discretized in the k dimension. The domain $-\pi/2\Delta_x < k \leq \pi/2\Delta_x$ may be discretized into an arbitrary number of mesh points N_k . However, the numerical solution of the Liouville equation is simplified if we choose the mesh so that $k=0$ is not one of the mesh values. (At $k=0$ the gradient term of (5) degenerates, leading to zeros on the diagonal of the super-operator. Such zeros require that row interchanges be performed in the Gaussian elimination procedure. If the mesh is chosen so that these zeros do not occur, it has been observed that no interchanges are required.) Thus we require that N_k be even, so as to have equal numbers of points for positive and negative k , and let the mesh straddle $k=0$: $k \in \{$

$(\pi/\Delta_x)[(j-\frac{1}{2})/N_k-\frac{1}{2}] \quad |j=1,2,\dots,N_k\}$. The k mesh spacing is therefore $\Delta_k = \pi/N_k\Delta_x$. Equation (6) for the potential operator then takes the discretized form:

$$V(x,k) = \frac{2}{N_k} \sum_{\{\xi\}} \sin(k\xi) [v(x+\frac{1}{2}\xi) - v(x-\frac{1}{2}\xi)]. \quad (12)$$

Discretization of the Liouville equation (5) requires some care, as the gradient (drift) term must be replaced by a finite-difference approximation. There is a potential ambiguity in this procedure, because the gradient can be expressed as either a left-hand difference: $(\nabla f)(x) = [f(x) - f(x - \Delta_x)]/\Delta_x$, or as a right-hand difference: $(\nabla f)(x) = [f(x + \Delta_x) - f(x)]/\Delta_x$. This ambiguity is naturally resolved by considering the boundary conditions. Let us imagine that the boundary conditions (9) will be represented by extra rows of mesh points placed just outside of the domain of f , as illustrated in Figure 3. The values of f along these boundary rows will be regarded as fixed. There will be a row along $x = -\Delta_x$ for $k > 0$ and a row along $x = l + \Delta_x$ for $k < 0$. Now consider $k > 0$. If the boundary conditions are to be coupled into the domain at all, we must use the left-hand difference for the gradient, at least next to the left-hand boundary. If we want the discrete version of the fundamental theorem of calculus to hold for integration with respect to x , we must then use the left-hand difference for all x . A similar argument leads to the use of the right-hand difference for all x for $k < 0$. This sort of scheme for discretization of the gradient is the phase-space equivalent of a scheme which is known as an "upstream" or "upwind" difference in the context of classical fluid dynamic calculations.²⁷ Similar schemes have been employed in neutron-transport calculations.²⁸ The use of this upwind difference is what permits the argument of Eq. (11) to hold in the discrete case, and is thus the key element in obtaining stable solutions for the Wigner distribution function. The discretized Liouville equation can thus be written as:

$$\partial f(x,k)/\partial t = -\frac{\hbar k}{m\Delta_x} \left\{ \begin{array}{l} f(x+\Delta_x) - f(x) \quad |k < 0 \\ f(x) - f(x-\Delta_x) \quad |k > 0 \end{array} \right\} - \frac{1}{\hbar} \sum_{\{k'\}} V(x, k'-k) f(k'). \quad (13)$$

The discretized continuity equation is derived from the discretized Liouville equation (13). In a simple discretization scheme, the vector quantities such as electric field or current density are most naturally associated with the *intervals* between mesh points rather than with the mesh points themselves.²⁹ Thus we may

expect the discretized continuity equation to have the form:

$$\partial n(x) / \partial t = [j(x + \frac{1}{2}\Delta_x) - j(x - \frac{1}{2}\Delta_x)] / \Delta_x. \quad (14)$$

If the density is defined as

$$n(x) = \sum_{\{k\}} \frac{\Delta_k}{2\pi} f(x, k), \quad (15)$$

then the form of the discretized Liouville equation (13) requires that the current density be

$$j(x + \frac{1}{2}\Delta_x) = \frac{\Delta_k}{2\pi} \left[\sum_{k < 0} \frac{\hbar k}{m} f(x + \Delta_x, k) + \sum_{k > 0} \frac{\hbar k}{m} f(x, k) \right]. \quad (16)$$

Using this definition of j , the current density calculated for a steady-state solution ($\partial f / \partial t = 0$) is independent of x .

The derivation of the discrete continuity equation (14) from the discrete Liouville equation (13) requires that

$$\sum_{\{k\}} V(x, k) = 0, \quad (17)$$

for all x . This condition follows from the antisymmetry of V and from the Fourier completeness relation:

$$\sum_{\{k\}} e^{ik\xi} = N_k \delta_{\xi, 0}. \quad (18)$$

This is significant because one is very tempted to employ a smaller set of k values to reduce the computation time. If the k 's included in the computation do not span the "Brillouin zone" defined by the ξ discretization [and thus satisfy (18)], however, the continuity equation will not be satisfied. This can lead to steady-state solutions in which the current density is not constant, and to transient solutions in which there is a significant gain or loss of particle density inside the device.

V. STEADY-STATE BEHAVIOR

The steady-state behavior of the resonant-tunneling diode was numerically calculated by solving the discretized Liouville equation (13) for the condition $\partial f/\partial t = 0$. The boundary conditions (9) supply the inhomogeneous source terms. The present calculations used $N_x = 80$, $N_k = 60$. The mesh spacing was taken to be $\Delta_x = 0.565$ nm to make the assumed layer thicknesses commensurate with the atomic layer spacing of the (Al,Ga)As system. The discrete Liouville equation was solved by Gaussian elimination, which requires storage proportional to $N_x N_k^2$ and time proportional to $N_x N_k^3$.

The device structure assumed in the present calculations consists of a 4.5 nm wide quantum well of GaAs bounded by identical 2.8 nm wide barrier layers of $\text{Al}_{0.3}\text{Ga}_{0.7}\text{As}$. The conduction-band discontinuity was taken to be 0.60³⁰ of the total bandgap discontinuity.³¹ 17.5 nm of the GaAs electrode layer was included in the simulation domain on each side of the device. Because Hartree self-consistency was not incorporated into the present calculations, the applied bias voltages were assumed to be dropped uniformly across the well and barriers, as illustrated in Fig. 1. The electron density assumed in the boundary reservoirs was $2 \times 10^{18} \text{ cm}^{-3}$. (This is the only place in the computation where the doping density appears if self-consistency is not implemented.) All calculations were performed at a temperature of 300 K.

The assumed barriers are rather thin compared to those of typical experimental devices^{3,6} because thicker layers result in narrower resonances in the transmission coefficient. This requires that one use more meshpoints in k in order to adequately resolve the narrower resonances. The presently assumed structure is one whose Wigner function can be adequately represented by the discrete model described above.

The steady-state calculation was performed for a range of bias voltages, and the current density was evaluated from the resulting Wigner function. The current-voltage characteristic from this calculation is shown in Fig. 4, along with the curve derived from a scattering calculation which was done in a finite-difference approximation¹⁷ with the same mesh spacing Δ_x . (In the scattering calculation the wavefunctions were evaluated recursively³² using an energy-dependent initial

condition which matched the wavefunction to a traveling wave.) The Wigner-function calculation predicts a higher current density and lower peak-to-valley current ratio than the scattering calculation. The voltages at which the peak and valley occur agree very well. The Wigner-function calculation more nearly resembles the experimental results at 300 K, but at lower temperatures it seriously underestimates the peak-to-valley ratio. Moreover, the presently neglected phonon scattering processes, which account for most of the temperature dependence, will tend to reduce the peak-to-valley ratio. Thus, at present, the scattering theory is more likely to fit the experimental data⁶ when such processes are taken into account. The difference between the Wigner and scattering calculations is probably due to the difference in the boundary conditions. The boundary conditions (9) impose a constraint upon the standing-wave patterns of the underlying wave functions, whereas the energy-dependent boundary conditions of the scattering analysis do not do so. A result of this effect is that the current-voltage curves calculated from the Wigner function depend weakly on the assumed position of the boundaries.

The voltage at which the peak current occurs in both theoretical calculations of Fig. 4 is significantly lower than that at which the peak occurs in the experimental data of Fig. 1. The reason for this is the neglect of self-consistency in the evaluation of the electrostatic potential.³³ In particular, the upstream accumulation and downstream depletion layers in the experimental devices drop much of the applied voltage, and there is also the Ohmic drop in the contact layers. The theoretical calculations predict a current density about an order of magnitude larger than the experimental data. This is due to the thinner barriers assumed in the theoretical calculations. The current density decreases exponentially with increasing barrier thickness.^{34,35}

The steady-state Wigner functions for different bias voltages are plotted in Figures 5-7. The zero-bias (equilibrium) case is shown in Fig. 5. The large electron density in the electrode regions, and much smaller density in the vicinity of the barriers is evident. Small oscillations appear in various regions, reflecting the underlying quantum interference. Fig. 6 shows the steady-state Wigner function for a bias of 0.11 V, which corresponds to the peak of the $I(V)$ curve. The oscillations are in this case much more pronounced, including a strong negative peak. This is evidence that strong quantum-interference effects are present, as expected. In contrast, the Wigner function (shown in Fig. 7) for a *larger* bias voltage, 0.22 V,

which corresponds to the current "valley", is quite similar to that of the equilibrium case.

Much more information can be obtained from the steady-state calculations than just the I(V) curve. An example is the electron density in the quantum well as shown in Fig. 8. The maximum electron density of $1.5 \times 10^{11} \text{ cm}^{-2}$ occurs at a somewhat lower bias voltage than the current peak. The shift in the electrostatic potential due to the occupation of the well is therefore of the order of 0.02 V if one assumes that the effective separation of the charge dipole is 10 nm. (The charge in the well will be neutralized by a change in the mobile charge density at that location which minimizes the voltage shift. In the case of the RTD this will be in the accumulation layer that forms against the upstream barrier. The distance from the center of the well to the centroid of the accumulation layer is of the order of 10 nm.) The 0.02 V shift due to the charge in the quantum well is properly compared to the voltage axis of Fig. 1, 4, or 8, and is readily seen to be negligible.

VI. TRANSIENT BEHAVIOR

To obtain the transient response of a quantum device, the discretized Liouville equation (13) may be integrated. This requires a further discretization of the equation with respect to time. The way in which this discretization is performed also has a profound effect on the numerical stability of the resulting solutions, but the considerations here are well known within the context of "stiff" differential equations.³⁶ To illustrate the connection between the numerical approach and the more familiar techniques of quantum-mechanical calculations, let us discuss this issue using a more quantum-mechanical notation.

The general solution of the Liouville equation can be written as

$$f(t) = \left[\exp \left(\frac{1}{i\hbar} \int_{t_0}^t L(t') dt' \right) \right] f(t_0). \quad (19)$$

The conventional approach to evaluating this expression is to find a part of L whose effect can be integrated analytically, and then to expand the remaining part of L in a perturbation series. The simple non-perturbative numerical approaches approximate the integral in the exponential by a finite sum, thereby obtaining a product expansion of the operator exponential

$$\exp\left(\frac{1}{i\hbar} \int_{t_0}^t L dt'\right) \approx \exp\left(\frac{1}{i\hbar} \sum_{t'=t_0}^t L(t')\Delta_t\right) \approx \prod_{t'=t_0}^t \left(1 + \frac{L(t')\Delta_t}{i\hbar}\right), \quad (20)$$

where $t' \in \{t_0, t_0 + \Delta_t, t_0 + 2\Delta_t, \dots, t\}$, to obtain a simple iterative scheme (in this case Euler's formula) which I will call the explicit scheme:

$$f(t + \Delta_t) = f(t) + \Delta_t(L/i\hbar) f(t). \quad (21)$$

(Note that this approach to evaluating the time-development operator trivially resolves the issue of time-ordering the operator product.³⁷) The usefulness of this scheme is limited by the existence of large negative eigenvalues of $(L/i\hbar)$. Consider the eigenfunction f_λ corresponding to such an eigenvalue λ . Each iteration of equation (21) multiplies the f_λ component of the solution by a factor $(1 + \lambda\Delta_t)$. If the modulus of this factor is greater than unity, the solution will diverge, even though the criterion for stability of the continuum problem [$\text{Re}(\lambda) \leq 0$] is satisfied. The modulus of the factor $(1 + \lambda\Delta_t)$ can be made less than unity by choosing Δ_t to be sufficiently small, but the resulting values often lead to impractically large requirements for computer time.

An absolutely stable integration scheme is the implicit, or backward Euler method. It is obtained by expanding the operator exponential as

$$\exp\left(\frac{1}{i\hbar} \int_{t_0}^t L dt'\right) \approx \prod_{t'=t_0}^t (1 - L(t')\Delta_t/i\hbar)^{-1}. \quad (22)$$

This leads to the following iteration equation:

$$(1 - \Delta_t L/i\hbar) f(t + \Delta_t) = f(t) \quad (23)$$

In this scheme each eigenfunction of the Liouville operator is multiplied by a factor of $(1 - \lambda\Delta_t)^{-1}$ which has a modulus less than unity for any value of Δ_t if $\text{Re}(\lambda) < 0$. The price to be paid for this stability is that one must solve a linear system of equations at each time step (computation proportional to $N_x N_k^3$), as opposed to simply multiplying by a matrix as in the explicit scheme (computation proportional to $N_x N_k^2$). The use of larger time-steps Δ_t , however, makes the implicit method the more effective one. This scheme was employed in the present calculations.

The stability of the calculation is guaranteed in the implicit method for arbitrarily large time-steps Δ_t , but there is also the issue of the accuracy of the calculation. The potential inaccuracy arises because one is trying to approximate $\exp(\lambda\Delta_t)$ by $(1 - \lambda\Delta_t)^{-1}$, which is clearly inadequate when $|\lambda\Delta_t| > 1$. [Recall that $\text{Re}(\lambda) \leq 0$.] If all of the eigenfunctions of the Liouville operator were present in the Wigner function solution, this condition for accuracy of the implicit scheme is equivalent to the criterion for stability of the explicit scheme. The benefits of the implicit scheme are due to the fact that not all of the eigenfunctions are present in the desired solution. In particular, the eigenfunctions of the large eigenvalues (the "stiff" components) are not significantly present. These eigenfunctions correspond to the occupation of higher-energy states. We may estimate the magnitude of the important eigenvalues by estimating the maximum occupied energy levels in a given situation. In the case of the resonant-tunneling diode this would be the Fermi level, plus a few times kT , plus the applied bias, or the bias voltage plus 0.1 to 0.2 V for the assumed design at room temperature. The present calculations employed a time step $\Delta_t = 1$ fs, which corresponds to an energy of 0.6 eV. Thus this time step is small enough to realistically represent the transient response.

The results of the calculations of the transient response of the resonant-tunneling diode model are shown in Figs. 9 and 10. Since the negative-resistance characteristic is the interesting feature of this device, the transient response calculations were performed for switching events across this region of the $I(V)$ curve. Figure 9 shows the current density in the device as a function of position and time for an event in which the initial bias of 0.11 V (corresponding to the peak in the current) was suddenly switched to 0.22 V (corresponding to the bottom of the valley) at $t=0$. More specifically, the steady-state Wigner function for a bias of 0.11 V was used as an initial value, and the time evolution under the Liouville operator for 0.22 V bias was evaluated. The response of the current is complex, as might be expected, but shows some features that are readily interpreted. The current density initially increases throughout the structure, so that the device displays a positive resistance over a short time. The destructive interference which underlies the negative resistance takes some tens of femtoseconds to manifest itself. The current has settled quite near to its steady-state value after 200 fs. Of course the response of real devices will be limited by the time required to charge the device capacitance through the parasitic series resistance of the contacts. Such effects were deliberately omitted

from the present model in order to observe the intrinsic response of the tunneling process itself.

A simulation of the reverse transition is shown in Figure 10. That is, the bias was suddenly switched from 0.22 V to 0.11 V. The response shows a similar short-time positive resistance, as the current density initially drops. After 200 fs the steady state has not quite been reached, as indicated by the slightly higher current density through the left-hand barrier as compared to that through the right-hand barrier. This indicates that the process of filling the quantum well is not yet complete. The difference in speed of response between peak-to-valley and the valley-to-peak transitions may be understood in terms of the shape of the energy barriers as a function of bias voltage. The higher bias voltage, and thus the higher electric field, leads to more "triangular" barriers. The more triangular barriers are effectively narrower and are therefore more transparent to tunneling currents. Thus there is more tunneling current available to complete the peak-to-valley transition, and it proceeds more quickly.

VII. DISCUSSION

The present model of an open quantum system clearly reproduces the essential features of the current-voltage curve of the resonant-tunneling diode. In addition, by incorporating the open-system irreversibility, it permits detailed calculations of the time-domain response of the device to externally applied voltages.

The open-system boundary conditions (9) are equally applicable to quantum and classical systems. In particular, they are the appropriate boundary conditions for the classical Liouville and Boltzmann equations for those cases in which a transporting medium connects two or more reservoirs (which covers the great majority of cases of interest). The demonstration (11) of the stability of the system under these boundary conditions is equally valid in the classical case.

An examination of the drift term in the discrete Liouville equation (13) shows that it has the form of a master operator. (That is, it has a "gain-loss" form and could therefore appear in a master equation.³⁸) This suggests that an implicit Markov assumption must have been made in the derivation of (13). The Markov assumption is inherent in the boundary conditions (9). By expressing the effect of the reservoir as a boundary condition, we have suppressed the internal degrees of

freedom of the reservoir. In general, such a procedure leads to a non-Markovian equation for the time-evolution of the system, as the effects of the suppressed degrees of freedom are "folded" into a memory functional.³⁹ Some further approximation is then required to derive the conventional (Markovian) macroscopic kinetic equations.⁴⁰ In the present case, it is assumed that such a Markovian approximation exists. Physically, we would expect that the ideal reservoir behavior would be obtained when the correlation time of the reservoir is very short,⁴¹ or equivalently, that the scattering rate in the reservoir is very high. In other words, the Markovian behavior results from the loss of information about the state of an electron as soon as it passes out of the system and into a reservoir and is quickly scattered.

The shape of the domain of the Wigner function as illustrated in Fig. 2 is significant. The density matrix $\rho(x,x')$ is essentially a spatial correlation function. In Fig. 2, the long-dashed lines indicating the system-reservoir interfaces in x and x' divide the domain into regions corresponding to the various possible system-system, system-reservoir, and reservoir-reservoir correlation functions. The domain of the Wigner function (bounded by the short-dashed lines) necessarily extends into the domain of the system-reservoir correlation function. This appears to be an essential element in the description of open quantum systems. It specifically enters the present calculations in the evaluation of equation (6) or (12) for the potential operator. These equations require values for the potential $v(x)$ at positions $x < 0$ and $x > l$. For this purpose the potential was assumed to extend into the reservoirs with a constant value equal to that at the system-reservoir boundary.

A consequence of the abrupt change in band structure at a heterojunction is that the effective mass also changes abruptly. This must be taken into account in the construction of the effective-mass hamiltonian^{42,43} and this effect is readily incorporated into a density-matrix calculation.¹⁷ When the Liouville operator is transformed into the Wigner-Weyl representation, however, the effect of the effective-mass discontinuity becomes nonlocal.⁴⁴ If the discontinuity in the effective mass is small, we may use a semi-classical (local) approximation by placing the effective mass factor in equations (5) and (13) *inside* the gradient operator. This should adequately describe the GaAs-Al_xGa_{1-x}As heterojunction for Al mole fractions in the direct-gap range, and this approximation was used in the present calculations.

There is no dissipation due to random scattering within the device in the present model. Energy dissipation occurs through the loss of energetic electrons to the reservoirs. The inclusion of random scattering would not seriously complicate the present calculations so long as the collision super-operator $C(x,k; x',k')$ is local in the sense that it has the form $C(k, k')\delta(x-x')$. (By "not seriously complicate the calculations," I mean that the collision operator would not add to the sparsity structure of the Liouville super-operator as defined in (13). The elements of C would of course have to be evaluated and added to the corresponding elements of L , but the algorithms and data structures required to solve for the Wigner function would remain unchanged.) The collision operator has been shown to take this form in the case of a uniform field.^{45,46} An obvious first approximation would be to use a classical Boltzmann collision operator. This has not yet been done.

It would be desirable to have more detailed microscopic models of the coupling between a device and its contacts, while still treating the contact as a reservoir. Techniques such as those used to integrate out the heat-bath variables in studies of dissipative systems^{7,21,39,41} might be applied to integrate out the reservoir variables. The boundary conditions used here are perhaps a crude model, but they illustrate the essential physics of the system-reservoir interaction.⁸

VIII. RELATION TO OTHER WORK

The more traditional approach to modeling tunneling devices is to evaluate stationary scattering states.^{22-24,35,47-49} This is an excellent way to obtain the steady-state behavior, particularly the $I(V)$ curve. When this approach is applied to time-dependent phenomena, however, the results are much less satisfactory. The result is expressed as a single "characteristic time."^{35,47,48} (It is clear from Figs. 9 and 10 that the transient response of a tunneling device actually involves several different time constants.) There is a marked contrast between the rather qualitative nature of the derivation of this characteristic time scale and the highly detailed and precise calculations of steady-state properties in the same papers. This contrast suggests that the scattering theory is inherently unsuited to the calculation of transient phenomena.

The problem with scattering theory concerns the formulation of boundary conditions for the time-dependent Schroedinger equation. As pointed out in the

discussion of Eq. (1) it is not possible to describe the transient transition from one steady state to another with finite boundary conditions that leave the Hamiltonian Hermitian. Conceptually, there is no problem if the boundary conditions are allowed to approach infinity. (The irreversibility that results in such a case comes from the infinite propagation of disturbances in the wavefunctions.) Boundary conditions at infinity, however, are very difficult to treat computationally. Kundrotas and Dargys⁵⁰ have dealt with this problem for the case of tunneling out of the bound state of a delta-function potential. To do so, they invoked the special properties of the bound state. The present statistical approach makes no such assumptions, and in fact does not require that a distinction be made between bound and free states.

The use of the Wigner distribution function in semiconductor device problems has been previously advocated by other workers. The published works on this subject are either primarily concerned with the formulation of the problem (rather than its solution)^{44,46,51,52}, or report calculations that suffer from numerical instabilities.⁵³ The missing element has been a proper formulation of the open-system boundary conditions. When these boundary conditions (and the logically consequent discretization scheme) are included, the direct solution of the Liouville equation for the Wigner distribution function becomes a practical technique for the analysis of quantum semiconductor devices.

ACKNOWLEDGEMENTS

This work was supported in part by the Office of Naval Research and the Army Research Office. I would also like to acknowledge helpful discussions with R. T. Bate, C.D. Cantrell, D.K. Ferry, K. Hess, A. J. Leggett, W. Pötz, M. A. Reed and L. E. Reichl.

REFERENCES

- ¹R. Dingle, W. Wiegmann and C. H. Henry, *Phys. Rev. Lett.* **33**, 827 (1974).
- ²L. L. Chang, L. Esaki and R. Tsu, *Appl. Phys. Lett.* **24**, 593 (1974).
- ³T. C. L. G. Sollner, W. D. Goodhue, P. E. Tannenwald, C. D. Parker and D. D. Peck, *Appl. Phys. Lett.* **43**, 588 (1983).
- ⁴G.H. Heilmeier, IEEE International Electron Device Meeting, Technical Digest 1984, p.2.
- ⁵W.R. Frensley, *Phys. Rev. Lett.* **57**, 2853 (1986).
- ⁶M.A. Reed, J.W. Lee, and H.L. Tsai, *Appl. Phys. Lett.* **49**, 158 (1986).
- ⁷E.B. Davies, *Quantum Theory of Open Systems* (Academic Press, London, 1976) and references therein.
- ⁸R. Landauer, *Philos. Mag.* **21**, 863 (1970); also in *Localization, Interaction and Transport Phenomena in Impure Metals*, edited by B. Kramer, G. Bergmann, and Y. Bruynseraede (Springer-Verlag, Berlin, 1985).
- ⁹I. Langmuir and K.T. Compton, *Rev. Mod. Phys.* **2**, 191 (1931).
- ¹⁰A. Messiah, *Quantum Mechanics*, Vol. 1 (Wiley, New York, 1962), p. 120.
- ¹¹G.V. Chester, *Rep. Prog. Phys.* **26**, 411 (1963).
- ¹²U. Fano, *Rev. Mod. Phys.* **29**, 74 (1957).
- ¹³E. Wigner, *Phys. Rev.* **40**, 749 (1932).
- ¹⁴L.P. Kadanoff and G. Baym, *Quantum Statistical Mechanics* (Benjamin/Cummings, Reading, Mass., 1962).
- ¹⁵R.P. Feynman and A.R. Hibbs, *Quantum Mechanics and Path Integrals* (McGraw-Hill, New York, 1965).
- ¹⁶W.R. Frensley, unpublished.

- 17W. R. Frensley, *J. Vac. Sci. Technol. B* **3**, 1261 (1985).
- 18W. Shockley, *Electrons and Holes in Semiconductors* (Van Nostrand, Princeton, 1950), sec. 12.5.
- 19H.K. Gummel, *IEEE Trans. Electron Devices* **ED-11**, 455 (1964).
- 20E.M. Conwell, *High Field Transport in Semiconductors* (Academic Press, New York, 1967).
- 21A. O. Caldeira and A. J. Leggett, *Physica A* **121**, 587 (1983).
- 22C.B. Duke, *Tunneling in Solids* (Academic Press, New York, 1969).
- 23E.L. Wolf, *Principles of Electron Tunneling Spectroscopy* (Oxford University Press, New York, 1985), Ch. 2.
- 24R. Tsu and L. Esaki, *Appl. Phys. Lett.* **22**, 562 (1973).
- 25P. A. Lebowitz and P. J. Price, *Appl. Phys. Lett.* **19**, 530 (1971).
- 26C. Jacoboni and L. Reggiani, *Rev. Mod. Phys.* **55**, 645 (1983).
- 27P.J. Roache, *Computational Fluid Dynamics* (Hermosa Publishers, Albuquerque, NM, 1976), pp. 64-72.
- 28J.J. Duderstadt and W.R. Martin, *Transport Theory* (Wiley, New York, 1979), pp. 431-8.
- 29S. Selberherr, *Analysis and Simulation of Semiconductor Devices* (Springer-Verlag, Wien, 1984), sec. 6.1.
- 30R.C. Miller, D.A. Kleinman, and A.C. Gossard, *Phys. Rev. B* **29**, 7085 (1984).
- 31B. Monemar, K.K. Shih, and G.D. Pettit, *J. Appl. Phys.* **47**, 2604 (1976).
- 32R. Haydock, in *Solid State Physics*, edited by H. Ehrenreich, F. Seitz, and D. Turnbull (Academic Press, New York, 1980), vol. 35, p.215.

- 33H. Ohnishi, T. Inata, S. Muto, N. Yokoyama, and A. Shibatomi, *Appl. Phys. Lett.* **49**, 1248 (1986).
- 34W.R. Frensley, *IEEE International Electron Device Meeting, Technical Digest 1986*, p. 571.
- 35D.D. Coon and H. C. Liu, *Appl. Phys. Lett.* **49**, 94 (1986).
- 36L. Lapidus and J.H. Seinfeld, *Numerical Solution of Ordinary Differential Equations* (Academic Press, New York, 1971), ch. 6.
- 37R.P. Feynman, *Phys. Rev.* **84**, 108 (1951).
- 38C.W. Gardiner, *Handbook of Stochastic Methods* (Springer-Verlag, Berlin, 1985), ch. 7.
- 39R. Zwanzig, *J. Chem. Phys.* **33**, 1338 (1960).
- 40H. Spohn, *Rev. Mod. Phys.* **53**, 569 (1980).
- 41W. H. Louisell, *Quantum Statistical Properties of Radiation* (Wiley, New York, 1973), ch. 6.
- 42G. Bastard, *Phys. Rev. B* **24**, 5693 (1981).
- 43T. Ando and S. Mori, *Surf. Sci.* **113**, 124 (1982).
- 44J.R. Barker, D.W. Lowe, and S. Murray in *The Physics of Submicron Structures*, edited by H.L. Grubin, K. Hess, G.J. Iafrate, and D.K. Ferry (Plenum, New York, 1984), p. 277.
- 45I. B. Levinson, *Zh. Eksp. Teor. Fiz* **57**, 660 (1969) [*Sov. Phys. JETP* **30**, 362 (1970)].
- 46J. Lin and L.C. Chu, *J. Appl. Phys.* **57**, 1373 (1985).
- 47B. Ricco and M. Ya. Azbel, *Phys. Rev. B* **29**, 1970 (1984).
- 48P.J. Price, *Superlattices and Microstructures* **2**, 593 (1986).
- 49M.O. Vassell, J. Lee, and H.F. Lockwood, *J. Appl. Phys.* **54**, 5206 (1983).

50J. Kundrotas and A. Dargys, *Phys. Status Solidi B* 134, 267 (1986).

51G.J. Iafrate, H.L. Grubin, and D.K. Ferry, *J. Phys. (Paris)* 42, suppl. C7, 307 (1981).

52J.R. Barker and S. Murray, *Phys. Lett. A* 93, 271 (1983).

53U. Ravaioli, M.A. Osman, W. Pötz, N. Klusdahl, and D.K. Ferry, *Physica B* 134, 36 (1985).

FIGURE CAPTIONS

Figure 1. Potential diagram and experimental $I(V)$ curve for a resonant-tunneling diode. The barriers are thin layers of a wider-gap semiconductor, typically (Al,Ga)As, and the quantum well and the regions outside the barriers are GaAs. A size-quantized state is confined in the well; its energy is indicated by the dashed line. (a) shows the structure in equilibrium. When a voltage is applied (b) electrons can resonantly tunnel out of occupied states (shaded region) through the confined state. As the voltage is increased (c) the resonant state is pulled below the occupied levels and the tunneling current decreases, leading to a negative-resistance characteristic, as the current decreases with increasing voltage. The experimental data are courtesy of M.A. Reed (Ref. 6).

Figure 2. Domain of the density matrix and Wigner distribution calculations. The arguments of the density matrix are x and x' . The Wigner function is obtained by transforming to the coordinates χ and ξ , followed by a Fourier transform with respect to ξ . The long-dashed lines indicate the system-reservoir boundaries, and they partition the domain into regions corresponding to various system-system, system-reservoir, and reservoir-reservoir correlations. The short-dashed lines represent the boundaries of the domain of the Wigner function calculation. Note that the Wigner function domain includes regions which represent correlation with the reservoirs.

Figure 3. Discretization scheme for the gradient (or drift) term of the Liouville equation. The flow of probability between meshpoints is indicated by the arrows, which also indicate the sense of the finite-difference approximation for the gradient. The upwind difference means that a flow toward the right implies a left-hand difference approximation, and *vice versa*. Note that the sense of the finite-difference is uniquely determined by the form of the boundary conditions.

Figure 4. Current vs. voltage for a resonant-tunneling diode consisting of 2.8 nm layers of $\text{Al}_{0.3}\text{Ga}_{0.7}\text{As}$ bounding a 4.5 nm GaAs well, at a temperature of 300 K. The current derived from a calculation of the Wigner function (solid line) is compared to that derived from a more conventional scattering calculation (dashed line).

Figure 5. Wigner distribution function for the steady-state calculation of Fig. 4, at zero bias voltage (thermal equilibrium). In the electrode regions, the distribution is approximately Maxwellian (as a function of k). The density is significantly reduced in the vicinity of the quantum well due to size-quantization effects.

Figure 6. Wigner function for 0.11 V bias, corresponding to the peak current in Fig. 4. The standing-wave patterns and strong negative peak indicate that significant quantum interference effects are occurring.

Figure 7. Wigner function for 0.22 V bias, corresponding to the valley current in Fig. 4. Note the similarity of this plot to that of the equilibrium case in Fig. 5.

Figure 8. Current density (solid line) and electron density in the quantum well (dashed line) as functions of bias voltage. The electron density in the well is a measure of the occupation of the resonant state.

Figure 9. Transient response of the resonant-tunneling diode of Fig. 4. Current density is plotted as a function of time and position within the device. The potential profile illustrates the device structure. At $t=0$, the voltage was suddenly switched from 0.11V (corresponding to the peak current) to 0.22V (corresponding to the valley current). After an initial peak, the current density approaches the lower steady-state value in 100-200 fs.

Figure 10. Transient response for a switching event opposite to that of Fig. 9. At $t=0$ the voltage was switched from 0.22 V to 0.11 V.

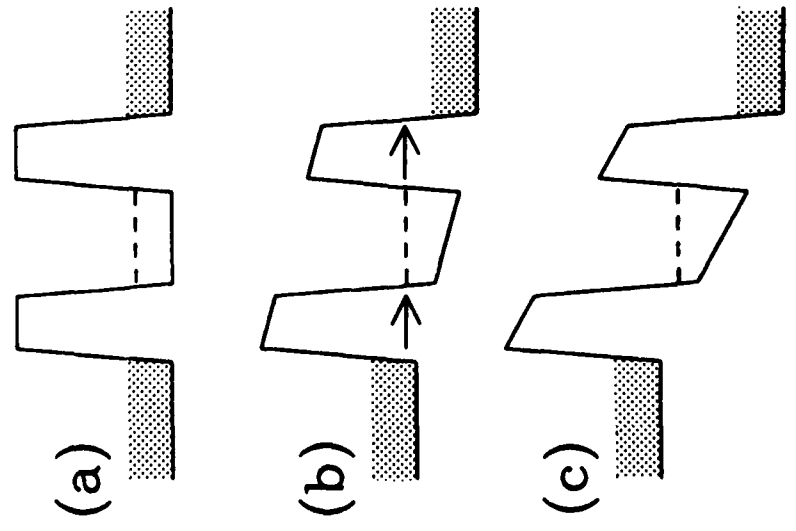
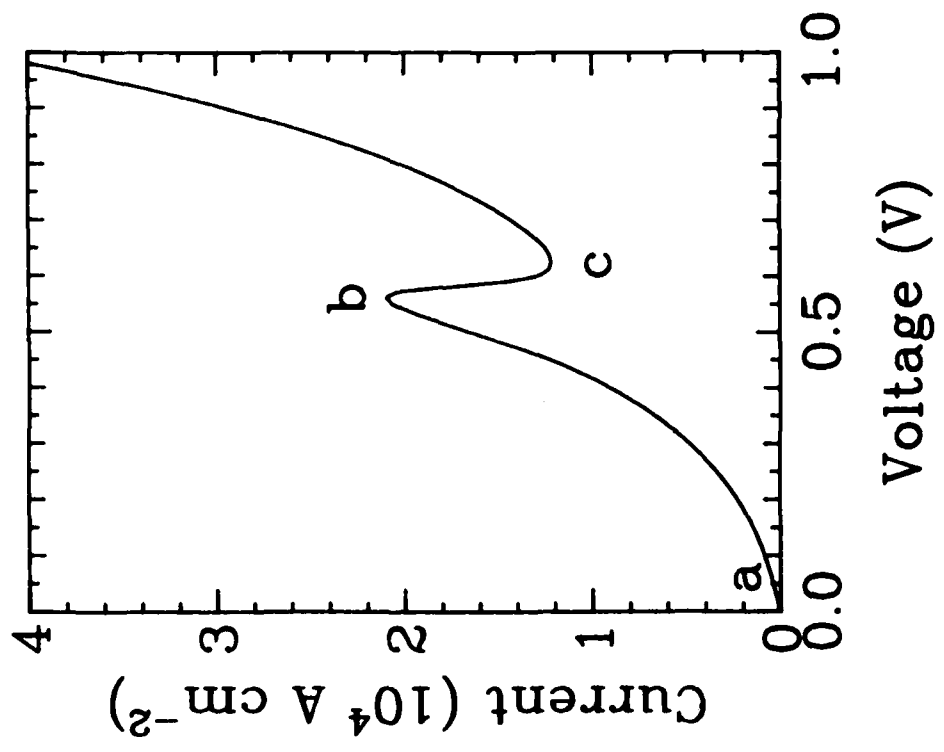
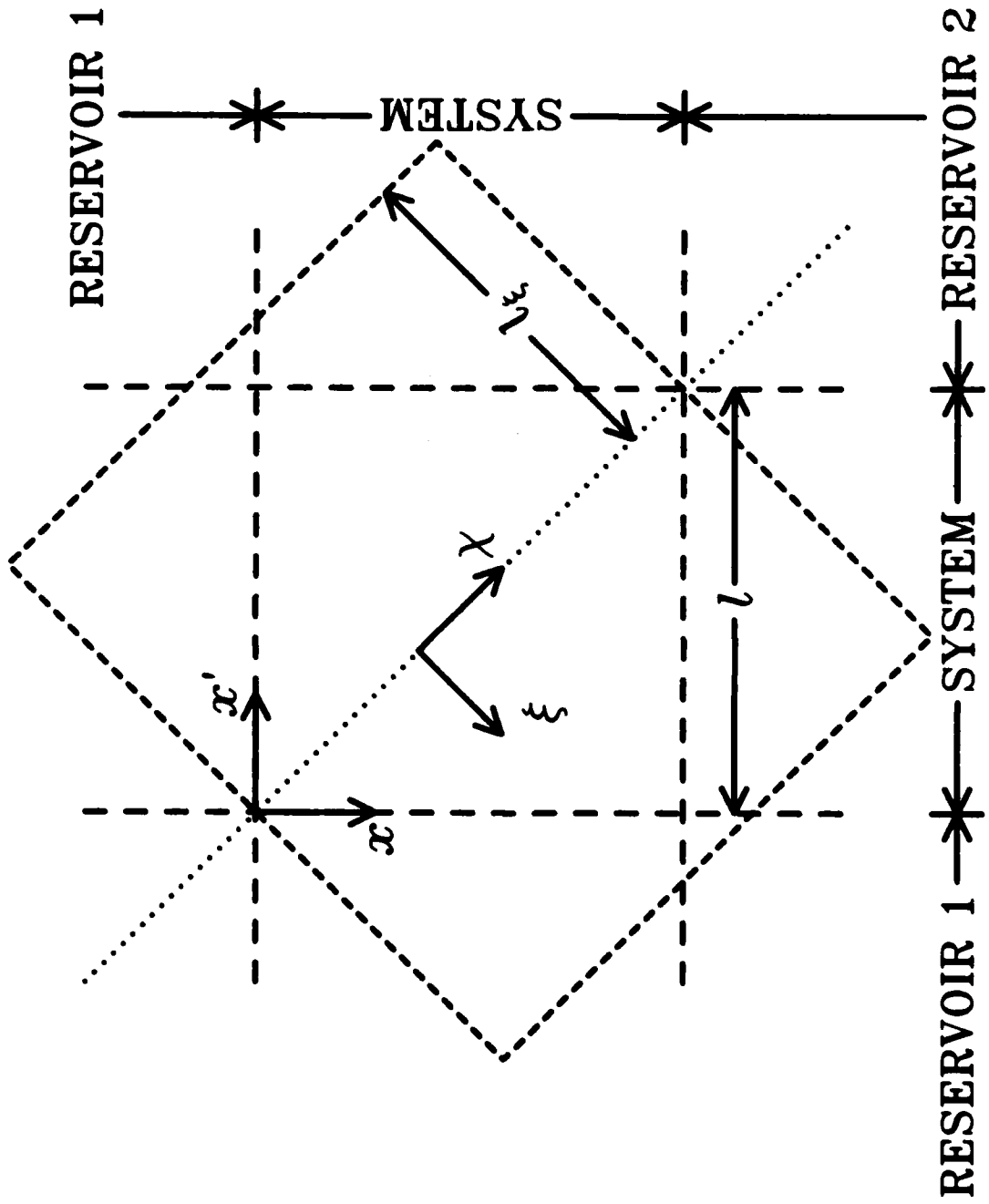


Figure 1



15 10 2

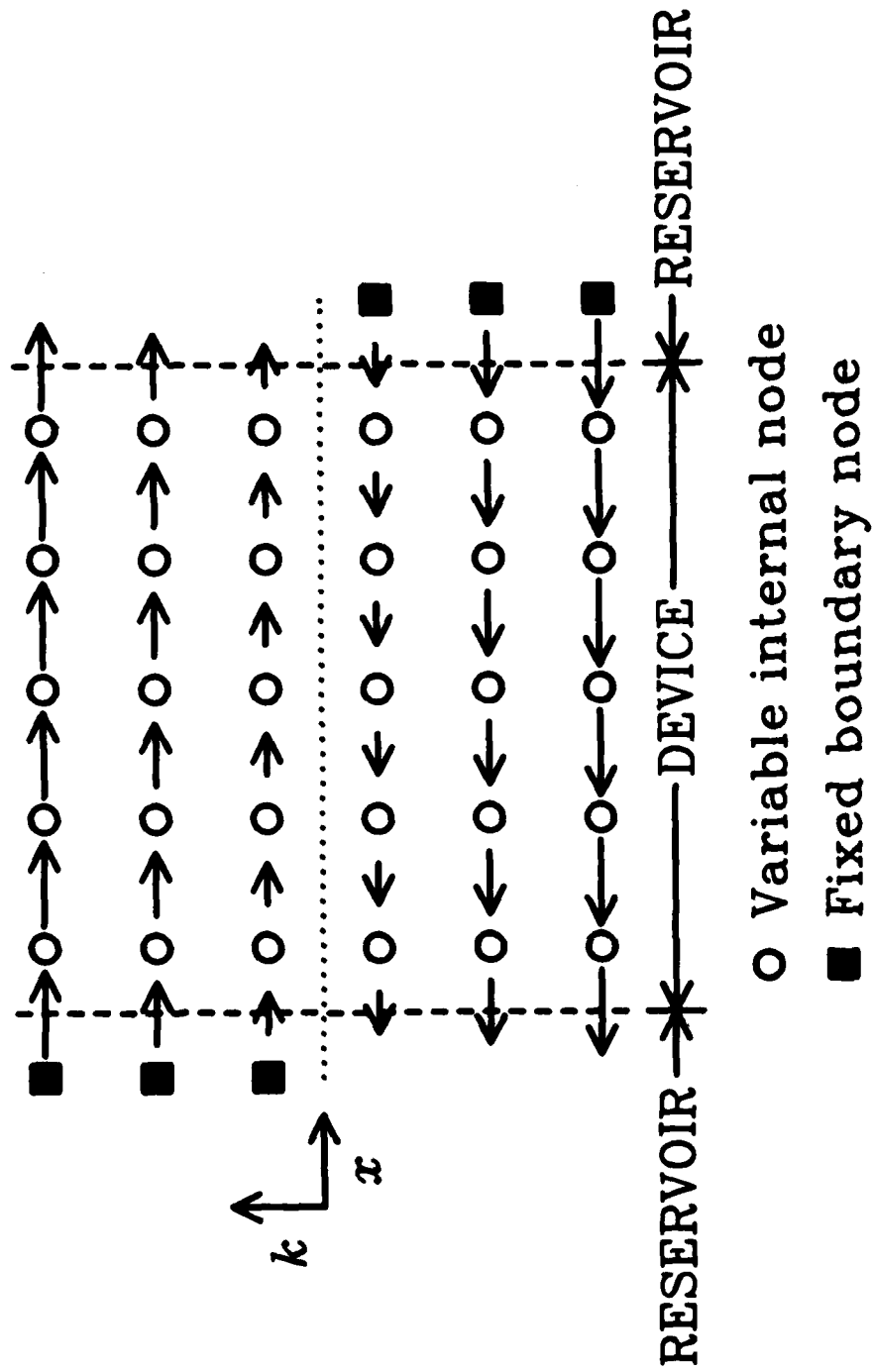
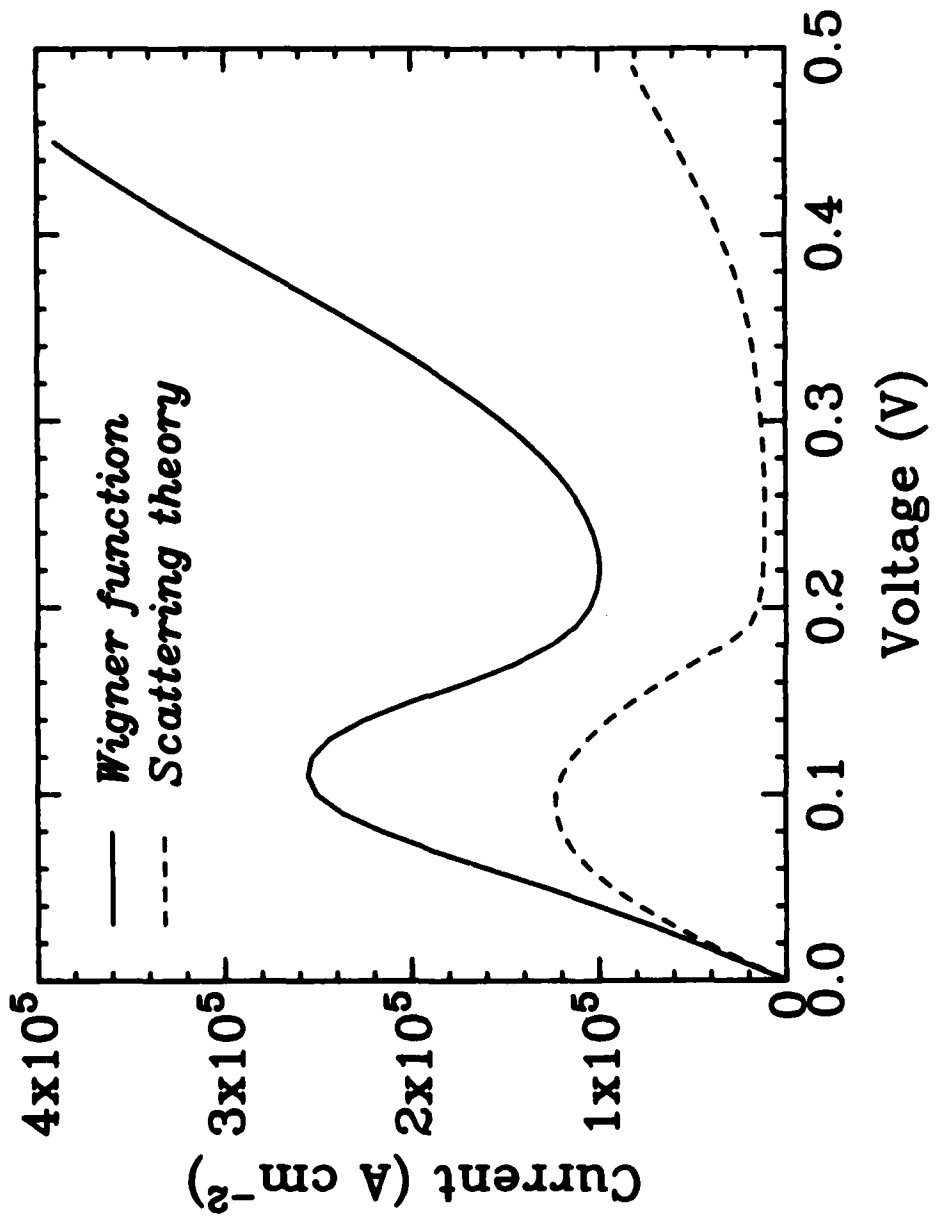


Fig. 2



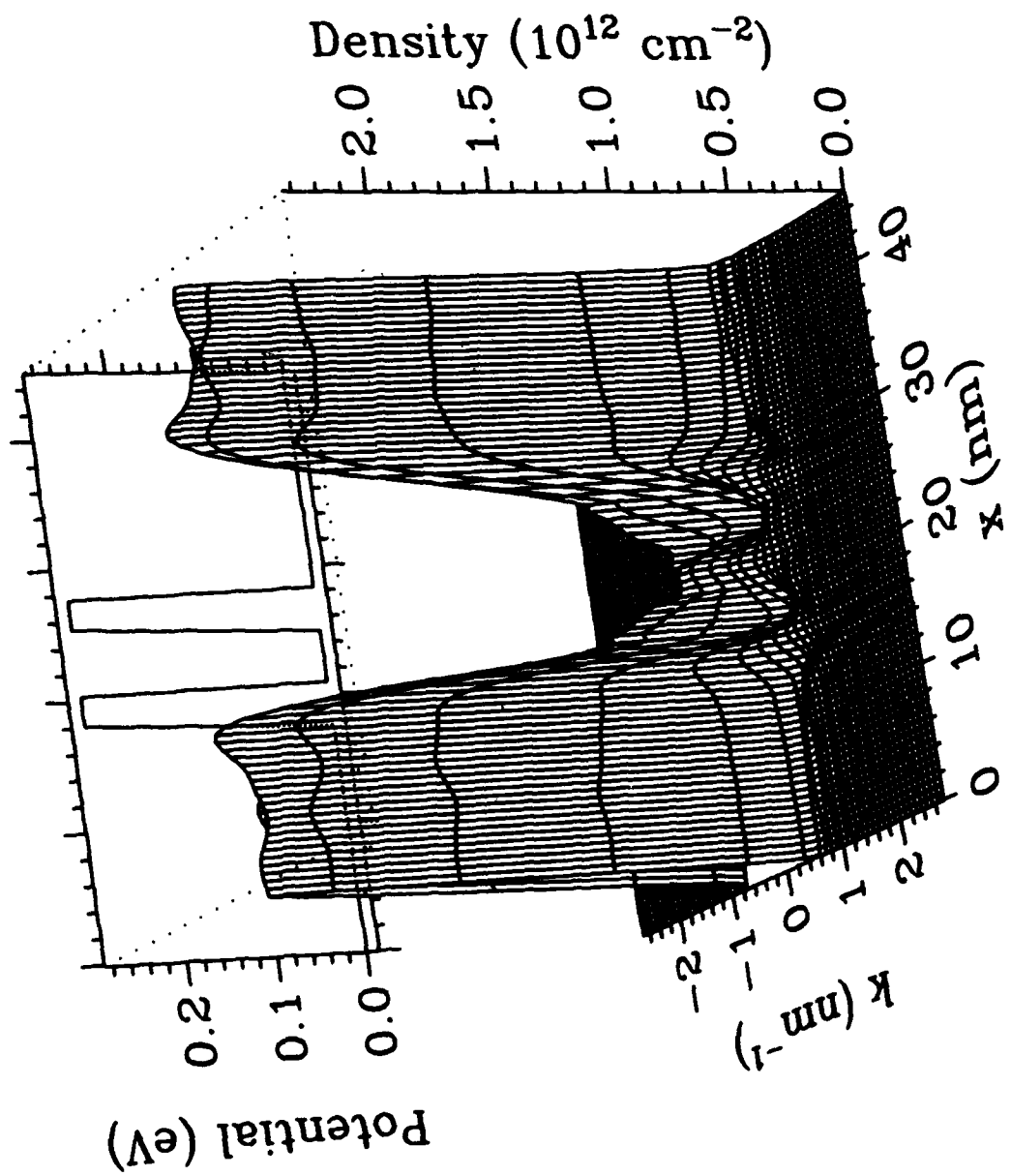


Figure 1

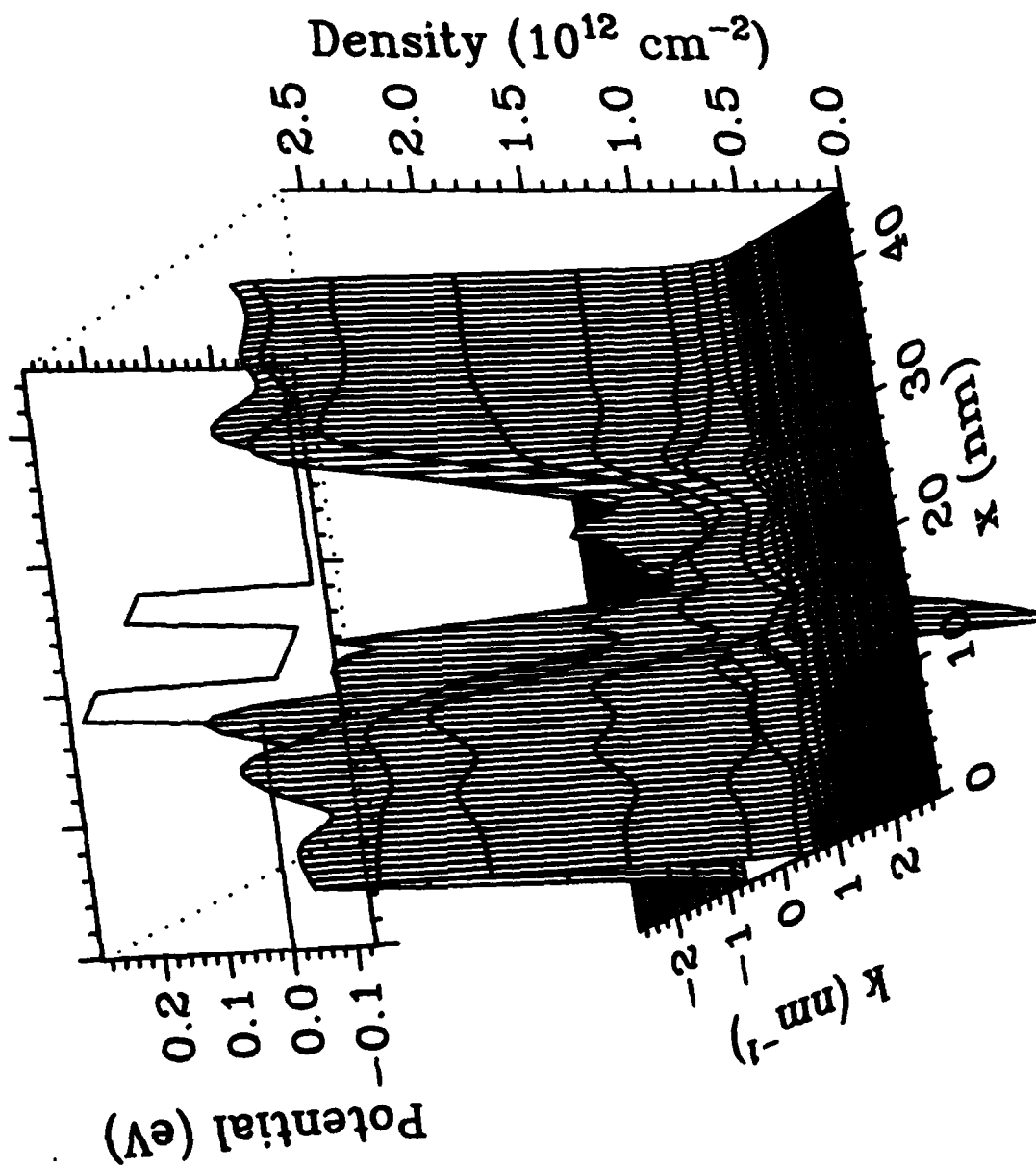


Figure 6

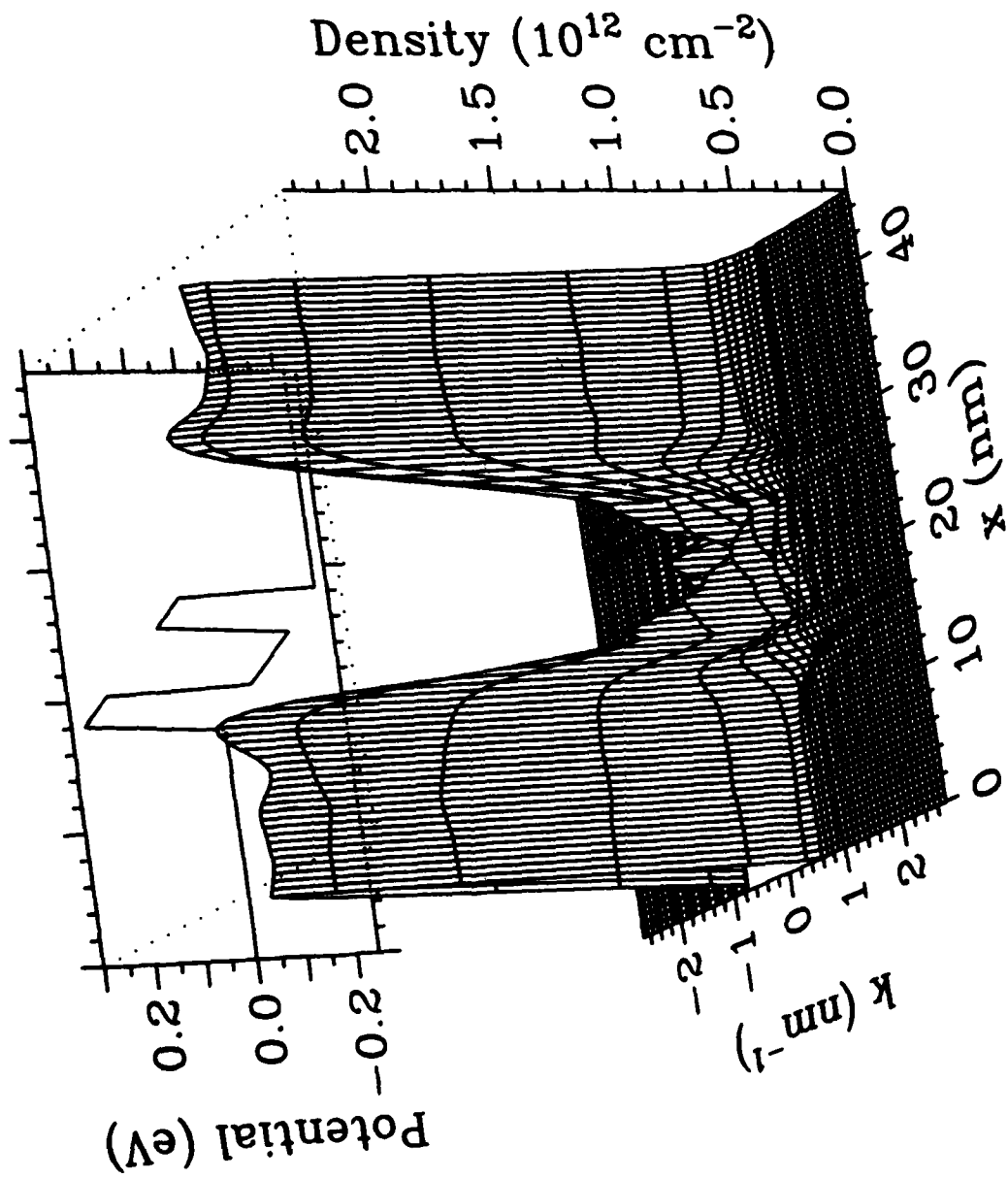


Figure 7

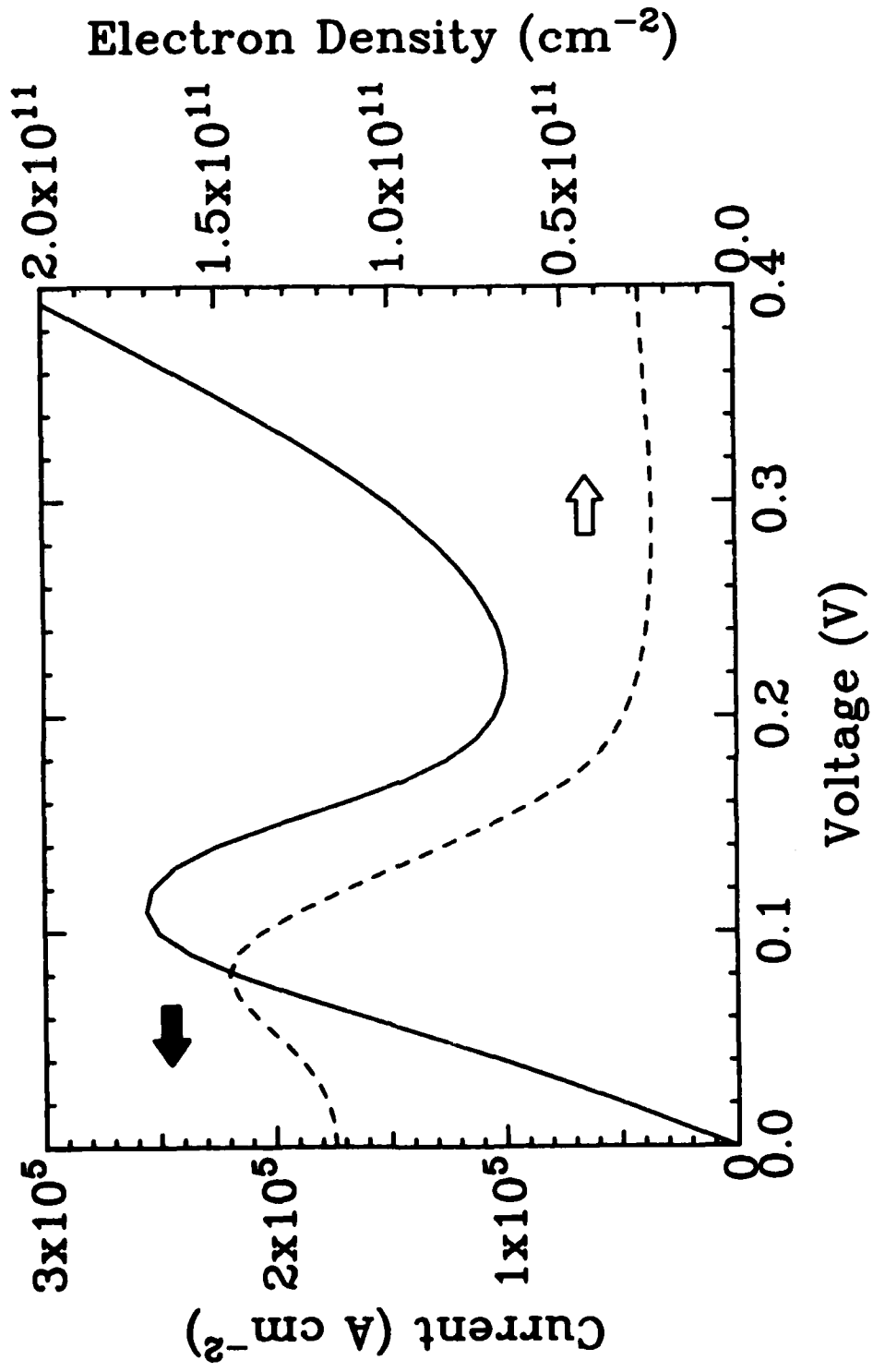


Figure 2

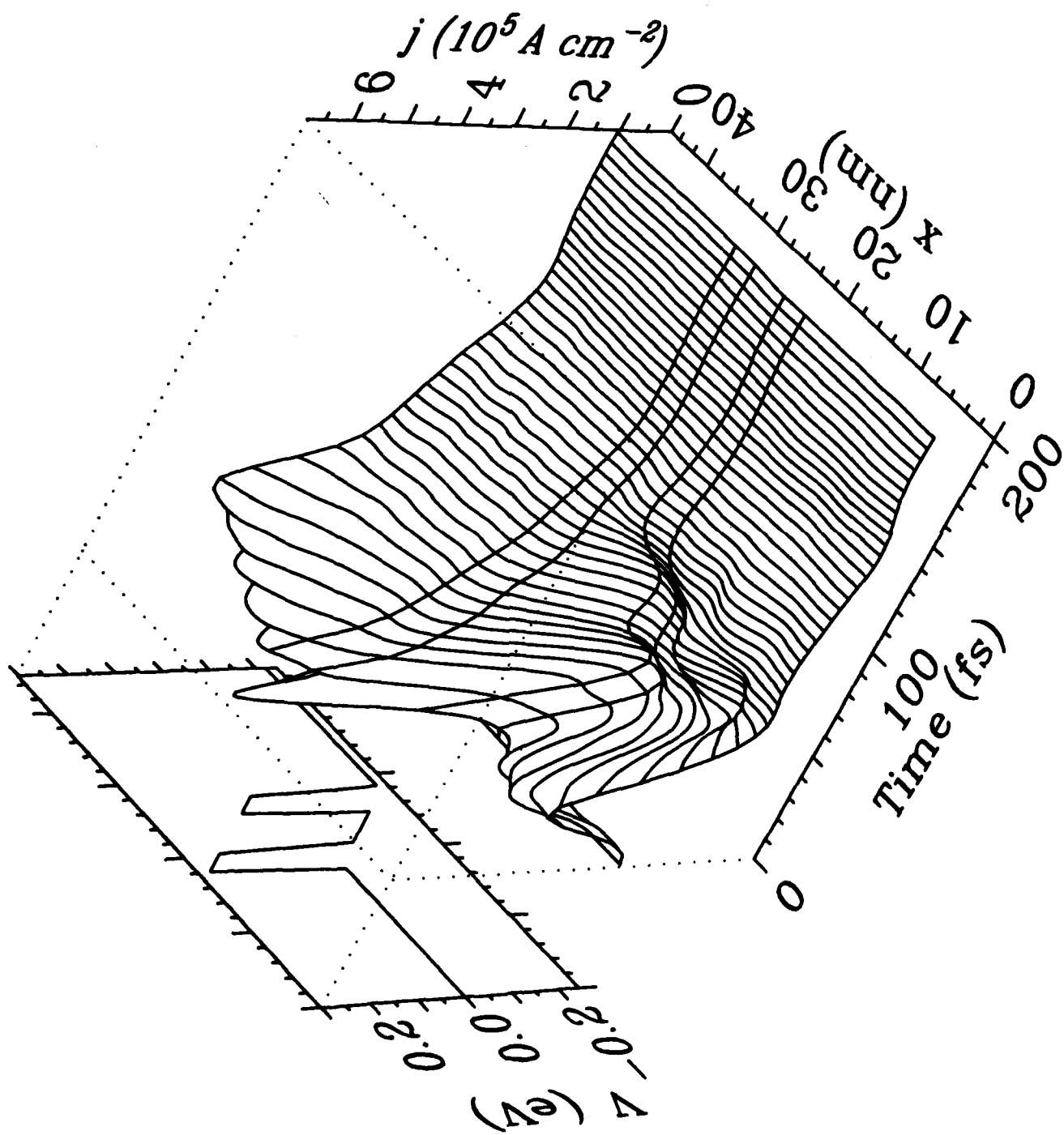


Figure 9

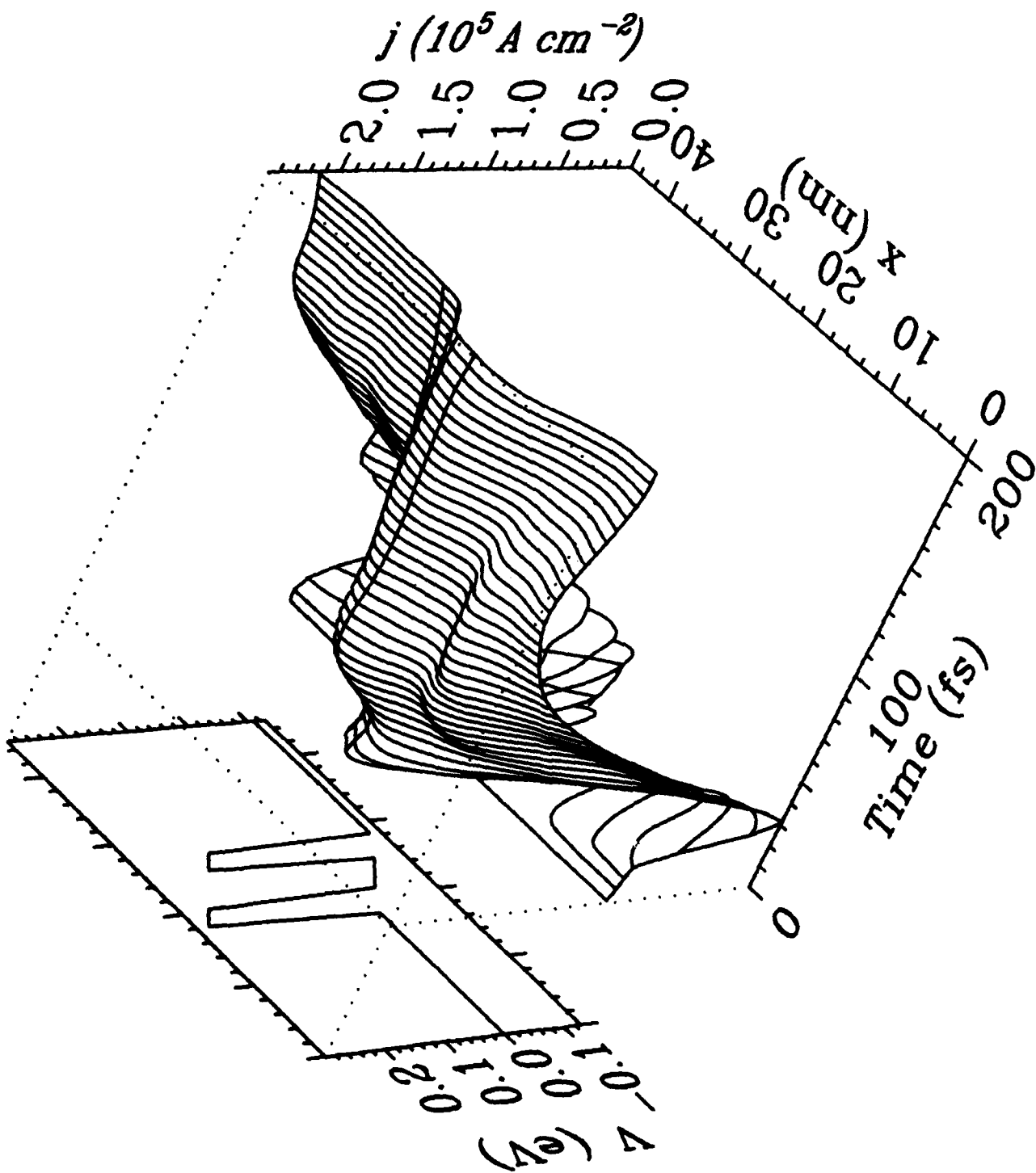


Figure 10

APPENDIX B

QUANTUM TRANSPORT SIMULATION OF THE
RESONANT-TUNNELING DIODE

Quantum Transport Simulation of the Resonant-Tunneling Diode

William R. Frensley

Texas Instruments Incorporated
Dallas, Texas 75265

ABSTRACT

The quantum-well resonant-tunneling diode is modeled by calculation of the Wigner distribution function. Boundary conditions applied to the Wigner function model the Ohmic contacts to the device and provide the required dissipative behavior. The Liouville equation is solved to obtain the steady-state response, or integrated to obtain the transient response. The steady-state I-V curves show the expected negative resistance, though the calculated peak-to-valley current ratio is smaller than that obtained from more conventional calculations and is smaller than the better experimental devices at low temperatures. The calculations of the detailed transient response are the first reported for a tunneling device, and resolve the question of the response time of the tunneling current. For a structure with 2.8 nm AlGaAs barriers, the current switches from its peak to its valley value in about 0.2 ps. The response time increases with the thickness of the barriers.

INTRODUCTION

The progress of semiconductor fabrication technology has made it possible to build devices whose operation depends upon quantum effects. The use of such devices provides a scenario in which the present exponential trends of increase in functionality may be continued beyond the limits of conventional IC technology [1].

The most widely studied example of a quantum size effect device is the resonant tunneling diode (RTD) [2,3]. This device exhibits interesting properties in the form of a negative-resistance region of its characteristic curve, and there are indications that its response time might be very short [3]. In the present work the RTD was taken as a prototype quantum device for the development of techniques for the analysis of such devices.

MODEL

The general features of the present model of the RTD are illustrated in Figure 1. The device is considered to be a finite region of semiconductor, characterized by a potential that includes the effects of applied voltages and of heterojunction band offsets. The boundaries of the device are taken to be interfaces to particle reservoirs, by which the terminals of the device are modeled. The internal state of the device is represented by the Wigner distribution function [4]

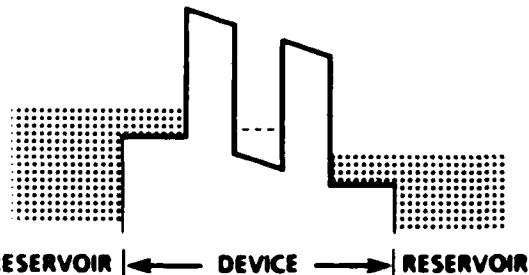


Figure 1. Energy diagram of the resonant-tunneling diode model. The device is coupled to electron reservoirs which model the contacts. Shading indicates occupied electron states.

which is the quantum analog of the classical distribution function $f(x,v)$ where x is the position and v is the velocity.

Regarding the contacts as particle reservoirs gives a well-defined model of the open-system nature of the device. The interaction between the reservoir and the device is simply described: Electrons in the device which impinge upon the reservoir pass into the reservoir without reflection and the distribution of electrons entering the device from the reservoir is given by the equilibrium distribution of the reservoir.

These boundary conditions are a crucial aspect of the model, because they permit the existence of steady-state solutions under applied bias and they lead to a stable approach to those steady-state solutions after the bias voltage is changed.

The time evolution of the Wigner function is described by the Liouville equation

$$\frac{d}{dt} = -\frac{\hbar k}{m} \frac{d}{dx} - \frac{1}{\hbar} \int_{-\infty}^{\infty} \frac{d\hbar'}{2\pi} V(x, \hbar' - \hbar) f(x, \hbar') \quad (1)$$

where the kernel of the potential operator is given by

$$V(x, \hbar) = 2 \int_0^{\infty} dy \sin(\hbar y) [v(x + \frac{1}{2}\hbar y) - v(x - \frac{1}{2}\hbar y)] \quad (2)$$

The open system boundary conditions are

$$\begin{aligned} f(\hbar, k) &= F(\mu, T) \quad \hbar > 0 \\ f(\hbar, k) &= F(\mu, T) \quad \hbar < 0 \end{aligned} \quad (3)$$

where F is the Fermi distribution function (integrated

over the transverse momenta), $\mu_{l,r}$ are the Fermi levels, and $T_{l,r}$ are the temperatures of the respective contacts.

Equation (1) is discretized on a uniform mesh in the phase space (x,k) . The boundary conditions lead to a natural discretization of the gradient term with a right-hand difference for $k > 0$ and a left-hand difference for $k < 0$. This is an "upwind" difference and is the means by which the boundary conditions stabilize the solutions of the Liouville equation.

STEADY-STATE BEHAVIOR

The dc characteristics of the RTD are obtained by solving the Liouville equation for $d/dt=0$. Figure 2 shows the Wigner distribution function which results from this procedure. A mesh with 80 points in x and 60 points in k was used. The time required to solve this discrete linear system is about 4 minutes on a VAX 11/785.

The steady-state calculation is repeated for a number of values of bias voltage to obtain the $I(V)$ curve. Figure 3 shows the results of the $I(V)$ calculation using the Wigner function and using a more conventional scattering-state model. The Wigner function predicts a higher current density than does the scattering theory. In particular, the valley current is significantly higher, leading to a lower predicted peak-to-valley ratio. Because the phonon scattering processes which are responsible for most of the temperature dependence of the $I(V)$ curve are not included in the present model, the $I(V)$ curve calculated for lower temperatures shows a similar peak-to-valley ratio. At these lower temperatures, the Wigner function calculations in their present form significantly underestimate the peak-to-valley ratio as compared to the better experimental devices [5].

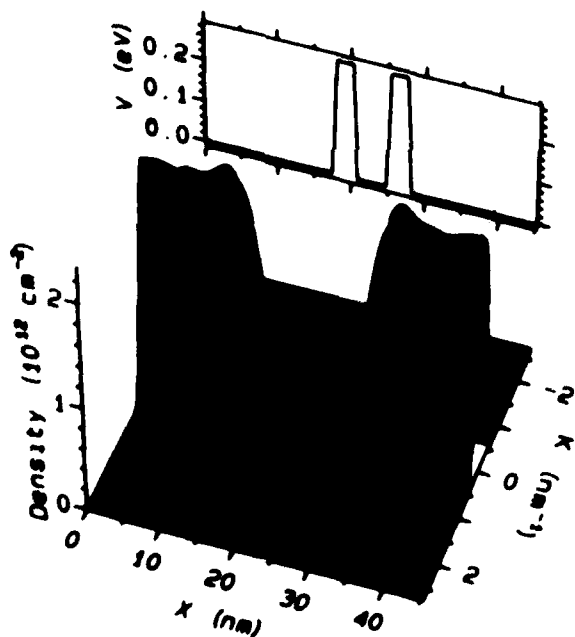


Figure 2. Wigner distribution function for zero bias.

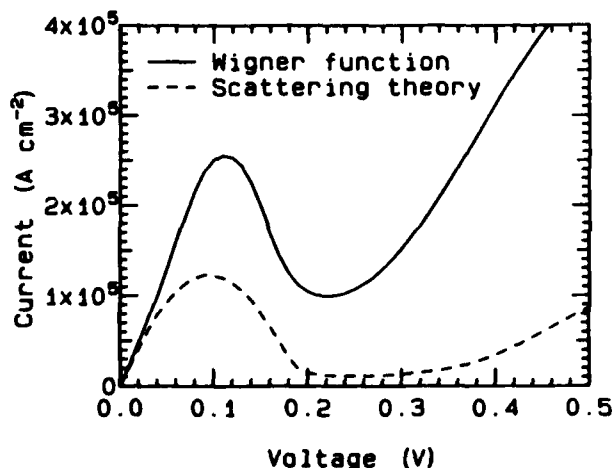


Figure 3. $I(V)$ characteristics derived from the Wigner function calculation and from a conventional scattering theory calculation. The assumed device structure had 2.8 nm barriers of $\text{Al}_{0.3}\text{Ga}_{0.7}\text{As}$ around a 4.5 nm quantum well. The temperature was 300 K.

The Wigner function can be used to derive other useful information about the internal state of the device. One quantity of interest is the net electron density in the quantum well. It has been speculated that occupation of the resonant-tunneling state could lead to significant shifts in the device potential profile, possibly leading to unstable oscillation [6]. To test this idea, the electron density was integrated over the quantum well, and the result is displayed in Figure 4. The peak electron density in this particular structure is about $1.5 \times 10^{11} \text{ cm}^{-2}$. If the field lines originating from these electrons were terminated at a depletion layer edge 10 nm away from the center of the well, the resulting contribution to the potential would be only 0.02 V. In reality, the field will certainly be accommodated by a slight decrease in the density of the

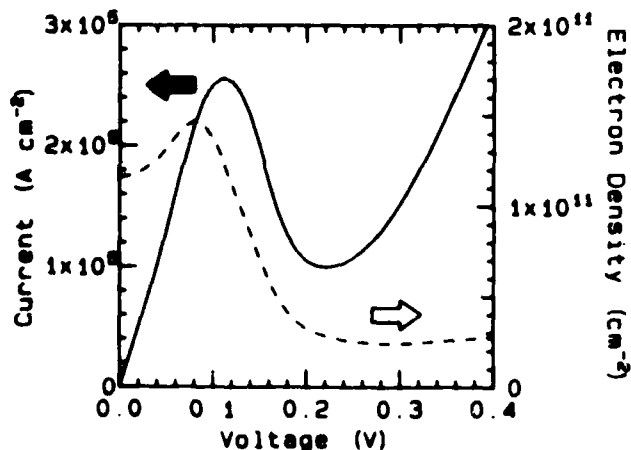


Figure 4. Current and total electron density in the quantum well as functions of voltage. The device structure was the same as that of Fig. 3.

accumulation layer on the cathode side of the structure, at a distance of more like 5 nm, and consequently the potential shift will be even less. Therefore, it seems likely that the effects of the self-consistent potential due to the electrons in the quantum well will be negligible.

TRANSIENT BEHAVIOR

The main advantage of a quantum transport theory approach is that it can provide a detailed description of the transient behavior of a tunneling device. The problem of estimating the response time has been extensively studied recently, usually from the point of view of scattering theory [6-8]. A perturbation approach applied to the scattering states will give a single characteristic time. The present approach demonstrates that the transient response of a tunneling device is a considerably more complex phenomenon than is envisioned in scattering analysis.

To obtain the transient response, one must integrate the Liouville equation with respect to time. The linear system of differential equations which results from the discretization in phase space is "stiff" in that the eigenvalues of the Liouville operator span a large range of magnitudes. To assure the stability of the solution, a fully implicit or backward-difference approach was used for the time integration. The steady-state solution for an appropriate bias voltage was used as the initial value for the Wigner function.

The calculated transient response of the RTD is shown in Figure 5. For this calculation, the device was assumed to be initially in the steady state at the peak of the I(V) curve. The bias voltage was suddenly switched at $t=0$ to the value at the bottom of the I(V)

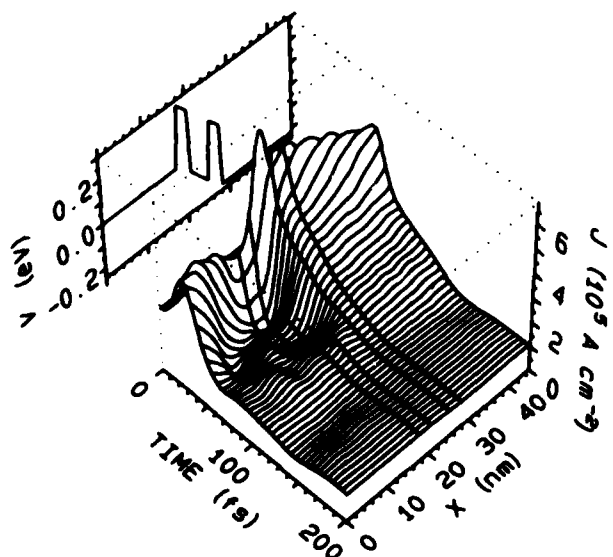


Figure 5. Transient response of the resonant-tunneling diode. Current density is plotted as a function of position within the device and as a function of time after a sudden change in bias voltage. At $t=0$ the bias voltage was changed from 0.11 V (corresponding to the peak current) to 0.22 V (the bottom of the valley).

curve. The device shows positive resistance behavior for a short time, as the current increases. There is a particularly prominent peak in the current at the downstream side of the quantum well after 5 fs. This is due to the electrons in the well piling up against the barrier. The current has essentially reached its steady-state value by 200 fs.

EFFECT OF BARRIER WIDTH

The characteristics of the RTD are quite sensitive to the width of the barrier layers. As shown in Figure 6, the peak current density varies exponentially with the width of the barrier. The peak electron density in the quantum well also varies, but much less sensitively. A simple estimate of the response time of the device may be obtained from $t=qn/j$, where q is the electron charge, n is the electron density in the well, and j is the current density. This estimate of the response time is also plotted in Figure 6. The response time estimated in this way certainly gives the same order of magnitude as that which is obtained from the detailed transient response calculations described above. It also varies approximately exponentially with the barrier width.

The detailed calculations of transient response do not show as great a sensitivity to the barrier width as does the simple estimate of response time. If we consider barrier widths of 1.7 and 3.4 nm, Figure 6 indicates that the response times should vary by a factor of four. The detailed calculations show something that is more like a factor of two. The transient response calculations are summarized in Figures 7 and 8. The tail of the response generally persists about twice as long for the 3.4 nm barrier structure. The initial positive-resistance transient (for

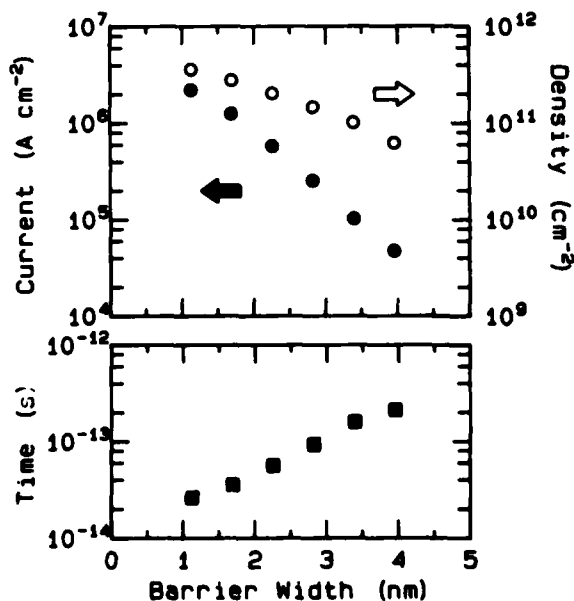


Figure 6. Peak values of current density (solid circles) and electron density in the quantum well (open circles) as a function of barrier width for a 4.5 nm quantum well. The simple estimate of response time $t=qn/j$ is plotted in the lower graph.

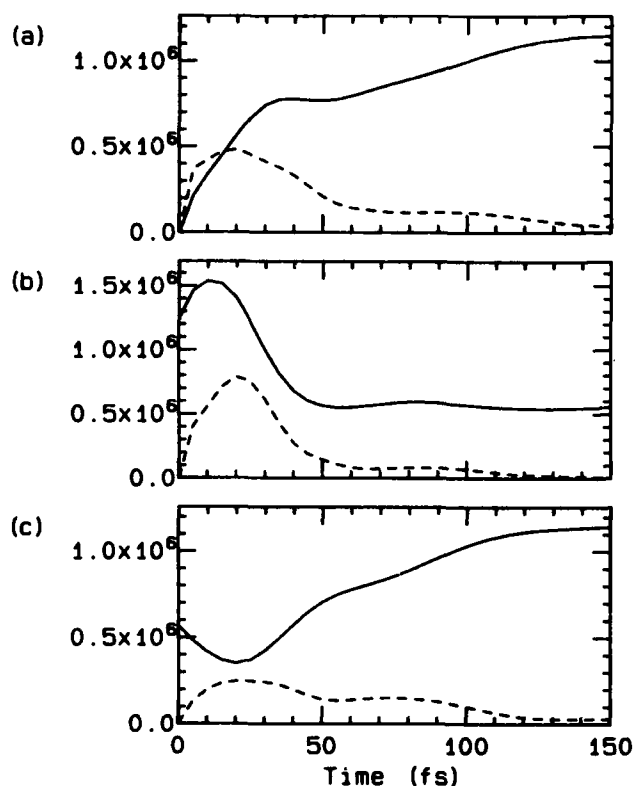


Figure 7. Summary of transient response calculations for a device with 1.7 nm barriers. The solid line shows the current density (in A cm^{-2}) averaged over the structure and the dashed line shows the standard deviation from this average. In (a), the voltage was switched from 0 to the peak value at $t=0$. In (b) it was switched from the peak to the valley. In (c) it was switched from the valley to the peak.

cases (b) and (c) shows much less dependence on barrier width, enduring for about 40 fs in each structure.

In each structure, the transition from peak to valley (b) seems to require about one-half as much time as the transition from the valley to the peak (c). This can be explained by the influence of the electric field on the effective barrier width. The higher electric field due to the higher bias voltage at the valley point leads to a more "triangular" barrier which is thus effectively narrower. The same effect probably explains why the response time does not increase with barrier width as rapidly as simple analyses would predict.

ACKNOWLEDGEMENT

This work was supported in part by the Office of Naval Research and the Army Research Office.

REFERENCES

[1] G.H. Heilmeyer, "Microelectronics: End of the Beginning or Beginning of the End?" Technical Digest, 1984, IEEE IEDM, pp. 2-5.

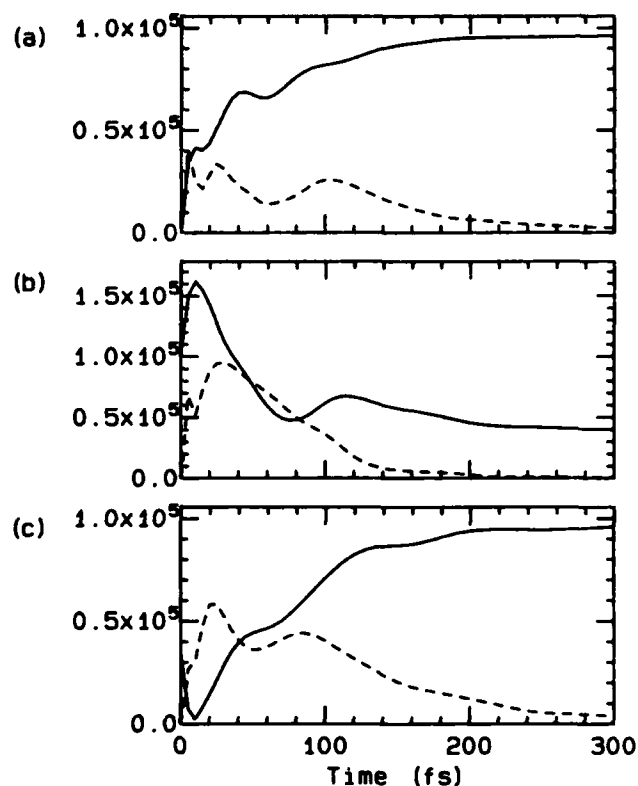


Figure 8. Summary of transient response calculations for a device with 3.4 nm barrier. The conventions are the same as those of Figure 7.

[2] L.L. Chang, L. Esaki, and R. Tsu, "Resonant Tunneling in Semiconductor Double Barriers," *Appl. Phys. Lett.*, Vol. 24, pp. 593-5 (1974).

[3] T.C.L.G. Sollner, W.D. Goodhue, P.E. Tannenwald, C.D. Parker, and D.D. Peck, "Resonant Tunneling through Quantum Wells at Frequencies up to 2.5 THz," *Appl. Phys. Lett.*, Vol. 43, pp. 588-90 (1983).

[4] E. Wigner, "On the Quantum Correction for Thermodynamic Equilibrium," *Phys. Rev.*, Vol. 40, pp. 749-59 (1932).

[5] M.A. Reed, J.W. Lee, R.K. Aldert, and A.E. Wetsel, "Investigation of Quantum Well and Tunnel Barrier Growth by Resonant Tunneling," *J. Mater. Res.*, Vol. 1, pp. 337-42 (1986).

[6] B. Ricco and M.Ya. Azbel, "Physics of Resonant Tunneling. The One-Dimensional Double-Barrier Case," *Phys. Rev. B*, Vol. 29, pp. 1970-1981 (1984).

[7] S. Luryi, "Frequency Limit of Resonant-Tunneling Double-Barrier Oscillators," *Appl. Phys. Lett.*, Vol. 45, pp. 490-2 (1985).

[8] P.J. Price, "Resonant Tunneling Properties of Heterostructures," 2nd Int. Conf. on Superlattices, Microstructures and Microdevices, Göteborg, 1986.

APPENDIX C

QUANTUM-TRANSPORT CALCULATION OF THE SMALL-SIGNAL
RESPONSE OF A RESONANT-TUNNELING DIODE

**Quantum-transport calculation of the small-signal response of
a resonant-tunneling diode**

**William R. Frensley
Central Research Laboratories
Texas Instruments
P.O. Box 655936, MS 154
Dallas Texas 75265**

ABSTRACT

The linear and lowest-order nonlinear response of a quantum-well resonant-tunneling diode is evaluated using quantum transport theory. The calculations show that the negative conductance persists up to about 5 THz, although parasitic circuit elements will limit the maximum oscillation frequency to a much lower value. The nonlinear response (rectification) remains significant to frequencies near 10 THz and shows a resonant peak near 4 THz. These calculations support the interpretation of the experimental data of Sollner *et al.* [Appl. Phys. Lett. 43, 588 (1983)] that rectification at 2.5 THz was observed in their devices.

PACS numbers: 73.40.Lq, 05.60.+w, 73.40.Gk, 85.30.De

Recent interest in the quantum-well resonant-tunneling diode¹ can be attributed to the work of Sollner *et al.*², who demonstrated nonlinear electrical response in these devices at frequencies up to 2.5 THz. The inference that this reflects the inherent speed of response of the tunneling mechanism has been questioned on the basis of theoretical estimates suggesting a much slower response.³ The present paper reports detailed calculations of the small-signal linear and nonlinear ac response of a model resonant-tunneling device, using a recently developed implementation of quantum transport theory which is well adapted to quantum semiconductor device problems.^{4,5}

The physical model of the resonant-tunneling diode is summarized in Fig. 1. The form of the potential is shown in (a). The electric field due to the dc bias voltage V and ac signal of amplitude v is superimposed upon the heterostructure barriers. For the purpose of obtaining the electrostatic potential, the contact layers on either side of the quantum-well barriers are assumed to be ideally metallic (i.e. the accumulation and depletion layers are taken to be of infinitesimal width). The equivalent circuit of the device is shown in (b). The series resistance R_s is due to the combined effects of all contacting layers, semiconducting and metallic, and as such is a quantity that depends purely on the device design and fabrication technology. The capacitance C is due to the depletion of electrons in the vicinity of the quantum well structure. The current source j responds to the voltage applied across it, and represents the electronic response of the intrinsic device. For a fixed dc bias voltage V , the current density j can be expanded in a power series in v , and to second order it is given by:

$$j(t) = j_0(V) + \frac{1}{2}(yve^{i\omega t} + cc) + \frac{1}{2}a_{rect}v^2 + \frac{1}{2}(a_{2\omega}v^2e^{2i\omega t} + cc) + \dots, \quad (1)$$

where cc denotes the complex conjugate. Here ω is the angular frequency, j_0 is the dc current density, and y is the linear admittance (which equals dj_0/dV at $\omega = 0$). The nonlinear coefficients a_{rect} and $a_{2\omega}$ describe rectification and second-harmonic generation, respectively, and both are equal to d^2j_0/dV^2 at $\omega = 0$.

The present calculations apply the techniques of Refs. 4 and 5. The internal state of the device is represented by the Wigner distribution function $f(x, k)$, where x denotes the position within the device and k is the electron momentum. The Wigner function is evaluated by solving the Liouville equation

$$\partial f / \partial t = (L / i\hbar) f \quad (2)$$

where L is the (integro-differential) Liouville super-operator. The boundary conditions on the Liouville equation represent the coupling of the tunneling device to ideal particle reservoirs and introduce time-irreversibility into the model. Inelastic scattering processes involving phonons (within the simulation domain) are not presently included in the model. A discretization approximation (finite-difference and finite-sum) is used to cast equation (2) into the form of a large set of coupled linear equations suitable for computer solution.

To obtain the small-signal ac response, we apply a simple form of perturbation theory to equation (2). The Liouville operator can be written as:

$$L = L_0 + \frac{1}{2}\lambda(L_\omega e^{i\omega t} + cc). \quad (3)$$

The dc part L_0 includes the kinetic energy term and the dc potential as shown in Fig. 1(a). The ac part L_ω includes only the effect of the time-varying potential and thus is proportional to v . λ is a perturbation parameter introduced solely to keep track of the order of the perturbation, which will ultimately be set equal to unity. The Wigner function f can be expanded in a perturbation series, which to second order is given by

$$f = f_0 + \frac{1}{2}\lambda(f_\omega e^{i\omega t} + cc) + \lambda^2 f_{rect} + \frac{1}{2}\lambda^2(f_{2\omega} e^{2i\omega t} + cc) + \dots \quad (4)$$

Here f_0 is the dc part of the Wigner function, f_ω contains the linear ac response, and again f_{rect} and $f_{2\omega}$ describe rectification and second-harmonic generation, respectively. The perturbation equations are obtained by inserting (3) and (4) into (2) and collecting terms of equal frequency and equal order in λ . The resulting equations are:

$$L_0 f_0 = 0. \quad (5a)$$

$$f_\omega = -\frac{1}{L_0 + \hbar\omega} L_\omega f_0. \quad (5b)$$

$$f_{rect} = \frac{1}{2L_0} \text{Re} \left(L_\omega^* \frac{1}{L_0 + \hbar\omega} L_\omega f_0 \right) \quad (5c)$$

$$f_{2\omega} = \frac{1}{L_0 + 2\hbar\omega} L_\omega \frac{1}{L_0 + \hbar\omega} L_\omega f_0. \quad (5d)$$

The resolvent expressions in (5b-d) are evaluated by the numerical techniques described in Ref. 5.

The contribution of a component f_i of the Wigner distribution to the terminal current density is obtained by averaging the current operator over the momentum, and over the active region of the device in accordance with the Ramo-Shockley theorem:^{6,7}

$$\mathcal{J}[f_i] = \frac{1}{x_r - x_l} \int_{x_l}^{x_r} dx \int_{-\infty}^{\infty} \frac{dk}{2\pi} \frac{\hbar k}{m^*} f_i(x, k). \quad (6)$$

The coefficients in (1) are thus given by:

$$j_0 = \mathcal{J}[f_0]. \quad (7a)$$

$$y = \mathcal{J}[f_\omega] / v. \quad (7b)$$

$$a_{rect} = \frac{1}{2} \mathcal{J}[f_{rect}] / v^2. \quad (7c)$$

$$a_{2\omega} = \frac{1}{2} \mathcal{J}[f_{2\omega}] / v^2. \quad (7d)$$

The device structure assumed in the present calculations is similar to the sample number 2 of Sollner *et al.*⁸ The model structure consists of a 4.5 nm wide quantum well of GaAs bounded by identical 2.8 nm wide barrier layers of $\text{Al}_{0.3}\text{Ga}_{0.7}\text{As}$. GaAs electrode layers 17.5 nm wide and doped at $2 \times 10^{17} \text{ cm}^{-3}$ were included in the simulation domain on each side of the device. All calculations were performed for a temperature of 300 K. The dc

$j(V)$ curve was evaluated by solving (5a) as described in Refs. 4 and 5, and the result is shown in Fig. 2.

The linear admittance was evaluated from (5b) and (7b), for $V = 0.17$ V, which is near the center of the negative resistance region. The resulting admittance as a function of frequency is shown in Fig. 3. The real conductance is negative at lower frequencies, as expected. The negative conductance "rolls off" in the THz region and goes positive at about 6 THz. The imaginary part of the electronic admittance is negative and proportional to ω at lower frequencies, and thus resembles an inductance. This is due to the phase shift resulting from the electrons' inertia.⁹

To provide an understanding of the role of the parasitic elements of Fig. 1(b), the capacitive susceptance ωC is also plotted in Fig. 3. If we represent the tunneling current by its conductance $g = \text{Re}(y)$ [and neglect $\text{Im}(y)$] then the resistance of the parallel conductance and capacitance is

$$R(g||C) = g^{-1} [1 + (\omega C/g)^2]^{-1}. \quad (8)$$

In the frequency range of interest g is negative, leading to a negative resistance which rolls off as $[1 + (\omega C/g)^2]^{-1}$. This factor becomes significant when $|\omega C/g| \approx 1$. From Fig. 3 it is apparent that this will occur around 40 GHz, well below the cutoff frequency of the tunneling current itself. As shown in Ref. 8, this leads to the "circuit limit" on the maximum oscillation frequency, which is reached when the negative resistance from (8) can no longer cancel the series resistance R_s . In the present calculation the capacitance per unit

area was taken to be $\epsilon/(x_r - x_l)$, to be consistent with the assumption of perfectly metallic contact layers, but this is a pessimistic estimate because the depletion layer in the real semiconductor layers will decrease the capacitance.

The rather complex behavior of the electronic admittance above 10 THz reflects other resonant processes in the system. In this frequency range the current response is quite nonlocal. For example, a rather different admittance curve is obtained if the current is averaged over a different region of the device than that specified in (6).

The nonlinear coefficients were evaluated from (5c,d) and (7c,d) for $V = 0.13$ V, at the resonant peak of the $j(V)$ curve. The modulus of a_{rect} and of $a_{2\omega}$ are plotted in Fig. 4 as functions of frequency. The interesting point is that the calculations predict an enhancement in the coefficient for rectification between 1 and 8 THz. This agrees with the observations of Sollner *et al.*² of rectification at 2.5 THz in their experimental devices. The quantity a_{rect} is the same as that which is denoted r in Ref. 2.

From the form of Eqs. (5) it is apparent that the eigenvalues of L_0 produce poles in the frequency response, and the numerical calculations imply that the smallest eigenvalues correspond to submillimeter-wave frequencies. Time-domain calculations of the full transient response^{4,5} also indicate that the smallest eigenvalues of L_0/\hbar are of the order of 10^{13} s⁻¹ for the present structure. This is of the same order of magnitude as the reciprocal of the frequently invoked delay time estimate \hbar/Γ , where Γ is the width of the

resonant peak in the transmission amplitude.¹⁰⁻¹² It is quite likely that a close relationship exists between this formula and the smallest eigenvalues of L_0 , but the details of this relationship have not yet been documented.

Luryi³ has suggested that the response of a resonant-tunneling device is limited by the rate at which the well can be filled or emptied and that this rate can be estimated by a simple RC model. Because this model yields a response time that is much longer than that experimentally observed, Luryi further suggested that some mechanism other than coherent resonant tunneling must be invoked. In fact, the RC model of Ref. 3 is not the appropriate way to calculate the response of the device, either including or excluding the parasitic elements. The model presented here assumes only coherent processes within the device and thus implements the conventional picture of resonant tunneling.^{1,2,10-12} It also exactly satisfies the continuity equation⁵ and thus describes the process of filling the quantum well. The resulting response time of the order of 10^{-13} s is the intrinsic response of the tunneling process. The frequency response of the tunneling current does resemble that of an RC circuit, in the sense that the intrinsic negative conductance decreases with frequency due to the poles in the response function. When the parasitic capacitance is included, a pole occurs at a much lower frequency, as shown by (8). This is the true RC limit of the device.

Another element of Luryi's analysis does apply to the conventional resonant-tunneling model. This is the dependence of the resonant-tunneling current on the barrier parameters, which is quite similar to that of the single-

AD-A186 969

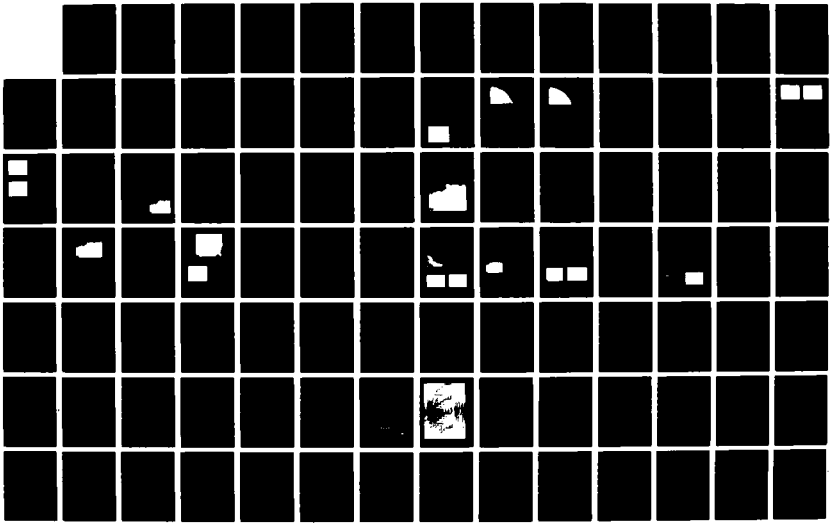
NANO-ELECTRONICS(U) TEXAS INSTRUMENTS INC DALLAS
R T BATE ET AL. 14 AUG 87 TI-88-87-50 ARO-21243.11-EL
DAGG29-84-C-0009

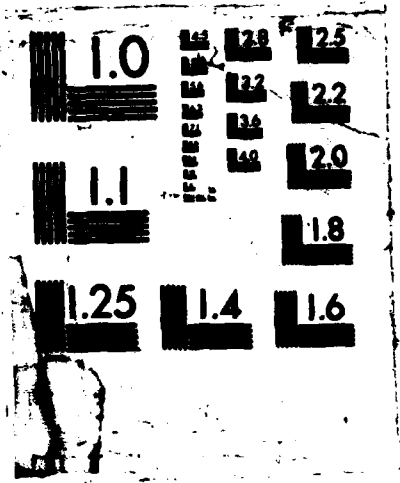
2/3

UNCLASSIFIED

F/G 28/10

NL





barrier case. In particular, the current density decreases exponentially as the width of the barrier is increased,^{11, 13} and this will be reflected in the time required to fill the quantum well. (This comes from the variation of Γ and illustrates the point that it is not the transmission probability, but only its integral over the appropriate distribution function, that is of significance.) Thus the concerns which motivated Luryi's analysis are well-founded, but his formula for the response time is not appropriate. There appears to be no compelling reason to invoke incoherent processes to explain the behavior of a normal resonant-tunneling diode near the peak of the $I(V)$ curve. [Such processes do become significant when the resonant tunneling current is very small, in the valley of the $I(V)$ curve or for devices with wide barriers.]

This work was supported in part by the Office of Naval Research and the Army Research Office.

REFERENCES

- 1L. L. Chang, L. Esaki and R. Tsu, Appl. Phys. Lett. 24, 593 (1974).**
- 2T. C. L. G. Sollner, W. D. Goodhue, P. E. Tannenwald, C. D. Parker and D. D. Peck, Appl. Phys. Lett. 43, 588 (1983).**
- 3S. Luryi, Appl. Phys. Lett. 47, 490 (1985).**
- 4W.R. Frensley, Phys. Rev. Lett. 57, 2853 (1986).**
- 5W.R. Frensley, submitted to Phys. Rev. B.**
- 6S. Ramo, Proc. IRE 27, 584 (1939).**
- 7W. Shockley, J. Appl. Phys. 9, 635 (1938).**
- 8T.C.L.G. Sollner, E.R. Brown, W.D. Goodhue, and H.Q. Le, Appl. Phys. Lett. 50, 332 (1987).**
- 9K.S. Champlin, D.B. Armstrong, and P.D. Gunderson, Proc. IEEE 52, 677 (1964).**
- 10B. Ricco and M. Ya. Azbel, Phys. Rev. B 29, 1970 (1984).**
- 11D.D. Coon and H. C. Liu, Appl. Phys. Lett. 49, 94 (1986).**
- 12P.J. Price, Superlattices and Microstructures 2, 593 (1986).**
- 13W.R. Frensley, IEEE International Electron Device Meeting, Technical Digest 1986, p. 571.**

FIGURE CAPTIONS

FIGURE 1. (a) shows the potential diagram of the resonant-tunneling diode. A dc bias V and a small ac signal of amplitude v are applied to the intrinsic device. The equivalent circuit of the device is shown in (b). Electron conduction through the intrinsic device is represented by a current source, whose specification is the purpose of this paper. A parallel displacement current flows through the parasitic capacitance C . The series resistance R_s represents the effects of the contacts.

FIGURE 2. The current-voltage curve derived from the steady-state Wigner function calculation. The linear response shown in Fig. 3 was evaluated at the dc bias shown as point "a", and the nonlinear response of Fig. 4 was evaluated at point "b".

FIGURE 3. Electron admittance as a function of frequency. The electron conductance is $Re(y)$ and the electron susceptance, due to inertial effects, is $Im(y)$. The negative conductance at lower frequencies is apparent. The susceptance due to the parasitic capacitance ωC is shown to provide a measure of the effect of the parasitic elements.

FIGURE 4. The nonlinear response coefficients as functions of frequency. Rectification is described by a_{rect} and second-harmonic generation is described by $a_{2\omega}$. The persistence of the rectification effect to terahertz frequencies is in agreement with the experimental results of Ref. 2.

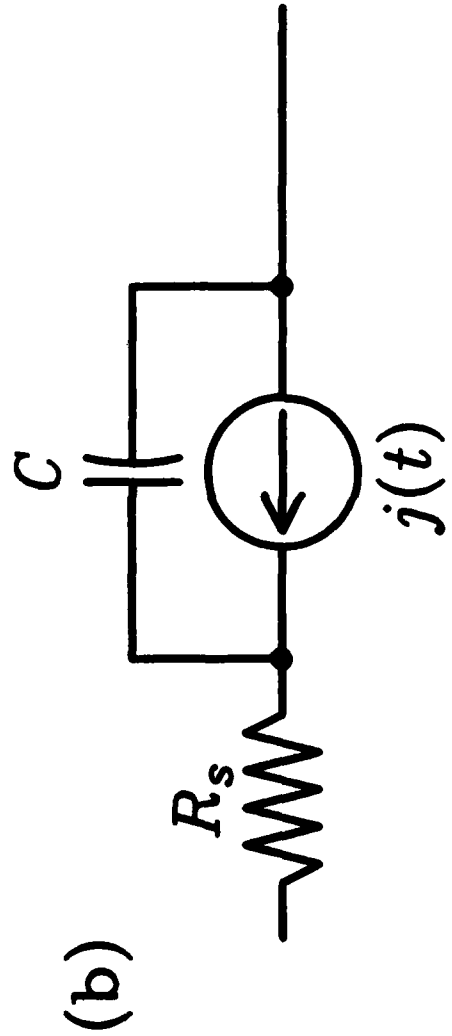
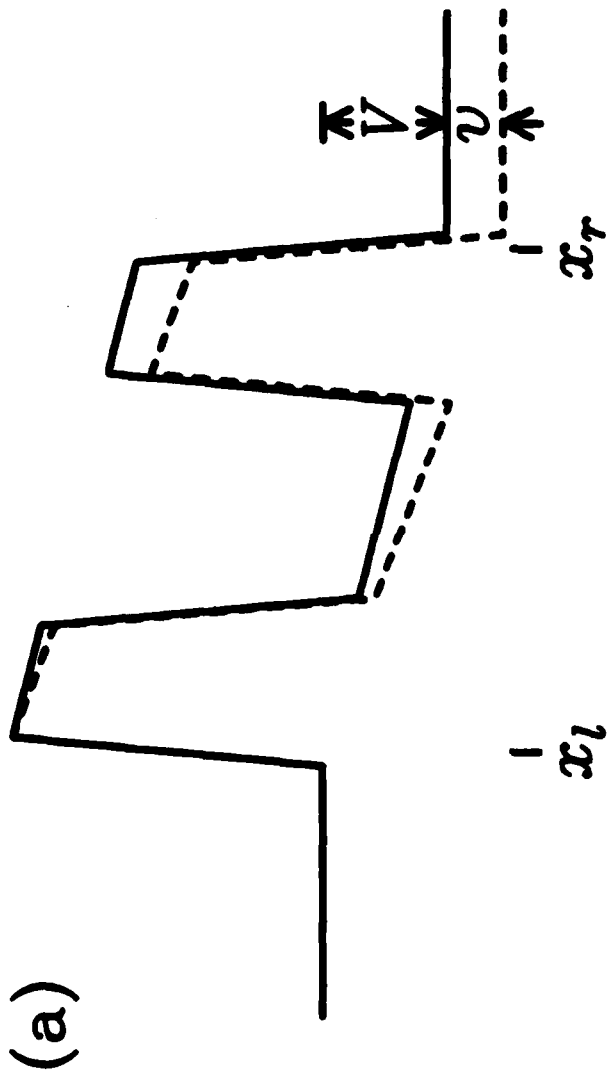


Figure 1

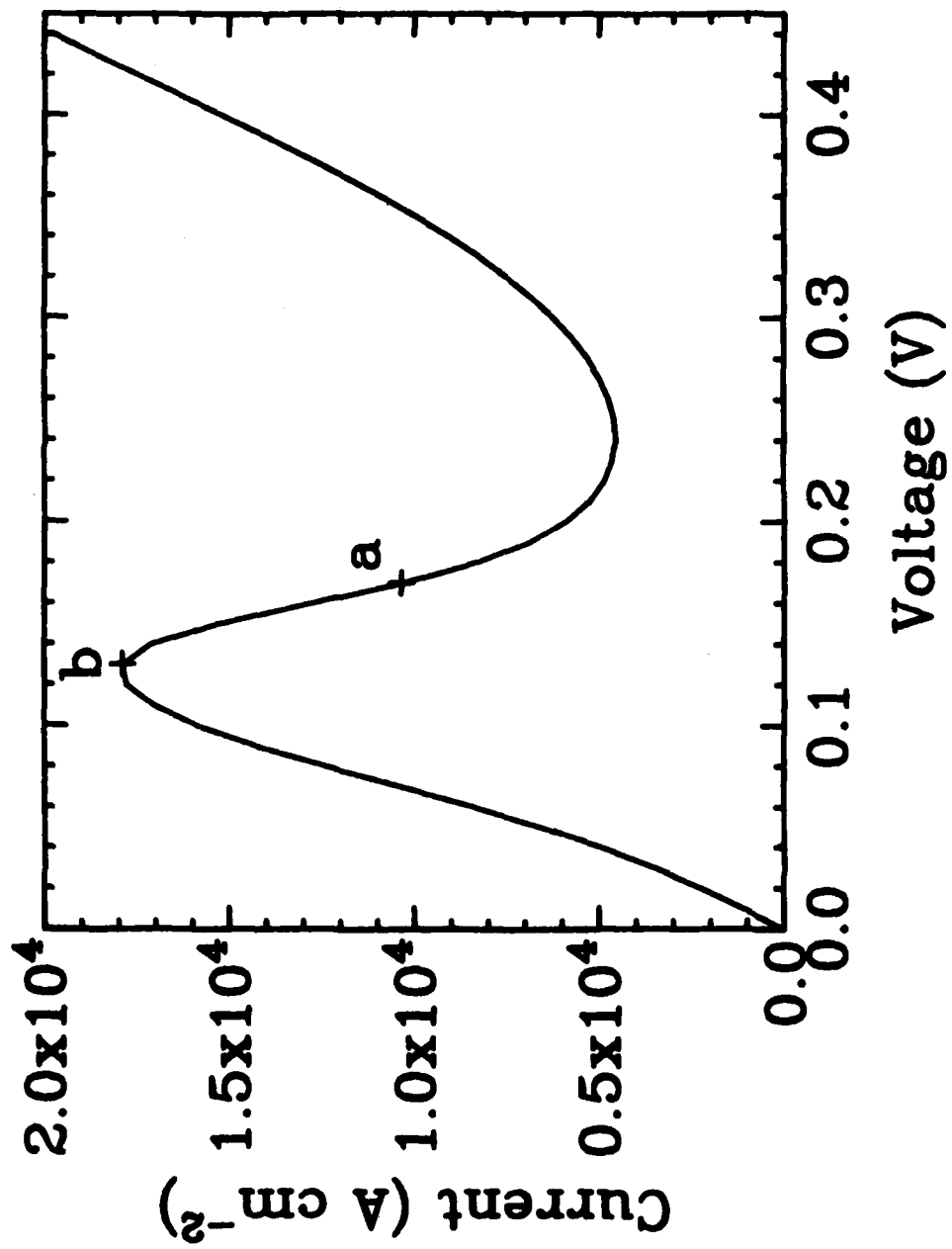


Figure 2

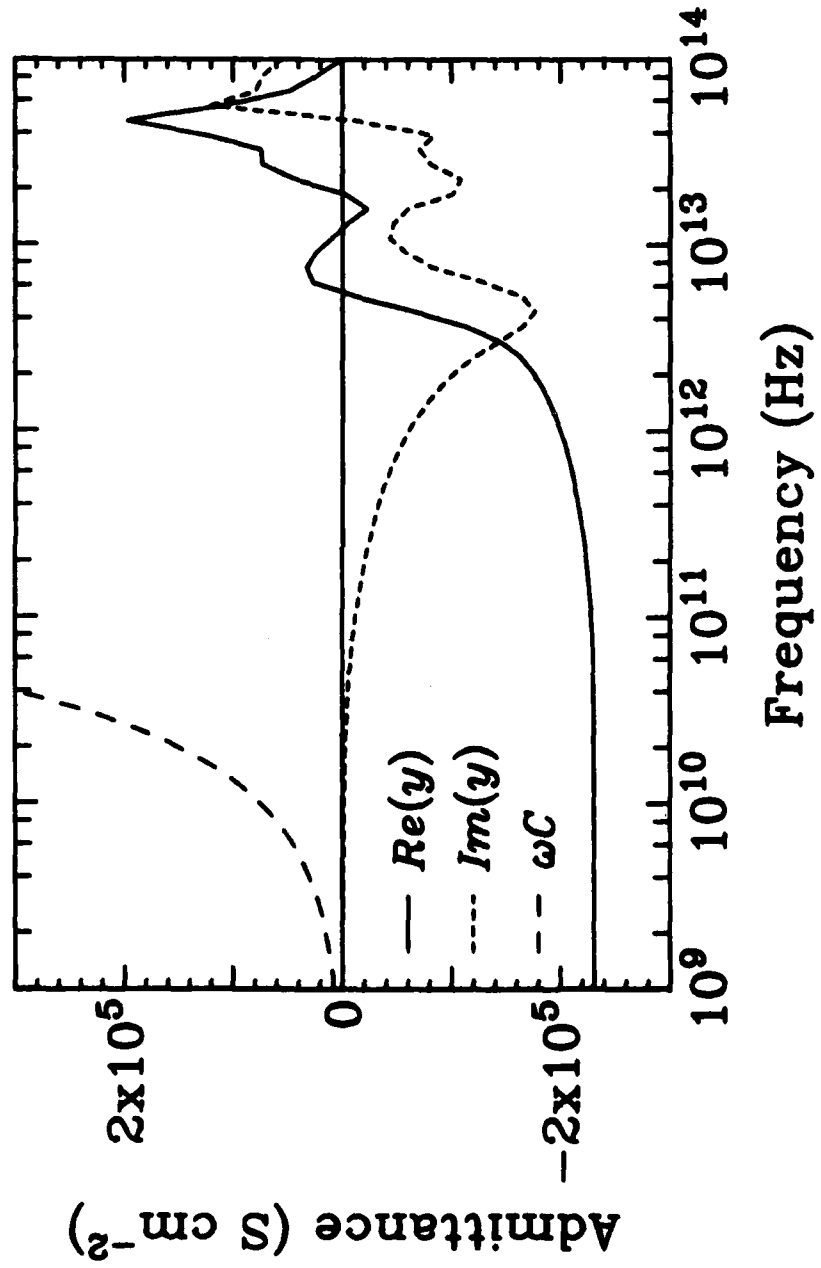


Figure 3

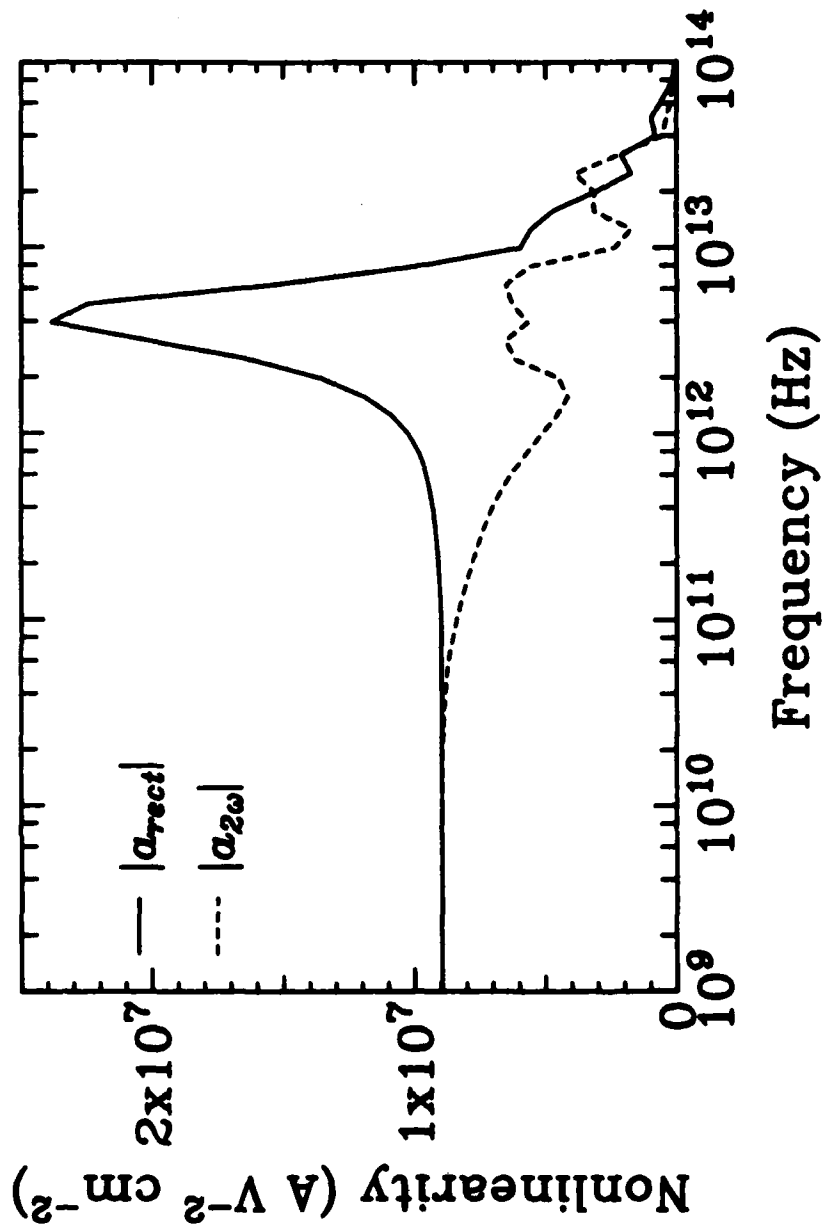


Figure 4

APPENDIX D

**QUANTUM-TRANSPORT MODELING OF
RESONANT-TUNNELING DEVICES**

QUANTUM TRANSPORT MODELING OF RESONANT-TUNNELING DEVICES

William R. Frensley

Texas Instruments Incorporated
P.O. Box 655936, M.S. 154
Dallas, Texas 75265

ABSTRACT

A form of quantum transport theory has been developed to model the resonant-tunneling diode and similar devices in which quantum interference effects play a significant role. The internal state of the device is represented by the Wigner distribution function, with boundary conditions which model the effects of the electrical contacts to the device. Inelastic scattering processes are approximated by a classical Boltzmann collision operator, and the effects of different scattering processes on the device characteristics are evaluated numerically.

KEYWORDS

Quantum transport; Wigner distribution function; Resonant tunneling; Electron-phonon interaction; Transient response; Nanoelectronics.

INTRODUCTION

The progress of semiconductor fabrication technology has permitted the fabrication of devices whose behavior is dominated by quantum-interference effects. The most widely studied example of a quantum size-effect device is the resonant tunneling diode (RTD) (Chang, Esaki, and Tsu, 1974; Sollner and colleagues, 1983). This device exhibits interesting properties in the form of a negative-resistance region of its characteristic curve which unambiguously shows the quantum-mechanical nature of electron transport through this structure. The central issue in the theory of such devices concerns the proper description of the dissipative processes which determine their behavior. Such processes can be grouped into two categories: interactions of conduction electrons with other kinds of particles in the crystal (such as phonons), and the exchange of those electrons with the elements of the external electrical circuit. Previous work (Frensley 1986, 1987a, 1987b) has demonstrated that a consistent model of a tunneling device may be obtained by invoking only the latter type of interaction. The present paper extends this model to include phonon scattering.

TRANSPORT MODEL

In the present model the device is considered to be a finite region of semiconductor, characterized by a potential that includes the effects of applied voltages and of heterojunction band offsets. The internal state of the device is represented by the single-particle Wigner distribution function $f(x, k, t)$ where x is the position and k is the momentum (Wigner, 1932). The Wigner function is assumed to obey a Markovian kinetic equation of the form

$$\frac{\partial f}{\partial t} = \frac{L}{i\hbar} f + Cf \quad (1)$$

where L is the Liouville super-operator which describes ballistic electron motion and C is a collision super-operator which describes random scattering. The boundary conditions on f describe the coupling of the device to electron reservoirs which model the electrical contacts to the device. The boundary conditions specify only the distribution of electrons entering the device, and thus introduce time-irreversibility into the model independently of the collision operator. The Wigner function f is calculated in a discrete approximation, which reduces the integro-differential equation (1) to a large system of linear algebraic equations which are solved numerically (Frensley, 1987a).

The collision super-operator C is assumed to be of the classical form:

$$[Cf](x, k, t) = \int dk' [W_{k'k} f(x, k', t) - W_{k'k} f(x, k, t)], \quad (2)$$

where $W_{k'k}$ is the transition rate from k' to k , etc.

SIMPLE COLLISION MODELS

There are two readily available approximations for the collision operator C , both of which have the form (2). One is the well-known relaxation term:

$$|C_{relax}f|(k) = (1/\tau) [f_0(k) \int dk' f(k') - f(k)], \quad (3)$$

where τ is a relaxation time, and f_0 is the normalized equilibrium distribution function. The other simple approximation to C is the dissipation operator derived from the Fokker-Planck or Kramers equation for Brownian motion (Caldeira and Leggett, 1983; Kubo, Toda, and Hashitsume, 1985):

$$|C_{FP}f|(k) = -\frac{1}{\tau} \left[\frac{\partial}{\partial k} (kf) + \frac{m}{\beta \hbar^2} \frac{\partial^2 f}{\partial k^2} \right]. \quad (4)$$

This approximation assumes a very high rate of low momentum-transfer collisions.

These simple collision terms were tested in numerical calculations of the dc $I(V)$ curve of a resonant-tunneling diode, by solving (1) for steady state. A relaxation time τ of 100 fs was assumed for both the relaxation and Fokker-Planck models, corresponding to a mobility of 5000 cm²V⁻¹s⁻¹ for GaAs. The resulting characteristic curves are shown in Fig. 1. The relaxation term (3) greatly reduces the peak-to-valley current ratio, both decreasing the peak current and increasing the valley current. The Fokker-Planck term (4), however, leads to an increase in the current at all voltages.

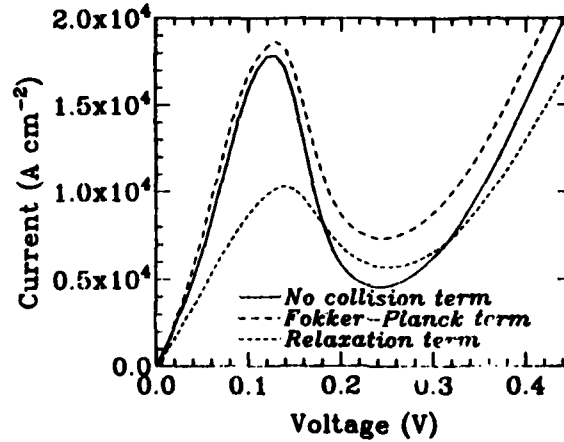


Fig. 1. Effect of simple collision terms on the $I(V)$ characteristic of a resonant-tunneling diode.

REALISTIC PHONON SCATTERING

The sensitivity of the $I(V)$ curve to the form of the collision operator demonstrated by these simple models implies that we need to use more realistic models of random scattering processes in the device. An obvious first step in this direction is to retain the classical Boltzmann form (2), and use the Fermi golden rule to calculate the transition rates W . The work of Levinson (1970) and of Lin and Chiu (1985) suggests that this is an appropriate approximation when the electron-phonon interaction can be treated semi-classically. Because only a single spatial dimension is resolved in the numerical model, we must make some assumptions about the dependence on the transverse components of the momentum k . The obvious assumption is that the distribution is Maxwellian with respect to the transverse wavevector k_{\perp} . Then integrating the resulting distribution function with respect to k_{\perp} , we obtain

$$W_{kk'} = \frac{2\pi}{\hbar} \frac{V}{(2\pi)^3} \int d^2k_{\perp} \int d^2k'_{\perp} | \langle k | H' | k' \rangle |^2 \delta(E_k - E_{k'} \mp \hbar\omega) \frac{2\pi\beta\hbar^2}{m} \exp\left\{ -\frac{\beta\hbar^2 k'_{\perp}{}^2}{2m} \right\}. \quad (5)$$

Here H' is the Hamiltonian which describes the particular electron-phonon interaction. The numerical collision operators obtained from (5) and (2) were checked for consistency with the requirements of detailed balance by applying the operator to an equilibrium distribution function and verifying that the result was zero.

In the present calculations the deformation potential interaction was included for scattering with acoustic phonons and the Fröhlich interaction was included for scattering with longitudinal optical (LO) phonons (Conwell, 1967). The effects of these phonon scattering mechanisms on the $I(V)$ curve of the RTD are shown in Fig. 2. Acoustic phonon scattering has a nearly negligible effect on the $I(V)$ curve. The effect of LO phonon scattering is rather more pronounced, primarily in the reduction of the peak current. When both acoustic and LO phonons are included in the calculation, the resulting $I(V)$ curve is indistinguishable from that obtained with LO scattering only.

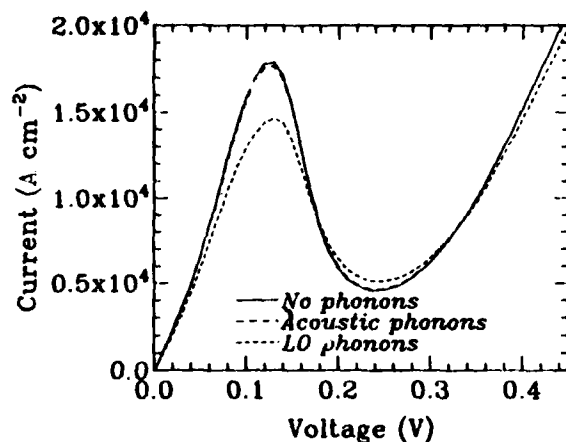


Fig. 2. Effect of semi-classical phonon-scattering operators on the $I(V)$ characteristic of a resonant-tunneling diode.

The effect of phonon scattering on the dynamic behavior of the resonant-tunneling diode was investigated by performing transient-response calculations (Frensley, 1986, 1987a) both with and without the collision operator. The particular transient event that was simulated was an instantaneous switching of the applied voltage from the peak of the $I(V)$ curve to the valley. The current through the RTD (averaged with respect to position within the structure) is illustrated in Fig. 3. Both curves show an initial peak and small oscillations around a generally exponential decay to the new steady state. Somewhat surprisingly, these oscillations are larger for the calculation including phonon scattering.

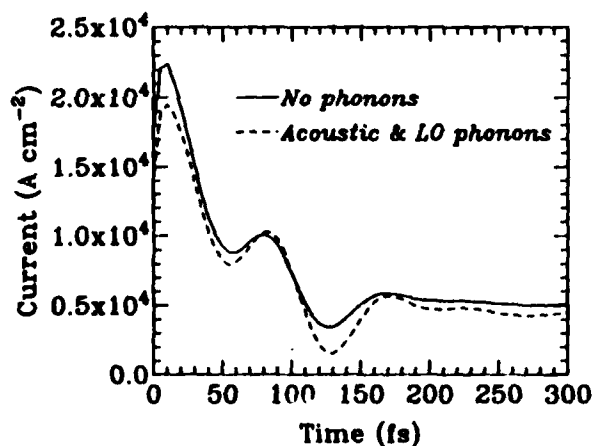


Fig. 3. Transient response of a resonant-tunneling diode with and without phonon scattering.

CONCLUSIONS

The present work represents an initial effort to include phonon scattering effects in a transport theory of tunneling devices. The diversity of results obtained from the simpler approximations to the collision operator clearly indicates that meaningful results (and reliable insights into the effects of stochastic processes on nanoelectronic devices) will only be obtained from realistic models of these phenomena.

ACKNOWLEDGEMENT

This work was supported in part by the Office of Naval Research and the U.S. Army Research Office.

REFERENCES

- Caldeira, A.O. and A.J. Leggett (1983). Path integral approach to quantum Brownian motion. *Physica*, 121A, 587-616.
- Chang, L.L., L. Esaki, and R. Tsu (1974). Resonant tunneling in semiconductor double barriers. *Appl. Phys. Lett.*, 24, 593-5.
- Conwell, E.M. (1967). *High Field Transport in Semiconductors*. Academic Press, New York, ch. 5.
- Frensley, W.R. (1986). Transient response of a tunneling device obtained from the Wigner function. *Phys. Rev. Lett.*, 57, 2853-6.
- Frensley, W.R. (1987a). Wigner function model of a resonant-tunneling semiconductor device. *Phys. Rev. B*. Accepted for publication.
- Frensley, W.R. (1987b). Quantum-transport calculation of the small-signal response of a resonant-tunneling diode. *Appl. Phys. Lett.* Accepted for publication.
- Kubo, R., M. Toda, and N. Hashitsume (1985). *Statistical Physics II. Nonequilibrium Statistical Mechanics*. Springer-Verlag, Berlin, p. 55.
- Levinson, I.B. (1970). Translational invariance in uniform fields and the equation of motion for the density matrix in the Wigner representation. *Soviet Physics JETP*, 30, 362-7.
- Lin, J. and L.C. Chiu (1985). Quantum theory of electron transport in the Wigner formalism. *J. Appl. Phys.*, 57, 1373-6.
- Sollner, T.C.L.G., W.D. Goodhue, P.E. Tannenwald, C.D. Parker, and D.D. Peck (1983). Resonant tunneling through quantum wells at frequencies up to 2.5 THz. *Appl. Phys. Lett.*, 43, 588-90.
- Wigner, E. (1932). On the quantum correction for thermodynamic equilibrium. *Phys. Rev.*, 40, 749-59.

APPENDIX E

SPATIAL QUANTIZATION IN GaAs-AlGaAs
MULTIPLE QUANTUM DOTS

Spatial quantization in GaAs-AlGaAs multiple quantum dots

M. A. Reed, R. T. Bate, K. Bradshaw, W. M. Duncan, W. R. Frensley, J. W. Lee, and H. D. Shih

Central Research Laboratories, Texas Instruments Incorporated, Dallas, Texas 75265

(Received 12 June 1985; accepted 23 September 1985)

We present results of the fabrication and investigation of totally spatially localized crystalline structures. Low temperature photoluminescence exhibits structure that is best explained by a bottleneck for hole energy loss. This bottleneck is believed to be a direct consequence of the modification of the band structure by the fabrication-imposed potential and is believed to be the first evidence for total spatial quantization in a fabricated heterojunction system.

The physics of spatially quantized systems has been the subject of intense investigation since molecular beam epitaxy (MBE) and metal-organic chemical vapor deposition (MOCVD) have made possible the fabrication of atomically sharp heterojunction interfaces. Quantum wells have been exhaustively examined since the seminal works of Dingle *et al.*¹ More recently, studies on quantum wires² have yielded interesting new properties. Here we present data on a completely spatially quantized system (which by extrapolation we define as "quantum dots") where the carriers have zero degrees of freedom (denoted as "0 DOF"). This paper discloses evidence for the modification of carrier-phonon scattering rates by the imposition of complete spatial quantization on GaAs-AlGaAs multiple quantum wells. The photoluminescence spectrum of the 0 DOF structures exhibits striking structure in the normal intrinsic exciton luminescence of the confined quantum well states. This photoluminescence structure does not occur for structures of higher dimensionality, and is best explained by a bottleneck for electron/hole energy loss. We believe that this bottleneck is a direct consequence of the quantization of the electronic and/or phonon dispersion relations.

The samples used in these experiments were grown by MBE and are shown schematically in Fig. 1(a). The samples were grown on (100) Cr-doped GaAs substrates and consisted of a 0.1 μ GaAs MBE buffer layer followed by a 1 μ Al_xGa_{1-x}As buffer, twenty 20 \AA GaAs wells with 100 \AA Al_xGa_{1-x}As ($x = 0.3$) barriers, followed by a 100 \AA GaAs cap layer. All samples were nominally undoped. Patterning of the bulk multiple quantum well samples was done by direct e-beam writing in a film of polymethylmethacrylate (PMMA) on the sample surface. Conventional lift-off techniques were used to define 1000 \AA thick Au metal patterns on the sample surface. The metal mask (which exhibited little degradation during the fabrication) served as both an etch mask and a semitransparent film. The metal patterns were transferred to the underlying sample by a BCl₃ reactive ion etch that extended into the AlGaAs buffer. The lateral dimension for both the 1 DOF and 0 DOF structures was 0.25 μ . Figure 1(b) shows a schematic of a single quantum dot structure. Quantum wire (1 degree of freedom, or 1 DOF) structures were fabricated simultaneously on the same sample as the quantum dot (0 DOF) structures. Arrays of these structures were fabricated to achieve measur-

able photoluminescence intensity and the stack of quantum wells was used for sufficient absorption of the excitation radiation.

Photoluminescence measurements were performed (at 45° incidence and detection) in a helium flow Janis optical cryostat. The sample was excited by the 2.54 eV line of a focused Ar⁺ laser and the photoluminescence radiation was collected by a 1.0 m Chromatix spectrometer of 7 $\text{\AA}/\text{mm}$ focal plane dispersion. Conventional detection techniques were used.

Figure 2 shows the photoluminescence spectra of sample A for the three distinct DOF cases previously discussed. The 7300 \AA luminescence peak is the ($n = 1$) electron-($n = 1$) heavy hole recombination radiation, prominent in all three DOF cases. Note that the quantum well size is adjusted so that the luminescence under investigation is spaced between the GaAs and AlGaAs peaks to eliminate any possibility of impurity effects from the bulk substrates. We have normalized the three different DOF spectra to the same intensity at

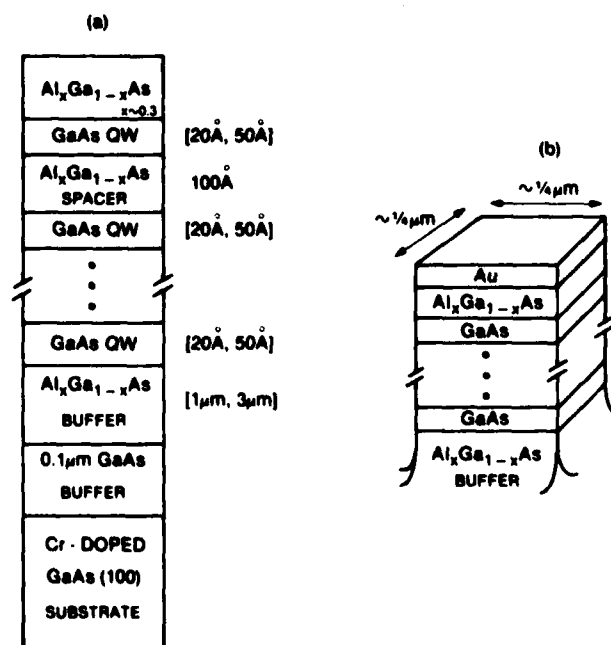


FIG. 1. (a) Schematic cross sectional view of the GaAs quantum well MBE samples. Discussion in the text is on the 20 \AA quantum well samples. (b) Schematic cross sectional view of a quantum dot (0 DOF) structure.

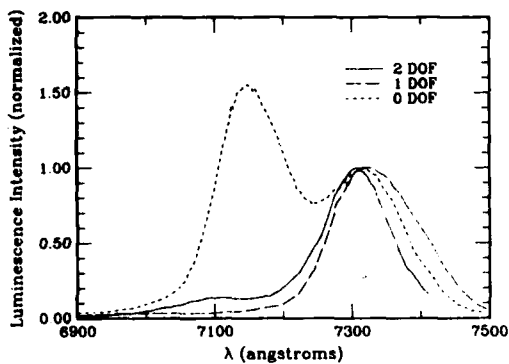


FIG. 2. Photoluminescence spectra of GaAs-AlGaAs quantum wells (2 DOF), quantum wires (1 DOF), and quantum dots (0 DOF) at $T = 4.2$ K. The photoluminescence intensities are normalized for comparison purposes.

this wavelength for comparison purposes. The small shifts in the 7300 Å peak positions are probably due to residual surface damage or strain resulting from the plasma etch. The loss in photoluminescence signal was readily accounted for by loss of sample volume, indicating that nonradiative loss mechanisms due to sidewall damage are not large.

The outstanding structure at ~ 7100 Å in the 0 DOF spectra, also seen at smaller relative intensity in the 2 DOF case, is the $(n = 1)$ electron- $(n = 1)$ light hole recombination radiation. The absence of this structure in the 1 DOF case is probably due to the singularity in the density of states for a 1 DOF structure which depletes holes of higher (than zone minima) energy. The appearance of the light hole peak in the quantum dot case was not a local effect; all sections of the sample investigated exhibited the same spectrum. The 1 DOF and 0 DOF structures were fabricated adjacent to each other on the sample to eliminate any systematic errors due to the plasma etch.

Figure 3 schematically diagrams the relaxation mechanisms in the luminescence process of the ground state of a quantum well. $\tau_{hh,intra}$, $\tau_{lh,intra}$, and $\tau_{e,intra}$ are the intra-branch phonon relaxation times of heavy holes, light holes, and electrons, respectively, down their respective branches. τ_{inter} is the light-to-heavy hole scattering time. τ_{recomb} is the electron-hole radiative recombination time. We shall assume that the heavy and light hole-electron recombination times are approximately equal and energy independent. Relaxation mechanisms involving any existing excited states, the split-off band, or interface defects, have been ignored. Carrier-carrier scattering has also been neglected in this treatment, but will be approximately constant in the three different dimension cases. This would not be true for higher excitation intensities.

Upon initial excitation, the three DOF cases have similar thermalization dynamics. The crossover from essentially three-dimensional behavior to the specific DOF case is complex and will not be treated here. When the carriers reach the region $E \sim \hbar\omega_{LO}$, the crossing from the light hole to heavy hole branch can occur.³ The interbranch scattering time, τ_{inter} , will be limited by the phase space available at the crossover. If τ_{inter} is sufficiently large, a "bottleneck" results and an appreciable population of light holes can be formed.

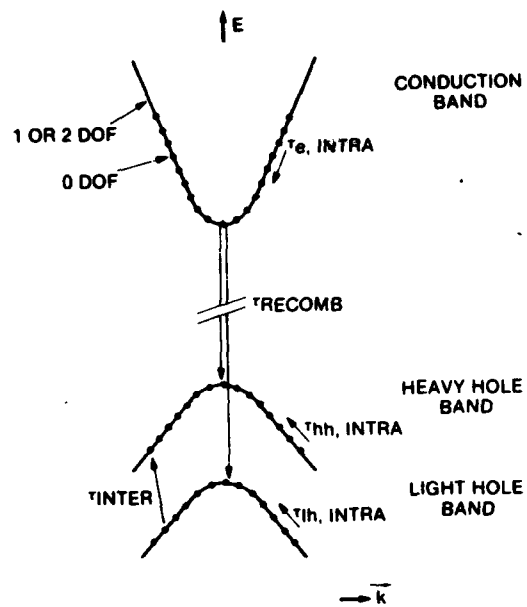


FIG. 3. Electronic dispersion relation of the $n = 1$ ground state for quantum wells and wires (solid lines) and for quantum dots (points). The notation is defined in the text.

Thus the formation of discrete points in the dispersion relation due to the 0 DOF boundary conditions increases τ_{inter} sufficiently to make the light hole peak observable. Additionally, the elimination of selected small k modes in the phonon spectrum will enhance the light hole transient population.

Observation of this bottleneck in light-to-heavy hole scattering by photoluminescence in bulk GaAs is impractical since $\tau_{recomb}/\tau_{inter} \sim 10^3$. We have reduced this rate not only by the fabrication-imposed increase of τ_{inter} but also by the decrease of τ_{recomb} due to the enhancement of the radiative transition probability in a quantum well with sufficiently narrow well thickness.⁴ Band filling can be eliminated as an alternative explanation since the linewidths are approximately the same, do not exhibit high energy tails, and the excitation power dependence exhibited no change in the heavy hole peak : light hole peak ratio. Bound impurity effects can be eliminated by the 1 DOF control, while nonradiative recombination can be eliminated as a cause by the normalized luminescence intensity.

An intriguing possibility is the direct observation of spatial quantization from the discrete (multiply degenerate) electronic levels in the 0 DOF quantum dots. The spectrum was investigated in sufficiently high resolution to observe fine structure in the quantum well luminescence with the sample immersed in superfluid helium. The negative results for this search are best explained by an effect analogous to inhomogeneous line broadening; the variation of the dot size across the array will produce fluctuations in the discrete line positions. For the experimental resolution of 0.1 Å and the above dot parameters, a fluctuation of $\sim 1\%$ is sufficient to mask the discrete lines.

A possible solution to the inhomogeneous line broadening problem is to observe the photoluminescence from a single

quantum dot. Such a structure was fabricated and investigated, but the attempt was unsuccessful due to insufficient photoluminescence intensity.

In summary, we have observed the photoluminescence from a series of spatially quantized quantum structures and believe we have observed the first indirect evidence for total spatial quantization by a fabrication-imposed potential. The effect of the discrete dispersion relations of the electrons and/or phonons is to modify the relaxation kinetics of carriers in the quantum structures, and this is observable in the photoluminescence spectrum.

Acknowledgments: We wish to thank T. Kaluza, P. Tackett, A. Wetsel, and J. Williams for technical assistance. We

are grateful for illuminating discussions with L. Cooper, J. Erskine, G. Iafrate, L. Kleinman, and P. Stiles. This work was supported in part by the Office of Naval Research and in part by the U.S. Army Research Office.

¹R. Dingle, A. C. Gossard, and W. Wiegmann, *Phys. Rev. Lett.* **34**, 1327 (1975).

²W. J. Skocpol, L. D. Jackel, E. L. Hu, R. E. Howard, and L. A. Fetter, *Phys. Rev. Lett.* **49**, 951 (1982).

³E. M. Conwell, in *Solid State Physics Supplement No. 9*, edited by F. Seitz, D. Turnbull, and H. Ehrenreich (Academic, New York, 1967).

⁴J. Christen, D. Bimberg, A. Steckenborn, and G. Weimann, *Appl. Phys. Lett.* **44**, 84 (1984).

APPENDIX F

**INVESTIGATION OF QUANTUM WELL AND
TUNNEL BARRIER GROWTH BY RESONANT TUNNELING**

Investigation of quantum well and tunnel barrier growth by resonant tunneling

M. A. Reed, J. W. Lee, R. K. Aldert, and A. E. Wetsel¹⁾
Central Research Laboratory, Texas Instruments Incorporated, Dallas, Texas 75265

(Received 1 November 1985; accepted 10 March 1986)

We present the first known systematic mapping of quantum well and tunnel barrier thicknesses in a resonant tunneling structure by transport measurements. The technique derives a 1 Å averaged resolution for quantum well and barrier thicknesses, independently for the quantum well and adjacent tunnel barriers. Contour maps of the structure reveal an asymmetric shallow ring growth structure for one of the epilayers. Current-voltage characteristics and temperature dependence of the resonant tunneling structures will also be discussed.

I. INTRODUCTION

Negative differential resistance (NDR) devices utilizing double barrier resonant tunneling structures¹ have recently undergone a renaissance²⁻⁴ due to improved GaAs/AlGaAs molecular beam epitaxy (MBE) techniques. The ultimate applications (such as microwave oscillators⁵) of resonant tunneling devices may depend on the ease in which single quantum wells (and adjacent tunnel barriers) can be characterized and the uniformity with which such structures can be grown. Likewise, such characterization techniques can be utilized in general for the characterization of device structures that employ isolated quantum well structures.

Photoluminescence (PL), transmission electron microscopy (TEM), and x-ray characterization techniques have proven invaluable to the characterization of superlattice and multiple quantum well structures. However, the problem of characterization is not a trivial one for a single buried quantum well and adjacent tunnel barriers. Extrapolation from multiple wells and/or near-surface structures is dangerous. Transmission electron microscopy will give the required resolution of single layers, but is destructive and not suitable for studying lateral growth variations of epilayers. Photoluminescence is suitable for lateral mapping, but has difficulty for deeply buried structures, as well as signal intensity problems for single wells. Likewise, x-ray techniques have signal intensity problems with isolated wells. Development of a technique to easily determine thickness contours for these structures is valuable for studying growth kinetics, comparison of growth techniques [MBE versus metal-organic chemical vapor deposition (MOCVD)], and as a nondestructive diagnostic tool for device design and fabrication.

In this paper we present the first known systematic study of quantum well and barrier thickness variations in a resonant tunneling structure by transport measure-

ments. The technique derives a 1 Å averaged resolution for quantum well and barrier thicknesses, independently for the quantum well and adjacent tunnel barriers. An investigation over nearly $\frac{1}{4}$ of a MBE wafer produced contour maps for the quantum well and barriers that revealed an asymmetric ring growth structure for one of the epilayers.

II. THEORY

Tunneling phenomena in multibarrier structures were first studied theoretically by Tsu and Esaki⁶ who predicted negative differential conductivity due to resonant tunneling through discrete bound states (in the one-dimensional approximation) of the confined quantum wells. These predictions were confirmed experimentally¹ in double barrier, single well structures that are the subject of this paper. The recent work of Sollner *et al.*² revived interest in these structures when peak-to-valley ratios as large as 6:1 were demonstrated.

We will apply the transport model of Tsu and Esaki to the specific case of the double barrier, single quantum well. Let us assume that the conduction band (under zero bias) can be treated as shown in Fig. 1(a). We will assume the effective mass approximation for the unperturbed structure, thus separating out the transverse energy of the carriers to treat the problem as one dimensional; i.e., the potential will be written as $V(x)$, where x is along the direction of the barriers. The global single-particle transmission coefficient T_{Total} for this structure can be solved exactly,⁶ and can be written as

$$T_{\text{Total}} = C_0 \left(C_1 T_{\text{left}} T_{\text{right}} + C_2 \frac{T_{\text{left}}}{T_{\text{right}}} + C_3 \frac{T_{\text{right}}}{T_{\text{left}}} + \frac{C_4}{T_{\text{left}} T_{\text{right}}} \right)^{-1}, \quad (1)$$

where T_{left} and T_{right} are the single-particle transmission coefficients through the left and right barriers, respectively, and the C_i are phase factors depending on the wave vectors. Table I lists the relevant phase factors

¹⁾ Present address: Harvard University, Cambridge, Massachusetts.

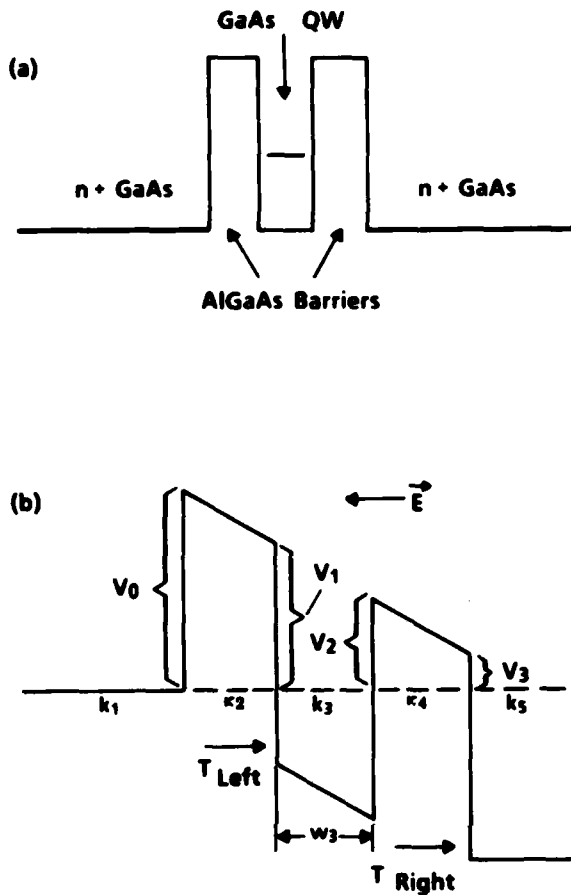


FIG. 1(a) Conduction band structure for the single quantum well, double tunnel barrier heterostructure considered in this study. (b) The same structure under bias by an electric field E . The wave vectors are k_1 , κ_2 , k_3 , κ_4 , and k_5 in the left contact, barrier, quantum well, barrier, and right contact, respectively. The width of the well is w_3 .

derived for this geometry. The transmission through the single barriers is calculated in the WKB approximation⁷ by

$$T = \exp\left(-\frac{2}{\hbar}(2m^*)^{1/2} \int_{\text{barrier}} [V - E(x)]^{1/2} dx\right), \quad (2)$$

where m^* is the effective mass of the carrier in the barrier, $E(x)$ is the energy at x of the carrier, and \hbar is Planck's constant. Let us now apply an electric field E to the structure and assume that the voltage is dropped across the (relatively) nonconducting barrier structure as shown in Fig. 1(b). Using the notation defined in this figure, and noting that $dE = e|E|dx$, it can be shown⁸ that

$$T_{\text{left}} = \exp\left(-\frac{4}{3} \frac{(2m^*)^{1/2}}{\hbar} \frac{V_0^{3/2} - V_1^{3/2}}{e|E|}\right) \quad (3)$$

and

$$T_{\text{right}} = \exp\left(-\frac{4}{3} \frac{(2m^*)^{1/2}}{\hbar} \frac{V_2^{3/2} - V_3^{3/2}}{e|E|}\right). \quad (4)$$

Substituting Eqs. (3) and (4) into Eq. (1) will now give well-defined peaks in the global transmission coefficient as a function of device bias. Physically, the peaks occur at biases such that the resonant energies of the quantum well cross the Fermi energy of the electrons in the left-hand contact. The decrease in current with increased bias (i.e., NDR) results from the inability of carriers to conserve energy and (transverse) momentum simultaneously during resonant tunneling. We will utilize these expressions to determine the quantum well width from the experimentally observed peak positions.

Likewise, we can use the observed current density to determine the effective barrier width. Although the expression for the current density at any device bias is known,⁶ at resonance we can approximate the current density in a much simpler form. The tunneling current density through a barrier of average height V and thickness d can be estimated as^{7,9}

$$J(V) = (2\pi e V / d^2 \hbar) \exp[-2d(2m^* V / \hbar)^{1/2}], \quad (5)$$

where m^* is the effective mass of the electron in the barrier and \hbar is Planck's constant. This is used for both of the barriers measured in series; thus one can only determine the total thickness of the barriers. Although this estimate for well thickness may not be as precise as others⁶ for absolute thickness determination, it should be equally precise for relative thickness variations of one

TABLE I. Phase factors for Eq. (1), as applied to the geometry of Fig. 1.^a

$$C_0 = \frac{2^3 k_1 \kappa_2^2 k_3^2 \kappa_4^2 k_5}{(k_1^2 + \kappa_2^2)(\kappa_2^2 + k_3^2)(k_3^2 + \kappa_4^2)(\kappa_4^2 + k_5^2)},$$

$$C_1 = \exp[i(\phi_1 - \phi_2 - \phi_3 - \phi_4 - \phi_5)] - \exp[i(-\phi_1 - \phi_2 + \phi_3 + \phi_4 - \phi_5)],$$

$$C_2 = \exp[i(\phi_1 - \phi_2 - \phi_3 + \phi_4 + \phi_5)] - \exp[i(-\phi_1 - \phi_2 + \phi_3 - \phi_4 + \phi_5)],$$

$$C_3 = \exp[i(\phi_1 + \phi_2 + \phi_3 - \phi_4 - \phi_5)] - \exp[i(-\phi_1 + \phi_2 - \phi_3 + \phi_4 - \phi_5)],$$

$$C_4 = \exp[i(-\phi_1 + \phi_2 + \phi_3 + \phi_4 + \phi_5)] - \exp[i(\phi_1 + \phi_2 - \phi_3 - \phi_4 + \phi_5)],$$

$$\phi_1 = k_3 w_3, \quad \phi_2 = \tan^{-1}(\kappa_2/k_1), \quad \phi_3 = \tan^{-1}(\kappa_2/k_3),$$

$$\phi_4 = \tan^{-1}(\kappa_4/k_3), \quad \phi_5 = \tan^{-1}(\kappa_4/k_5).$$

^aThe variables k , and w , are described in Fig. 1.

barrier, assuming that the other barrier is constant. Previous measurements on the lateral variation of the AlAs mole fraction for MBE material¹⁰ imply that the composition is laterally uniform, so we can directly determine the barrier width instead of as a function of (d^2V).

III. EXPERIMENTAL

The samples used in this study were GaAs/ $\text{Al}_{0.3}\text{Ga}_{0.7}\text{As}$ structures grown in a Riber MBE-2300 on a (100) GaAs substrate doped *n* type with Si at $2-3 \times 10^{18} \text{ cm}^{-3}$. Following a highly doped (*n*-type, Si at $2 \times 10^{18} \text{ cm}^{-3}$) buffer layer, the active resonant tunneling structure region was then grown. The active region consisted of an undoped $\text{Al}_x\text{Ga}_{1-x}\text{As}$ barrier (50 Å, $x = 0.3$), GaAs quantum well (50 Å), and similar barrier. The active region was followed by a highly doped (*n*-type, Si at $2 \times 10^{18} \text{ cm}^{-3}$) top contact $\sim 0.5 \mu$ thick. Devices, ranging from 2–225 μ in diameter, were fabricated by defining mesas on the surface with conventional photolithography techniques. Ohmic contacts covered the top surface of the mesa and were made by evaporating Au–Ge, Ni, then Au, followed by an anneal. For devices too small to accommodate a direct bond, a silicon nitride layer (for isolation) was deposited over the sample, followed by a Au-evaporated bonding pad.

To investigate the lateral uniformity of the electrical characteristics, large area devices (160 μ diameter) were fabricated over nearly $\frac{1}{2}$ of the MBE slice (approximately 400 μ device spacing). The devices were probed on the undiced wafer in a 77 K cold chuck to produce a topographic mapping. The I – V characteristics of a typical device (an active area of $2 \times 10^{-4} \text{ cm}^{-2}$) at 77 K is shown in Fig. 2. The transition from the lower voltage, higher current characteristic to the higher voltage, low-

er current characteristic occurs along load line intersections of the device I – V at the NDR inflection points. A noticeable “hysteresis” (i.e., multivalued current at a given voltage) is observed in these devices and is due to the parasitic resistance of the device. This hysteresis will be observed if the value of the parasitic resistance is greater than that of the negative resistance.

The procedure for determining the barrier thickness [Eq. (5)] was applied to the measured current density to derive the barrier thickness. Here one barrier was assumed laterally homogeneous. The result of the barrier thickness derived for each device on a section of the MBE slice, approximately $\frac{1}{4}$ of the slice and cleaved along (110) directions, is shown in Fig. 3. The MBE AlGaAs barrier exhibits shallow growth rings and an axial asymmetry. A preferential growth direction is not plausible since this effect is cumulative and would be observable for thick layers. A more plausible explanation of the axial asymmetry is the finite open shutter time; because the substrate rotates during growth and the ratio of the deposition time to the rotation period is not necessarily an integer (in this case, = 1.8), there will exist a region of the sample with a thinner epilayer. The outside ring of inoperative devices is caused by the shadow of the substrate holder used during growth. Measurements on these conductive structures did not show any variation in resistance, indicating that there was no appreciable variation in Ohmic contact fabrication.

Previous qualitative results¹¹ of zero-bias resistance measurements of MOCVD material claimed monolayer fluctuations, but no comparison between MBE and MOCVD can be made due to the limited MOCVD sample size¹² and unspecified thickness resolution. We believe the present technique is the most accurate contour determination of buried ultrathin epilayers ever made.

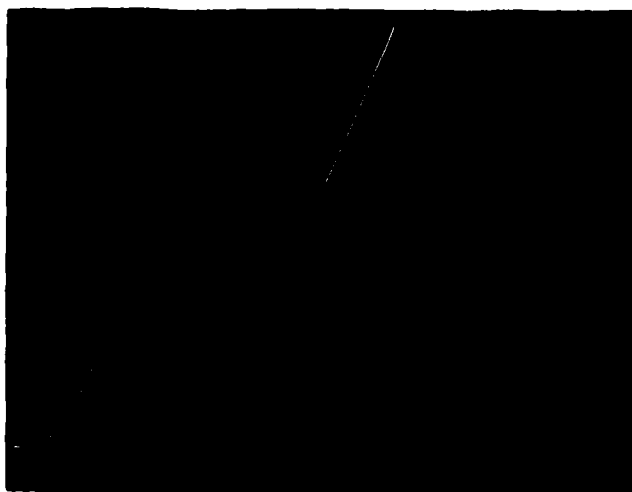


FIG. 2. Typical I – V characteristic at $T = 77 \text{ K}$ of a resonant tunneling device used in this study.

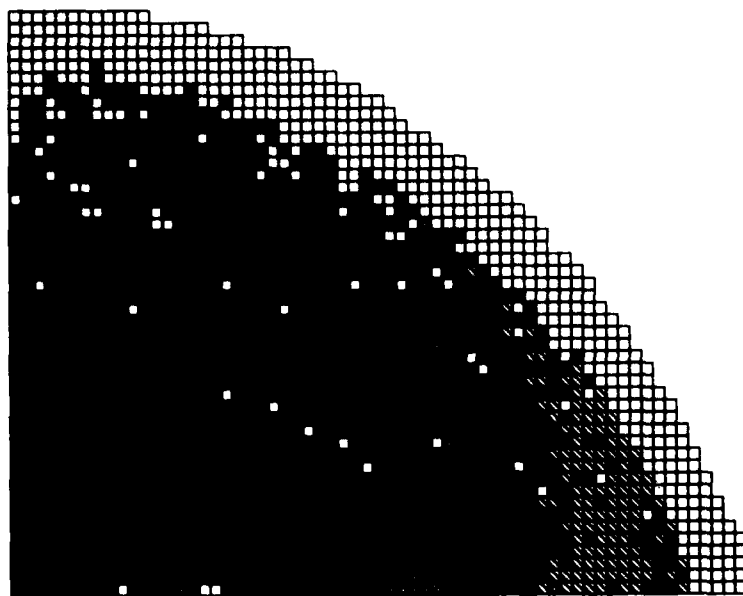


FIG. 3. Mapping of a $\text{Al}_{0.3}\text{Ga}_{0.7}\text{As}$ tunnel barrier thickness determined by current density variations on a section of a MBE-grown wafer containing a single well, double barrier resonant tunneling structure. Measurements were taken at $T = 77\text{ K}$. An axial asymmetry is present.

Deposition rate = $2\text{ \AA}/\text{sec}$
 Rotation rate = $4\text{ rev}/\text{min}$

+ slice center (rotation axis)

$T = 77\text{ K}$

Legend

- greater than 55 Angstroms
- 54 - 55 Angstroms
- 53 - 54 Angstroms
- 52 - 53 Angstroms
- 51 - 52 Angstroms
- less than 51 Angstroms
- anomalous or non-functional devices

We can also independently determine the quantum well thickness. The measured resonant bias voltage positions, corrected for the parasitic resistance empirically determined from the outside ring of control devices, were then used with Eqs. (1)–(4) to determine the quantum well thickness. The results are shown in Fig. 4. The quantum well contours are considerably less well defined than the tunnel barrier contours, suggesting that well width determination with this technique is at the resolution limit at the 1 \AA level. However, the well does not appear to exhibit the same axial asymmetry as the barriers. Indeed, the center-to-edge variation is approximately the same (5 \AA) along the orthogonal cleavage directions for the quantum well, whereas the barriers exhibit $2\text{--}3\text{ \AA}$ in one direction and 6 \AA in the orthogonal direction.

The application of this technique is not limited to cryogenic temperatures and large device size; indeed, smaller probe sizes and room temperature operation are desirable for characterization during device fabrication. Measurements were made on smaller devices fabricated on a second, similar MBE sample to demonstrate this

ability. The I - V characteristics of a typical device, with an active area of $25\text{ sq }\mu$, is shown in Fig. 5 at 300 K , 77 K , and at 4.2 K . The I - V characteristics do not change appreciably below $\sim 150\text{ K}$. The device demonstrates a 3.2 NDR region at 300 K , equal to the best known room temperature report to date¹³ and suitable for this measurement technique. The I - V characteristic does exhibit a small asymmetry seen elsewhere⁴ that has been attributed to the inferior GaAs-on-AlGaAs inverted interface. We, as yet, have no alternative explanation for the observed asymmetry. The complex structure in the NDR region of the I - V is due to undamped oscillations of the device under test.⁵

IV. CONCLUSIONS

We have presented a simple characterization technique for single quantum wells and adjacent tunnel barriers utilizing a resonant tunneling technique. This technique has been applied to characterize the thickness of a MBE-grown single well, double barrier resonant tunneling structure to an averaged resolution of 1 \AA . Contour

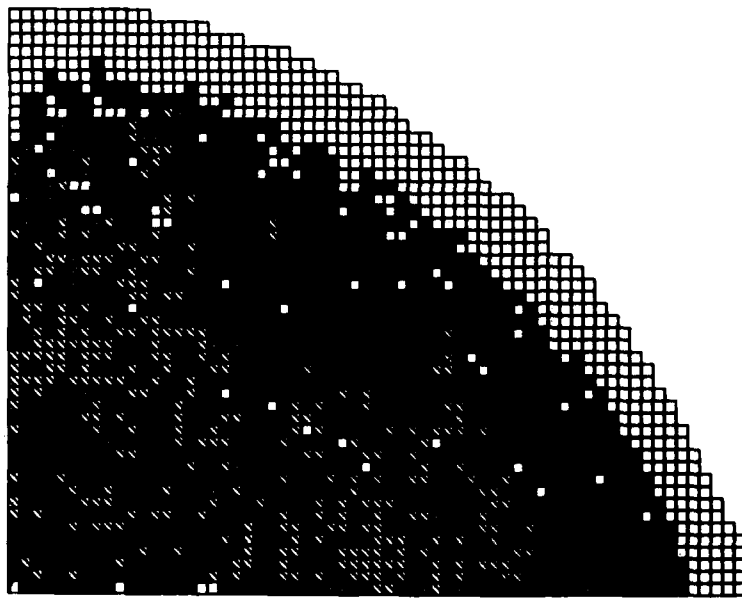


FIG. 4. Mapping of a GaAs quantum well thickness determined by resonant bias variations on a section of a MBE-grown wafer containing a single well, double barrier resonant tunneling structure. Measurements were taken at $T = 77$ K.

Deposition rate = 2Å/sec

Rotation rate = 4 rev/min

+ slice center (rotation axis)

$T = 77$ K

Legend

- greater than 52 Angstroms
- ▨ 51 - 52 Angstroms
- ▩ 50 - 51 Angstroms
- ▧ 49 - 50 Angstroms
- ▦ 48 - 49 Angstroms
- less than 48 Angstroms
- anomalous or non-functional devices

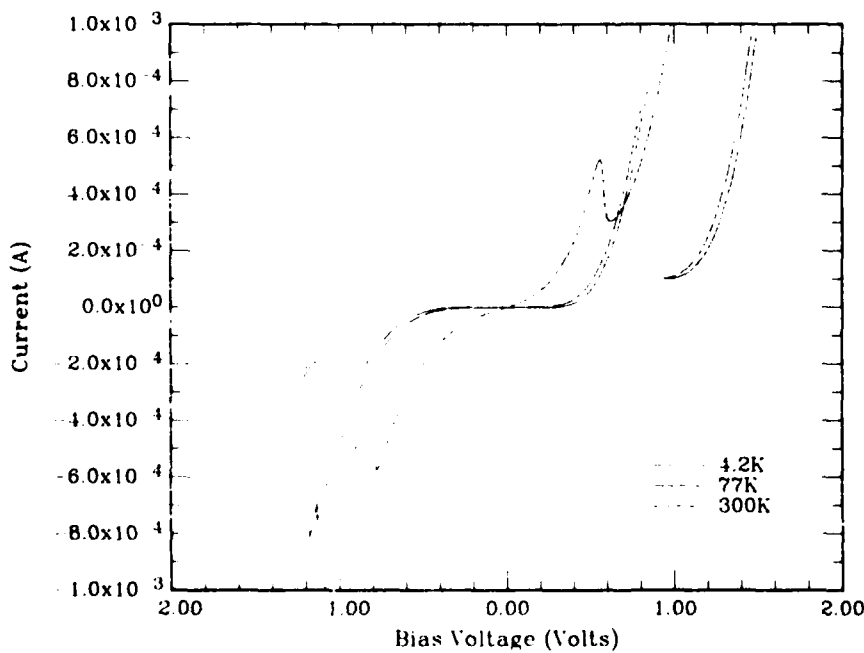


FIG. 5. Temperature dependence of the I - V characteristics of a small area ($25 \text{ sq. } \mu$) resonant tunneling device exhibiting room temperature NDR.

maps produced by this technique exhibited pronounced growth rings, different for the quantum well and adjacent tunnel barriers. We observe, for the first time, an asymmetric growth ring for the AlGaAs barrier. Application of this technique to the comparison of MBE versus MOCVD for similar structures is possible.

ACKNOWLEDGMENTS

We would like to thank R. Bate, W. Frensley, and D. Shaw for helpful discussions, and N. Gabriel and J. Williams for assistance in device fabrication.

This work has been sponsored in part by the Army Research Office and in part by the Office of Naval Research.

REFERENCES

- ¹L. L. Chang, L. Esaki, and R. Tsu, *Appl. Phys. Lett.* **24**, 593 (1974).
- ²T. C. L. G. Sollner, W. D. Goodhue, P. E. Tannenwald, C. D. Parker, and D. D. Peck, *Appl. Phys. Lett.* **43**, 588 (1983).
- ³A. R. Bonnefoi, R. T. Collins, T. C. McGill, R. D. Burnham, and F. A. Ponce, *Appl. Phys. Lett.* **46**, 285 (1985).
- ⁴T. J. Shewchuk, P. C. Chapin, P. D. Coleman, W. Kopp, R. Fisher, and H. Morkç, *Appl. Phys. Lett.* **46**, 508 (1985).
- ⁵T. C. L. G. Sollner, H. Q. Le, C. A. Correa, and W. D. Goodhue, *Appl. Phys. Lett.* **45**, 1319 (1984).
- ⁶R. Tsu and L. Esaki, *Appl. Phys. Lett.* **22**, 562 (1973).
- ⁷J. G. Simmons, *J. Appl. Phys.* **34**, 1793 (1963).
- ⁸B. Ricco and M. Ya Azbel, *Phys. Rev. B* **29**, 1970 (1984).
- ⁹S. Luryi, *Appl. Phys. Lett.* **47**, 490 (1985).
- ¹⁰A. Y. Cho and K. Y. Cheng, *Appl. Phys. Lett.* **38**, 360 (1981).
- ¹¹A. R. Bonnefoi, T. C. McGill, and R. D. Burnham, *Appl. Phys. Lett.* **47**, 307 (1985).
- ¹²The largest lateral distance between data points of Ref. 11 is 16% of the larger cleaved side of Fig. 3.
- ¹³Following submission of this paper, a value of 2.2:1 was reported (H. Sakaki, 1985 IEDM Tech. Dig.).

APPENDIX G

EXCITED STATE RESONANT TUNNELING IN
GaAs-AlGaAs DOUBLE BARRIER HETEROSTRUCTURES

EXCITED STATE RESONANT TUNNELING IN GaAs-Al_xGa_{1-x}As DOUBLE BARRIER HETEROSTRUCTURES

Mark A. Reed
Central Research Laboratories
Texas Instruments Incorporated
Dallas, TX 75265

(Received 8 December 1985)

Resonant tunneling through the ground and first excited state of single quantum well, double barrier GaAs-Al_xGa_{1-x}As heterostructures is reported. Negative differential resistance from both quantum well states is observable up to room temperature in one of these structures. The observed positions of the quantum well states agree well with theory, though there exists an asymmetry in the current-voltage characteristics about the origin.

Negative differential resistance (NDR) devices utilizing double barrier resonant tunneling structures¹ have recently undergone a renaissance²⁻⁴ due to improved GaAs-AlGaAs molecular beam epitaxy (MBE) techniques. In these devices, the essential carrier transport mechanism is electron (or hole) tunneling, specifically through ultrathin (~50 Å) Al_xGa_{1-x}As tunnel barriers and a GaAs quantum well. The potential for millimeter wave oscillators,⁵ mixers, and logic devices utilizing resonant tunneling devices are intriguing. The ability to vary the NDR bias position and device current density independently, through dimensional control during MBE growth, is an attractive feature of these structures to device designers.

A class of devices,⁶ such as frequency multipliers, multistate memories, and high speed analog-to-digital converters become possible if designers can utilize multiple NDR regions in resonant tunneling devices. Measurements by other workers^{1,3} have established the existence of resonant tunneling through multiple states in quantum wells, but the effects were weak and observable only at low temperature. This paper reports NDR for transport through the ground and excited states of single well, double barrier resonant tunneling structures and the existence of excited state resonant tunneling at room temperature.

The prototype resonant tunneling structure is a one-dimensional, double barrier, single quantum well heterostructure.¹⁻⁴ The center quantum well has a spectrum of discrete, higher allowed eigenstates (relative to the GaAs conduction band edge) than the electrons in the highly doped contacts. At low device bias, the eigenstate (band) in the central quantum well is too high in energy to allow resonant tunneling of electrons through the eigenstate. Tunneling through the entire structure is allowed, but

exponentially small. As the device bias increases, the quantum well state is lowered with respect to the Fermi level of the input contact, and carriers are allowed to tunnel through the structure. When the device bias is increased to the point that the allowed state in the quantum well is lower in energy than the conduction band edge of the input contact, elastic tunneling is no longer allowed due to the conflicting requirements of energy and momentum conservation. This decreases the tunneling current, producing NDR. Higher energy eigenstates will produce the same phenomena as they are biased to the Fermi level. An eventual increase in current at high device bias will be seen due to Fowler-Nordheim tunneling. The search for NDR from these higher states is the subject of this investigation.

The samples used in this study were grown by molecular beam epitaxy in a Riber MBE-2300 on a 2-inch (100) n⁺ Si-doped Sumitomo GaAs substrate. Following a highly doped (n-type, Si @ 2x10¹⁸ cm⁻³) buffer layer, the active resonant tunneling structure region was then grown. The undoped Al_xGa_{1-x}As barrier (50 Å, x=.3), undoped GaAs quantum well, and similar Al_xGa_{1-x}As barrier were then grown, followed by a similar top contact ~ 0.5 micron thick. The substrate was directly heated in a rotating substrate holder. Samples with quantum well widths of 50 Å and 100 Å were studied to observe the positions of the quantum well eigenstates as a function of well width.

Mesa diodes with diameters ranging from 2 to 225 microns were fabricated by conventional photolithography techniques. Ohmic contacts covered the top surface of the mesa and were made by evaporating Au-Ge, Ni, then Au, followed by an anneal. For devices too small to accommodate a direct bond, a silicon nitride layer (for isolation) was deposited over the sample followed by an Au evaporated bonding pad. Both backside and



Figure 1. I-V characteristic of a 50 Å quantum well resonant tunneling device at room temperature. The active device area is 100 square microns.

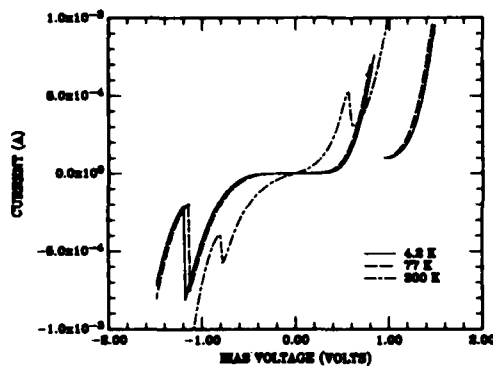


Figure 2. Temperature dependence of the I-V characteristics of a 50 Å quantum well resonant tunneling device. The active device area is 25 square microns.

planar contacts were used. The devices were either probed on a 77°K cold chuck or inserted into a variable-temperature helium-flow Janis cryostat for measurements in the temperature range 1.2°K to 300°K.

The I-V characteristics of a typical device (an active area of 100 square microns) for the 50 Å quantum well MBE sample at 300°K is shown in Figure 1. The NDR region exhibits a 1.7:1 peak-to-valley current ratio to room temperature and 7:1 at 77°K. Figure 2 shows the I-V characteristics of a similar device, with an active area of 25 square microns (though perhaps as small as 16 square microns due to undercutting by the mesa definition etch), at 300°K, 77°K, and at 4.2°K. There is little difference in the characteristics of these devices below ~150°K. The peak shift with temperature is primarily due to the change of parasitic resistance with temperature, and the increase of the valley

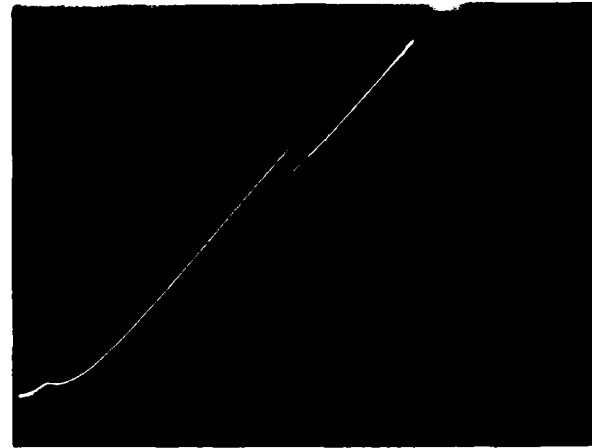


Figure 3. I-V characteristic of a 100 Å quantum well resonant tunneling device at 77°K. The peak at 150 mV is due to resonant tunneling through the ground state of the quantum well, and the peak at 1.45 V is due to resonant tunneling through the first excited state of the quantum well.

current with increasing temperature is due to inelastic current generation. The breaks in the 4.2°K and 77°K data curves are regions where the device undergoes self-oscillatory phenomena. This device demonstrated a 3:2 NDR region at 300°K. The I-V characteristics exhibit a slight asymmetry about the origin seen elsewhere,⁴ which has been attributed to the inferior GaAs-on-AlGaAs inverted interface. No additional features in the I-V due to excited state tunneling were observable at any temperature.

Measurements were performed on similar devices for the 100 Å quantum well MBE sample. There was no observable NDR at room temperature, but two clear peaks were evident at 77°K as shown in Figure 3. The lower voltage peak can be identified with resonant tunneling through the ground state of the quantum well, and the higher voltage peak resonant tunneling through the first excited state. Figure 4 shows the lower voltage peak on an expanded scale, demonstrating clear NDR for resonant tunneling through the quantum well ground state. The low voltage peaks also exhibited a pronounced asymmetry (160 mV vs 300 mV) and the excited state peak was not observable on the 300 mV side.

The theoretical positions of the resonant peaks for the 100 Å well were derived using a transfer-matrix technique.⁷ In terms of device bias voltage, the resonant positions are 83 mV for the ground state and 0.35 V for the first excited state. The experimental results are in excellent agreement with theory when the series parasitic resistance of 16 Ω is taken into account. This resistance also explains the apparent "hysteresis" of the excited state peak, which is due to the resonant tunneling diode - parasitic resistor series combination. This apparent hysteresis will appear whenever the value of the series resistance



Figure 4. Expanded scale of Fig. 3 showing negative differential resistance due to resonant tunneling through the quantum well ground state.



Figure 5. I-V characteristic of a 50 Å quantum well resonant tunneling device at 77°K. The higher voltage peak is due to resonant tunneling through the first excited state of the quantum well. Both of these peaks exhibited weak NDR (1 to 2%) at room temperature.

is less than the absolute magnitude of the negative resistance produced by resonant tunneling.

A second set of devices were fabricated from the 50 Å sample to search for any evidence of resonant tunneling through weakly bound or virtual states in narrow wells. In this case the bottom contact (i.e., the contact to the bottom of the mesa diode) was a topside planar Schottky barrier. Figure 5 demonstrates an observation made at 77°K in 2 out of 14 devices fabricated. The lower voltage peak agrees well with the

predicted value (0.24 V) of resonant tunneling through the ground state of the 50 Å well when the Schottky barrier and parasitic resistance are taken into account. The higher voltage peak is ascribed to tunneling through the first excited state. The transfer-matrix technique does not predict a second bound state in the well, though the approximations of this model cannot be considered valid at high bias voltage. The experimental bias position of the excited state indicates a state very near the top of the 50 Å quantum well. That this peak does not appear in all devices may be due to quantum well thickness fluctuations across the sample that are sufficient to unbind the loosely bound state. The peak-to-valley ratio of the excited state NDR, as well as the ground state, weakened with increasing temperature but was still observable as a 1-2% peak-to-valley NDR at room temperature. The inferior room temperature performance of the 100 Å quantum well sample should not be taken as intrinsic since no effort was made to iteratively optimize the structure, as was performed on the 50 Å structure.

In summary, NDR from resonant tunneling through quantum well excited states has been observed in two MBE samples of different quantum well size. The voltage positions of the resonant peaks agree well with theory. The NDR in the excited states of one sample was observable at room temperature.

Acknowledgement - I am indebted to H.D. Shih and J.W. Lee for the MBE samples, R.T. Bate, W.R. Frensley, and D. Shaw for helpful discussions and critical evaluation, R.K. Aldert for measurements, and N. Gabriel and J. Williams for assistance in device fabrication. This work was supported in part by ARO and ONR.

REFERENCES

1. L. L. Chang, L. Esaki, and R. Tsu, *Applied Physics Letters* 22, 562 (1973).
2. T. C. L. G. Sollner, W. D. Goodhue, P. E. Tannenwald, C.D. Parker, and D. D. Peck, *Applied Physics Letters* 43, 588 (1983).
3. A. R. Bonnefoi, R. T. Collins, T. C. McGill, R. D. Burnham, and F. A. Ponce, *Applied Physics Letters* 46, 285 (1985).
4. T. J. Shewchuk, P. C. Chapin, P. D. Coleman, W. Kopp, R. Fisher, and H. Morkoç, *Applied Physics Letters* 46, 508 (1985).
5. T. C. L. G. Sollner, H. Q. Le, C. A. Correa, and W. D. Goodhue, *Applied Physics Letters* 45, 1319 (1984).
6. F. Capasso and R. A. Kiehl, *Journal of Applied Physics* 58, 1366 (1985).
7. B. Ricco and M. Ya. Azbel, *Physical Review* 29B, 1970 (1984).

APPENDIX H

**RESONANT TUNNELING THROUGH A DOUBLE
GaAs/AlAs SUPERLATTICE BARRIER**

Resonant tunneling through a double GaAs/AIAs superlattice barrier, single quantum well heterostructure

M. A. Reed, J. W. Lee, and H-L. Tsai

Central Research Laboratories, Texas Instruments Incorporated, Dallas, Texas 76265

(Received 18 April 1986; accepted for publication 20 May 1986)

Resonant tunneling has been demonstrated through a double barrier, single quantum well heterostructure in which the barriers have been replaced by thin, short period binary superlattices. The superlattice structure does not exhibit the asymmetry around zero bias in the electrical characteristics normally observed in the conventional $\text{Al}_x\text{Ga}_{1-x}\text{As}$ barrier structures, suggestive of reduced roughness at the inverted interface by superlattice smoothing. The structure exhibits an anomalously low barrier height and a peak to valley tunnel current ratio of 1.8:1 at 300 K.

The phenomenon of resonant tunneling in double barrier heterostructures, first investigated in the seminal work of Chang, Esaki, and Tsu,¹ has recently undergone a renaissance²⁻⁴ due to recent improvements in epitaxial growth techniques. The dc and high-frequency transport in these structures has been the subject of intense investigation following the remarkable submillimeter wave experiments of Sollner *et al.*,² which has been interpreted as coherent resonant tunneling through the heterostructure. This renewed interest has led to the observation of large room-temperature peak to valley tunnel current ratios,⁴ resonant tunneling of holes,⁵ the observation of multiple negative differential resistance (NDR) peaks due to resonant tunneling,⁶ and the observation of sequential resonant tunneling through a multi-quantum well (MQW) superlattice.⁷

The initial investigations of this structure, typically in the GaAs/ $\text{Al}_x\text{Ga}_{1-x}\text{As}$ system, have utilized "square" (i.e., constant Al mole fraction) barriers to confine the central quantum well. A number of intriguing physical phenomena can be examined by tailoring the barrier(s) in real space, such as equally spaced resonant peaks arising from a parabolic quantum well.⁸ However, the variety of tunneling structures that can be investigated is limited by the practical constraints on the $\text{Al}_x\text{Ga}_{1-x}\text{As}$ barrier (or well) growth and the rate the Al mole fraction can be changed over the region of interest, typically $\sim 100 \text{ \AA}$. A possible solution to the Al mole fraction gradient constraint is the emulation of the desired $\text{Al}_x\text{Ga}_{1-x}\text{As}$ alloy barrier structure with a GaAs/ $\text{Al}_x\text{Ga}_{1-x}\text{As}$ superlattice of fixed (even 100%) Al mole fraction.⁹⁻¹¹ In this letter we report the first study of resonant tunneling through a double barrier, single quantum well heterostructure in which the barriers have been replaced by thin, short period binary superlattices. This is the first demonstration that quantum well states can be confined by very thin, short period superlattices and that resonant tunneling transport through a compositional modulated barrier is possible.

The samples used in this study were grown by molecular beam epitaxy in a Riber MBE-2300 on a 2-in. (100) n^+ Si-doped Sumitomo GaAs substrate utilizing a directly heated rotating substrate holder. Following a highly doped (n type, $\text{Si} \odot 1 \times 10^{18} \text{ cm}^{-3}$) buffer layer, the active resonant tunneling structure region was then grown. For comparison, a con-

ventional $\text{Al}_x\text{Ga}_{1-x}\text{As}$ alloy barrier structure of similar barrier and quantum well dimension was fabricated, as well as one with a larger quantum well size. The conventional $\text{Al}_x\text{Ga}_{1-x}\text{As}$ barrier sample consisted of an undoped $\text{Al}_x\text{Ga}_{1-x}\text{As}$ barrier (50 \AA , $x = 0.35$), followed by an undoped GaAs quantum well (50 and 100 \AA), similar barrier, and a top contact $\sim 0.5 \mu\text{m}$ thick. For the binary superlattice barrier structure, each barrier consists of three 7 \AA layers of AIAs separated by two 7 \AA layers of GaAs. The GaAs quantum well in this sample is 45 \AA and the remainder of the structure is identical to the $\text{Al}_x\text{Ga}_{1-x}\text{As}$ barrier samples. A cross-sectional transmission electron micrograph of the superlattice barrier structure is shown in Fig. 1. Devices were fabricated by defining mesas on the surface with conventional photolithography techniques, bonded for mechanical stability, and inserted into a variable-temperature helium-flow Janis cryostat or into a stabilized oven for variable temperature measurements.

Figure 2(a) shows the room-temperature static current-voltage (I - V) characteristics of a typical conventional alloy barrier, 50- \AA -wide quantum well, resonant tunneling structure. This structure exhibits a room-temperature peak to val-



FIG. 1. Cross-sectional transmission electron micrograph of the superlattice barrier resonant tunneling structure. The width of the GaAs quantum well is 45 \AA and the widths of the two GaAs and three AIAs superlattice barrier components are 7 \AA .

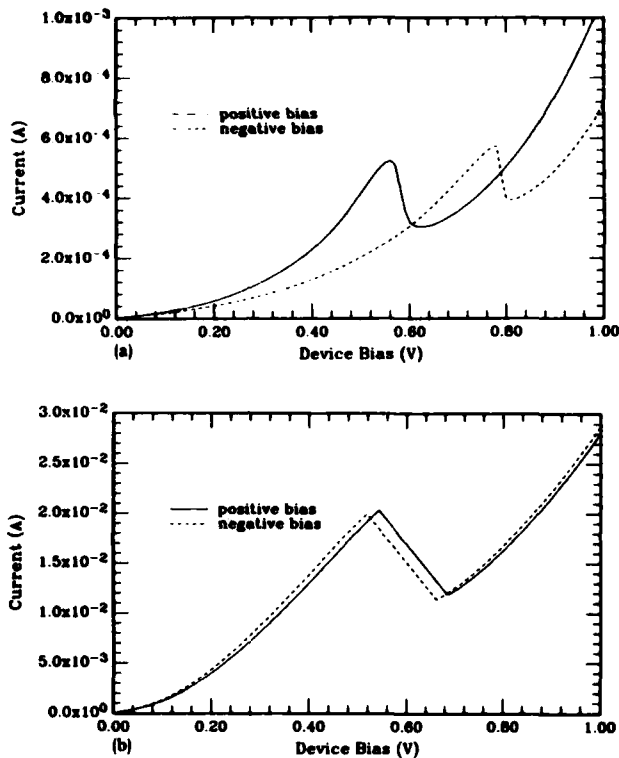


FIG. 2. (a) Room-temperature static I - V characteristics of a typical conventional 50 Å alloy barrier, 50 Å wide quantum well, resonant tunneling structure. Device mesa area = 25 μm^2 . Positive and negative bias are shown. (b) Room temperature static I - V characteristics for the superlattice barrier structure. Device mesa area = 25 μm^2 . The symmetry for positive and negative bias is excellent.

ley tunnel current ratio of 1.75:1 which increases typically to 7:1 at low temperatures (< 100 K). We have plotted the negative bias data reflected into the first quadrant to emphasize the observed asymmetry in the current-voltage characteristics of these structures. This asymmetry has been ascribed to the inferior inverted interface morphology of the quantum well and contact region.⁴ This is consistent with our observations; our convention of positive bias means electron injection from the backside superior GaAs contact. A higher resonant bias for the inverted configuration would be expected from an extended inverted region. The room temperature I - V characteristics for the superlattice barrier structure, designed to have the same resonant bias voltage, is shown in Fig. 2(b). The symmetry for positive and negative bias is excellent. This observation suggests that the inverted interface is indeed responsible for the observed asymmetry in the alloy barrier structure and that the superlattice barrier improves the interface by lessening trapping of undesired impurities and/or prevents surface roughening. This improvement has been observed previously in photoluminescence experiments.¹⁰ The superlattice barrier structure exhibits a 1.8:1 peak to valley ratio at room temperature and exhibits NDR up to 100 °C.

The observed resonant bias positions can be compared to the theoretical predictions of a transfer matrix model¹² if the parasitic resistances in the structure are independently known. Since this is unknown for the structures, we employ

the technique¹³ of low bias thermal activation of carriers over the effective barrier to determine the position of the quantum well bound state relative to the Fermi level of the contact. In this case the effective thermal barrier presented to the electrons, at low bias, is not the full barrier but the Γ point of the quantum well bound state. This is demonstrated in Fig. 3(a) for the alloy barrier structure with a 50 Å quantum well, which yields an activation energy of 70 meV. Similar measurements on an alloy barrier structure with a quantum well width of ~ 100 Å gave an activation energy of 15 meV, demonstrating that the activation energy decreases with increasing well size as expected. It should be noted that the ground state only is observed due to the large energetic separation of the excited state.

The activation energy gives the quantum well energy relative to the conduction-band edge when corrected for the assumed degeneracy in the contact due to the high doping ($N_D \approx 1 \times 10^{18}$ cm^{-3} , which gives $E_F \approx 55$ meV). The derived quantum well state is 120 meV which is in excellent agreement with the values of 116 meV predicted from an envelope function approximation¹⁴ using a 60% conduction-band offset. This technique was used to derive the position of the center quantum well state for the superlattice barrier structure and is shown in Fig. 3(b) for two devices of different mesa dimension. The thermal activation measurement for both gives a quantum well state of 121 meV, the same as the 50 Å alloy barrier structure which was expected from the identical resonant bias positions (without the inverted bias asymmetry complication) of Fig. 2.

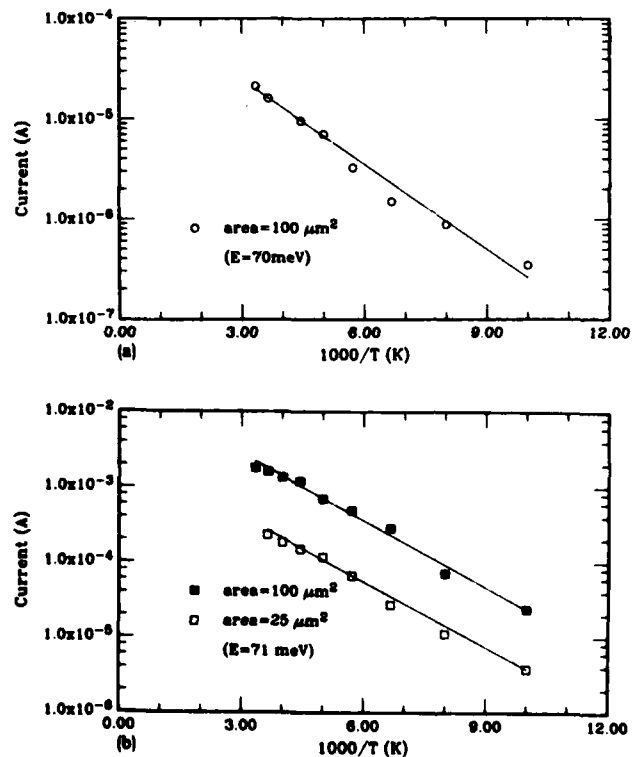


FIG. 3. (a) Low bias thermally activated current for the 50 Å quantum well alloy barrier structure. The thermal activation measurement gives $E = 70$ meV. (b) Low bias thermally activated current for the superlattice barrier structure, showing identical activation energies independent of current density. The current does not exactly scale with top mesa dimension due to mesa undercut. The thermal activation measurement gives $E = 71$ meV.

There are two independent approaches to determine the effective barrier height ΔE_c^* of the superlattice barrier once the quantum well energy is known. Firstly, we can use the energy of the quantum well state (determined above) to derive the effective barrier height ΔE_c^* assuming that the envelope function approximation for thick barriers is valid. Using a 45 Å quantum well, we obtain an effective barrier height $\Delta E_c^* = 290$ meV, or an equivalent alloy composition of 0.296.

Secondly, we can compare the transmitted resonant current densities of the conventional alloy barrier structure and the superlattice barrier structure. Considering single particle transmission coefficients, it can be shown that the effective barrier height ΔE_c^* can be expressed as

$$\Delta E_c^* = E_{QW,0}^{sl} + \frac{\hbar^2}{8m^*d_{sl}^2} \times \left(\ln \frac{J_{sl}}{J_A} + \frac{2d_A}{\hbar} [2m^*(\Delta E_c^A - E_{QW,0}^A)]^{1/2} \right),$$

where d_{sl} is the width of the superlattice barrier, d_A is the width of the alloy barrier, J_A and J_{sl} are the measured current densities for the alloy barrier and superlattice barrier, respectively, ΔE_c^A is the conduction-band offset for the alloy barrier case, and the $E_{QW,0}^A$ are the ground state energies of the quantum wells. Using a 60% conduction-band offset and a 35 Å superlattice barrier width, we get $\Delta E_c^* = 240$ meV, slightly lower than the barrier computed above. A monolayer fluctuation at the interfaces of the barrier gives $\Delta E_c^* = 275$ meV, in good agreement with the envelope function prediction. The evanescent tail contribution, clearly important here, lowers the thick barrier envelope function prediction for the quantum well state.

The superlattice barrier height is much lower than would be expected from an averaged alloy composition of 0.60, which gives a barrier height of 587 meV. Photoluminescence experiments on thick superlattice barrier confined isolated quantum wells¹⁰ also found disagreement with an averaged alloy composition model, although an equivalent alloy composition higher than the average alloy composition was found. An envelope function approximation to a superlattice of infinite extent to determine the effective barrier height as the first conduction minizone edge gives an even greater discrepancy. Thus the superlattice barrier allows appreciable wave function penetration while maintaining a high-energy quantum well state, as has been previously suggested.¹⁰ The observation of an anomalously low barrier

height to transport is indicative of the enhanced evanescent tail.

The ability to emulate barriers with superlattices permits a number of intriguing suggested investigations for tunneling structures, such as equally spaced resonances from a parabolic well, an increase in transmission coefficient from a structure symmetric at resonant bias, band-gap engineered contacts, an increase in sequential multiquantum well resonant current, and the investigation of the influence of barrier symmetry on resonant bias and transmission. The flexibility of design and enhanced evanescent tail are also important to MQW lasers and high-frequency resonant tunneling devices.

In summary, we have reported the first study of a double short period binary superlattice barrier, single quantum well heterostructure. This is the first demonstration that quantum well states can be confined by very thin, short period superlattices. The superlattice structure does not exhibit the asymmetry around zero bias in the electrical characteristics normally observed in the conventional $Al_xGa_{1-x}As$ barrier structures, and exhibits an anomalously low barrier height demonstrating an enhanced evanescent tail in the superlattice barrier.

We are thankful to R. T. Bate, W. R. Frensley, and C. H. Hoel for discussions and R. Aldert, R. Thomason, and J. Williams for technical assistance. This work was supported in part by the Office of Naval Research and the U.S. Army Research Office.

- ¹L. L. Chang, L. Esaki, and R. Tsu, *Appl. Phys. Lett.* **24**, 593 (1974).
- ²T. C. L. G. Sollner, W. D. Goodhue, P. E. Tannenwald, C. D. Parker, and D. D. Peck, *Appl. Phys. Lett.* **43**, 588 (1983).
- ³A. R. Bonnefoi, R. T. Collins, T. C. McGill, R. D. Burnham, and F. A. Ponce, *Appl. Phys. Lett.* **46**, 285 (1985).
- ⁴T. J. Shewchuk, P. C. Chapin, P. D. Coleman, W. Kopp, R. Fisher, and H. Morkoç, *Appl. Phys. Lett.* **46**, 508 (1985).
- ⁵E. E. Mendez, W. I. Wang, B. Ricco, and L. Esaki, *Appl. Phys. Lett.* **47**, 415 (1985).
- ⁶M. A. Reed, *Superlattices and Microstructures* (in press).
- ⁷F. Capasso, K. Mohammed, and A. Y. Cho, *Appl. Phys. Lett.* **48**, 478 (1986).
- ⁸F. Capasso and R. A. Kiehl, *J. Appl. Phys.* **58**, 1366 (1985).
- ⁹W. D. Laidig, P. J. Caldwell, K. Kim, and J. W. Lee, *Electron. Device Lett.* **4**, 212 (1983).
- ¹⁰H. Sakaki, M. Tsuchiya, and J. Yoshino, *Appl. Phys. Lett.* **47**, 295 (1985).
- ¹¹K. Fujiwara, J. L. de Miguel, and K. Ploog, *Jpn. J. Appl. Phys. Part 2*, **24**, L405 (1985).
- ¹²B. Ricco and M. Ya. Azbel, *Phys. Rev. B* **29**, 1970 (1984).
- ¹³A. C. Gossard, W. Brown, C. L. Allyn, and W. Wiegmann, *J. Vac. Sci. Technol.* **20**, 694 (1982).
- ¹⁴G. Bastard, *Phys. Rev. B* **24**, 5693 (1981).

APPENDIX I

RESONANT TUNNELING IN A DOUBLE GaAs/AlAs
SUPERLATTICE BARRIER HETEROSTRUCTURE

Resonant tunneling in a double GaAs/AlAs superlattice barrier heterostructure

M A Reed and J W Lee

Central Research Laboratories
Texas Instruments Incorporated
Dallas, Texas 76265 USA

Abstract. Resonant tunneling has been demonstrated through a double barrier, single quantum well heterostructure in which the barriers have been replaced by thin, short period binary superlattices. The structure exhibits an anomalously low barrier height and a peak to valley tunnel current ratio of 1.8:1 at 300°K.

1. Introduction

The phenomena of resonant tunneling in double barrier heterostructures, first investigated in the seminal work of Chang, Esaki, and Tsu (1974), has recently undergone a renaissance due to recent improvements in epitaxial growth techniques. The DC and high frequency transport in these structures has been the subject of intense investigation following the remarkable submillimeter wave experiments of Sollner et al (1983) which has been interpreted as coherent resonant tunneling through the heterostructure. This renewed interest has led to the observation of large room temperature peak to valley tunnel current ratios (Shewchuk et al 1985), resonant tunneling of holes (Mendez et al 1985), the observation of multiple negative differential resistance (NDR) peaks due to resonant tunneling (Reed 1986) and the observation of sequential resonant tunneling through a multi-quantum well (MQW) superlattice (Capasso et al 1986).

The initial investigations of this structure, typically in the GaAs/Al_xGa_{1-x}As system, have utilized "square" (i.e., constant Al mole fraction) barriers to confine the central quantum well. A number of intriguing physical phenomena can be examined by tailoring the barrier(s) in real space, such as equally spaced resonant peaks arising from a parabolic quantum well. However, the variety of tunneling structures that can be investigated is limited by the practical constraints on the Al_xGa_{1-x}As barrier (or well) growth and the rate the Al mole fraction can be changed over the region of interest, typically ~100Å. A possible solution to the Al mole fraction gradient constraint is the emulation of the desired Al_xGa_{1-x}As alloy barrier structure with a GaAs/Al_xGa_{1-x}As superlattice of fixed (even 100%) Al mole fraction (Laidig 1983 and Sakaki 1985). In this letter we report the first study of resonant tunneling through a double barrier, single quantum well heterostructure in which the barriers have been replaced by thin, short period binary superlattices. This is the first demonstration that quantum well states can be confined by very thin, short period superlattices and that resonant tunneling transport through a compositionally modulated barrier is possible.

2. Experimental procedure

The samples used in this study were grown by molecular beam epitaxy in a Riber MBE-2300 on a 2-inch (100) n^+ Si-doped Sumitomo GaAs substrate utilizing a directly heated rotating substrate holder. Following a highly doped (n -type, Si @ $1 \times 10^{18} \text{ cm}^{-3}$) buffer layer, the active resonant tunneling structure region was then grown. For comparison, a conventional $\text{Al}_x\text{Ga}_{1-x}\text{As}$ alloy barrier structure of similar barrier and quantum well dimension was fabricated, as well as one with a larger barrier quantum well size. The conventional $\text{Al}_x\text{Ga}_{1-x}\text{As}$ barrier sample consisted of an undoped $\text{Al}_x\text{Ga}_{1-x}\text{As}$ barrier (50Å, $x = .35$), followed by an undoped GaAs quantum well (50Å or 100Å), similar barrier, and a top contact ~ 0.5 micron thick. For the binary superlattice barrier structure, each barrier consists of three 7Å layers of AlAs separated by two 7Å layers of GaAs. The GaAs quantum well in this sample is 45Å and the remainder of the structure is identical to the $\text{Al}_x\text{Ga}_{1-x}\text{As}$ barrier samples. A cross-sectional transmission electron micrograph of the superlattice barrier structure is shown in Figure 1. Devices were fabricated by defining mesas on the surface with conventional photolithography techniques, bonded for mechanical stability, and inserted into a variable-temperature helium-flow Janis cryostat or into a stabilized oven for variable temperature measurements.



Figure 1 Cross-sectional transmission electron micrograph of the superlattice barrier resonant tunneling structure. The width of the GaAs quantum well is 45Å and the widths of the two GaAs and three AlAs superlattice barrier components are 7Å.

3. Results

Figure 2 shows the room temperature static current-voltage (I-V) characteristics of a typical conventional alloy barrier, 50Å wide quantum well, resonant tunneling structure. This structure exhibits a room temperature peak to valley tunnel current ratio of 1.75:1 which increases typically to 7:1 at low temperatures ($\leq 100^\circ\text{K}$). We have plotted the negative bias data reflected into the first quadrant to emphasize the observed asymmetry in the current-voltage characteristics of these structures. This asymmetry has been ascribed to the inferior inverted interface morphology of the quantum well and contact region (Shewchuk et al 1985). This is consistent with our observations; our convention of positive bias means electron injection from the backside superior GaAs contact. A higher resonant bias for the inverted configuration would be expected from an extended inverted region. The room temperature I-V characteristics for the superlattice barrier structure, designed to have the same resonant bias voltage, is shown in Figure 3. The symmetry for positive and negative bias is excellent. This observation suggests that the inverted interface is indeed responsible for the observed asymmetry in the alloy barrier structure and that the superlattice barrier improves the interface by lessening trapping of undesired impurities and/or prevents surface roughening. This improvement has been observed previously in photoluminescence experiments (Sakaki et al 1985). The superlattice barrier structure exhibits a 1.8:1 peak to valley ratio at room temperature and exhibits NDR up to 100°C .

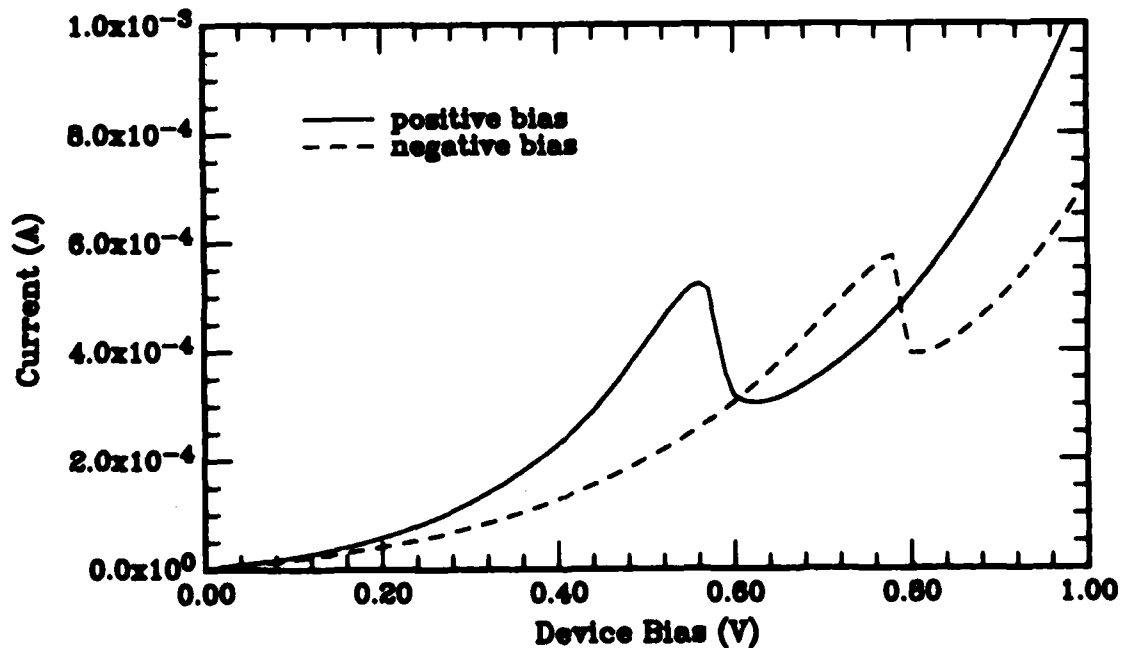


Figure 2. Room temperature static I-V characteristics of a typical conventional 50Å alloy barrier, 50Å wide quantum well, resonant tunneling structure. Device mesa area = $25\ \mu\text{m}^2$. Positive and negative bias are shown.

The observed resonant bias positions can be compared to the theoretical predictions of a transfer matrix model (Ricco and Azbel 1984) if the parasitic resistances in the structure are independently known. Since this is unknown for the structures, we employ the technique (Gossard et al 1982) of low bias thermal activation of carriers over the effective barrier to determine the position of the quantum well bound state relative to the Fermi level of the contact. In this case the effective thermal barrier presented to the electrons, at low bias, is not the full barrier but the Γ -point of the quantum well bound state. This is demonstrated in Figure 4 for the alloy barrier structure with a 50Å quantum well, which yields an

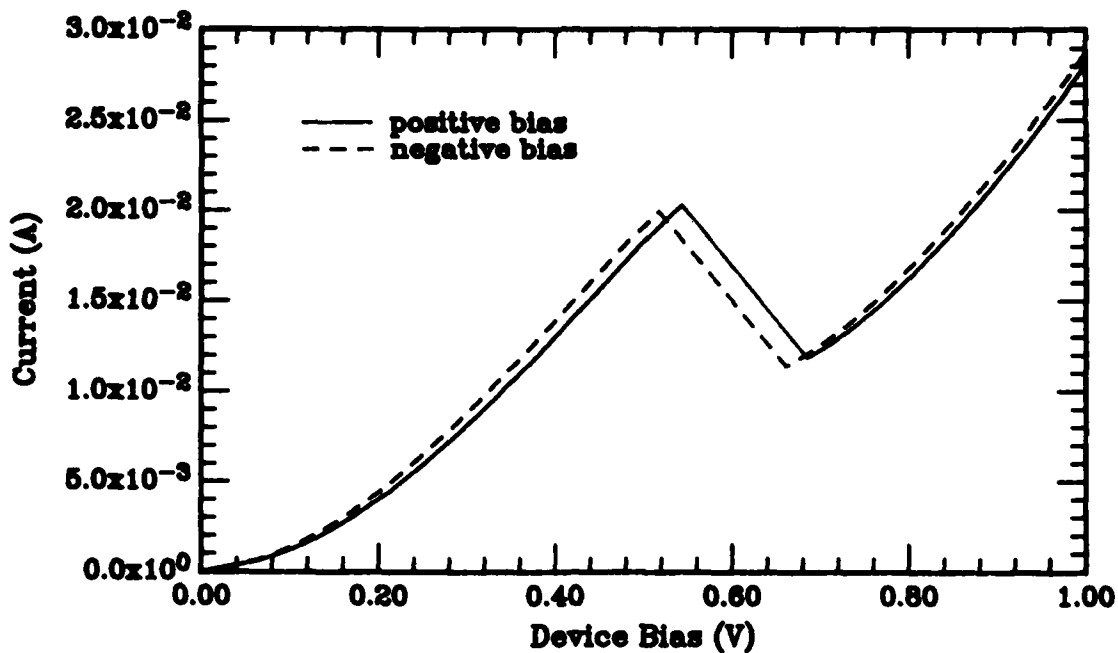


Figure 3. Room temperature static I-V characteristics for the superlattice barrier structure. Device mesa area = $25 \mu\text{m}^2$. The symmetry for positive and negative bias is excellent.

activation energy of 70 meV. Similar measurements on an alloy barrier structure with a quantum well width of $\sim 100\text{\AA}$ gave an activation energy of 15 meV, demonstrating that the activation energy decreases with increasing well size as expected. It should be noted that the ground state only is observed due to the large energetic separation of the excited state.

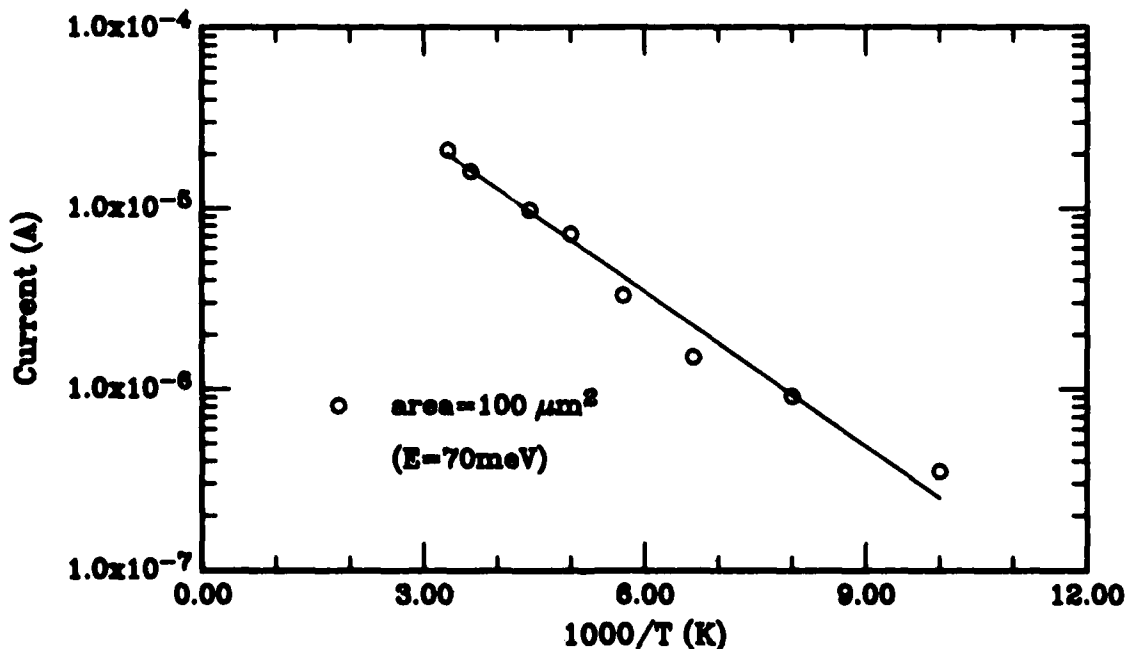


Figure 4. Low bias thermally activated current for the 50\AA quantum well alloy barrier structure. The thermal activation measurement gives $E = 70 \text{ meV}$.

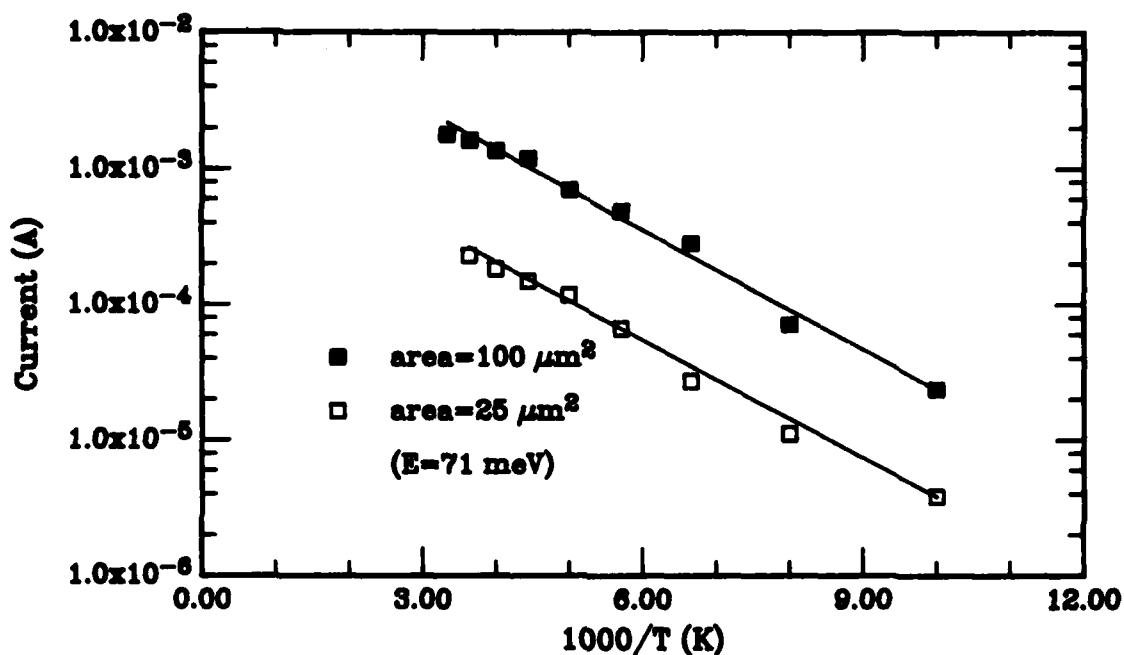


Figure 5. Low bias thermally activated current for the superlattice barrier structure, showing identical activation energies independent of current density. The current does not exactly scale with top mesa dimension due to mesa undercut. The thermal activation measurement gives $E = 71$ meV.

The activation energy gives the quantum well energy relative to the conduction band edge when corrected for the assumed degeneracy in the contact due to the high doping ($N_D \approx 1 \times 10^{18} \text{ cm}^{-3}$, which gives $E_F \approx 55$ meV). The derived quantum well state is 120 meV which is in excellent agreement with the values of 116 meV predicted from an envelope function approximation (Bastard 1981) using a 60% conduction band offset. This technique was used to derive the position of the center quantum well state for the superlattice barrier structure and is shown in Figure 5 for two devices of different mesa dimension. The thermal activation measurement for both gives a quantum well state of 121 meV, the same as for the 50Å alloy barrier structure which was expected from the identical resonant bias positions of Figures 2 and 3.

There are two independent approaches to determine the effective barrier height ΔE_c^* of the superlattice barrier once the quantum well energy is known. First, we can use the energy of the quantum well state (determined above) to derive the effective barrier height ΔE_c^* assuming that the envelope function approximation for thick barriers is valid. Using a 45Å quantum well, we obtain an effective barrier height: $\Delta E_c^* = 290$ meV, or an equivalent alloy composition of 0.296. Secondly, we can compare the transmitted resonant current densities of the conventional alloy barrier structure and the superlattice barrier structure. Considering single particle transmission coefficients, it can be shown that the effective barrier height ΔE_c^* can be expressed as

$$\Delta E_c^* = E_{QW,0}^{SL} + \frac{\hbar^2}{8m^* d_{SL}^2} \left\{ \ln \frac{J_{SL}}{J_A} + \frac{2d_A}{\hbar} \left[2m^* (\Delta E_c^A - E_{QW,0}^A) \right] \right\} \quad [1]$$

where d_{SL} is the width of the superlattice barrier, d_A is the width of the alloy barrier, J_A and J_{SL} are the measured current densities for the alloy barrier and superlattice barrier, respectively, ΔE_c^A is the conduction band offset for the alloy barrier case, and the $E_{QW,0}^A$ are the ground state energies of the quantum wells.

Using a 60% conduction band offset and a 35Å superlattice barrier width, we get $\Delta E_c^* = 240$ meV, slightly lower than the barrier computed above. A monolayer fluctuation at the interfaces of the barrier gives $\Delta E_c^* = 275$ meV, in good agreement with the envelope function prediction.

The superlattice barrier height is much lower than would be expected from an averaged alloy composition of 0.60, which gives a barrier height of 587 meV. Photoluminescence experiments on thick superlattice barrier confined isolated quantum wells (Sakaki et al 1985) also found disagreement with an averaged alloy composition model, though an equivalent alloy composition higher than the average alloy composition was found. An envelope function approximation to a superlattice of infinite extent to determine the effective barrier height as the first conduction minizone edge gives an even greater discrepancy. Thus the superlattice barrier allows appreciable wavefunction penetration while maintaining a high energy quantum well state, as has been previously suggested. The observation of an anomalously low barrier height to transport is indicative of the enhanced evanescent tail.

4. Summary

In summary, we report the first study of a double short period binary superlattice barrier, single quantum well heterostructure. This is the first demonstration that quantum well states can be confined by very thin, short period superlattices. The superlattice structure does not exhibit the asymmetry around zero bias in the electrical characteristics normally observed in the conventional $Al_xGa_{1-x}As$ barrier structures, and exhibits an anomalously low barrier height demonstrating an enhanced evanescent tail in the superlattice barrier. The ability to emulate barriers with superlattices permits a number of intriguing suggested investigations for tunneling structures, such as equally spaced resonances from a parabolic well, an increase in transmission coefficient from a structure symmetric at resonant bias, bandgap engineered contacts, an increase in sequential multi-quantum well resonant current, and the investigation of the influence of barrier symmetry on resonant bias and transmission. The flexibility of design and enhanced evanescent tail are also important to MQW lasers and high frequency resonant tunneling devices.

We are thankful to R. T. Bate, W. R. Frensley and C. H. Hoel for discussions and R. Aldert, R. Thomason, and J. Williams for technical assistance. This work was supported in part by the Office of Naval Research and the U. S. Army Research Office.

5. References

- Bastard G 1981 Phys. Rev. **24B** 5693
 Capasso F, Mohammed K, and Cho A Y 1986 Appl. Phys. Lett. **48** 478
 Chang L L, Esaki L, and Tsu R 1974 Appl. Phys. Lett. **24** 593
 Gossard A C, Brown W, Allyn C L, and Wiegmann W 1982 J. Vac. Sci. Technol. **20** 694 (1982).
 Laidig W D, Caldwell P J, Kim K, and Lee J W 1983 ELD **4** 212
 Mendez E E, Wang W I, Ricco B, and Esaki L 1985 Appl. Phys. Lett. **47** 415
 Reed M A 1986 Superlattices and Microstructures **2** 65
 Ricco B and Azbel M Ya 1984 Phys. Rev. **29B** 1970
 Sakaki H, Tsuchiya M, and Yoshino J 1985 Appl. Phys. Lett. **47** 295
 Shewchuk T J, Chapin P C, Coleman P D, Kopp W, Fisher R, and Morkoç H 1985 Appl. Phys. Lett. **46** 50
 Sollner T C L G, Goodhue W D, Tannenwald P E, Parker C D, and Peck D D 1983 Appl. Phys. Lett. **43** 588

APPENDIX J

RESONANT TUNNELING IN DOUBLE SUPERLATTICE
BARRIER HETEROSTRUCTURES

RESONANT TUNNELING IN DOUBLE SUPERLATTICE BARRIER HETEROSTRUCTURES

Mark A. Reed and Jhang W. Lee
Central Research Laboratories
Texas Instruments Incorporated
Dallas, TX 75265

(Received 18 August 1986)

We have investigated resonant tunneling in double barrier heterostructures in which the tunnel barriers have been replaced by short period superlattices, and have shown for the first time quantum well confinement in a single quantum well bounded by superlattices. These results also demonstrate the first utilization of short period binary superlattices as effective tunnel barriers to replace the conventional $\text{Al}_x\text{Ga}_{1-x}\text{As}$ barriers. The superlattice structure does not exhibit the asymmetry around zero bias in the electrical characteristics normally observed in the conventional $\text{Al}_x\text{Ga}_{1-x}\text{As}$ barrier structures, suggestive of reduced roughness at the inverted interface by superlattice smoothing. The superlattice barrier also exhibits an anomalously low barrier height. The performance of this symmetric superlattice structure is compared with an intentionally constructed asymmetric double barrier superlattice structure, which exhibits pronounced asymmetry in the electrical characteristics. The observed behavior supports the view that resonant enhancement occurs in the quantum well.

Negative differential resistance (NDR) devices utilizing double barrier resonant tunneling structures¹ have recently undergone a renaissance²⁻⁴ due to improved GaAs-AlGaAs molecular beam epitaxy (MBE) techniques. In these devices, the essential carrier transport mechanism is electron (or hole) tunneling, specifically through ultrathin ($\sim 50\text{\AA}$) $\text{Al}_x\text{Ga}_{1-x}\text{As}$ tunnel barriers and a GaAs quantum well. This renewed interest has led to the observation of large room temperature peak to valley tunnel current ratios,⁴ resonant tunneling of holes,⁵ the observation of multiple negative differential resistance (NDR) peaks due to resonant tunneling⁶ and the observation of sequential resonant tunneling through a multiquantum well superlattice.⁷

Until now, investigation of this structure in the GaAs/AlGaAs system has been limited to quantum well confinement barriers that have a constant Al mole fraction. There exist a number of intriguing structures that can be fabricated with barriers that are tailored in real space. However, there exist practical constraints on the rate in which the Al mole fraction (i.e., the height of the barrier with respect to the GaAs conduction band) can be changed, thus limiting the structures that can be investigated. To solve the Al mole fraction gradient constraint, we have investigated the possibility of replacing the AlGaAs alloy barrier with a superlattice of fixed Al mole fraction. Thus, tailoring of the barrier height

reduces to a simpler problem of dimensional control of the superlattice layers.

We present the first study of such a heterostructure utilizing superlattice barriers, in this case binary superlattices. It should be pointed out that the additional degree of freedom of an Al mole gradient in a superlattice barrier structure adds tremendous superlattice miniband tailoring possibilities. This report is the first demonstration that a quantum well state can be created in the single quantum well structure with superlattices, and that confinement can be achieved with thin superlattices. Though quantum well confinement by superlattices has been previously investigated by photoluminescence,⁸ the superlattices were much thicker, had a longer period, and was investigated in a multiple quantum well structure.

The samples used in this study were grown by molecular beam epitaxy in a Riber MBE-2300 on a 2-inch (100) n^+ Si-doped Sumitomo GaAs substrate. The substrate was directly heated in a rotating substrate holder. Following a highly doped (n -type, Si @ $\sim 1 \times 10^{18} \text{ cm}^{-3}$) buffer layer, the active resonant tunneling structure region was then grown. For the alloy barrier structure, the undoped $\text{Al}_x\text{Ga}_{1-x}\text{As}$ barrier (50Å, $x = .35$), undoped GaAs quantum well, and similar $\text{Al}_x\text{Ga}_{1-x}\text{As}$ barrier were then grown, followed by a similar top contact ~ 0.5 micron thick. For the superlattice barrier structure, the same procedure was used, replacing the superlattices for the alloy

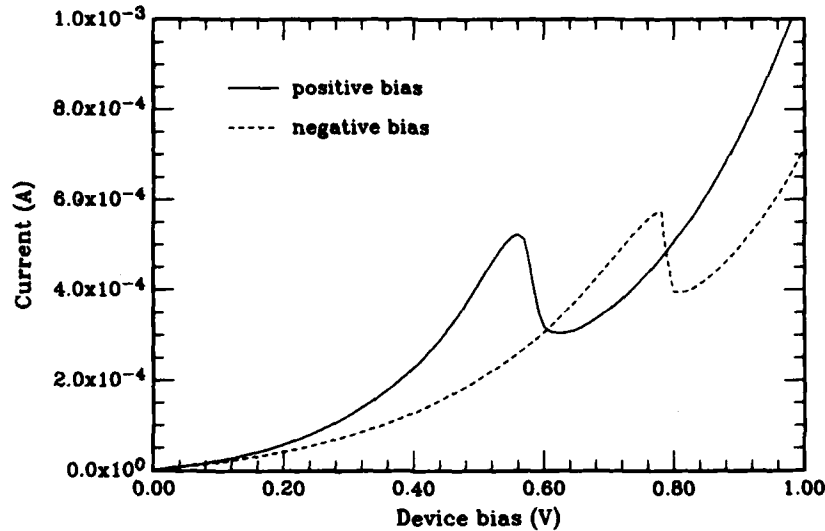


Figure 1. Current - voltage characteristics of a 50 Å GaAs quantum well / 50 Å Al_{0.35}Ga_{0.65}As double barrier heterostructure. The device mesa area =

25 μm² and T = 300°K. Both positive and negative bias are shown for comparison. The asymmetry around zero bias is evident.

barriers. Devices were fabricated by defining mesas on the surface with conventional photolithography and microfabrication techniques, bonded for mechanical stability, and inserted into a variable temperature cryostat for measurements in the range 1.2°K to 300°K.

Figure 1 shows the static current-voltage (I-V) characteristics of a typical conventional alloy barrier, 50Å wide quantum well resonant tunneling structure at 300°K. The structure exhibits a peak to valley tunnel current ratio of 1.75:1 (which increases typically to 7:1 at T > 100°K). For comparison purposes, the negative bias data has been reflected into the first quadrant. There exists a noticeable asymmetry in the electrical characteristics about zero bias. This asymmetry has been attributed to the inverted interface morphology of the quantum well and contact region.⁴ This is consistent with our observations; positive bias implies electron injection from the superior backside GaAs contact. However, it is also possible to ascribe this asymmetry to dopant redistribution at the contacts due to the difference in diffusion times for the top and bottom contacts.

A superlattice barrier structure was fabricated and a cross-sectional TEM is shown in Figure 2. For this structure, each barrier consists of three 7Å layers of AlAs and two 7Å layers of GaAs. The GaAs quantum well width is 45Å. Figure 3 shows the static current-voltage (I-V) characteristics of this structure at 300°K. The structure exhibits a peak to valley tunnel current ratio of 1.8:1. The symmetry for positive and negative bias is excellent. This implies that the inverted interface is indeed responsible for the observed asymmetry. The possibility of dopant diffusion through the structure has been eliminated by observing that, with the application of intense broadband light

there is negligible peak shift due to the effect of DX centers in the barriers.

The observed resonant bias positions can be compared with the theoretical predictions of a transfer matrix model⁹ if the effects of the parasitic series resistances can be eliminated. However, there exists an unambiguous method to determine the energetic position of the quantum well state relative to the Fermi level of the contacts. Applying the technique of low bias thermal activation¹⁰ to the double barrier structure, we see that the effective barrier height presented to the contact electrons is not the entire barrier but the nearby Γ -point of the quantum well state. This was applied to the 50Å quantum well alloy barrier structure and is shown in Figure 4. This method gave an activation energy of 70 meV, which is in excellent agreement with a calculated value of 116 meV when adjusted for the energy of the Fermi level, approximately 50 meV.

The thermal activation analysis of the superlattice barrier structure is shown in Figure 5 for two different device mesa sizes. This gives a quantum well state of 121 meV. Using this energy to determine the energy of the effective barrier height ΔE_c^* , assuming equal barriers and that the envelope function approximation for thick barriers is valid, we obtain a ΔE_c^* of 290 meV. This was checked against comparing the transmitted resonant tunneling current densities of the superlattice barrier structure to the conventional alloy barrier structure. This gave a ΔE_c^* of 240 meV. A monolayer fluctuation of the GaAs quantum well gave 275 meV, in good agreement with the envelope function approximation.

The superlattice barrier height is much lower than one would expect from a naive averaged alloy composition of 0.60, which gives a barrier



Figure 2. Cross-sectional TEM of the binary superlattice barrier resonant tunneling structure. The width of the quantum well is 45 Å and the widths of the two GaAs and three AlAs superlattice barrier components are 7 Å. I-V characteristic of a 100 Å quantum well resonant

tunneling device at 77°K. The peak at 150 mV is due to resonant tunneling through the ground state of the quantum well, and the peak at 1.45 V is due to resonant tunneling through the first excited state of the quantum well.

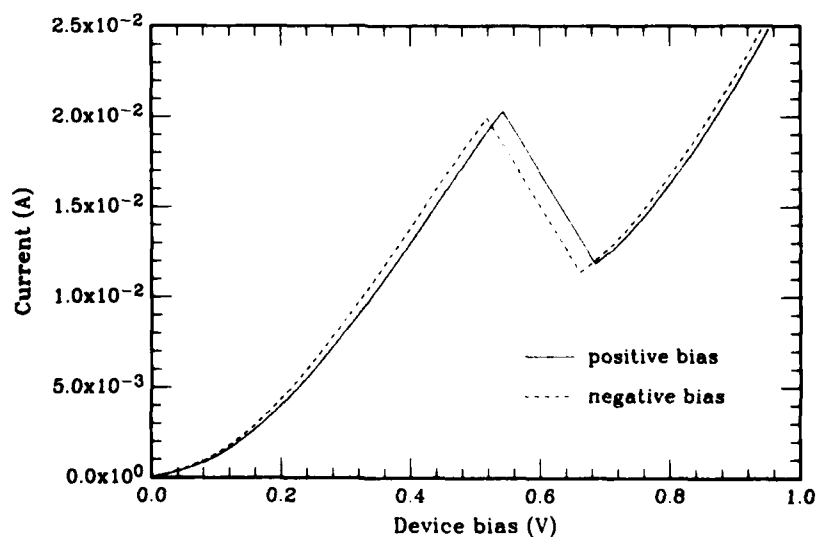


Figure 3. Current - voltage characteristics of the superlattice double barrier heterostructure. The device mesa area = 25 μm^2 and $T = 300^\circ\text{K}$. Both

positive and negative bias are shown for comparison. The symmetry around zero bias is excellent.

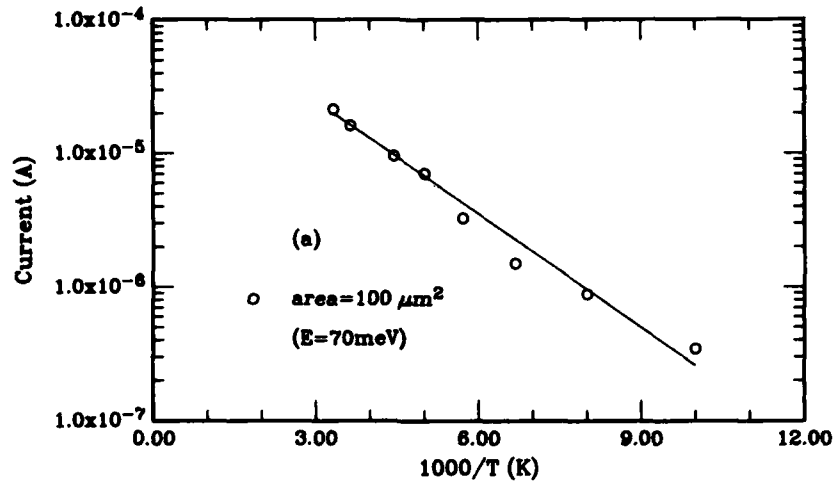


Figure 4. Low bias thermally activated current for the 50 Å alloy barrier structure. The device

mesa area = 100 μm^2 . The results are in excellent agreement with theory.

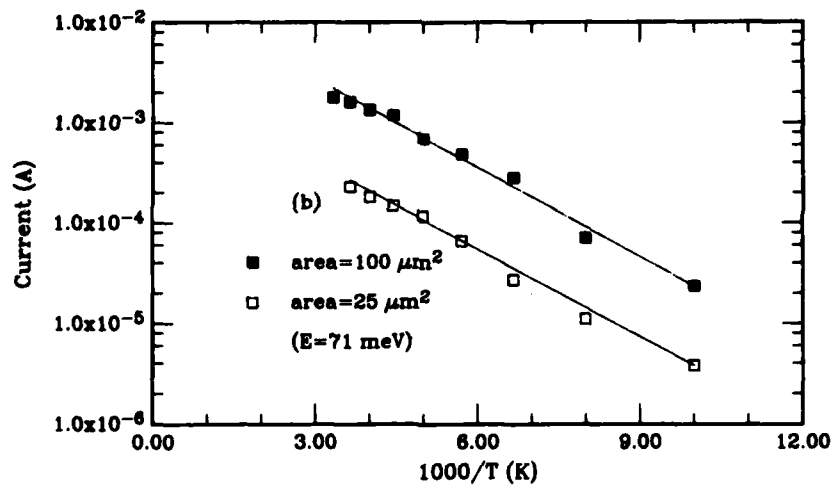


Figure 5. Low bias thermally activated current for the superlattice barrier structure. The device

mesa areas = 25 μm^2 and 100 μm^2 . The activation energy = 71 meV.

height of 587 meV. The observed barrier height of 290 meV is equivalent to an averaged alloy composition of 0.30. An envelope function approximation to a superlattice of infinite extent gives 677 meV for the conduction miniband edge. Thus, the superlattice barrier structure exhibits an anomalously low barrier height. The observation of an anomalously low barrier height is indicative of an enhanced evanescent tail.

We have also investigated a structure that has an asymmetric superlattice barrier construction. Figure 6 shows a cross-sectional TEM of the asymmetric binary superlattice barrier resonant tunneling structure. The 5 component superlattice barrier is the same as in the structure

discussed previously, but the "asymmetric" barrier has 7 Å AlAs component, a 7 Å GaAs component, and a 15 Å AlAs component. The width of the quantum well is 45 Å. This structure is intriguing since the effective barrier, going from the quantum well to the GaAs contact, slopes "up" with respect to the conduction band of the GaAs contact. This implies that (1) the I-V should be asymmetric; (2) the resonance should have a smaller peak to valley ratio going from the asymmetric barrier to the symmetric barrier than in the reverse direction.⁹

Figure 7 shows a static I-V measurement of the asymmetric resonant tunneling structure at 300°K. Positive bias corresponds to electron



Figure 6. Cross-sectional TEM of the asymmetric binary superlattice barrier resonant tunneling structure. The width of the quantum well is 45 Å. The 5 component superlattice barrier has two

GaAs and three AlAs components of 7 Å each, and the asymmetric barrier has a 7 Å AlAs component, a 7 Å GaAs component, and a 15 Å AlAs component.

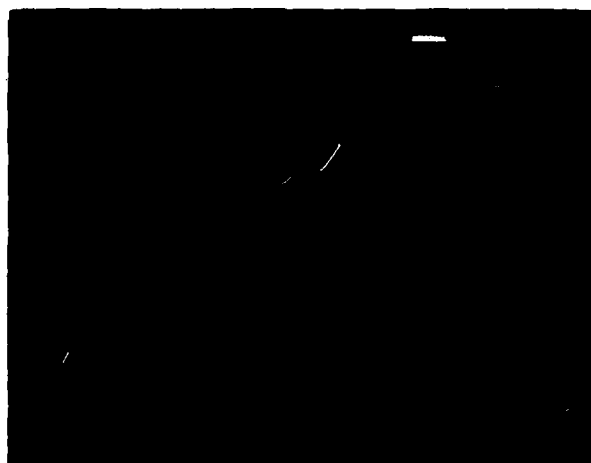


Figure 7. Current - voltage characteristics of the asymmetric superlattice resonant tunneling structure. The device mesa area = $100 \mu\text{m}^2$ and $T = 300^\circ\text{K}$. Positive bias corresponds to electron injection first through the "asymmetric" barrier.

injection first through the "asymmetric" barrier. There exists negligible voltage difference in the peak positions, implying that the weighted barrier height at resonance is approximately the

same for both barriers. However, the peak to valley is quite different for the different bias directions. This observation supports the view that the observed negative differential resistance is due to resonant enhancement ("coherent" resonant tunneling) in the structure versus the recently proposed¹¹ model of sequential resonant tunneling.

In summary, we have investigated resonant tunneling in structures where the normal alloy barriers have been replaced by superlattices. The structures do not exhibit the asymmetry in the electrical characteristics seen in the alloy barrier structures, and have an anomalously low barrier height. An asymmetric superlattice structure exhibited different peak to valley ratios in opposite bias configurations, supporting the view that resonant enhancement does occur in double barrier structures.

Acknowledgement - I am indebted to H.-L. Tsai for the cross-sectional TEM micrographs, to R.T. Bate and W.R. Frensley for helpful discussions and critical evaluation, and R.K. Aldert, R. Thomason, and J. Williams for technical assistance. This work was supported in part by ARO and ONR.

REFERENCES

1. L. L. Chang, L. Esaki, and R. Tsu, *Applied Physics Letters* **24**, 593 (1974).
2. T. C. L. G. Sollner, W. D. Goodhue, P. E. Tannenwald, C.D. Parker, and D. D. Peck, *Applied Physics Letters* **43**, 588 (1983).
3. A. R. Bonnefoi, R. T. Collins, T. C. McGill, R. D. Burnham, and F. A. Ponce, *Applied Physics Letters* **46**, 285 (1985).
4. T. J. Shewchuk, P. C. Chapin, P. D. Coleman, W. Kopp, R. Fisher, and H. Morkoç, *Applied Physics Letters* **46**, 508 (1985).
5. E. E. Mendez, W. I. Wang, B. Ricco, and L. Esaki, *Applied Physics Letters* **47**, 415 (1985).
6. M. A. Reed, *Superlattices and Microstructures* **2**, 65 (1986).
7. F. Capasso, K. Mohammed, and A. Y. Cho, *Applied Physics Letters* **48**, 478 (1986).
8. H. Sakaki, M. Tsuchiya, and J. Yoshino, *Applied Physics Letters* **47**, 295 (1985).
9. B. Ricco and M. Ya. Azbel, *Physical Review* **29B**, 1970 (1984).
10. A. C. Gossard, W. Brown, C. L. Allyn, and W. Weigmann, *Journal of Vacuum Science and Technology* **20**, 694 (1982).
11. S. Luryi, *Applied Physics Letters* **47**, 490 (1985).

APPENDIX K

RESONANT TUNNELING IN DOUBLE
BARRIER HETEROSTRUCTURES

Resonant tunneling in double barrier heterostructures

M. A. Reed, R. T. Bate, and J. W. Lee (a)

Central Research Laboratory
Texas Instruments Incorporated
Dallas, TX 75265

Abstract

Resonant tunneling in a variety of double barrier, single quantum well heterostructures has been investigated. Negative differential resistance has been observed by tunneling through both the ground and first excited quasistationary states of the quantum well. The peak positions agree well with a 65% conduction band offset. The tunnel barriers have been replaced by short period binary superlattices, where an anomalously low barrier height is observed. Resonant tunneling through a GaAs contact / double AlGaAs barrier / single InGaAs quantum well heterostructure has also been observed, where we have demonstrated tunneling through the first excited state above a "hidden" ground state of the quantum well. Finally, we have observed resonant tunneling through a double barrier, single quantum well HgTe/Hg_{1-x}Cd_xTe heterostructure where a peak-to-valley tunnel current ratio of 1.4:1 is observed at room temperature. This observation provides direct evidence for the existence of the proposed intrinsic interface state model.

Introduction

The phenomena of resonant tunneling in double barrier heterostructures, first investigated in the seminal work of Chang, Esaki, and Tsu,¹ has recently undergone a renaissance²⁻⁴ due to recent improvements in epitaxial growth techniques. In these devices, the essential carrier transport mechanism is electron (or hole) tunneling, specifically through ultrathin (approximately 50Å) Al_xGa_{1-x}As tunnel barriers and a GaAs quantum well. The DC and high frequency transport in these structures has been the subject of intense investigation following the remarkable submillimeter wave experiments of Sollner et al,² which has been interpreted as coherent resonant tunneling through the heterostructure. This renewed interest has led to the observation of large room temperature peak to valley tunnel current ratios,⁴ resonant tunneling of holes,⁵ the observation of multiple negative differential resistance (NDR) peaks due to resonant tunneling⁶ and the observation of sequential resonant tunneling through a multi-quantum well (MQW) superlattice.⁷

The prototype resonant tunneling structure is a one-dimensional, double barrier, single quantum well heterostructure, as shown in Figure 1(a). The center quantum well has a spectrum of discrete allowed eigenstates, higher in energy relative to the contact conduction band edge. At low device bias, the quasistationary state (band) in the central quantum well is too high in energy to allow resonant tunneling of electrons through the eigenstate. Tunneling through the entire structure is allowed, but is exponentially small. As the device bias increases, the quantum well state is lowered with respect to the Fermi level of the input contact, and carriers are allowed to tunnel through the quasistationary state in the quantum well (Figure 1(b)). When the device bias is increased to the point that the allowed state in the quantum well is lower in energy than the conduction band edge of the input contact (Figure 1(c)), elastic tunneling is no longer allowed due to the conflicting requirements of energy and momentum conservation. This decreases the tunneling current, producing negative differential resistance (Figure 1(d)). Higher energy eigenstates will produce the same phenomena as they are biased to the Fermi level.

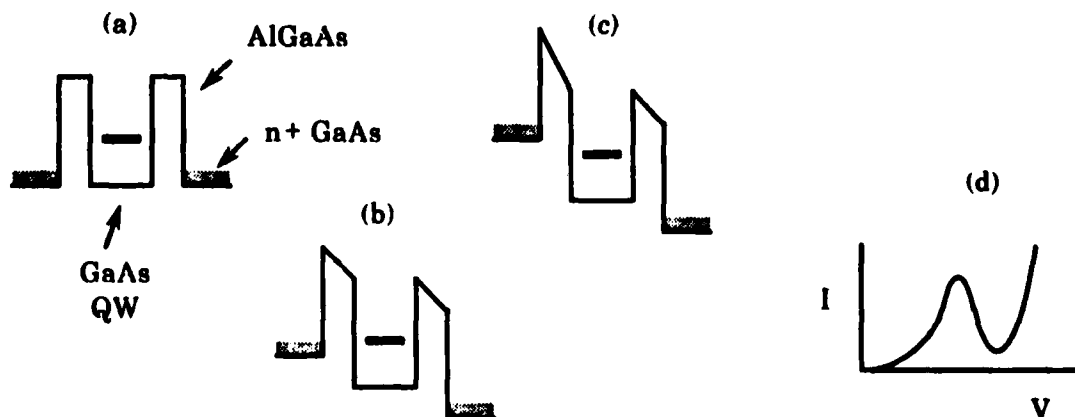


Figure 1. Conduction band diagram in real space of a resonant tunneling structure (a) at zero applied bias, (b) at resonant bias, and (c) at greater than resonant bias. (d) Schematic I-V characteristic.

Though this phenomenon has been explored for some time, the types of structures in which resonant tunneling has been observed have been surprisingly limited and unimaginative. Intriguing structures with barriers tailored in real space, devices utilizing multiple NDR regions (such as frequency multipliers, multistate memories, and high speed analog-to-digital converters), and multicomponent material systems are now possible with existing epitaxial capability. Here we present recent progress in these areas.

Experimental results: alloy barriers

The GaAs samples used in this study were grown by molecular beam epitaxy in a Riber MBE-2300 on a 2-inch (100) n^+ Si-doped Sumitomo GaAs substrate utilizing a directly heated rotating substrate holder. Following a highly doped (n -type, Si $\approx 1 \times 10^{18} \text{ cm}^{-3}$) buffer layer approximately 0.5 micron thick, the active resonant tunneling structure region was then grown. Prior to the growth of the tunnel barrier, the Si doping level was reduced to $1 \times 10^{16} \text{ cm}^{-3}$ and a thin spacer of 25Å of GaAs inserted. The double barrier structure was then grown. The structure, unless otherwise noted, was nominally grown to have inversion symmetry through a plane in the center of and parallel to the quantum well.

Conventional $\text{Al}_x\text{Ga}_{1-x}\text{As}$ alloy barrier structures with 50Å barriers and varying quantum well dimensions were fabricated. A cross-sectional transmission electron micrograph of a structure with a 50Å GaAs quantum well is shown in Figure 2. Devices, ranging from 2 - 225 micron square, were fabricated by defining mesas on the surface with conventional photolithography techniques. Ohmic contacts covered the top surface of the mesa and were made by evaporating Au-Ge, Ni, then Au, followed by an anneal. For devices too small to accommodate a direct bond, a silicon nitride layer (for isolation) was deposited over the sample, followed by a Au evaporated bonding pad. The samples were inserted into a variable-temperature helium-flow Janis cryostat or into a stabilized oven for variable temperature measurements. Figure 3 shows the static current-voltage (I-V) characteristics of this structure at 4.2K, 77K, and 300K. The structure exhibits a peak to valley tunnel current ratio of 1.75:1, which increases typically to 7:1 at T less than 100K.

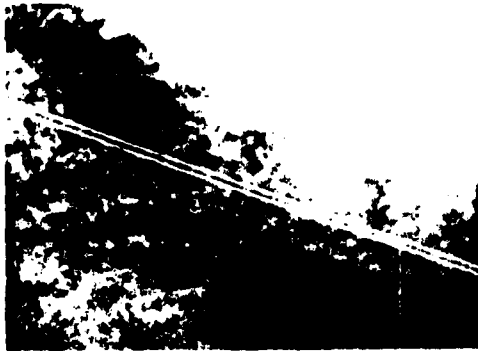


Figure 2. Cross-sectional TEM of a GaAs/AlGaAs resonant tunneling structure.

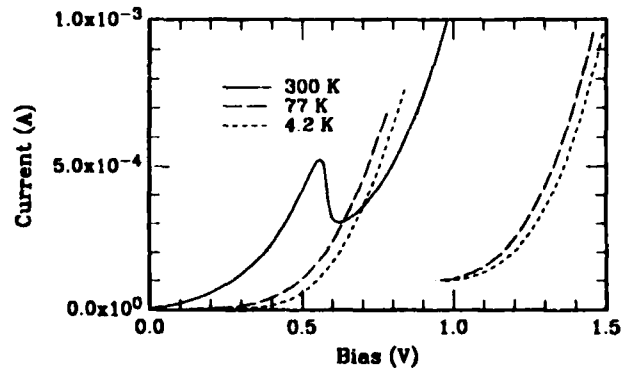


Figure 3. I-V characteristics of the resonant tunneling structure in Figure 2. Mesa area = 25 microns square.

Measurements were performed on similar devices for the 100Å quantum well MBE sample. Static I-V characteristics at 77 K are shown in Figure 4 and clearly show two resonant peaks. The lower voltage peak, on an expanded scale (Figure 4(a)), can be identified with resonant tunneling through the ground state of the quantum well, and the higher voltage peak (Figure 4(b)) resonant tunneling through the first excited state. The peak-to-valley ratio degraded as the temperature was increased to 300K. The NDR due to the ground state typically disappeared at 275K, while the excited state typically exhibited a 7% NDR at 300K.

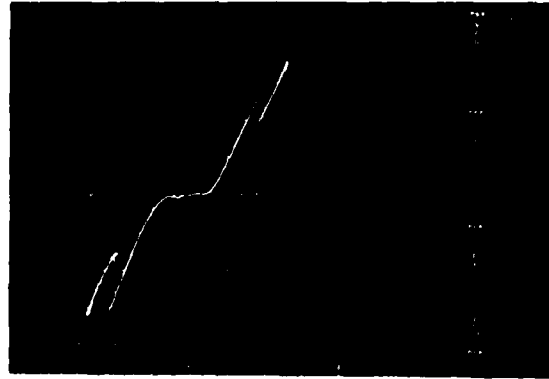


Figure 4. Resonant tunneling through (a) the ground state and (b) the excited state of a 100Å GaAs quantum well at 77K. The aluminum content in the AlGaAs barriers is 30%.

The theoretical positions of the resonant peaks for the 100Å well were derived using a transfer-matrix technique.⁸ In terms of device bias voltage, the resonant positions are 83 mV for the ground state and 0.35 V for the first excited state. The experimental results are in excellent agreement with theory when the series parasitic resistance of 40 ohms, due mostly to the measurement apparatus, is taken into account. This resistance also explains the apparent "hysteresis" of the excited state peak, which is due to the resonant tunneling diode - parasitic resistor series combination. This apparent hysteresis will appear whenever the value of the series resistance is less than the absolute magnitude of the negative resistance produced by resonant tunneling.

Experimental results: superlattice barriers

Until now, investigation of this structure in the GaAs/AlGaAs system has been limited to quantum well confinement barriers that have a constant Al mole fraction. There exist a number of intriguing structures that can be investigated with tailored barriers. However, there exist practical constraints on the rate at which the Al mole fraction (i.e., the height of the barrier with respect to the GaAs conduction band) can be changed, thus limiting the structures that can be investigated. To solve the Al mole fraction gradient constraint, we have investigated the possibility of replacing the AlGaAs alloy barrier with a superlattice of fixed Al mole fraction. Thus, tailoring of the barrier height reduces to a simpler problem of dimensional control of the superlattice layers.

A superlattice barrier structure was fabricated and a cross-sectional TEM is shown in Figure 5. For this structure, each barrier consists of three 7Å layers of AlAs and two 7Å layers of GaAs. The GaAs quantum well width is 45Å. Figure 6 shows the static current-voltage (I-V) characteristics of this structure at 300 K. The structure exhibits a peak-to-valley tunnel current ratio of 1.8:1. For comparison purposes, the negative bias data has been reflected into the first quadrant. The symmetry for positive and negative bias is excellent, unlike the alloy barrier structures where there exists a noticeable asymmetry in the electrical characteristics about zero bias. This asymmetry has been attributed to the inverted interface morphology of the quantum well and contact region.⁴ However, it is also possible to ascribe this asymmetry to dopant redistribution at the contacts due to the difference in diffusion times for the top and bottom contacts. The present result implies that the inverted interface is indeed responsible for the observed asymmetry. The possibility of dopant diffusion through the structure has been eliminated by observing that, with the application of intense broadband light there is negligible peak shift due to the effect of DX centers in the barriers.



Figure 5. Cross-sectional TEM of a GaAs/AlAs resonant tunneling superlattice barrier structure.

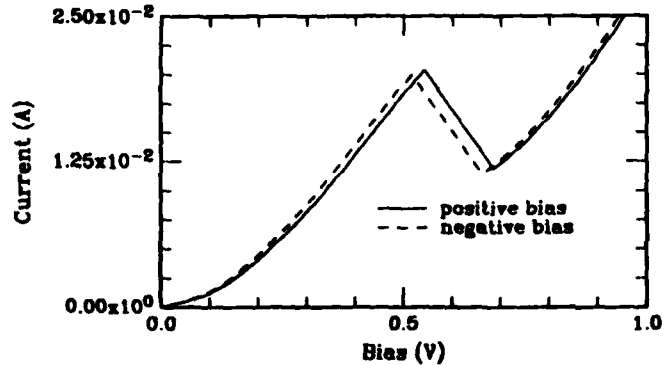


Figure 6. I-V characteristics of the superlattice barrier structure at 300K. Mesa area = 25 microns square.

The observed resonant bias positions can be compared with the theoretical predictions of a transfer matrix model⁸ if the effects of the parasitic series resistances can be eliminated. However, there exists an unambiguous method to determine the energetic position of the quantum well state relative to the Fermi level of the contacts. Applying the technique of low bias thermal activation⁹ to the double barrier structure, we see that the effective barrier height presented to the contact electrons is not the entire barrier but the nearby point of the quantum well state. This was applied to the 50Å quantum well alloy barrier structure and is shown in Figure 7. This method gave an activation energy of 70 meV, which is in excellent agreement with a calculated value of 116 meV when adjusted for the energy of the Fermi level, approximately 50 meV. Measurements on the 100Å GaAs quantum well sample also gave good agreement. It is interesting to note that, for the 100Å quantum well, only the ground state is observed with thermal activation due to the large energetic separation of the excited state.

The thermal activation analysis of the superlattice barrier structure is shown in Figure 8 for two different device mesa sizes. This gives a quantum well state of 121 meV. Using this energy to determine the energy of the effective barrier height E_C , assuming equal barriers and that the envelope function approximation for thick barriers is valid, we obtain a E_C of 290 meV. This was checked against comparing the transmitted resonant tunneling current densities¹⁰ of the superlattice barrier structure to the conventional alloy barrier structure. This gave a E_C of 240 meV. A monolayer fluctuation of the GaAs quantum well gave 275 meV, in good agreement with the envelope function approximation.

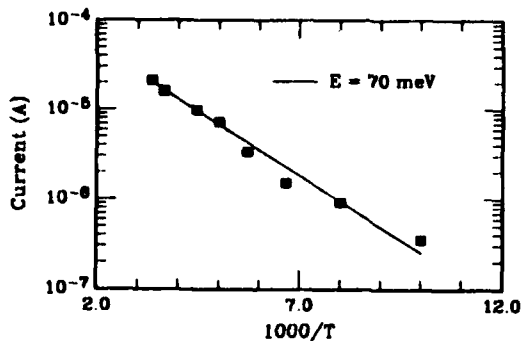


Figure 7. Low bias thermally activated current for the alloy barrier structure.

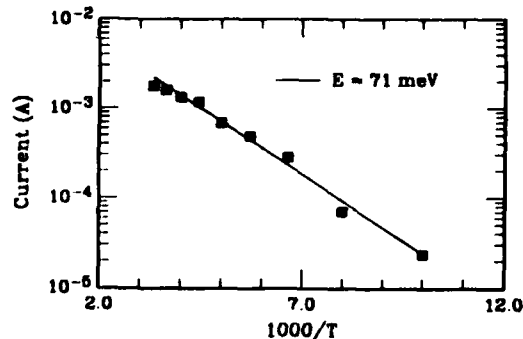


Figure 8. Low bias thermally activated current for the superlattice barrier structure.

The superlattice barrier height is much lower than one would expect from a naive averaged alloy composition of 0.60, which gives a barrier height of 587 meV. The observed barrier height of 290 meV is equivalent to an averaged alloy composition of 0.30. An envelope function approximation to a superlattice of infinite extent gives 677 meV for the conduction miniband edge. Thus, the superlattice barrier structure exhibits an anomalously low barrier height. The observation of an anomalously low barrier height is indicative of an enhanced evanescent tail.

We have also investigated a structure that has an asymmetric superlattice barrier construction. Figure 9 shows a cross-sectional TEM of the asymmetric binary superlattice barrier resonant tunneling structure. The 5 component superlattice barrier is the same as in the structure discussed previously, but the "asymmetric" barrier has a 7Å AlAs component, a 7Å GaAs component, and a 15Å AlAs component. The width of the quantum well is 45Å. This structure is intriguing since the effective barrier, going from the quantum well to the GaAs contact, slopes "up" with respect to the conduction band of the GaAs contact. This implies that (1) the I-V should be asymmetric; (2) the resonance should have a smaller peak to valley ratio going from the asymmetric barrier to the symmetric barrier than in the reverse direction.⁸

Figure 10 shows a static I-V measurement of the asymmetric resonant tunneling structure at 300 K. Positive bias corresponds to electron injection first through the "asymmetric" barrier. There exists negligible voltage difference in the peak positions, implying that the weighted barrier height at resonance is approximately the same for both barriers. However, the peak to valley ratio is quite different for the different bias directions. This observation qualitatively supports the view that the observed negative differential resistance is at least partially due to resonant enhancement ("coherent" resonant tunneling) in the structure versus the recently proposed¹¹ model of sequential ("incoherent") resonant tunneling.



Figure 9. Cross-sectional TEM of a GaAs/AlAs asymmetric superlattice barrier structure.



Figure 10. I-V characteristics of the asymmetric superlattice barrier structure at 300K. Mesa area = 25 microns square.

Experimental results: deep quantum wells

The ability to lower quantum well states with respect to GaAs contact layers (due to the higher electron affinity of InGaAs with respect to GaAs) is an important degree of freedom in tunneling device design. A previous investigation¹² of tunneling in a strained-layer heterostructure system exhibited catastrophic degradation upon thermal cycling. The high temperature performance and stability of these strained layer quantum well structures will be an important area of investigation.

The conduction band diagram of the resonant tunneling structure, at zero and applied resonant bias, is illustrated in Figure 11. The structure consists of two undoped $\text{Al}_{0.25}\text{Ga}_{0.75}\text{As}$ barriers on either side of an undoped $\text{In}_{0.2}\text{Ga}_{0.8}\text{As}$ quantum well. Cross sectional transmission electron microscopy of this structure revealed AlGaAs barrier thicknesses of 40Å and an InGaAs quantum well thickness of 60Å (both plus/minus 10Å). No misfit dislocations were found during an extensive search of the quantum well structure.

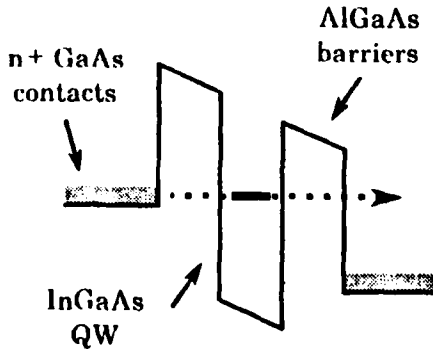


Figure 11. Schematic conduction band diagram in real space of the InGaAs quantum well resonant tunneling structure.

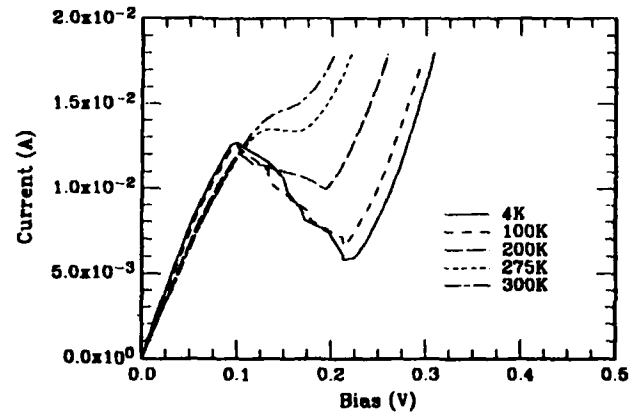


Figure 12. I-V characteristics of the InGaAs quantum well resonant tunneling structure at various temperatures.

Figure 12 shows the temperature variation of the static current-voltage characteristics of a typical device. The structure exhibits a 2.6:1 peak-to-valley ratio at low temperatures, which starts to degrade at approximately 100 K, the same temperature at which conventional $\text{GaAs}/\text{AlGaAs}$ alloy barrier structures also start to exhibit a degradation. Negative resistance persists up to 275 K, and to 300 K in a small number of devices. The absence of peak shift with temperature indicates the absence of any parasitic contact resistance. These devices were cycled repeatedly to low temperatures and did not show any thermal degradation as was noted in a similar strained layer structure.

The expected resonant peak position was calculated by using a transfer matrix method⁹ and is shown in Figure 13 as a function of In fraction in the InGaAs quantum well. Two parameters which have a degree of uncertainty are the quantum well thickness (due to the attainable resolution of the cross section micrograph) and the conduction band offset of the $\text{AlGaAs}/\text{InGaAs}$ heterointerfaces: these are treated as free parameters. We have used effective masses linearly extrapolated between the pure binary effective masses, a composition of 0.25 for the Al content and a 65% conduction band offset for the $\text{GaAs}/\text{AlGaAs}$ heterojunctions. The error bars on the observed peak position in the figure indicate the width of the experimental resonant peak (for all temperatures) and the uncertainty in the In fraction obtained from growth data.

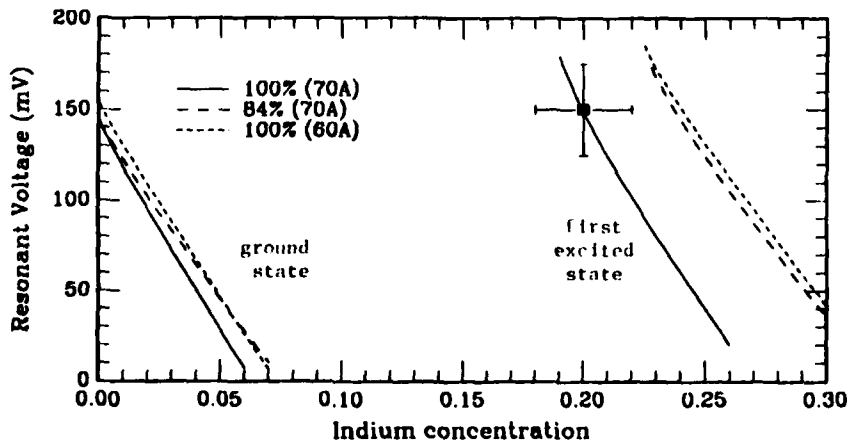


Figure 13. Calculated resonant tunneling peak voltage versus In fraction for the double barrier structure. Plotted are the voltage positions for tunneling through the ground and first excited state (labeled) for quantum well sizes of 60Å and 70Å (in parenthesis), with $\text{AlGaAs}/\text{InGaAs}$ conduction band offsets of 84% and 100%. The data point is the observed peak position, with the error bars denoting the experimental width of the resonance and the uncertainty in In fraction.

The calculated peak positions have two sets of curves for a given set of parameters (AlGaAs/InGaAs conduction band offset and quantum well width); the set at low In fraction corresponds to resonant tunneling through the ground state of the quantum well, whereas the high In fraction set corresponds to resonant tunneling through the first excited state of the quantum well. Clearly the observed peak is due to resonant tunneling through the first excited state. Additionally, it can be seen that the fit to a 60 Å well (labeled "100% (60Å)") is bad for any value of the conduction band offset for the AlGaAs/InGaAs heterojunction (given in terms of the percentage of the band gap difference that occurs in the conduction band). Using the maximum uncertainty in the well width (which gives 70 Å), we have plotted the fits for 100% conduction band offset and 84% conduction band offset (which had previously been measured in a GaAs/InGaAs heterojunction¹³). The observed peak position is quite bad for the 84% conduction band offset, but is in excellent agreement with a maximum conduction band offset of 100%. These measurements imply a InGaAs/AlGaAs conduction band offset very close to 100% of the bandgap difference.

Experimental results: HgCdTe

The recent achievement of epitaxial superlattices in the HgTe/CdTe system^{14,15} has led to the speculation that resonant tunneling can be observed in this system.¹⁶ However the basic physics of resonant tunneling in the HgTe/CdTe system is distinctly different from the now familiar GaAs/AlGaAs system. Although CdTe (or the alloy HgCdTe for sufficiently small Hg concentration) has a normal Γ_6 conduction band and Γ_8 degenerate light and heavy hole band structure, HgTe has a symmetry-induced inverted band structure with the Γ_8 conduction band and the Γ_6 heavy hole valence bands degenerate at the zone center, producing a zero-gap semimetal. The Γ_6 light hole band lies 0.3 eV below the Γ_8 edges due to relativistic corrections. Thus, the conduction and light hole valence bands have inverted symmetries. Since the light Γ_6 mass changes sign across the heterojunction, and since the valence band offset is conjectured to be small relative to the CdTe bandgap and negative with respect to the HgTe heavy hole valence band,^{17,18} an intrinsic interface state has been proposed to form.¹⁹ The observation of resonant tunneling in this system would provide important experimental evidence for the verification of the interface state model.

The epitaxial HgTe/Hg_{1-x}Cd_xTe double barrier structure studied was grown by molecular beam epitaxy on a CdTe (112) Te substrate. The CdTe surface was prepared for deposition with a 0.5% Br₂-methanol static etch for 30 seconds followed by a 10 minute anneal in vacuum at 275-300°C to remove any excess tellurium. A 0.40 micron CdTe buffer layer was then deposited using a CdTe effusion cell at 1.1 Å/sec. with the substrate temperature near 275°C. To assure a uniform Hg vacancy concentration, the composition modulation in the double barrier structure was achieved by alternating the Te and CdTe cell shutters with a fixed open Hg cell shutter. The double barrier structure was deposited at a substrate temperature of 180°C with a HgTe growth rate of 4.70 Å/sec. and a Hg_{1-x}Cd_xTe barrier layer growth rate of 0.63 Å/sec.

An epitaxial HgTe layer was also grown under nominally identical conditions as in the double barrier structure and exhibited an electron carrier density of $4.7 \times 10^{17} \text{ cm}^{-3}$ and a carrier mobility of $2.75 \times 10^4 \text{ cm}^2 \text{ V}^{-1} \text{ s}^{-1}$ at 300K by low field Hall measurements. Similarly, an epitaxial CdTe layer was grown in the presence of a Hg flux under nominally identical conditions as in the double barrier structure and exhibited an electron carrier density of $9.3 \times 10^{12} \text{ cm}^{-3}$ and a carrier mobility of $2.5 \times 10^3 \text{ cm}^2 \text{ V}^{-1} \text{ s}^{-1}$ at 300K. Electron microprobe measurements (5-10 kV) indicated the film had incorporated approximately 20% HgTe. None of the epilayers were intentionally doped. The 10 kV reflection high energy electron diffraction patterns with sharp streaks and intense Kikuchi bands for all the layers were indicative of high-quality single crystal growth.

Figure 14 illustrates the layers for the double barrier structure. Following the CdTe buffer layer growth, the bottom contact of 1.01 micron HgTe was deposited. The double barrier structure followed, consisting of 43 Å Hg₂Cd₈Te barriers and a 71 Å HgTe quantum well. The top contact, identical to the bottom contact, was then grown, followed by a 380 Å Hg₂Cd₈Te protective capping layer.

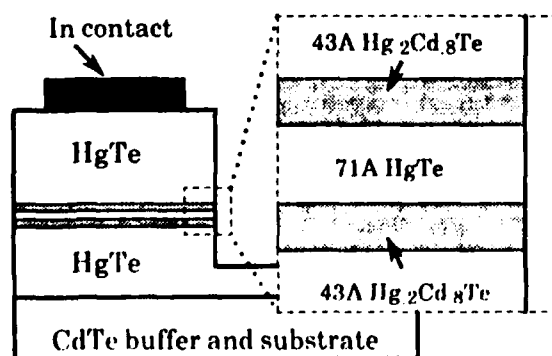


Figure 14. Cross-sectional schematic of the HgTe/HgCdTe heterostructure. Top mesa and backside indium contacts are diagrammed. A 380 Å Hg₂Cd₈Te protective cap was removed prior to device fabrication.

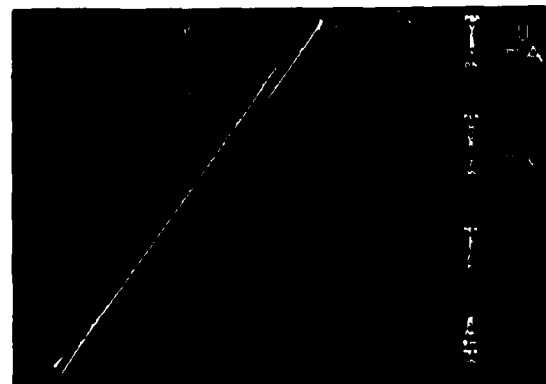


Figure 15.(a) Static I-V characteristics of the HgTe/HgCdTe heterostructure at room temperature. Mesa area = 50 square microns. Positive bias corresponds to the top mesa contact positive with respect to the backside contact.

Mesa devices of various mesa size were fabricated by first removing the protective cap layer and then evaporating an In alloy onto the ion-milled HgTe surface to define Ohmic top contacts. Following a photoresist protection of the In contacts, the mesas were created by etching the structure in a 1/8 % Br - methanol solution until the double barrier structure is isolated. The electrical isolation of mesas was verified by noting a increase in resistance between mesas after the etch due to removal of the (shorting) top conductive layer between topside In contacts. Backside contact was defined by an identical In evaporation onto the etched HgTe surface.

Static current-voltage (I-V) characteristics of the mesa structures were measured at room temperature in conventional swept voltage mode. The room temperature I-V characteristics of a device with mesa area 50 micron square is shown in Figure 15. Positive bias corresponds to the top mesa contact positive with respect to the backside contact. The structure exhibits a 1.4:1 peak to valley tunnel current ratio, a resonant voltage of 440 meV, an asymmetry of the resonant positions about zero bias, and a current density at resonance of 1.5×10^3 A-cm⁻². More than 25 similar devices over a 4 mm x 7 mm area were sampled and all devices exhibited negative differential resistance. There was negligible variation in resonant peak position for the devices sampled, but the peak to valley characteristics varied from 1.1:1 to 1.4:1.

The apparent hysteresis in the I-V characteristic (i.e., multi-valued current at voltages around resonance) is the well known effect of the addition of a parasitic series resistance with a negative resistance device.²⁰ The resistance in the present case is due to the probe apparatus, independently measured to be 5 ohms. This gives a corrected (true) resonant voltage for the heterostructure of 240 mV. The resonant peak positions are in good agreement with the interface state calculations of Schulman and Anderson¹⁶ and clearly excludes the use of single band models using the CdTe (or HgCdTe) conduction band minimum, providing direct evidence for the existence of the proposed interface state. Figure 16 shows a calculation of the resonant peak positions for the single band model and the interface state model for different valence band offsets. The present experiment implies a zero valence band offset.

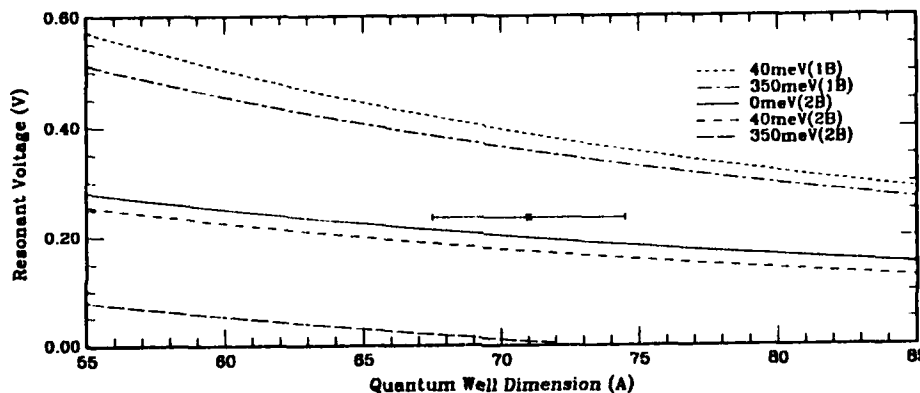


Figure 16. Calculated resonant tunneling peak voltage versus quantum well width for the HgTe/HgCdTe double barrier structure. The two sets of calculated peak positions are for a single band or interface state models, for various valence band offsets. The data point is the observed peak position, with the error bars denoting the experimental width of the cross-sectional TEM.

The demonstration of resonant tunneling in the HgTe/Hg_{1-x}Cd_xTe system makes possible a number of important investigations. A careful study of the resonant peak current densities and resonant voltages as a function of quantum well and barrier width can give an accurate determination of the valence band offset. Alternatively, moving the shifted Γ_6 valence band in the contact and quantum well layers by uniformly varying the Cd mole fraction not only gives the offset but allows the transition to a "GaAs-like" resonant tunneling structure for x greater than 0.16. The behavior of these structures around the transition ($x = 0.16$) value are sensitive probes of the Hg_{1-x}Cd_xTe heterojunction band structure.

Conclusion

In summary, we report a study of resonant tunneling in a variety of double barrier, single quantum well heterostructures. Tunneling through the ground and excited states of a GaAs/AlGaAs quantum well is observed and is consistent with a conduction band offset of 65%. We have shown that the tunnel barriers can be replaced by short period binary superlattices, which eliminates the asymmetry around zero bias in the electrical characteristics normally observed in the conventional Al_xGa_{1-x}As barrier structures. The performance of this symmetric superlattice structure is compared with an intentionally constructed asymmetric double barrier superlattice structure, which exhibits pronounced asymmetry in the electrical characteristics. The observed behavior supports the view that resonant enhancement occurs in the quantum well. Tunneling through a GaAs contact / double AlGaAs barrier / single InGaAs quantum well heterostructure has also been observed, where we have demonstrated tunneling through the first excited state above a "hidden" ground state of the quantum well. We have been able to fit the observed peak position for the AlGaAs/InGaAs heterojunction with a conduction band offset of nearly 100%. Finally, we have observed resonant tunneling through a double barrier, single quantum well HgTe/Hg_{1-x}Cd_xTe heterostructure where a peak-to-valley tunnel current ratio of 1.4:1 is observed at room temperature. The observed

resonant peak positions are in good agreement with the interface state calculations of Schulman and Anderson, which provides direct evidence for the existence of the proposed intrinsic interface state model.

Acknowledgments

We are thankful to W. R. Frensley, M. W. Goodwin, C. H. Hoel, M. A. Kinch, R. J. Koestner, H. Schaake, and H-L. Tsai for discussions and R. Aldert, P. Stickney, R. Thomason, and J. Williams for technical assistance. This work was supported in part by the Office of Naval Research and the U. S. Army Research Office.

References

- (a) Now at Kopin Corp., 695 Myles Standish Blvd., Taunton, MA 02780.
1. L. L. Chang, L. Esaki, and R. Tsu, "Resonant Tunneling in Semiconductor Double Barriers", Appl. Phys. Lett. **24**, 593 (1974).
 2. T. C. L. G. Solner, W. D. Goodhue, P. E. Tannenwald, C. D. Parker, and D. D. Peck, "Resonant Tunneling through Quantum Wells at Frequencies up to 2.5 THz", Appl. Phys. Lett. **43**, 588 (1983).
 3. A. R. Bonnefoi, R. T. Collins, T. C. McGill, R. D. Burnham, and F. A. Ponce, "Resonant Tunneling in GaAs/AlAs Heterostructures Grown by Metalorganic Chemical Vapor Deposition", Appl. Phys. Lett. **46**, 285 (1985).
 4. T. J. Shewchuk, P. C. Chapin, P. D. Coleman, W. Kopp, R. Fisher, and H. Morkoc, "Resonant Tunneling Oscillations in a GaAs-Al_xGa_{1-x}As Heterostructure at Room Temperature", Appl. Phys. Lett. **46**, 508 (1985).
 5. E. E. Mendez, W. I. Wang, B. Ricco, and L. Esaki, "Resonant Tunneling of Holes in AlAs-GaAs-AlAs Heterostructures", Appl. Phys. Lett. **47**, 415 (1985).
 6. M. A. Reed, "Excited State Resonant Tunneling in GaAs-Al_xGa_{1-x}As Double Barrier Heterostructures", Superlattices and Microstructures **2**, 65 (1986).
 7. F. Capasso, K. Mohammed, and A. Y. Cho, "Sequential Resonant Tunneling through a Multiquantum Well Superlattice", Appl. Phys. Lett. **48**, 478 (1986).
 8. B. Ricco and M. Ya Azbel, "Physics of Resonant Tunneling. The One-Dimensional Double-Barrier Case", Phys. Rev. **29B**, 1970 (1984).
 9. A. C. Gossard, W. Brown, C. L. Allyn, and W. Wiegmann, "Molecular Beam Epitaxial Growth and Electrical Transport of Graded Barriers for Nonlinear Current Conduction", J. Vac. Sci. Technol. **20**, 694 (1982).
 10. R. Tsu and L. Esaki, "Tunneling in a Finite Superlattice", Appl. Phys. Lett. **22**, 562 (1973).
 11. S. Luryi, "Frequency Limit of Double-Barrier Resonant-Tunneling Oscillators", Appl. Phys. Lett. **47**, 490 (1985).
 12. P. Gavrilovic, J. M. Brown, R. W. Kaliski, N. Holonyak and K. Hess, M. J. Ludowise, W. T. Dietze and C. R. Lewis, "Resonant Tunneling in a GaAs_{1-x}P_x - GaAs Strained-Layer Quantum-Well Heterostructure", Sol. State Comm. **52**, 237 (1984). The work on the InGaAs quantum well resonant tunneling structure was first presented by M. A. Reed and J. W. Lee, "Resonant Tunneling in Double Barrier Heterostructures", Proceedings of the 18th International Conference on the Physics of Semiconductors, 11-15 August 1986, Stockholm, to be published. Subsequent to this conference, two papers (H. Toyoshima, Y. Ando, A. Okamoto, and T. Itoh, "New Resonant Tunneling Diode with a Deep Quantum-Well", Jap. Jour. Appl. Phys. **25**, L786 (1986); and G. S. Lee, K. Y. Hsieh and R. M. Kolbas, "Room Temperature Negative Differential Resistance in Strained Layer GaAs-AlGaAs-InGaAs Quantum Well Heterostructures", Appl. Phys. Lett. **49**, 1528 (1986)) on similar structures have appeared.
 13. S. P. Kowalczyk, W. J. Schaffer, E. A. Kraut and R. W. Grant, "Determination of the InAs-GaAs (100) Heterojunction Band Discontinuities by X-ray Photoelectron Spectroscopy (XPS)", J. Vac. Sci. Technol. **20**, 705 (1982).
 14. J. P. Faurie, A. Million, and J. Piagnet, "CdTe-HgTe Multilayers Grown by Molecular Beam Epitaxy", Appl. Phys. Lett. **41**, 713 (1982).
 15. K. A. Harris, S. Hwang, D. K. Blanks, J. W. Cook, Jr., J. F. Schetzina, and N. Otsuka, "Growth of HgCdTe and Other Hg-Based Films and Multilayers by MBE", J. Vac. Sci. Technol. **A4**, 2061 (1986).
 16. J. N. Schulman and C. L. Anderson, "HgTe-CdTe Double Barrier Tunneling Structures", Appl. Phys. Lett. **48**, 1684 (1986).
 17. Y. Guldner, G. Bastard, J. P. Vieren, M. Voos, J. P. Faurie, and A. Million, "Magneto-Optical Investigations of a Novel Superlattice: HgTe-CdTe", Phys. Rev. Lett. **51**, 907 (1983).
 18. S. P. Kowalczyk, J. T. Cheung, E. A. Kraut, and R. W. Grant, "CdTe-HgTe (111) Heterojunction Valence-Band Discontinuity: A Common-Anion Rule Contradiction", Phys. Rev. Lett. **56**, 1605 (1986).
 19. Y.-C. Chang, J. N. Schulman, G. Bastard, Y. Guldner, and M. Voos, "Effects of Quasi-Interface States in HgTe-CdTe Superlattices", Phys. Rev. B **31**, 2557 (1985).
 20. I. A. Lesk, N. Holonyak, Jr., and U. S. Davidsohn, Tunnel Diode and Semiconductor Circuits, John M. Carroll, ed (McGraw-Hill, New York, 1960), pp. 15-18.

APPENDIX L

SEMICONDUCTOR HETEROJUNCTION
RESONANT TUNNELING DEVICES

Abstract for an Invited Paper
for the New York City Meeting of the
American Physical Society

16-20 March 1987

SEMICONDUCTOR HETEROJUNCTION RESONANT TUNNELING DEVICES*§
Mark A. Reed, *Central Research Laboratories, Texas Instruments Incorporated*

The resonant transmission of electrical carriers ("resonant tunneling") through the quasistationary states of artificially structured semiconductor materials has recently become possible due to advanced epitaxial techniques. In the simplest case, the quasistationary states of a double barrier / single quantum well heterostructure (typically a GaAs quantum well sandwiched between AlGaAs tunnel barriers) gives rise to dramatic negative resistance regions corresponding to transport through those states. Through the use of superlattices to emulate barrier and/or quantum well shapes, more complex heterostructures have been investigated. The implementation of multi-component systems allows the opportunity to observe some new physical phenomena, such as tunneling through excited states above "hidden" ground states. The difference of the effective masses in the quantum well and injection regions of this system allows the unique measurement of the effective mass of the electron while transiting the resonant tunneling structure. The first measurements of resonant tunneling in a double barrier II-VI compound heterostructure, HgTe/HgCdTe, will also be presented. The observations in this physically distinct system give a precise determination for the value for the valence band offset. Finally, the applications of these structures toward high speed devices will be discussed.

*In collaboration with R. T. Bate, W. R. Frenaley, M. W. Goodwin, R. J. Koestner, J. W. Lee, H. F. Schaake, and H.-L. Tsai.

§Supported in part by the Office of Naval Research and the U.S. Army Research Office.

APPENDIX M

QUANTUM SEMICONDUCTOR DEVICES

QUANTUM SEMICONDUCTOR DEVICES *

Mark A. Reed

Central Research Laboratories
Texas Instruments, Incorporated
P. O. Box 655936, M/S 154
Dallas, TX 75265 USA

The exponential growth in the semiconductor electronics industry is attributable to schemes that permit the physical downscaling of transistor-based ICs. This downscaling capability will eventually be brought to an end by the barriers of device scaling limits, interconnection saturation, and yield. Achievement of limiting geometries from historical extrapolation will occur in the mid-1990's. If there is to be a post-VLSI technology, it must employ simultaneous revolutionary solutions in design, architecture, and device physics to circumvent the interconnection problem. The construction of a quantum electronics technology will involve a concentrated effort in basic device physics, advanced fabrication, and novel architectures. This revolutionary approach in both device and architecture is inherent in the desire to scale far beyond present VSLI. The demonstration of the basic physics and the realization of the basic devices in this technology is underway.

1. INTRODUCTION

The exponential growth in the semiconductor electronics industry is attributable to schemes that permit the physical downscaling of transistor-based ICs. This downscaling capability will eventually be brought to an end by the barriers of device scaling limits, interconnection saturation, and yield. It has been shown [1] that the optimal device dimension for practical overall system performance in the present technology is approximately 0.3-0.5 micron. Achievement of this geometry from historical extrapolation will occur in the mid-1990's. Fundamental limitations on devices themselves occur in the 0.1-0.3 micron size scale.

The semiconductor markets could continue to grow for another 5 to 10 years after the maturation of the present technology due to the time lag between new technology and the saturation of applications. Unfortunately, the need for further improvements in performance and density will not disappear with ever-increasing demands by communications, artificial intelligence, and defense needs. Improvements in system architectures will postpone, but not avert, this impending crisis. The implications of a maturing semiconductor technology are sufficiently harsh to warrant the consideration of an alternative to transistor-based microelectronics. An important clue to new approaches is that lithography and processing, at least for unaligned structures, will not be fundamental barriers to

* Supported in part by ARO and ONR

scaling in the long term.

If there is to be a post-VLSI technology, it must employ simultaneous revolutionary solutions in design, architecture, and device physics to circumvent the interconnection problem. Though no one presently knows if or how the next generation of ICs will be realized, we can postulate a number of constraints;

- The key innovation will be the one which solves the interconnect problem.
- The basic device will not be the transistor, and will probably utilize new phenomena.
- The basic devices must perform more complex functions than switching, and there will thus be more than one basic device.

It should be stressed that this does not imply that the transistor will not be used. Indeed, for some switching functions and interfacing it is unlikely that the transistor will be replaced. However, the transistor will be too large relative to functional complexity to serve as a basic building block.

The need for a multiplicity of "functional" basic devices, necessary to eliminate the number and length of interconnects, implies a change in the historical separation of architecture and device design. A higher level of synthesis will be necessary in implementing this technology, and parallel research efforts in devices and architectures are necessary. Thus, the implementation of a revolutionary approach must consider both device and architecture issues.

2. QUANTUM DEVICES

One of the basic reasons for the failure of conventional transistors is that the depletion layers or potential barriers used to confine carriers do not operate satisfactorily as the device is scaled to the sub-0.1 micron regime. Specifically, the dimensions of these regions become comparable to the Bloch wavelength of the carriers in the structure. Carriers can then tunnel through these confinement regions, making the complete switching of current with this device impossible.

Devices that operate in the sub-0.1 micron regime will also exhibit effects due to the quantum mechanical confinement of carriers in the structure. The isolated device will exhibit an energy spectrum dependent on the dimensional details. This effect will become dominant as the device size shrinks. Such effects have already been observed in Si MOSFETs [2], small semiconductor particles [3], and a fabricated GaAs heterostructure [4]. Recent advances in the fabrication of these small GaAs heterostructures [5,6] have demonstrated sub-0.1 micron lateral dimensions and the first clear evidence for the creation of discrete electronic levels in these systems.

It is logical to require the next generation of devices be immune to these effects; indeed, because of the dominant size effects expected as the device size decreases, one would hope to utilize these effects. Concurrently, as the confinement barriers become thinner, tunneling will be a non-trivial effect. We will define devices which utilize

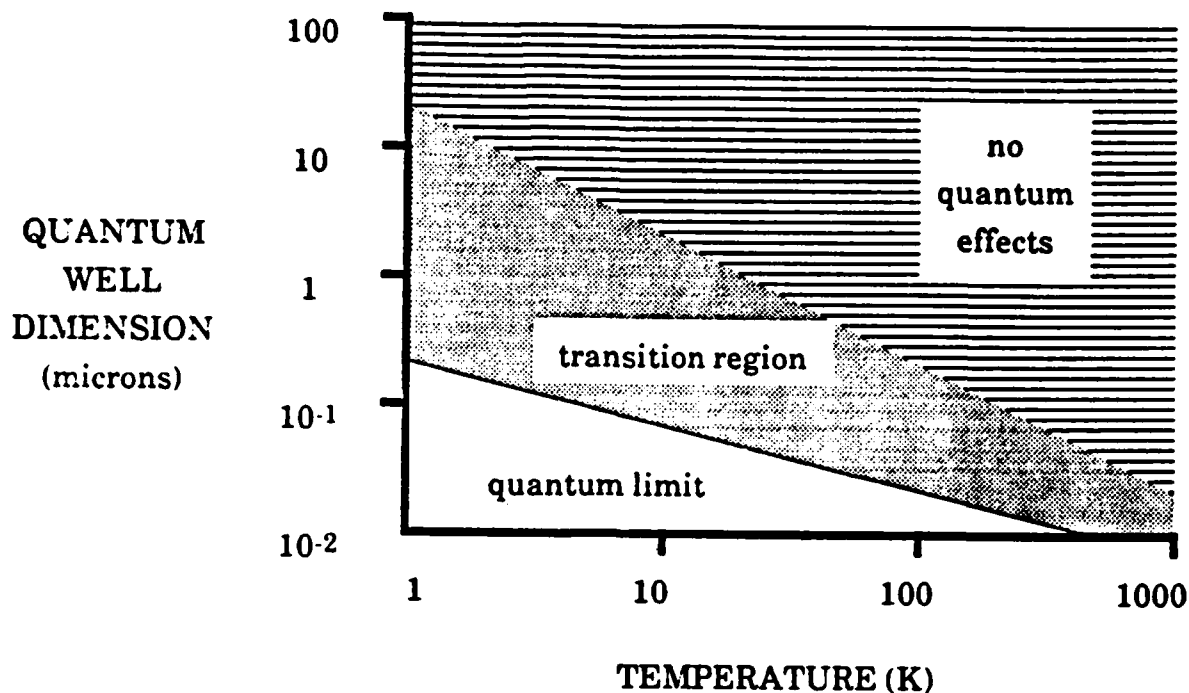


FIGURE 1

Size regimes for GaAs/AlGaAs quantum devices utilizing quantum size effects. The devices are expected to work well in the "quantum limit", degrading in performance through the "transition region", and should fail in the "no quantum effects" limit.

both quantum size effects and quantum mechanical tunneling as "quantum devices". The advent of MBE and MOCVD, combined with state-of-the-art nanolithography and processing, has allowed the realization of structures in this size domain. Due to the relative maturity of this technology in the III-V systems (specifically, GaAs/Al_xGa_{1-x}As), realizations of quantum devices will probably first occur in the GaAs/Al_xGa_{1-x}As system, though this technology is fundamentally material independent. The operating limits of these devices are temperature sensitive; Figure 1 shows the regimes in which devices utilizing quantum size effects are expected to operate in the GaAs system.

There exist a number of new device structures, such as the High Electron Mobility Transistor (HEMT) and the ballistic transistor, that utilize quantum phenomena in a conventional transistor structure. These structures are important new developments for custom high speed logic and microwave applications. However, the structures are essentially clever permutations of the conventional transistor structure, and will eventually fall victim to the same limitations as conventional transistors. Our definition of a quantum device is driven by the immunity to scaling into the sub-0.1 micron regime.

To demonstrate the operating principles of our first embodiments of this genre of device, let us consider a one-dimensional prototype quantum semiconductor device that employs both quantum size effects and quantum mechanical tunneling. The potential energy diagram (in real space) that we would want to realize is

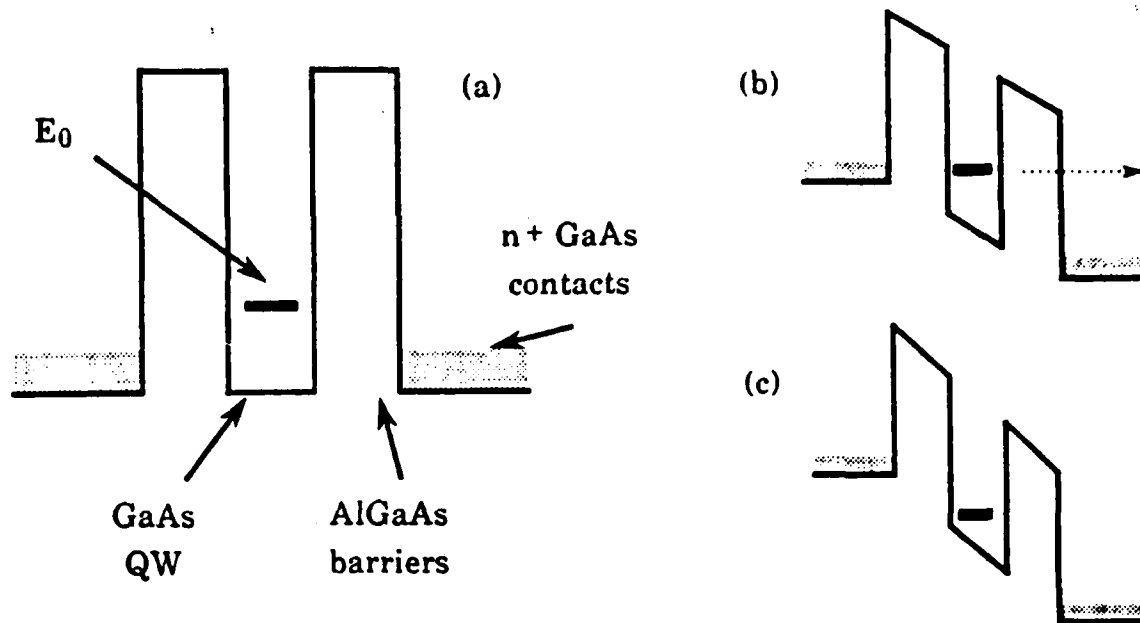


FIGURE 2

Real space conduction band diagram of a one-dimensional prototype quantum device, a "resonant tunneling diode". The center quantum well has a discrete, higher allowed eigenstate labelled E_0 . (a) No device bias. (b) Resonant bias, tunneling through E_0 . (c) High device bias, resonant tunneling no longer allowed.

diagrammed in Figure 2, and is called a "resonant tunneling diode" [7,8]. This structure can be realized by the conduction band of a composite heterostructure system, such as GaAs/ $\text{Al}_x\text{Ga}_{1-x}\text{As}$. When the width of the center lower bandgap region is small, it is called a "quantum well", and it exhibits discrete higher eigenstates (relative to the left- or right-hand lower conduction band edges) due to the quantum confinement by the barriers. These discrete eigenstates are the minima of parabolic bands in the three-dimensional embodiment of the structure (due to the two remaining unconstrained dimensions), though the treatment of the energies as discrete states is valid for low energy electrons in the GaAs/ $\text{Al}_x\text{Ga}_{1-x}\text{As}$ system. The higher bandgap confinement barriers must also be made sufficiently thin to allow tunneling of carriers.

At low device bias, electrons cannot elastically (without electron energy gain or loss) tunnel through the structure as the eigenstate in the quantum well is too high in energy. As the device bias increases, the quantum well state is lowered with respect to the Fermi level in the left contact, and carriers are allowed to resonantly tunnel through the structure. When the device bias is increased to the point that the allowed state (band) in the quantum well is lower in energy than the conduction band edge of the left contact, elastic tunneling is no longer allowed due to the conflicting requirements of energy and momentum conservation. An eventual increase in current at high device bias will be seen due to Fowler-Nordheim tunneling and thermal excitation over the barriers. These types of quantum devices

are characterized by sharp resonances in transmitted current, whose bias position is determined by dimensional control.

Such structures have been realized with MBE in the lattice-matched GaAs / $\text{Al}_x\text{Ga}_{1-x}\text{As}$ heterojunction system. The central undoped GaAs quantum well is "sandwiched" between two $\text{Al}_3\text{Ga}_7\text{As}$ barriers and n^+ GaAs contacts. The lack of dopants in the central active region is a lesson in the operating principles of this genre of device; dopants in the quantum well do not enhance the tunneling current, but instead decrease the tunneling current by acting as scattering centers for the tunneling carriers. Doping the well decreases the tunneling current by $\sim 10^{-2}$. The current - voltage characteristics of a typical device is shown in Figure 3. The negative differential resistance (NDR) is due to the shut-off of the elastic tunneling channel through the intermediate quantum well state. The finite valley current on the high-bias side of the NDR peak is due to inelastic tunneling via phonons and/or impurity-enhanced tunneling. Indeed, the initial reports [7,8] of this structure had degraded performance due to large inelastic tunnel currents and exhibited weak NDR only at low temperature. Careful elimination of scattering centers from the active region has suppressed the inelastic channels, with acceptable demonstrated room temperature performance and peak-to-valley ratios of 10:1 at 77°K. The NDR in these devices has been shown [8] to exist up to frequencies as high as 2.5 THz, and the ultimate speed of these devices is a subject of current investigation.

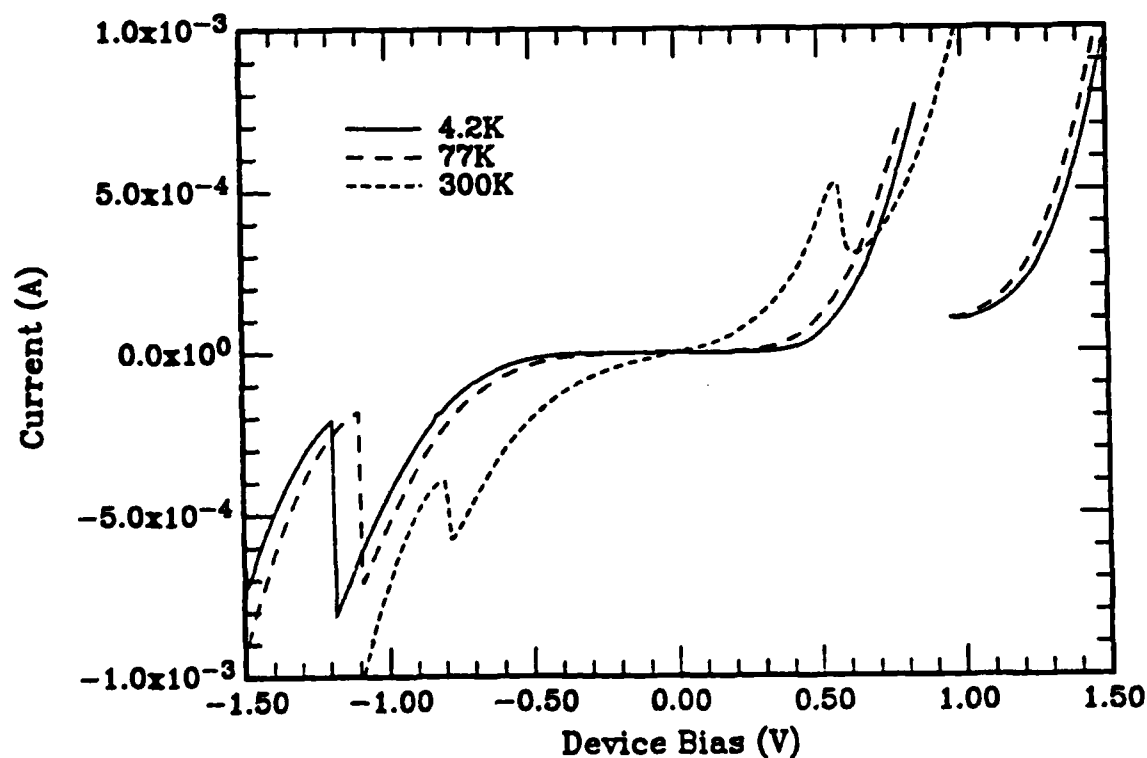


FIGURE 3

I-V characteristics of a 25 sq. micron resonant tunneling diode (nominally 50 Å well, 50 Å barriers, $x = 0.3$) at 4.2°K, 77°K, and 300°K. The breaks in the curves are where the device exhibits negative differential resistance.

The position of the NDR peak is determined by the width of the quantum well; i.e. the device function is reduced to dimensional control during MBE growth. Indeed, these structures can easily be designed to have not only a single NDR peak, but a spectrum of NDR peaks dependent on the GaAs quantum well size. Multiple NDR peaks have recently been observed [9] via tunneling through the excited states in these structures.

There exists a natural trend to incorporate these structures into conventional devices to utilize the potential speed of these devices. The recognition of multiple NDR peaks has revived interest in multi-state and "fuzzy" logic. Insertion of resonant tunneling structures into the base [10], emitter [11], or collector of conventional bipolar structures allows the creation of compact logic components, multi-state memories, and frequency multipliers. These constructs are essentially hybrid combinations, with little advantage over series constructs. For example, the Resonant tunneling Hot Electron Transistor (RHET) [11] has a resonant tunneling structure in the emitter of a hot electron transistor, which is essentially a resonant tunneling diode in series with a transistor. These constructs are an attempt in conventional terms to construct a three-terminal resonant tunneling structure. The naïve approach to directly contact the quantum well is not only fraught with fabrication difficulties but is useless due to parasitic base current. The construction with a bipolar-type structure is equally fruitless. To date, the realization of a truly three-terminal resonant tunneling device has not been accomplished. Though this device may have high speed analog and digital implications, it is not at all clear that pursuing a three-terminal device is necessary for the implementation of a quantum device technology.

The structures discussed so far only have a single dimension sufficiently small to observe size effects. The effects of size quantization have been observed in transport through "quantum wires", in silicon inversion layers [2] and optically in semiconductor "quantum dots" [4-6]. It is conceivable to utilize the properties of these structures in a type of device defined as a "quantum coupled device" (QCD), which employs resonant tunneling between discrete electronic energy levels. Though difficult, creation of this type of device is now becoming possible with state-of-the-art fabrication techniques.

In this generation of quantum device, not only are the levels in each device determined by quantum size effects, but the essential carrier transport mechanism is tunneling between devices. The discrete nature of the initial and final electronic states is a desirable situation, for it tends to suppress the parasitic inelastic tunneling channels that are available for the above one-dimensional case. This advantage may allow for acceptable digital performance even at room temperature.

In addition to the elimination of interconnects, this type of device technology inherently attacks the interdevice crosstalk limitations in VLSI as it is the operating principle of the QCD. The electrostatic coupling between devices is dominant in

determining selection rules when interdevice spacing approaches this dimensional scale. The need to synthesize device physics and system architecture now becomes obvious.

3. QUANTUM DEVICE ARCHITECTURES

The possibility of creating a revolutionary class of devices that operate on quantum size effects and tunneling phenomena exists. It is not obvious what type of architecture can usefully exploit these devices. The insertion of quantum devices into conventional VLSI architecture is antiproductive, since the interconnection dilemma has not been addressed. Recognizing that quantum devices will probably be ultra-submicron, multistate devices which exhibit strong local coupling, we can postulate a number of assumptions about the general structure of quantum device architectures.

Unlike conventional VLSI architecture, the notion of isolated, functionally independent active elements are not valid in the present embodiment of quantum devices. The requirement of strong, local coupling which is physically natural for quantum devices must be a central ingredient for quantum device architectures. We can sum up the proposed architecture requirements into a number of concise requirements;

- Few, if any, long interconnects.
- Periphery-only access.
- Fault tolerance in data flow and control.
- Functional reconfigurability at all levels.

Clearly the collective characteristics of this architecture cannot be expressed in terms of the local properties of the active components, called "nodes". In principle, we can arbitrarily interconnect a given node to any other node. The extreme case of interconnectivity is the globally coupled neural network which exhibits striking fault-tolerant and pattern recognition properties. Less extreme are sparsely-connected architectures, and the limiting case is nearest-neighbor connection architectures. Quantum devices, which only utilize a limited local coupling, naturally fit into architectures with only near-neighbor coupling.

A type of architecture that has these properties is called "cellular automata" (CA), where abstract, multistate nodes are located on a lattice structure and constrained to interact according to well-defined near-neighbor rules. A good deal of work has been performed on one-dimensional synchronous CA models [12] and the collective phenomena of the structure has exhibited degenerate, periodic, chaotic, and nondegenerate state transitions. These structures have also shown the ability to perform Boolean functions, though this is not necessarily an important property for the use of this architecture for quantum devices. It has been shown [12] that the evolution of line (one-dimensional) automata according to fixed near-neighbor interaction rules exhibit a wide range of possible transitions. It is important to note

that, even though these CAs are based on very local node interaction rules, the evolution indicates interactions that propagate between node groups. Therefore, effective long-range communication is possible between locally coupled nodes. The requirements of periphery access and no interconnects are naturally met.

The investigation of CA has largely been confined to simulations of one dimensional synchronous arrays with no noise. Though the simplest to classify, these are the least physically interesting CAs. Recent investigations have been extended to asynchronous arrays where self-organizing CAs have been discovered. Schemes that effectively synchronize node groups are also possible. It has also been shown that CAs can be stabilized against noise, making a CA/quantum-device architecture essentially "fail-soft", for fault tolerance requirements. For system requirements, synchronicity can be inserted at a higher level of complexity.

Two dimensional arrays are now being classified, and the creation of Boolean functions and replication functions have been done. The collective behavior is quite complex, and it is not clear if a classification of rule sets and behavior is useful or possible. Unlike conventional architectures, simulations may be the most efficient method to exploring the collective interactions of node groups in CA architectures. These simulations may well give rise to emergent properties that can be applied to quantum device architecture.

4. SUMMARY

The construction of a quantum electronics technology will involve a concentrated effort in basic device physics, advanced fabrication, and novel architectures. The basic physics on which devices in this technology will probably operate are quantum size effects and quantum mechanical tunneling, considerably different from conventional devices. Structures which exhibit these effects have been demonstrated. The realization of the basic devices in this technology is underway.

The prototype architectures in this technology must exploit strong local device coupling, and are known as "cellular automata". The need of such architectures is driven by the need to eliminate interconnects, and is natural for "quantum-coupled devices". This revolutionary approach in both device and architecture is inherent in the desire to scale far beyond present VSLI.

ACKNOWLEDGEMENTS

I am grateful to J. W. Lee and H. D. Shih for MBE support, R. T. Bate, G. A. Frazier, W. R. Frensley and P. A. Penz for helpful discussions, K. Bradshaw for e-beam lithography, and W. M. Duncan for photoluminescence measurements.

REFERENCES

- [1] P. K. Chatterjee, P. Yang, and H. Shichijo, *Proc. IEE* 130, 105 (1983).
- [2] W. J. Skocpol, L. D. Jackel, R. E. Howard, H. G. Craighead, L. A. Fetter, P. M. Mankiewich, P. Grabbe, and D. M. Tennant, *Surface Science* 142, 14 (1984).
- [3] R. Rossetti, J. L. Ellison, J. M. Bigson, and L. E. Brus, *J. Chem. Phys.* 80, 4464 (1984).
- [4] M. A. Reed, R. T. Bate, K. Bradshaw, W. M. Duncan, W. R. Frensley, J. W. Lee, and H.-D. Shih, *Jour. Vac. Sci. Technol.* 4B, 358 (1986).
- [5] K. Kash, J. M. Warlock, A. Scherer, M. C. Tamargo, and H. G. Craighead, presented at the 2nd International Conference on Superlattices, Microstructures, and Microdevices, Göteborg, 17-20 August 1986.
- [6] J. Cibert, P. M. Petroff, G. Dolan, D. J. Werder, S. J. Pearton, A. C. Gossard, and J. H. English, presented at the 2nd International Conference on Superlattices, Microstructures, and Microdevices, Göteborg, 17-20 August 1986.
- [7] L. L. Chang, L. Esaki, and R. Tsu, *Appl. Phys. Lett.* 22, 562 (1973).
- [8] T. C. L. G. Sollner, W. D. Goodhue, P. E. Tannenwald, C. D. Parker, and D. D. Peck, *Appl. Phys. Lett.* 43, 588 (1983).
- [9] M. A. Reed, *Superlattices and Microstructures* 2, 65 (1986).
- [10] F. Capasso and R. A. Kiehl, *J. Appl. Phys.* 58, 1366 (1985).
- [11] N. Yokoyama, K. Imamura, S. Muto, S. Hiyamizu, and H. Nishi, *Jap. Jour. Appl. Phys.* 24, L853 (1985).
- [12] S. Wolfram, *Physica* 10D, 1 (1984).

APPENDIX N

MICROSTRUCTURE FABRICATION AND TRANSPORT
THROUGH QUANTUM DOTS

Microstructure Fabrication and Transport Through Quantum Dots

J. N. Randall, M. A. Reed, T. M. Moore, R. J. Matyi and J. W. Lee*

**Central Research Laboratories
Texas Instruments Incorporated
Dallas, Texas**

Abstract

We report the microfabrication techniques used to produce devices which study electronic transport through quantum dots. Molecular beam epitaxy, e-beam lithography, and reactive ion etching have been utilized in this effort. The minimum physical lateral size of the dots reported here is 0.1×0.2 micrometer. Transport shows some degradation in I-V characteristics with respect to much larger resonant tunneling diodes. Current densities observed suggest the electrical size of the diodes is smaller than the physical size. A surface depletion region of 500 \AA may account for this effect. Telegraph noise is observed as a result of single electron trapping in the structure. No clear evidence of lateral quantization has been observed.

I. Introduction

The progress towards smaller and faster electronics will eventually push devices into regimes where quantum effects will dominate transport.^{1,2} Resonant tunneling diodes have been studied which show strong quantum effects in electronic transport due to electron confinement in one dimension.^{3,4} In this work we demonstrate resonant tunneling diode structures which we use to attempt to study lateral quantization effects. The microfabrication techniques which are used to create quantum dot structures which have direct electrical contact are described. Electronic transport through small arrays and single quantum dots is demonstrated. This type of device should allow the study of several different aspects of electronic transport on the quantum level and will also help understand some of the processing issues involved with producing quantum effect devices.

II. Microfabrication Approach

In order to study electron transport through quantum dots we have adopted a microfabrication approach which is summarized in Fig. 1. After molecular beam epitaxy (MBE) growth of a resonant tunneling diode structure, an e-beam lithography step is used to define an ensemble of quantum dots. A lift-off process will leave metal dots that will serve the dual purposes of an etch mask and topside ohmic contact. A highly anisotropic reactive ion etching (RIE) process will proceed through the quantum well structure, producing the desired lateral confinement of the GaAs dots. A planarizing layer of dielectric material will be deposited, and then etched-back to uncover the topside dot contacts. Finally a gold layer will connect the quantum dots with a bond pad. Details of these steps are given in the following sections.

III. MBE Growth

The resonant tunneling structure was grown by MBE in a Riber 2300 on a 2-inch n^+ (Si-doped, Sumitomo) GaAs substrate oriented 2 degrees off the $\langle 100 \rangle$. An indium-free, direct radiative substrate heater was used. Following the growth of a 0.5 micrometer-thick Si-doped ($2 \times 10^{18} \text{ cm}^{-3}$) GaAs buffer layer at 620C, the doping was graded down to less than 10^{16} cm^{-3} over a 200 Å distance. The undoped tunneling structure consisted of: 1) a 50 Å undoped GaAs spacer layer; 2) a 50 Å $\text{Al}_{0.27}\text{Ga}_{0.73}\text{As}$ barrier; 3) a 50 Å undoped GaAs quantum well. Following the growth of the second 50 Å $\text{Al}_{0.27}\text{Ga}_{0.73}\text{As}$ barrier and spacer layer, the doping was graded back up to $2 \times 10^{18} \text{ cm}^{-3}$ and the top contact (0.5 micrometer) was grown.

IV. E-beam Lithography

High resolution e-beam lithography was accomplished using a standard JEOL JSM-35 SEM modified for electron beam lithography. The lithography modification consists of a Tracor Northern TN-5500 X-ray analysis system with a digital imaging package, stage automation, and beam blanking.⁵ The patterns are stored as a 256 x 256 array and written as a 1024 x 512 array. The dose in each pixel is controlled by varying the duration of exposure. The beam energy was set at 39 KeV and the current for these exposures was typically 3pA.

Using stage automation, several patterns were written at a time adjacent to a previously defined metal pattern. ^{which} This later served as a registration guide and focusing pattern. Three different size dots were defined which were nominally 0.25, 0.15, and 0.1 micrometer in diameter. Each of the different sized dots were exposed as single dots as well as arrays of 4, 9, and 16 dots on one micrometer centers. The dose required for exposure of the different

sized dots ranged from approximately 50 microCoulombs/cm² for the 0.25 micrometer dots to over 200 microCoulombs/cm² for the 0.1 micrometer dots. This discrepancy is only partially explained by standard proximity effects.⁶

The resist system used was a polymethylmethacrylate (PMMA) bi-layer consisting of 1000 Å of 950,000 molecular weight (MW) material as a top layer and 3000 Å of 450,000 MW PMMA underneath. This system is designed to give undercut profiles which facilitate lift-off pattern transfer.⁷ The resist was developed in a 60/40 mixture of methylisobutylketone and isopropyl alcohol at room temperature.

The metal layer patterned by the e-beam lithography must serve the dual purpose of RIE etch mask and ohmic contact. For this purpose we use a three layer metallization consisting of 500 Å Au/Ge, 150 Å Ni, and 600 Å Au. These layers were evaporated consecutively in the stated order on to the e-beam exposed samples. The lift-off process was completed by soaking the samples in boiling acetone and then applying a vigorous acetone spray.

V. Reactive Ion Etching

The transfer of the metal dot pattern into the semiconducting material which contains the quantum well structure demands both extremely high anisotropy and reasonably low etch rate of the metal mask. The metal dots must not only physically survive the etch process but also must preserve their Ohmic contact characteristics.

The etch process developed used BCl₃ as an etch gas flowing at 30 SCCM with a pressure of 30 mTorr. The power delivered by a 13.56MHz rf generator was 1 watt/cm² and the self bias potential was 300V. The RIE chamber was custom built at TI. A Si wafer was used as the surface of the driven electrode on which the samples were placed. The etch rate of GaAs for these conditions was nominally 350Å/min. The etch rate of Au was approximately 20 Å/min. These conditions were selected because they provided excellent anisotropy while maintaining reasonable selectivity. An example of quantum dot structures successfully etched with this technique is seen in Figure 2.

VI. Contact

In order to make contact to the tops of the columns polyimide was spun on the wafer, cured, and then etched-back by oxygen RIE until the tops of the columns were exposed. The endpoint to the etching was accomplished by iterative etching and viewing in a SEM. A gold contact layer was lifted off which provided bonding pads for contact to either single dots or arrays of them.

VII. Transport Measurements

Figure 3 shows the I-V characteristic at room temperature of a large area (2 micrometers x 2 micrometers) resonant tunneling diode fabricated by chemical mesa etching from the MBE material discussed above. The structure exhibits a 1.6:1 peak to valley tunnel current ratio and a current density at resonance of 1.6×10^4 A/cm².

Figure 4 shows a similar I-V characteristic of a single quantum dot resonant tunneling structure at 300K. The lateral dimensions of this single dot structure is 0.15 micrometers x 0.25 micrometers. The structure clearly shows NDR, though the peak to valley is degraded from the large area structure, probably due to process damage. The I-V clearly exhibits a "noise" that is far above the system background noise. The origin of this noise is the so-called "single electron switching" phenomena⁸ that has been observed in narrow Si MOSFET wires. Traps in or near the narrow conduction channel and are near the Fermi level can emit or capture electrons with a temperature-dependent characteristic time. This can be seen in Fig. 5, where the switching is more well defined at 100K than at 300K due to the fast thermal activation of the traps at 300K. The lowering of specific traps through the Fermi level is also clearly evident (at .6V, .8V through .85V, 1.0V through 1.1V). These traps can be "frozen out", as we see in Fig. 6 where the temperature has been lowered to 4.2K.

Figures 7 and 8 show a time-dependent trace of the current through this device at fixed biases voltage (i. e., fixed voltages on Figure 5) at T=84K. Figure 7 shows the switching between two discrete resistance states at $V = 0.71$ V, implying the trapping and detrapping of single electrons onto the same trap. At higher device bias (Figure 8; 0.875 V), the switching due to a number of traps is evident.

It seems unlikely that such effects can be seen for the physical dimensions (0.15 micrometer x 0.25 micrometer) of the structure. However, the effects of depletion at the etched mesa surfaces has not been taken into account. Taking the observed current at resonance and assuming that the current density must be the same as in the large area device (assuming that the switching is a perturbation), we calculate that the effective (circular) conduction path diameter is $\sim 500\text{\AA}$, consistent with the observation of the switching phenomena. This implies a depletion layer of approximately 500\AA . However, transport was also seen in an array of dots 2000\AA by 1000\AA suggesting a depletion layer smaller than 500\AA .

At these lateral dimensions, splitting of the quantum well resonance due to lateral size quantization should be observable. High resolution scans similar to Fig. 6 have been performed, but no definite indications of lateral quantization have yet been observed.

VIII. Conclusions

We have demonstrated a successful microfabrication technique for studying electronic transport in quantum dots. Transport through the quantum dots shows single electron trapping events. While no clear evidence of lateral quantization has been observed, we believe that these microfabrication techniques should be able to yield dots sufficiently small to produce this effect.

Acknowledgements

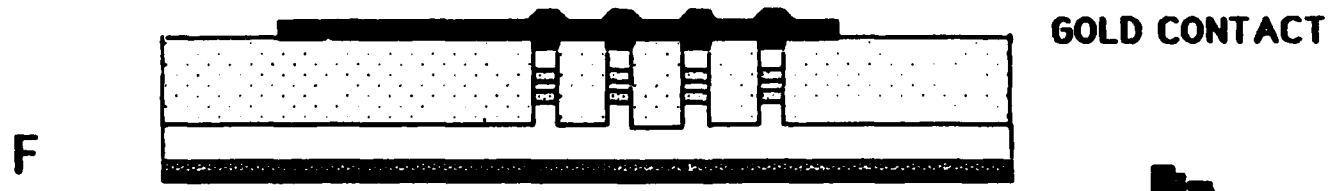
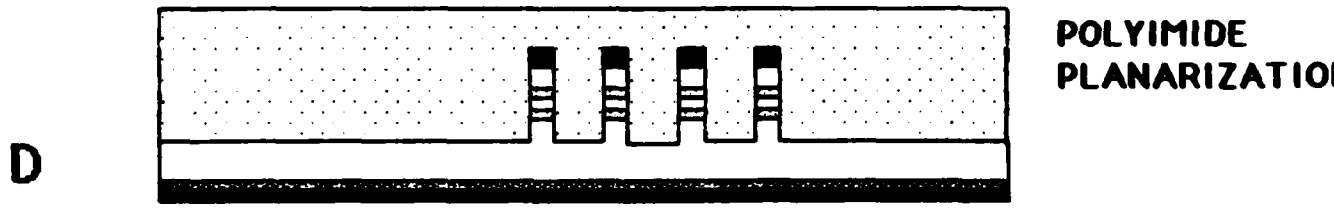
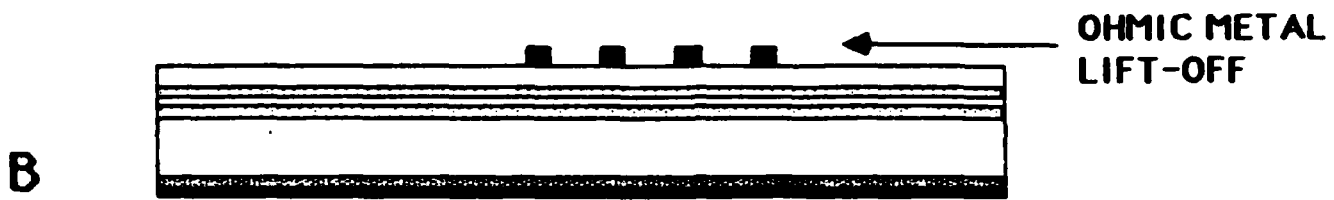
The authors wish to thank Randy Thomason, Doug Schultz, Pam Stickney, and Robert Aldert for technical assistance. We also are indebted to Bob Bate and Bill Frensley for valuable advice and discussions. This work was sponsored by the Army Research Office.

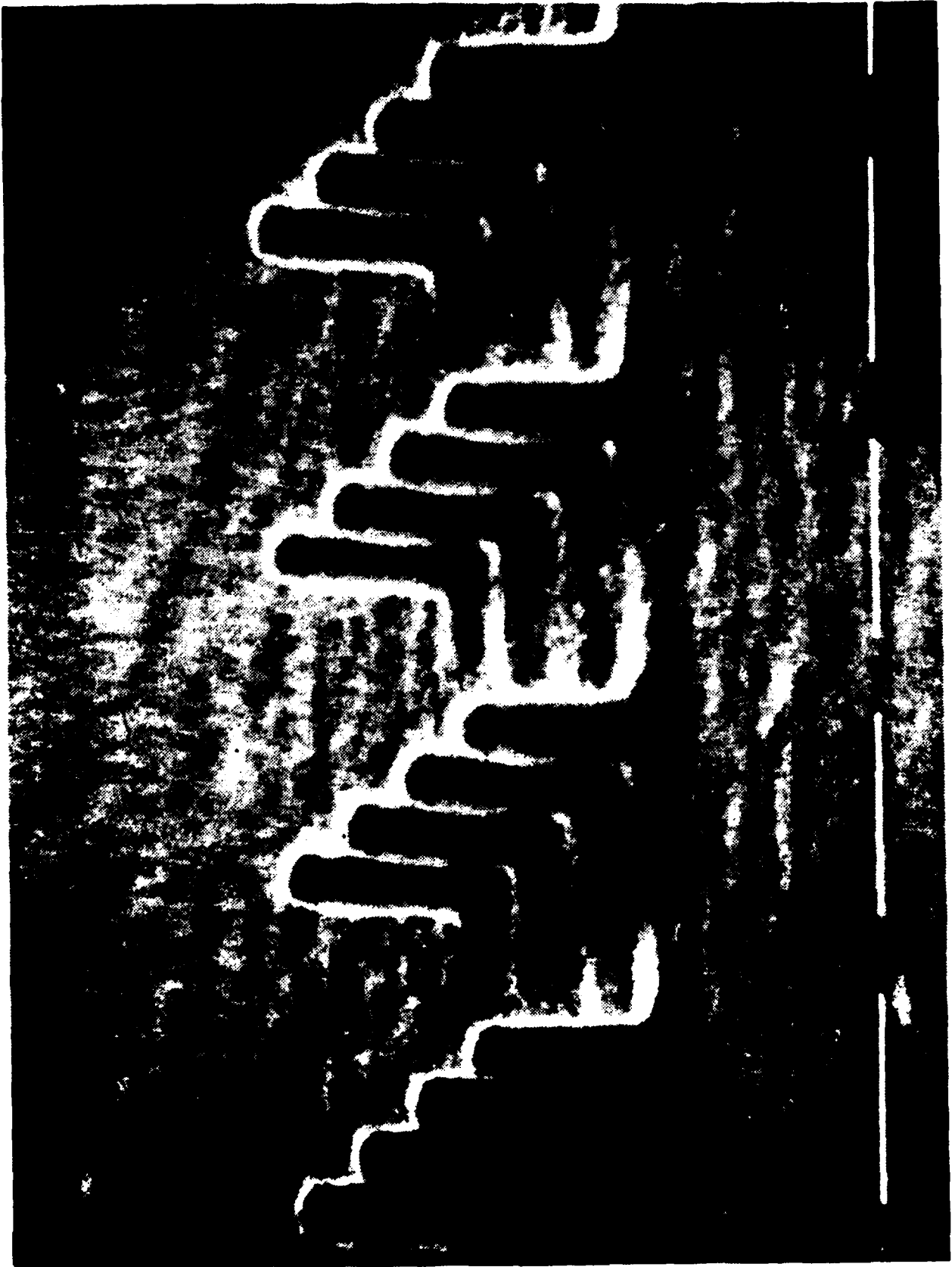
References

- * Present address: Kopin Corp., 695 Myles Standish Blvd., Taunton, MA 02780.
- 1. R. T. Bate, *Superlattices and Microstructures*, **2**, 9 (1986).
- 2. "Artificially Structured Materials", Report of a Panel of the Solid State Sciences Committee, National Research Council, (National Academy Press, Washington, D.C. 1985.)
- 3. L. L. Chang, L. Esaki, and R. Tsu, *Appl Phys. Lett.* **24**, 593 (1974).
- 4. T.C.L.G. Sollner, W. D. Goodhue, P. E. Tannenwald, C. D. Parker, and D. D. Peck, *Appl. Phys. Lett.* **43**, 588 (1983).
- 5. P. E. Russel, T. North, and T. M. Moore, *Microbeam Analysis - 1986*, Romig, A. D. and Chambers, W. F.(eds.), San Francisco Press, San Francisco, CA. pp.663-6, 1986.
- 6. J. A. Oro, Ph.D. Thesis, Electrical Engineering Dept., University of Houston, 1987.
- 7. M. J. Rooks, P. McEuen, S. Wind, and D. E. Prober, *Mat. Res. Soc. Symp. Proc.* **76**, 55 (1987).
- 8. K. S. Ralls, W. J. Skocpol, L. D. Jackel, R. E. Howard, L. A. Fetter, R. W. Epworth, and D. M. Tennant, *Phys. Rev. Lett.* **52**, 228 (1984).

Figure Captions

- Figure 1:** Schematic of fabrication sequence of quantum dot devices.
- Figure 2:** Scanning electron micrograph of anisotropically etched columns containing quantum dots.
- Figure 3:** I-V trace at room temperature of 2 micrometer x 2 micrometer resonant tunnelling diode which is fabricated from same vertical epitaxial structure as the quantum dot devices.
- Figure 4:** I-V characteristics at 300K of a single quantum dot which has lateral dimensions 0.25 x 0.15 micrometer.
- Figure 5:** I-V trace at 100K of a single quantum dot which has lateral dimensions 0.25 x 0.15 micrometer.
- Figure 6:** I-V trace at 4.2K of a single quantum dot which has lateral dimensions 0.25 x 0.15 micrometer.
- Figure 7:** Time dependent current fluctuations at a fixed bias of 0.71 V of a single quantum dot which has lateral dimensions 0.25 x 0.15 micrometer. T=84K.
- Figure 8:** Time dependent current fluctuations at a fixed bias of 0.875 V of a single quantum dot which has lateral dimensions 0.25 x 0.15 micrometer. T=84K.





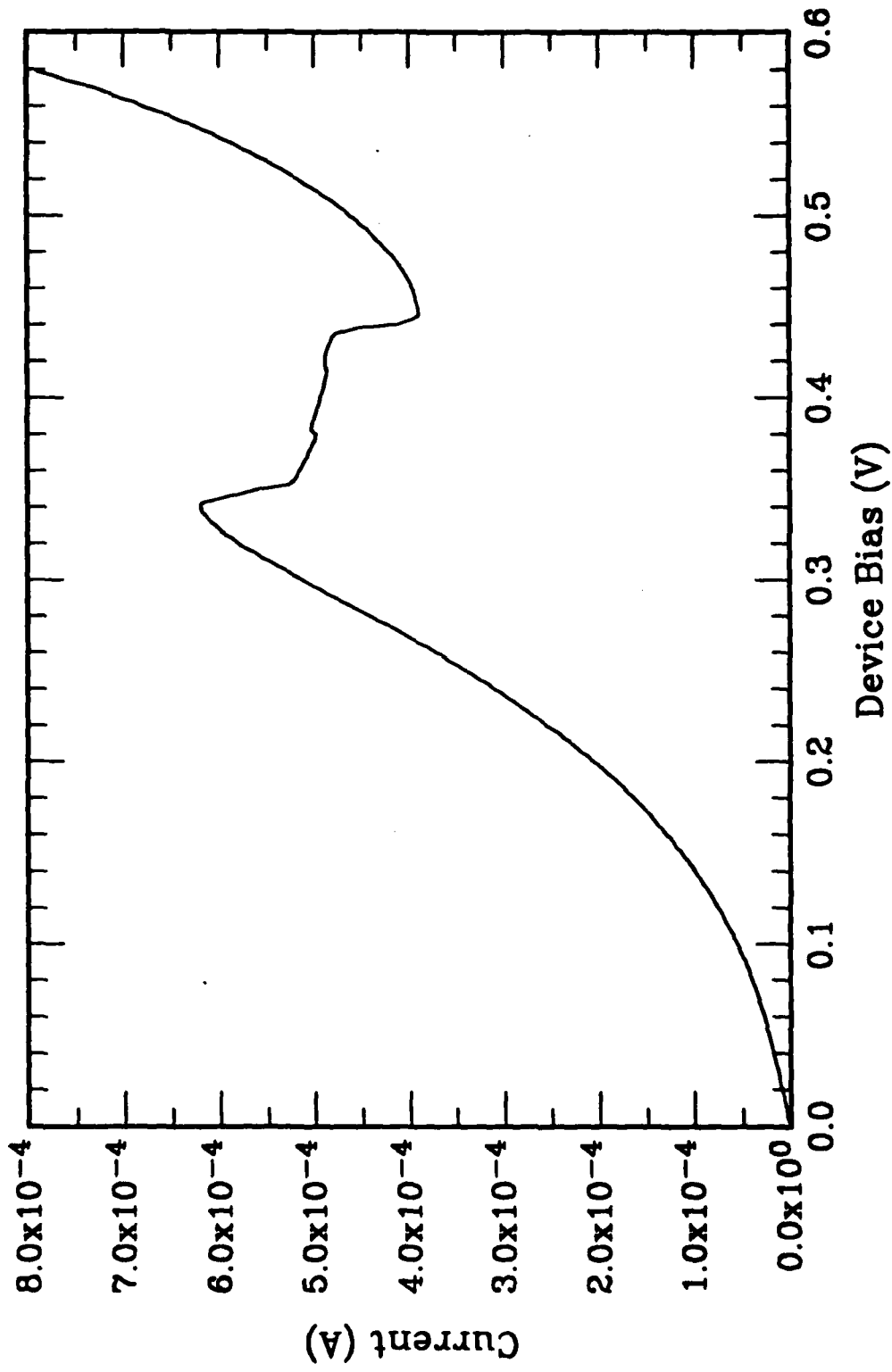


FIG. 3

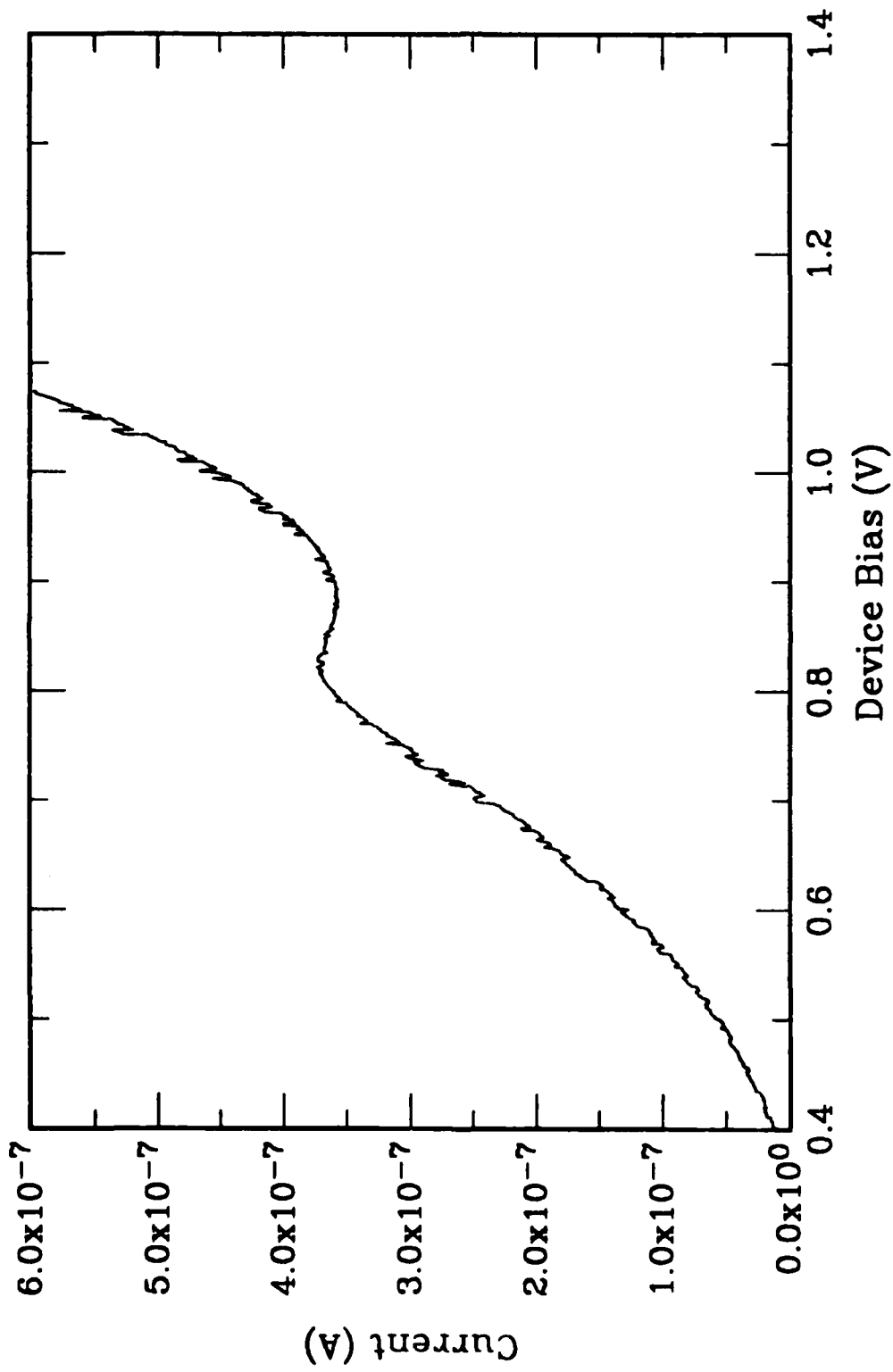


Fig. 4

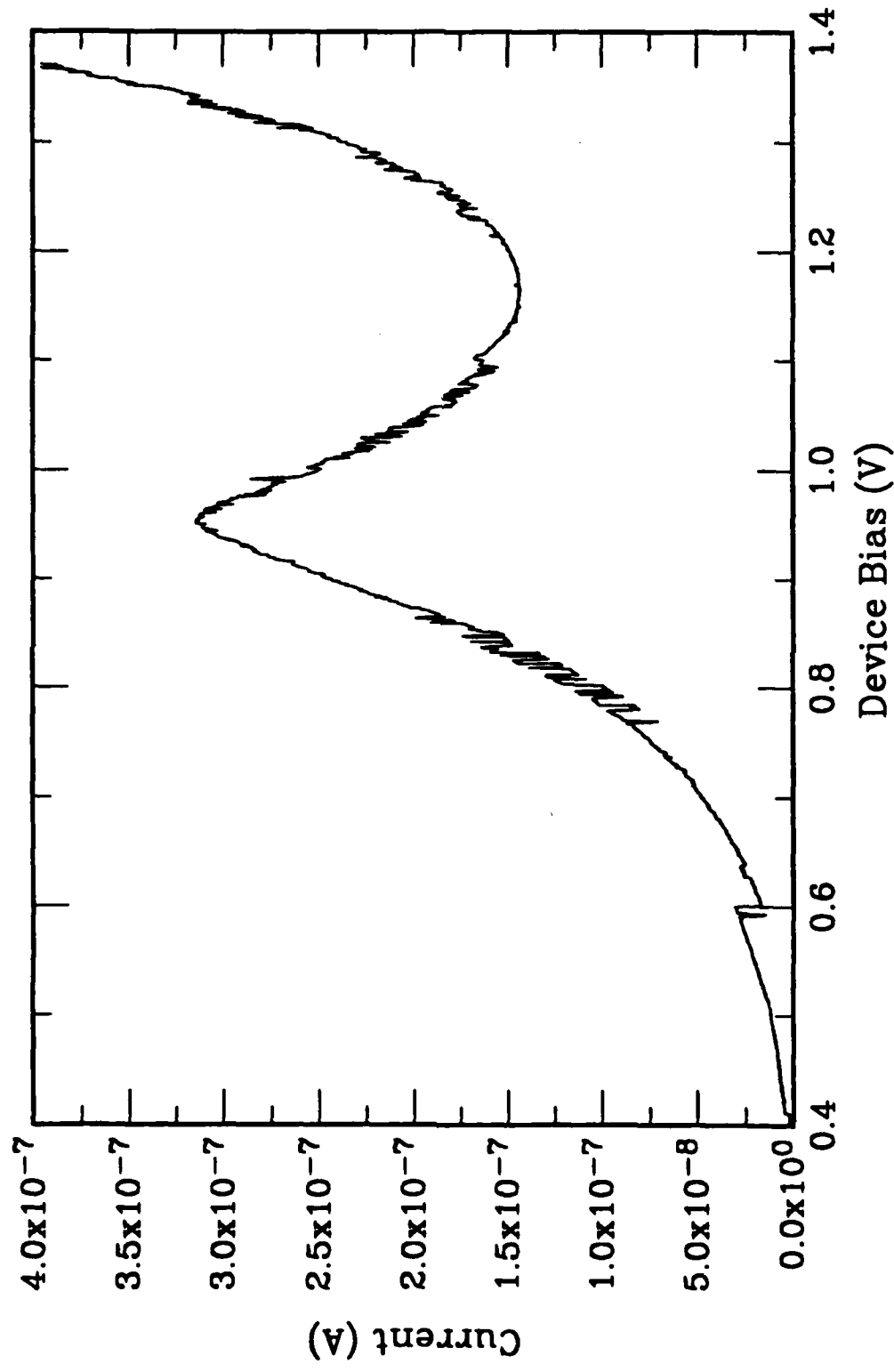


Fig. 5

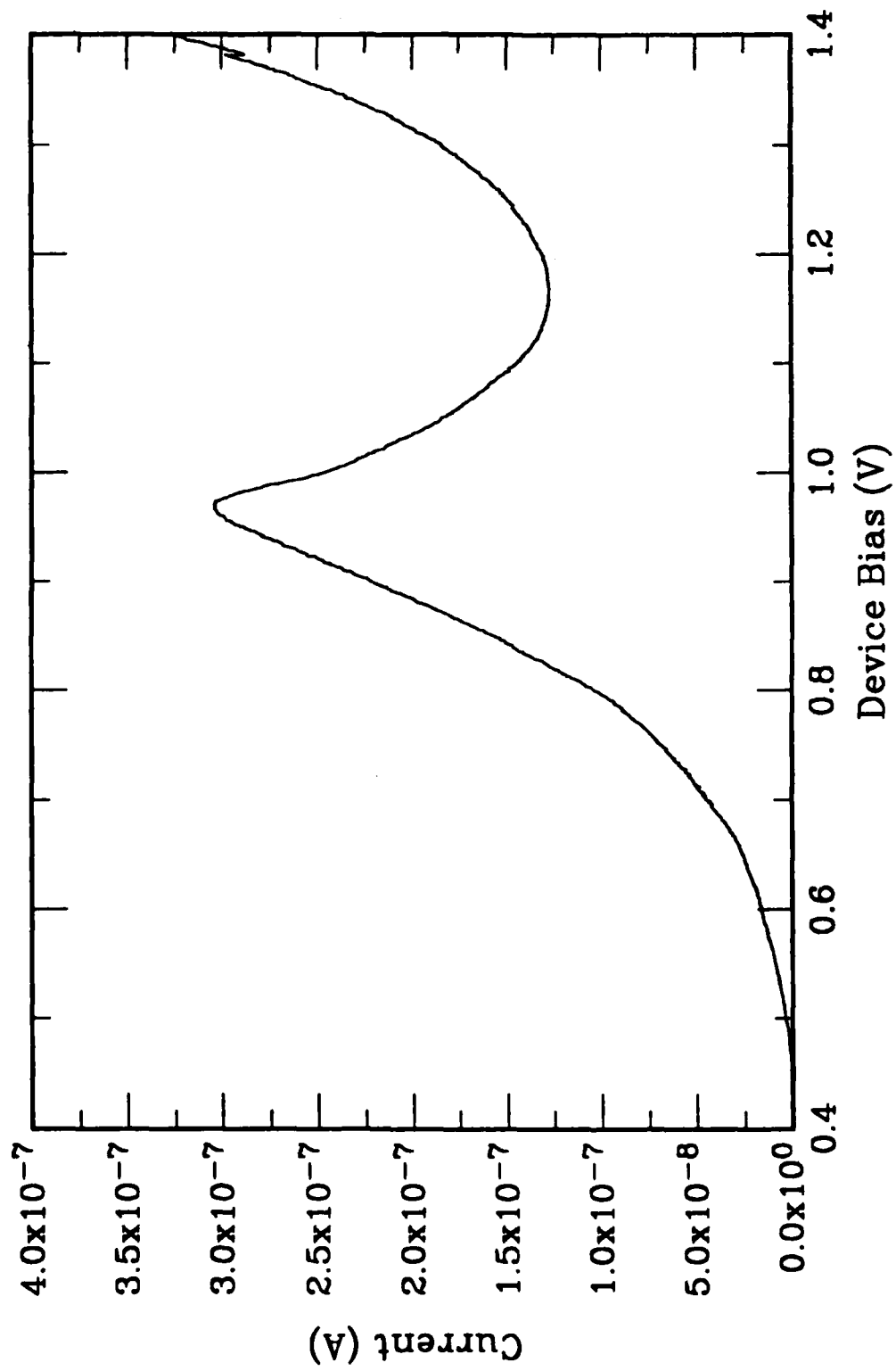


FIG. 6

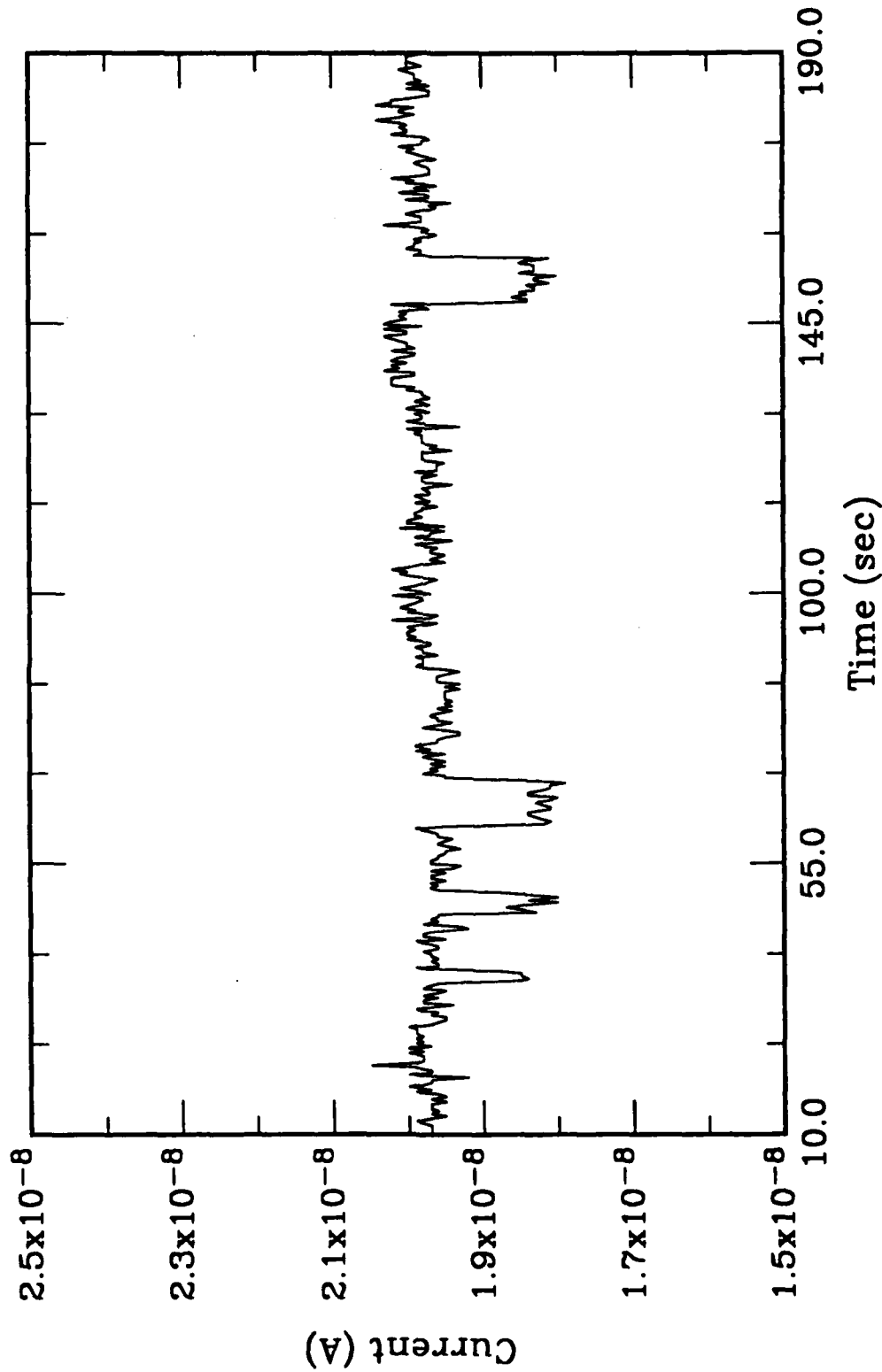


Fig. 7

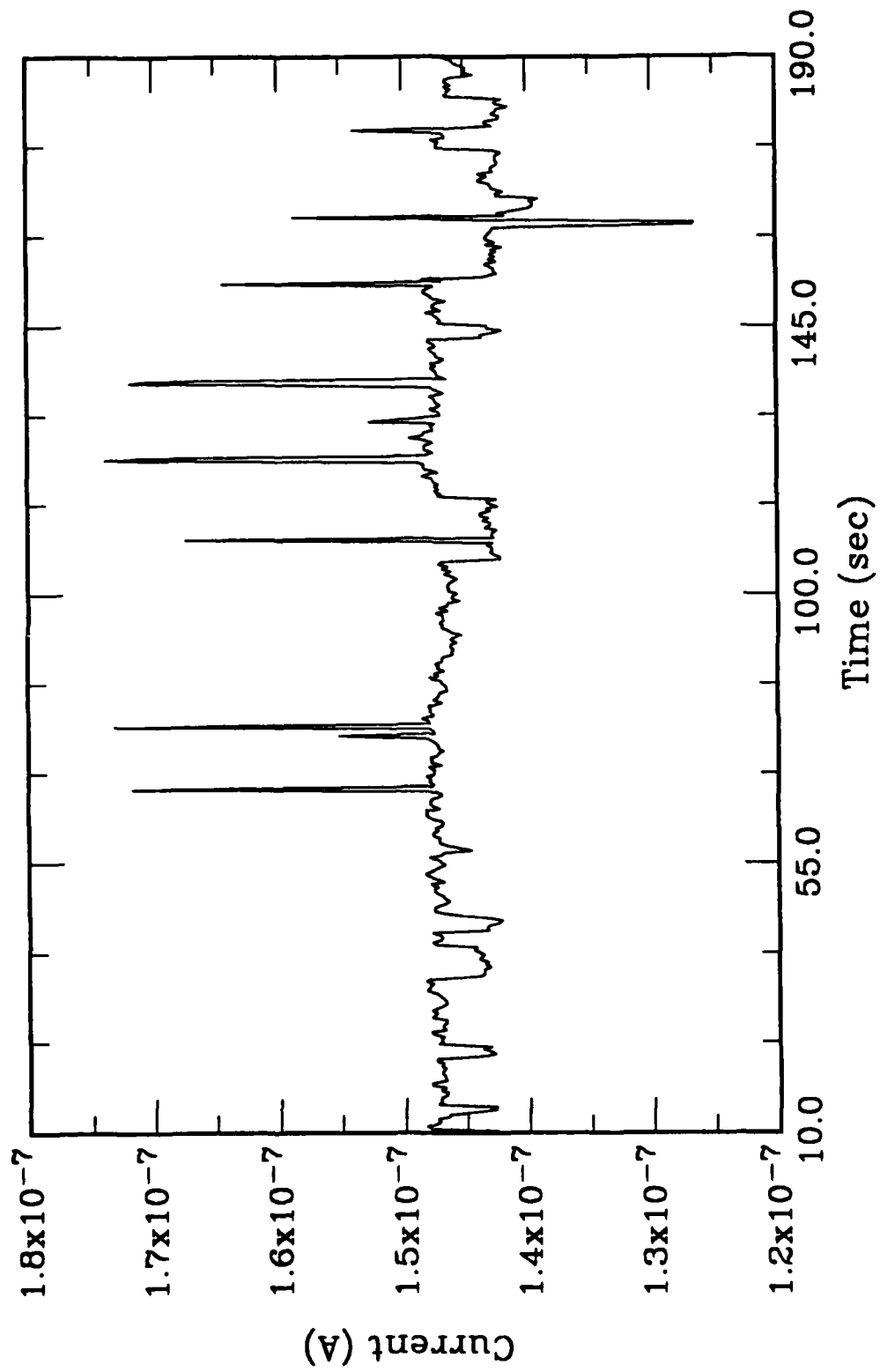


FIG. 8

APPENDIX 0

RESONANT TUNNELING IN A GaAs/AlGaAs BARRIER/InGaAs
QUANTUM WELL HETEROSTRUCTURE

Resonant tunneling in a GaAs/AlGaAs barrier/InGaAs quantum well heterostructure

M. A. Reed and J. W. Lee¹⁾

Central Research Laboratories, Texas Instruments Incorporated, Dallas, Texas 76265

(Received 31 October 1986; accepted for publication 27 January 1987)

Resonant tunneling through a GaAs contact/double AlGaAs barrier/single InGaAs quantum well strained-layer heterostructure was investigated. The structure exhibits negative differential resistance up to 275 K due to tunneling through the first excited state of the quantum well. Comparison of the observed peak positions with theory indicates that the conduction-band offset of the AlGaAs/InGaAs heterojunction is nearly 100%. Using the magnetic field dependence of the current-voltage characteristics, we have measured the effective mass of an electron while transiting a multicomponent quantum well tunneling structure. An effective mass for electrons in the InGaAs quantum well of approximately half the bulk effective mass is obtained.

InGaAs/(Al,Ga)As strained-layer heterostructures have been extensively studied in recent years for both optical and electronic device applications. Laser diodes,^{1,2} and recently InGaAs/AlGaAs modulation-doped field-effect transistors (MODFET's),³ have been demonstrated. In this letter, we report a detailed investigation of the first reported⁴ AlGaAs double barrier/single InGaAs quantum well resonant tunneling heterostructure. The ability to lower quantum well states with respect to GaAs contact layers (due to the higher electron affinity of InGaAs with respect to GaAs) is an important degree of freedom in tunneling device design. A previous investigation⁵ of tunneling in a strained-layer heterostructure system exhibited catastrophic degradation upon thermal cycling. The high-temperature performance and stability of these strained-layer quantum well structures will be an important area of investigation.

The conduction-band diagram of the resonant tunneling structure at zero and applied resonant bias is illustrated in Fig. 1. The sample used in this study was grown by molecular beam epitaxy in a Riber MBE-2300 on a 2-in. (100) n^+ Si-doped GaAs substrate. The structure consists of two undoped $\text{Al}_{0.25}\text{Ga}_{0.75}\text{As}$ barriers on either side of an undoped $\text{In}_{0.2}\text{Ga}_{0.8}\text{As}$ quantum well. The active structure was clad between two 0.6- μm -thick n^+ -GaAs contact layers. Cross-sectional transmission electron microscopy of this structure revealed AlGaAs barrier thicknesses of 40 Å (± 10 Å) and an InGaAs quantum well thickness of 60 Å (± 10 Å). No misfit dislocations were found during an extensive search of the quantum well structure.

Devices ranging from 2 to 100 μm^2 were fabricated by defining mesas on the sample surface with conventional photolithography techniques. AuGe/Ni/Au Ohmic contacts covered the top surface of the mesa device. Variable temperature measurements were performed in a helium-flow Janis cryostat or in a stabilized oven for higher temperature measurements.

Figure 2 shows the temperature variation of the static current-voltage characteristics of a typical device. The struc-

ture exhibits a 2.6:1 peak-to-valley ratio at low temperatures, which starts to degrade at approximately 100 K, the same temperature at which conventional GaAs/AlGaAs alloy barrier structures also start to exhibit a degradation. Negative resistance persists up to 275 K, and to 300 K in a small number of devices. The absence of peak shift with temperature indicates the absence of any parasitic contact resistance. These devices were cycled repeatedly to low temperatures and did not show any thermal degradation that was noted in a similar strained-layer structure.⁵

The asymmetry in the electrical characteristics noted in the conventional GaAs/AlGaAs double barrier structures also appears in this structure. One unusual aspect of this structure not seen in the GaAs/AlGaAs structures is the negative thermal activation of low bias current⁶ (i.e., decreasing current with increasing temperature), indicative that the quantum well state at zero bias does not lie below the Fermi level of the GaAs contact but above the GaAs conduction-band edge. This situation is achievable due to the negative conduction-band offset (with respect to the GaAs conduction band) of the InGaAs.

The expected resonant peak position was calculated by using a transfer matrix method⁷ and is shown in Fig. 3 as a function of In fraction in the InGaAs quantum well. Two parameters which have a degree of uncertainty are the quantum well thickness (due to the attainable resolution of the cross-section micrograph) and the conduction-band offset of the AlGaAs/InGaAs heterointerfaces: these are treated as free parameters. We have used effective masses linearly extrapolated between the pure binary effective masses, a composition of 0.25 for the Al content and a 65% conduction-band offset for the GaAs/AlGaAs heterojunctions. The error bars in the observed peak position in the figure indicate the width of the experimental resonant peak (for all temperatures) and the uncertainty in the In fraction obtained from growth data.

The calculated peak positions have two sets of curves for a given set of parameters (AlGaAs/InGaAs conduction-band offset and quantum well width); the set at low In fraction corresponds to resonant tunneling through the ground state of the quantum well, whereas the high In fraction set corresponds to resonant tunneling through the first excited

¹⁾ Now at Kopin Corp., 695 Myles Standish Blvd., Taunton, MA 02780.

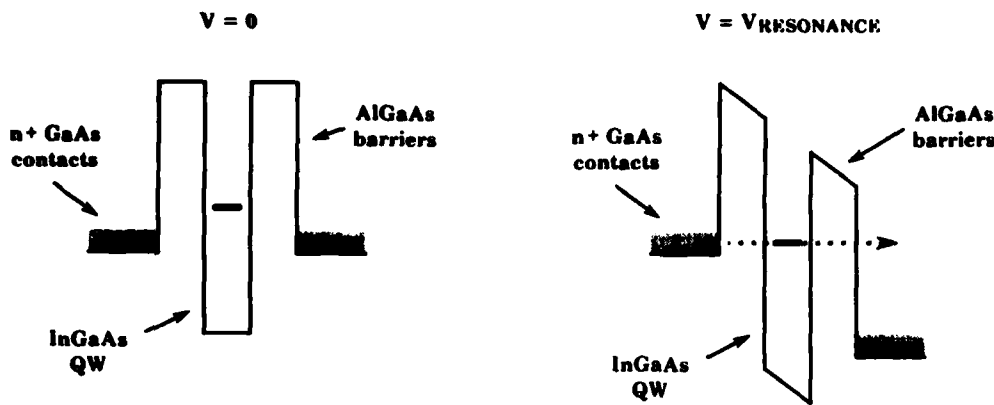


FIG. 1. Schematic conduction-band diagram for the GaAs contact/AlGaAs double barrier/InGaAs quantum well resonant tunneling structure under no bias (left) and resonant bias (right).

state of the quantum well. Clearly the observed peak is due to resonant tunneling through the first excited state. Additionally, it can be seen that the fit to a 60-Å well [labeled "100% (60 Å)"] is bad for any value of the conduction-band offset for the AlGaAs/InGaAs heterojunction (given in terms of the percentage of the band-gap difference that occurs in the conduction band). Using the maximum uncertainty in the well width (which gives 70 Å), we have plotted the fits for 100% conduction-band offset and 84% conduction-band offset (which had previously been measured in a GaAs/InGaAs heterojunction⁴). The observed peak position is quite bad for the 84% conduction-band offset, but is in excellent agreement with a maximum conduction-band offset of 100%. These measurements imply a InGaAs/AlGaAs conduction-band offset very close to 100%.

The presence of a multiple component system presents the unique opportunity to easily measure the effective mass of the tunneling electrons in the quantum well. Application of a magnetic field parallel to the current direction (perpendicular to the plane of the quantum well) offsets the $N = 0$ Landau level of the InGaAs quantum well with respect to the Fermi level in the GaAs contact due to the different effective masses of the two materials. Thus the resonant peak will shift with applied magnetic field, a mechanism that is physically distinct from the weak oscillations observed⁹ in the binary component system where the effective mass is the

same in the contact and the quantum well. Treating the effective mass of the GaAs as known, the effective mass of the InGaAs quantum well electrons, m_{InGaAs}^* , can be expressed by

$$\frac{1}{m_{\text{InGaAs}}^*} = \frac{1}{m_{\text{GaAs}}^*} + \frac{2a}{\hbar} \frac{\Delta V}{\Delta B}, \quad (1)$$

where $(\Delta V/\Delta B)$ is the change in the resonant peak position as a function of applied magnetic field, $a = 1$ if the applied bias is dropped totally across the double barrier structure and assuming that the bottom of the well shifts under bias by 1/2 eV.

The results for the peak shift with magnetic field are shown in Fig. 4, where a shift of $1.9 (\pm 0.2)$ mV/T for the positive bias peak and $2.7 (\pm 0.4)$ mV/T for the negative bias peak is observed in these samples. This yields an effective mass of $m_{\text{InGaAs}}^* = 0.032 (\pm 0.002)m_0$ for the positive bias peak and $m_{\text{InGaAs}}^* = 0.026 (+0.003, -0.002)m_0$ for the negative bias peak. This result is approximately half of the expected value for $0.058m_0$ for this composition material. Surprisingly the difference in the effective mass values for positive and negative bias conditions exceeds the experimental uncertainty. These results are probably experimental artifacts and imply that use of a sim-

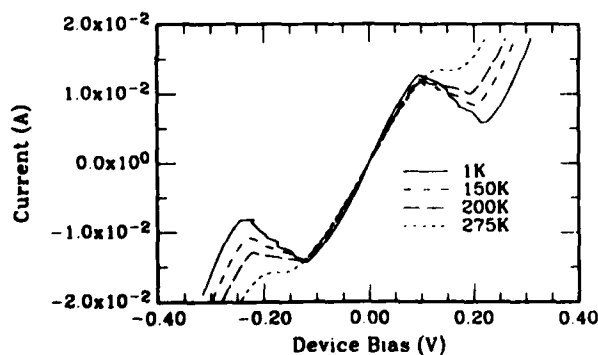


FIG. 2. Static current-voltage characteristics of the GaAs/AlGaAs/InGaAs double barrier resonant tunneling structure for different temperatures. Device mesa area = $25 (\mu\text{m})^2$.

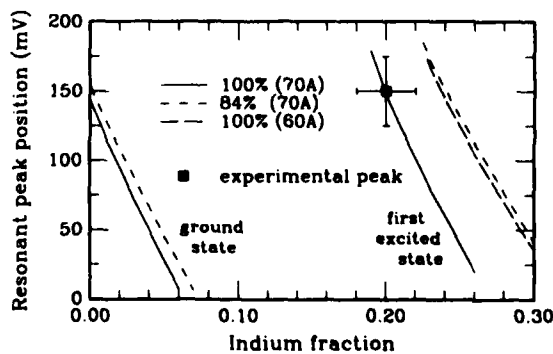


FIG. 3. Calculated resonant tunneling peak voltage vs In fraction for the double barrier structure. Plotted are the positions for tunneling through the ground and first excited state for quantum well sizes of 60 and 70 Å (in parenthesis), with AlGaAs/InGaAs conduction-band offsets of 84 and 100%. The data point is the observed peak position, with the error bars denoting the experimental width of the resonance and the uncertainty in the In fraction.

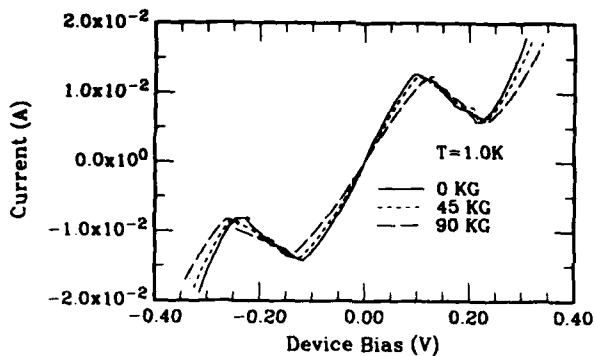


FIG. 4. Static current-voltage characteristics of the GaAs/AlGaAs/InGaAs double barrier resonant tunneling structure for the different magnetic fields. Device mesa area = $25 (\mu\text{m})^2$ and $T = 1.0 \text{ K}$.

plistic model for a resonant tunneling structure [as applied in Eq. (1)] is inadequate. It is expected that the effects of accumulation and depletion regions are significant in these structures. It has been suggested¹⁰ that the effects of these regions as well as the formulation of a space-charger layer by carriers in the quantum well can adequately account for such discrepancies.

In summary, we report the first study of a resonant tunneling structure where the center quantum well is of a different material than the contact or barrier regions, specifically a material that has a negative conduction-band offset with respect to the contact material. We have been able to fit the observed peak position for the AlGaAs/InGaAs heterojunc-

tion with a conduction-band offset of nearly 100%. We have also been able to measure the effective mass of electrons in this quantum well system and obtain an effective mass m_{InGaAs}^* of approximately $0.03m_0$, considerably less than the expected mass of 0.058. This result implies that accumulation and depletion regions in this structure are significant.

We are thankful to H.-L. Tsai for cross-sectional electron microscopy, R. T. Bate and W. R. Frensley for discussions, V. J. Goldman for sharing his unpublished results, and R. Aldert, R. Thomason, and P. Stickney for technical assistance. This work was supported by Texas Instrument Incorporated internal research funds.

¹M. J. Ludowise, W. T. Dietze, C. R. Lewis, M. D. Camras, N. Holonyak, B. K. Fuller, and M. A. Nixon, *Appl. Phys. Lett.* **42**, 487 (1983).

²W. D. Laidig, P. J. Caldwell, Y. F. Lin, and C. K. Peng, *Appl. Phys. Lett.* **44**, 653 (1984).

³A. Ketterson, M. Moloney, W. T. Masselink, C. K. Peng, J. Klem, R. Fischer, W. Kopp, and H. Morkoç, *IEEE Electron Device Lett.* **EDL-6**, 628 (1985).

⁴M. A. Reed and J. W. Lee, *Proceedings of the 18th International Conference on the Physics of Semiconductors, 11-15 August 1986, Stockholm* (to be published). Subsequent to this conference, two papers [H. Toyoshima, Y. Ando, A. Okamoto, and T. Itoh, *Jpn. J. Appl. Phys.* **25**, L786 (1986); and G. S. Lee, K. Y. Hsieh, and R. M. Kolbas, *Appl. Phys. Lett.* **49**, 1528 (1986)] on similar structures have appeared.

⁵P. Gavrilovic, J. M. Brown, R. W. Kaliski, N. Holonyak, K. Hess, M. J. Ludowise, W. T. Dietze, and C. R. Lewis, *Solid State Commun.* **52**, 237 (1984).

⁶M. A. Reed, J. W. Lee, and H.-L. Tsai, *Appl. Phys. Lett.* **49**, 158 (1986).

⁷B. Ricco and M. Ya. Azbel, *Phys. Rev. B* **29**, 1970 (1984).

⁸S. P. Kowalczyk, W. J. Schaffer, E. A. Kraut, and R. W. Grant, *J. Vac. Sci. Technol.* **20**, 705 (1982).

⁹E. E. Mendez, L. Esaki, and W. I. Wang, *Phys. Rev. B* **33**, 2893 (1983).

¹⁰V. J. Goldman, D. C. Tsui, and J. E. Cunningham (unpublished).

APPENDIX P

CONDUCTION PROCESSES IN THIN LAYER STACKS COMPOSED OF
ALUMINUM, INTRINSIC POLYCRYSTALLINE SILICON,
AND THERMAL SILICON DIOXIDE ON SILICON

APPENDIX P

Conduction Processes in Thin Layer Stacks Composed of Aluminum, Intrinsic Polycrystalline Silicon, and Thermal Silicon Dioxide on Silicon

by Richard Gale
Texas Instruments Incorporated

Abstract

Conduction at high fields in thin layer stacks of materials commonly used in silicon integrated circuit processing has been examined. These results show that Fowler-Nordheim tunneling is the dominant conduction process in metal-oxide-silicon single- and multiple-dielectric systems. When included in these structures, intrinsic (undoped) polycrystalline silicon is essentially depleted of carriers and acts as a second dielectric. Correction of the field strength in the oxides in these stacks to account for the bias dropped across the polysilicon results in a single set of parameters characterizing the tunneling process, which shows a rapid onset in the vicinity of 5 MV/cm. Conduction in series combinations of polycrystalline silicon and extremely thin oxides is dominated by Schottky barrier tunneling at Al-polysilicon interfaces, probably caused by defective thin oxides.

Introduction

The continuing economic success of semiconductor technology has been due in large part to reductions in size of constituent device components and increasing circuit complexity. A great deal of activity at Texas Instruments and other semiconductor manufacturers has been focused on the ultimate physical limitations governing the size of circuit primitives. Great strides have been made in designing and fabricating novel devices that take advantage of quantum effects to approach these ultimate physical limitations. Most of these advances have been made in GaAs because of the ease with which intrinsic material properties can be controlled, mainly concerned with bandgap control and through molecular beam epitaxy (MBE). The abruptness and

quality of the interfaces between dissimilar materials and the extreme thinness of layers afforded by this technology have made resonant tunnelling and quantum well structures possible.

The possibility of generating similar structures in silicon, and thus making available the extensive manufacturing experience in this material to the new generation of devices is attractive. The problem is that the "bandgap engineering" capability of MBE has no analog in silicon. There are two common materials in silicon technology with widely varying bandgaps: silicon (~ 1.1 eV) and silicon dioxide (~ 9 eV). These materials might be used to produce quantum well and superlattice structures in silicon. A major difficulty to this approach is the lattice mismatch between these materials, which has historically led to a disordered interface and transitional region. Indeed, several theories suggest that the disordered, transitional region may well be wider than the quantum well and superlattice spacing used in GaAs devices.^{1,2}

This program includes an effort to look at some of the problems involved in producing quantum coupled devices in silicon using these materials. The silicon effort was designed to be open-ended. That is, if the problems associated with the interface between silicon and silicon dioxide were solved, a major effort to produce quantum structures in silicon could be made as part of the program. The effort started with some basic questions about the nature of this interface: What conduction processes are dominant across the interface? What conduction processes are present in an oxide-polycrystalline silicon system? These questions need to be addressed before any esoteric silicon-on-insulator technology is investigated.

Experimental

Four lots of test devices were studied. In all cases the test devices consisted of capacitors ranging from 5.63×10^{-4} to 2.1×10^{-2} cm². Best results were obtained on the 5.63×10^{-4} cm² capacitors. In general, the vertical structure consisted of a thermal oxide on silicon, undoped polycrystalline silicon of various thicknesses, and an aluminum contact

layer. All oxides were grown at 900°C in dry oxygen. All poly layers were deposited at 600°C in a hydrogen ambient.

Lot 1 was fabricated on <100> p/p⁺ silicon wafers. The p layer was approximately 20 μm of $1 \times 10^{15} \text{ cm}^{-3}$ boron doped epitaxially grown silicon on a degenerately doped boron layer. Oxide thicknesses ranged from 60 to 80 Å. Following oxidation, two slices were metallized immediately with 8000 Å of Al, two slices had 80 Å of poly deposited before metallization, and two slices had 900 Å of poly. After the aluminum deposition, the capacitor pattern was defined and the metal and poly etched away.

Lot 2 will not be discussed in detail. This lot was used to test a procedure developed to answer the problem of making contact to quantum sized silicon structures based on oxygen transport blockage by silicon nitride. This technique, called bird's beak isolation, defines tunnel oxides or stacks in silicon nitride after the stack has been assembled. The slice is then heavily oxidized (~ 1 μm) so that the regions protected by the nitride layer will not be oxidized and will remain thin. Surrounding these areas is a thick protective oxide. Metal can then be deposited and patterned in such a way that the normal (Fowler-Nordheim) tunneling contribution will be through the thick oxide and will be negligible compared to the resonant tunneling through the protected regions. In addition, contact can be made to the metal overlying the thick regions to eliminate the risk of damage to the quantum structure by the probe or bond wire. Lot 2 showed that the desired isolation was achieved; however, incomplete removal of the nitride layer made it impossible to test these devices electrically.

Lot 3 starting material was changed to $1 \times 10^{19} \text{ cm}^{-3}$ <111> Sn doped silicon. This change was made after encountering difficulties associated with low carrier concentration at low temperatures in Lot 1. This lot consisted of MOS stack slices, metal-poly-oxide slices, and metal-poly-oxide-poly slices. This last stack was an attempt to create the type of structure required for resonant tunnelling devices. Experience on Lots 1 and 2 seemed to indicate that oxide and poly thicknesses could be controlled, but in Lot 3 a poly thickness of more than 1500 Å was obtained from the same (nominal)

deposition parameters that resulted in 80 Å of poly in Lot 1. As will be seen, the thick poly presented some difficulties during measurement.

Lot 4 consisted of 10 slices. Half of these were oxidized to various thicknesses and had a nominal 50 Å poly layer deposited, and the other half were oxidized to 30 Å and then had various thickness poly layers deposited. This lot was designed to determine to what degree oxide and poly thicknesses were controllable. Oxide thickness as measured by ellipsometry seemed to be quite reasonable, clearly in the linear regime (Figure 1), but poly thickness was more difficult to determine and apparently more variable (see Results below). Starting material in this case was $1 \times 10^{16} \text{ cm}^{-3}$ n-type Si.

All oxide thicknesses were measured by ellipsometry immediately after growth. Although in some cases reliable thickness measurements on the thinner oxides was difficult, it was possible to get repeatable figures on all slices. Following metal patterning, the high frequency capacitance versus voltage characteristic was obtained. In the case of MOS stacks this provided an independent measurement of oxide thickness, and where possible, was a reliable measure of poly thickness in stacks containing one or more poly layers. Slow sweep I-V characteristics were obtained on all devices, to breakdown on at least two devices on each slice.

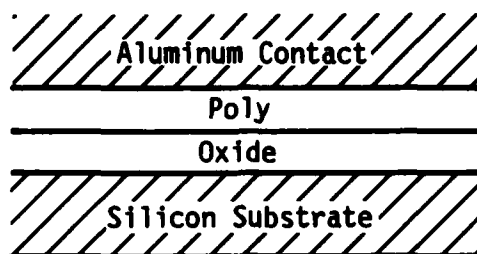
Results

Figure 2 shows the 1 MHz C-V characteristic of a capacitor from Lot 1 consisting of a metal-oxide-silicon stack. The oxide thickness in this sample is 80 Å. Figure 3 shows the I-V characteristic of this sample at room temperature. Note the onset of a conduction mechanism at approximately 5 V, an oxide field of slightly larger than 6 MV/cm. Also note breakdown at approximately 8 MV/cm. Figure 4 shows the I-V data plotted as $\ln(J/E_{ox}^2)$ vs $1/E_{ox}$ to facilitate analysis. This Fowler-Nordheim characteristic will be discussed in the next section. Figures 5, 6, and 7 present the same data for a metal-poly-oxide-silicon stack from the same lot with a poly thickness of 80 Å. Figures 8, 9, and 10 present C-V, I-V, and a Fowler-Nordheim plot for a metal-poly-oxide-silicon stack with a poly thickness of 900 Å. All oxide thicknesses in these samples were measured by ellipsometry to be 80 ± 5 Å.

Figures 11 through 19 show similar results (C-V, I-V, and $\ln(J/E_{ox}^2)$ vs $1/E_{ox}$) for representative structures from Lot 3. Figures 11, 12, and 13 are from a MOS stack with a 150 Å oxide layer. Figures 14, 15, and 16 are from a metal-poly-oxide-silicon stack with a 160 Å oxide and a 1640 Å poly layer. Figures 17, 18, and 19 were taken on a sample consisting of metal-oxide-poly-oxide-silicon. In this sample, the first oxide (grown on substrate) was measured by ellipsometry to be 160 Å, the poly layer 1310 Å, and the second oxide 160 Å. The poly layer was measured by ellipsometry using a multilayer program and the second oxide thickness inferred from the C-V results. A test of the inference was made on the metal-poly-oxide-silicon sample where the measured poly thickness and that inferred from the C-V measurements were in agreement (± 20 Å).

Figures 20 through 39 show I-V and $\ln(J/E_{ox}^2)$ vs $1/E_{ox}$ for the samples of Lot 4. It was not possible to obtain C-V characteristics for any of these samples because even the smallest area capacitors loaded the capacitance bridge. As will be discussed, this is thought to be the result of leakage, not the large capacitance values. Nor was it possible to obtain reliable ellipsometry figures for the poly layers, probably because of the extreme thinness of the underlying oxides. Hence, although the oxide thicknesses are known reliably, the overall stack thickness is not known. Poly thickness figures given are nominal values only. Figures 20 and 21 are from a metal-poly-oxide-silicon stack with a 30 Å oxide and 100 Å of poly. Figures 22 and 23 are from the same type of stack with a 30 Å oxide and 150 Å of poly. Figures 24 and 25 were taken on a sample with a 30 Å oxide and 200 Å of poly. Slice 4 had no poly, a MOS stack with a 30 Å oxide, and is shown in Figures 26 and 27. All the remaining slices had nominal poly layers 50 Å thick and varying oxide thicknesses. Figures 28 and 29 are from a structure with a 30 Å oxide. Figures 30 and 31 are from a structure with a 32 Å oxide. The structure from which Figures 32 and 33 were obtained had a 38 Å oxide. Figures 34 and 35 came from a stack with a 43 Å oxide. Figures 36 and 37 were taken on a sample with a 46 Å oxide, and Figures 38 and 39 from a stack with a 51 Å oxide. The stack parameters for the slices in Lot 4 are condensed in Table 1.

Table 1
Stack Parameters for Devices of Lot 4



Slice	Poly	Oxide
1	100	30
2	150	30
3	200	30
4	--	30
5	50	30
6	50	32
7	50	38
8	50	43
9	50	46
10	50	51

Note: all poly thicknesses nominal; all oxide thicknesses measured by ellipsometry.

Data reduction procedures, results, significance

Figure 2 confirms an oxide thickness of approximately 80 Å from C-V measurements for this MOS stack. When the I-V data of Figure 3 are plotted as $\ln(J/E_{ox}^2)$ (Figure 4), Fowler-Nordheim parameters of $E_0 = 254$ MV/cm, and $\ln(J/E_{ox}^2)_0 = -12.1$ are obtained. These are in excellent agreement with literature values, e.g., $E_0 = 240$ MV/cm and $\ln(J/E_{ox}^2)_0 = -12.4$.² These values were obtained from a least-squares fit to a visually selected range of the Fowler-Nordheim plot of Figure 4. Although in this particular plot the linear region is small, the fit is good in this regime. Other devices from this slice yielded similar results. Similar data from a metal-poly-oxide-

silicon stack in Figures 5-7 did not originally yield a linear region in the Fowler-Nordheim plot. However, the C-V data indicated a discrepancy between the oxide thickness measured by ellipsometer and that indicated by the capacitance. When the capacitance was modeled as the series combination of oxide and intrinsic silicon,

$$1/C = 1/C_{Ox} + 1/C_{Si}$$

$$1/C = d_{Ox}/e_{Ox}A + d_{Si}/e_{Si}A$$

where d and e represent the thicknesses of the layers and their dielectric constants, respectively, the poly thickness obtained agrees with that obtained from the double-dielectric ellipsometry results (80 Å). When the Fowler-Nordheim plot is corrected similarly to incorporate the oxide field strength, Figure 7 is the result. Figure 7 shows a reasonable linear region with a slope (200 MV/cm) that is significantly different from published results on MOS stacks and a serious discrepancy in the intercept (-4.4). Certainly the problem with the intercept [extrapolated $\ln(J/E_{Ox}^2)$ at infinite oxide field] can be attributed to an incorrectly or incompletely modeled poly/oxide or Al/poly interface, but there should exist a Fowler-Nordheim regime in which oxide tunneling is the dominant conduction mechanism. Figures 8 through 10 represent the same data for a metal-poly-oxide-Si stack with a 900 Å poly layer. Here the discrepancies are worse. In this device, the F-N intercept is closer to published values (-8.8), but still significantly different, and the slope is almost an order of magnitude different. A comparison of the I-V characteristics between the 80 Å poly stack and the 900 Å poly stack seems to indicate thinner poly in the 900 Å stack. This is not reflected in the capacitance data, which in the 900 Å case again agrees with the ellipsometry measurements. It seems likely that a different poly conduction mechanism is present in the 900 Å device, perhaps a grain boundary effect that is present only at high fields (not excited by the small signal capacitance measurements).

Figures 11 through 19 show C-V, I-V, and Fowler-Nordheim data for representative devices from lot 3. In this lot, again, the $\ln(J/E_{Ox}^2)$ vs $1/E_{Ox}$ plots for the structures with polysilicon layers exhibited no linear

region until the data were corrected for the voltage drop across a depleted poly layer. When this correction was made, the slopes obtained were in good agreement with published values: -226 MV/cm for the MOS stack, -266 MV/cm for the stack with a single oxide and 1640 Å of poly, and -247 MV/cm for the double oxide, 1310 Å poly stack. The intercept in the case of the MOS stack is in good agreement with other work, -12.4. The intercepts in the devices with poly layers are both approximately a factor of 2 different, however: -23.2 for the single oxide, and -23.7 for the double oxide. These discrepancies are again attributed to the oxide-poly or Al-poly interface. In general, these devices showed region in which the Fowler-Nordheim characteristic was quite linear and yielded good values for the slope. The disturbing feature of this lot was in the fabrication parameters. Oxidation temperatures and times identical to those used in the first lot, where the result was an 80 Å oxide, produced 160 Å oxides in this lot. Similarly, polysilicon deposition parameters that produced 80 Å layers in Lot 1 were entirely out of control in Lot 3, generating poly layers of 1310 Å and 1640 Å.

The devices of Lot 4 bear out the concern for control over processing parameters. Although the data of Figure 1 show that the oxidation is clearly in the linear regime, neither the 80 Å oxide of Lot 1 nor the 160 Å oxide of Lot 3 fit the straight line of Lot 4 oxidation times. This may be because of poor control over the oxidation times or because of poor control over the oxidation ambient. Fairly low concentrations of contaminant water vapor have been shown to have large effects on oxidation kinetics.⁴ As discussed previously, it was not possible to obtain polysilicon thicknesses in these devices. Readings from ellipsometry were erratic even for the thicker poly films, and the capacitance bridge showed current overload in the smallest area capacitors.

Figures 26, 28, 30, 32, 34, 36, and 38 show essentially identical I-V characteristics for the devices with a nominal 50 Å poly layer and oxides ranging in thickness from 28 Å to 51 Å. The lack of dependence of the I-V characteristic on oxide thickness in these devices implies that oxide conduction was not the limiting conduction mechanism. The lack of any threshold for conduction suggests that the oxides were not continuous, since

thresholds were observed in other samples in which Fowler-Nordheim tunneling was dominant. Finally, the similarity of the I-V characteristics for the MOS stack (Figure 26) and the metal-poly-oxide-silicon stack with a 29 Å oxide (Figure 28) suggests that conduction through the poly was not limiting. These two samples had identical oxide thickness. The device shown in Figure 26 had no poly; the device shown in Figure 28 had 50 Å of poly. Thus, it appears that the poly layer was not continuous. If the analysis of Lenzlinger and Snow⁵ is applied to these data, a metal-semiconductor Schottky barrier height of 0.36 eV is obtained, approximately correct for Al to $1 \times 10^{15} \text{ cm}^{-3}$ p-type Si.

None of the Fowler-Nordheim characteristics for the devices in this lot showed a reasonably linear regime. The plots (Figures 21, 23, 25, 27, 29, 31, 33, 35, 37, and 39) are included for comparison to F-N plots in other lots. The devices shown in Figures 20 through 25 were the stacks with thicker poly layers. Figure 20 (100 Å), Figure 22 (150 Å), Figure 24 (200 Å) show I-V characteristics that scale reasonably with the poly thickness. Oxide integrity is assumed to be a problem, since these oxides were grown at the same time as the other devices in this lot. The variability of the I-V slope in these three devices suggests that the poly was continuous and was essentially resistive.

Conclusions

It has been shown that Fowler-Nordheim tunnelling in thermal silicon dioxide is the limiting conduction mechanism in continuous metal-polysilicon-oxide-silicon stacks. Undoped polysilicon is depleted of carriers when included in these stacks. In studying thin layer stacks, control of process parameters and repeatability of processing conditions is of critical importance.

NO-R106 969

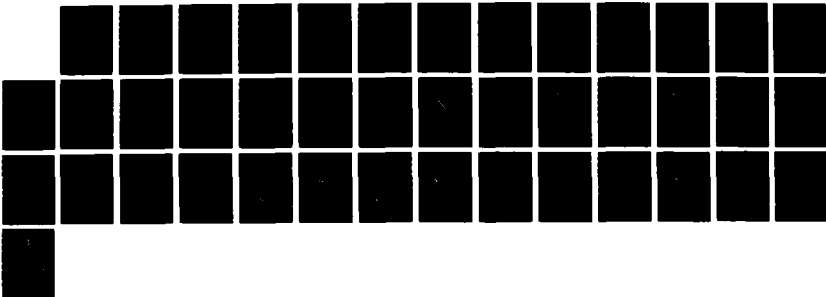
MANOELECTRONICS(U) TEXAS INSTRUMENTS INC DALLAS
R T BATE ET AL. 14 AUG 87 TI-88-87-50 ARO-21243.11-EL
DARG29-84-C-0009

3/3

UNCLASSIFIED

F/G 20/10

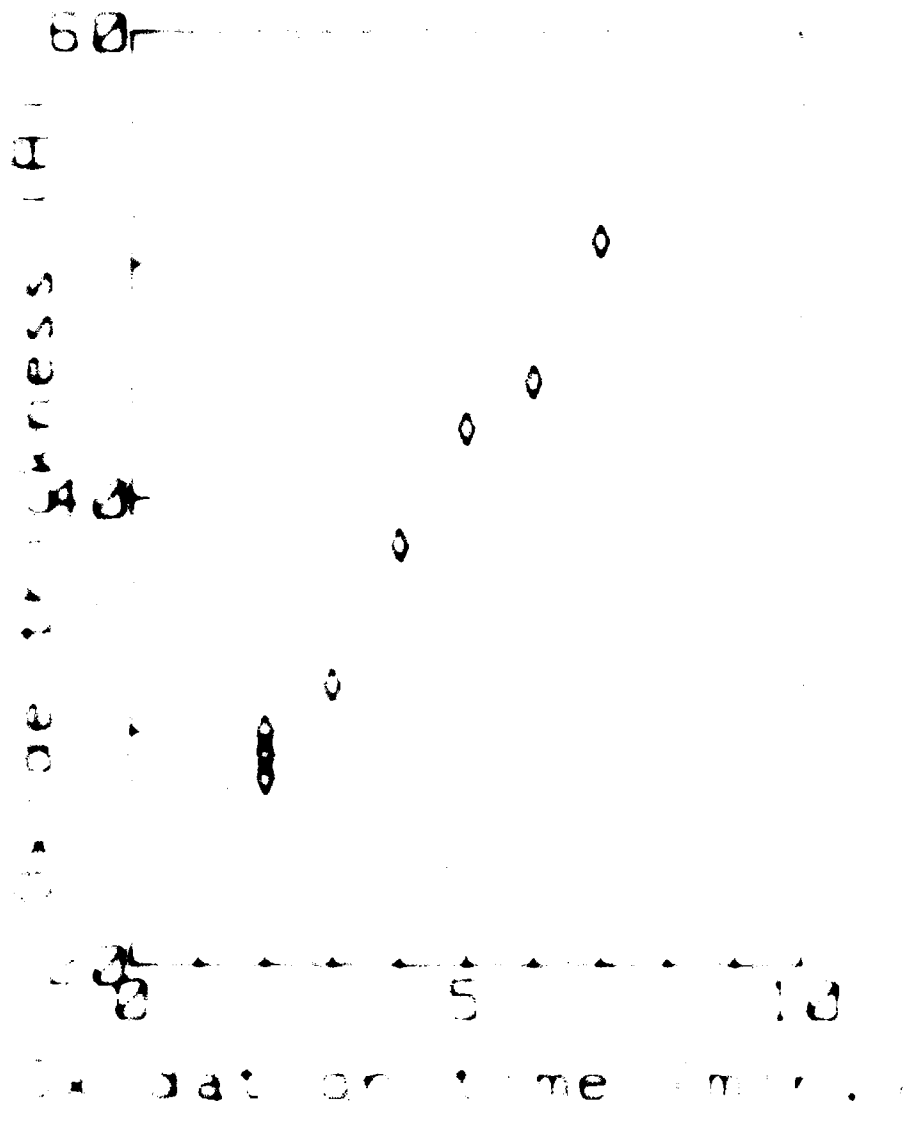
ML



1950
1951
1952
1953
1954
1955
1956
1957
1958
1959
1960

References

1. F. J. Grunthaner, P. J. Grunthaner, R. P. Volante, B. F. Lewis, J. Moorjian, and A. Hallauer, *J. Vac. Sci. Technol.* **15**, 1043 (1979).
2. J. Moorjian and G. Zeman, *J. Appl. Phys.* **53**, 940 (1982).
3. G. M. Huxford and G. C. Sarason, *Proc. Acad. Natl. Sci.* **1954**, p. 197.
4. A. J. Grove, *Physics and Technology of Semiconductor Devices*. (John Wiley & Sons, N.Y., 1967).
5. G. Lang Berger and I. M. Ross, *J. Appl. Phys.* **53**, 300 (1982).



across the gap

Device: MSd5TR, examined on 07/08/85

1. Characteristics:

- oxide thickness: 75 Angstroms, gate area: 1.42 cm²
- oxide doping density: approximately $+2.52E+16$ cm⁻³ (convergence not obtained)
- flatband capacitance of $+1.3E-10$ F, obtained at flatband voltage of -1.27 V
- low dC/dV at flatband of $+9.54E-10$ F/V
- inversion difference of -0.91 V
- area flatband shift of -0.26 V
- total charge density of $+6.92E+11$ cm⁻²

Figure 2

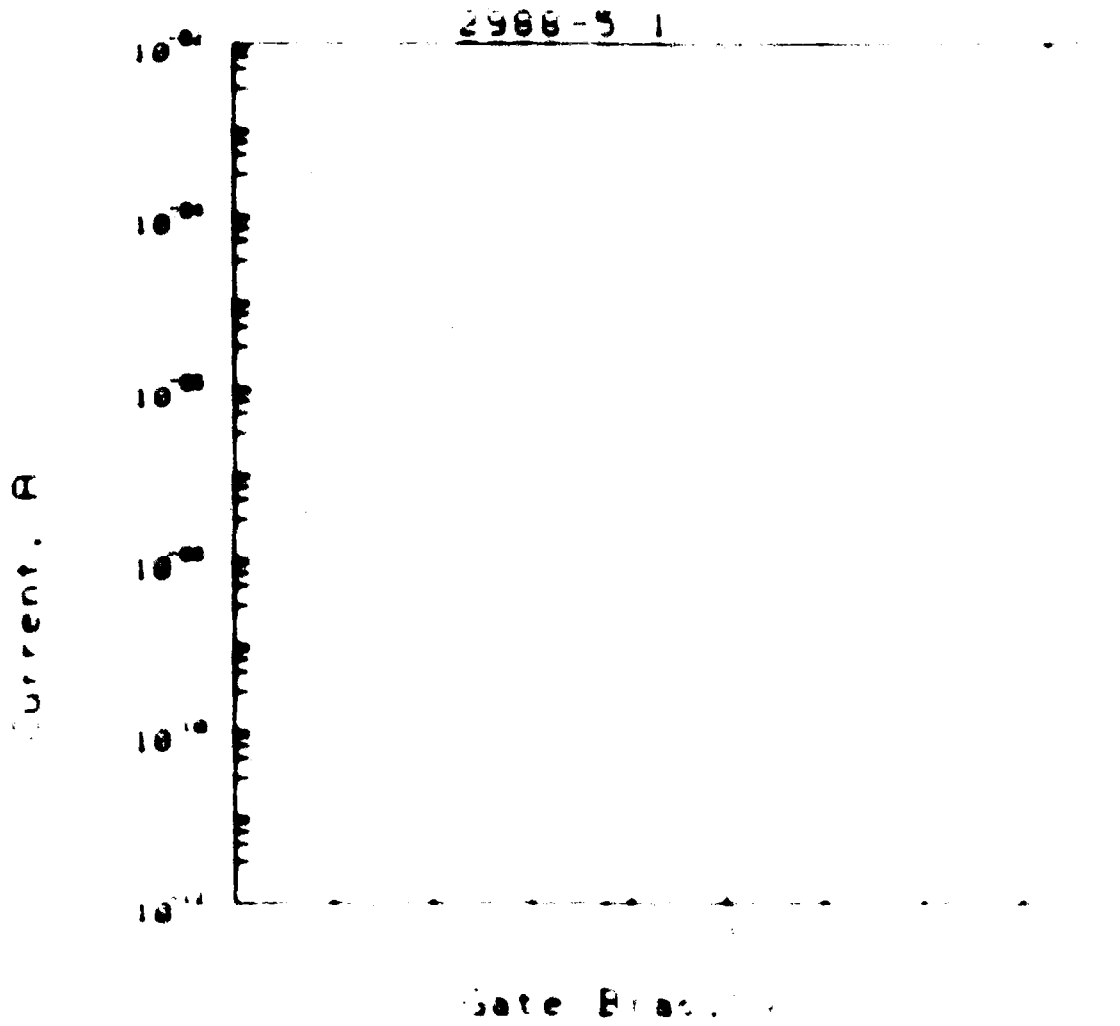
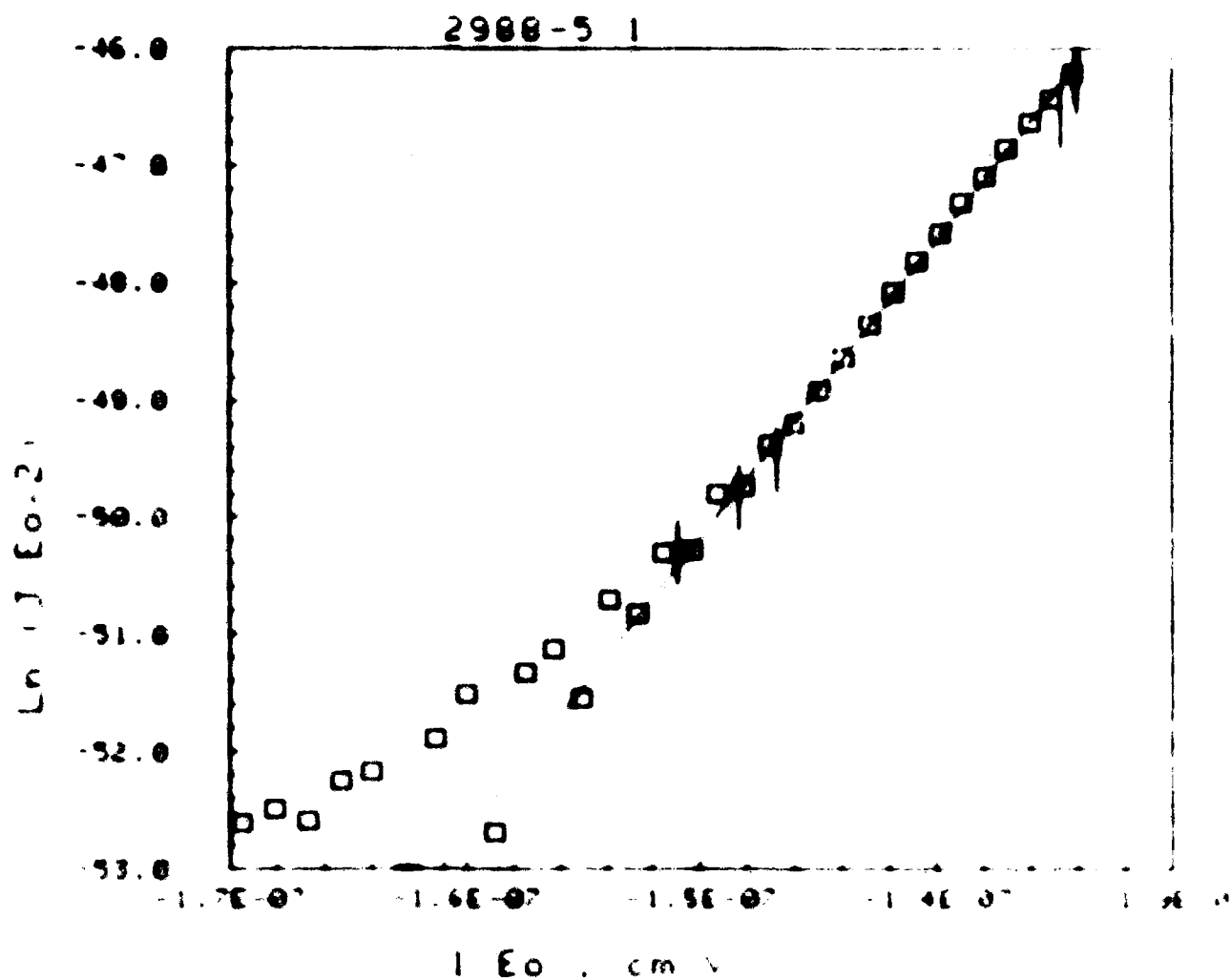


Figure 3



Slope η = $2.94E+00$ V/cm
 Intercept (zero potential) = $-1.21E+01$ A/cm²
 Coefficient of linear correlation = 0.9994, 31 degrees of freedom

Figure 4

Electrostatic Map

on 20881 IR, examined on 07-08/85

Characteristics:

- oxide thickness 100 Angstroms, gate area 2.14×10^{-2} cm²
- carrier doping density approximately 1.15×10^{13} cm⁻³ (convergence not obtained)
- flatband capacitance of 1.87×10^{-12} F, obtained at flatband voltage of +4.34 V
- capacitance (dC/dV) at flatband of 6.33×10^{-11} F/V
- junction difference of -0.62 V
- flatband shift of +4.96 V
- charge density of -1.05×10^{13} cm⁻²



Figure 5

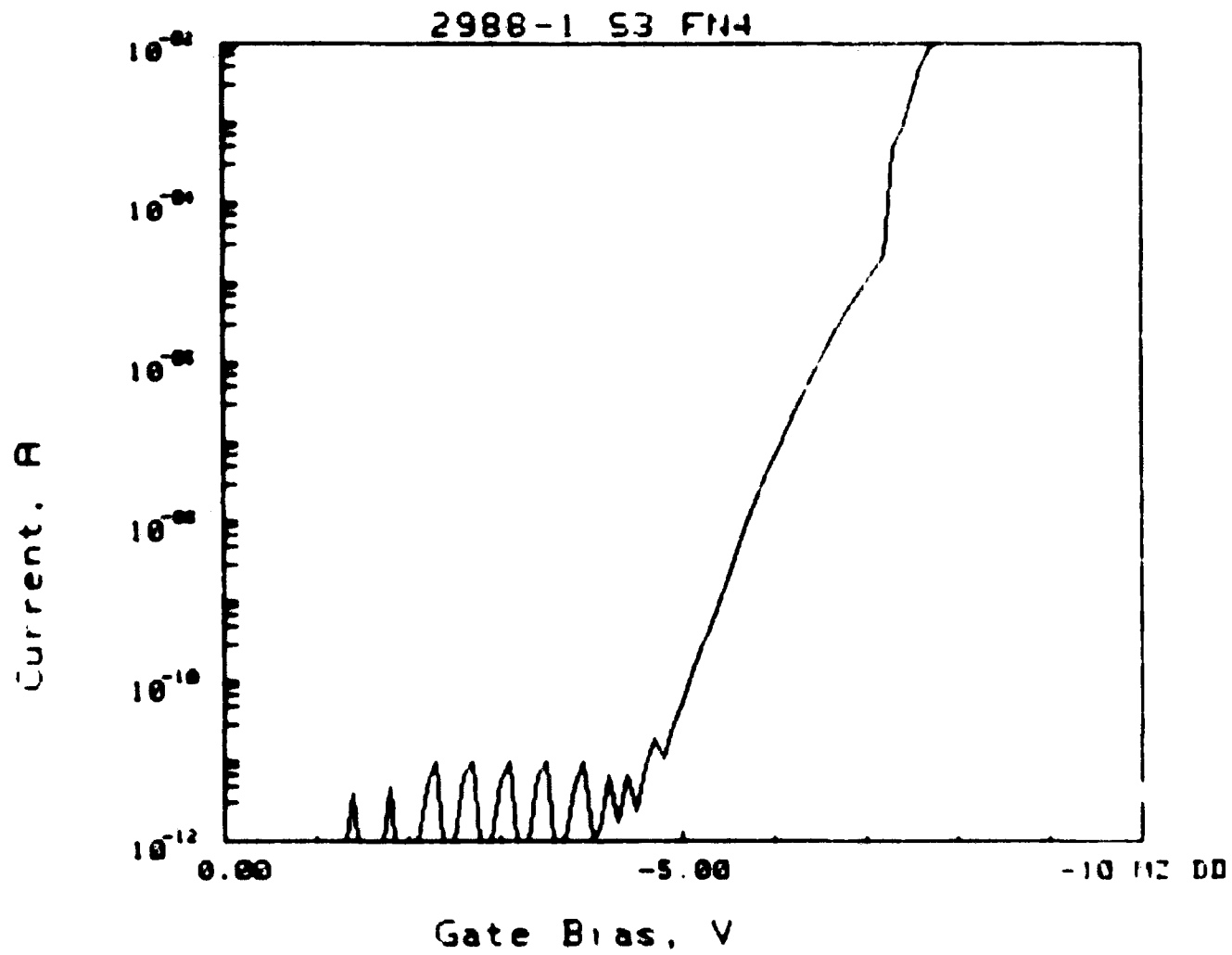
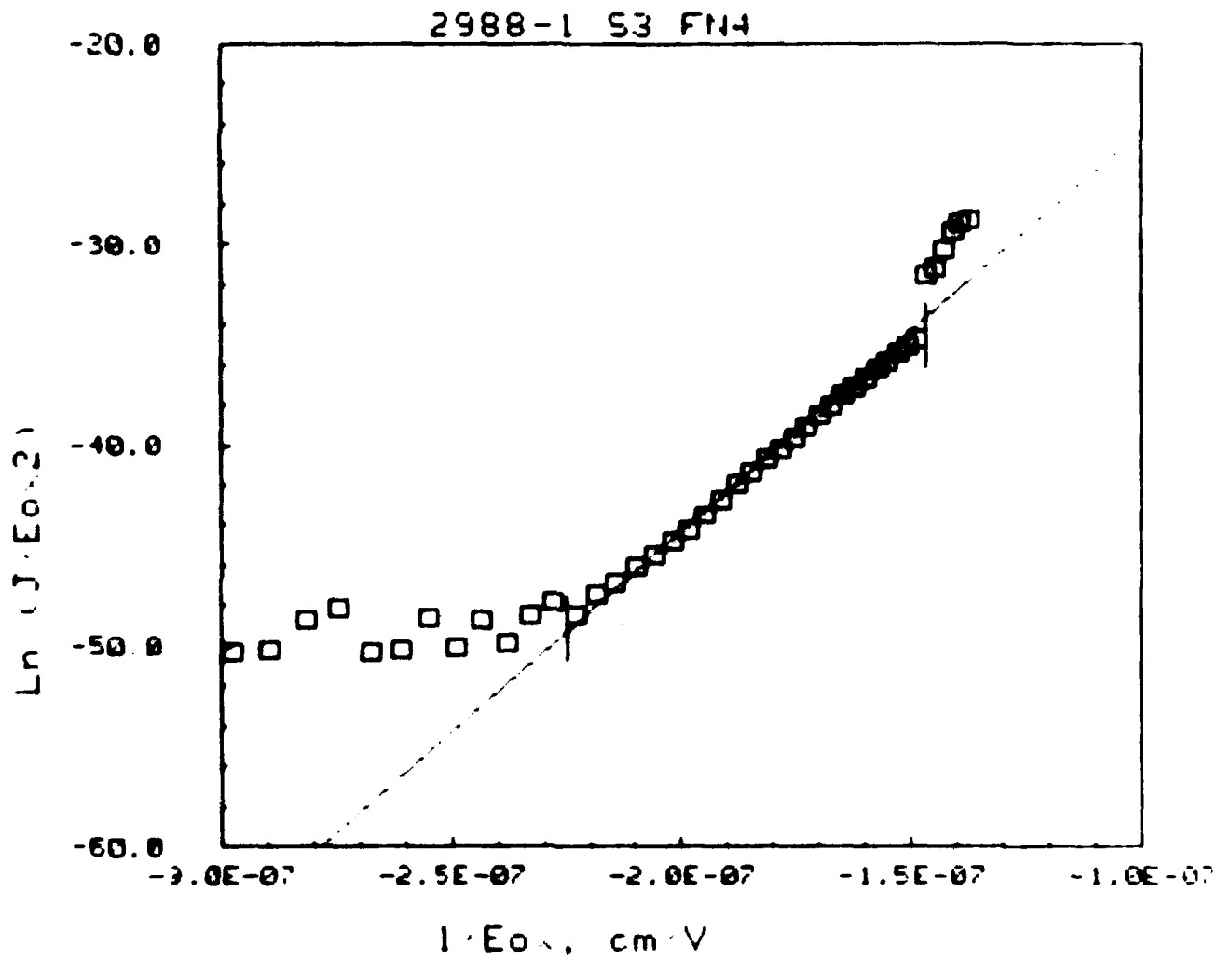


Figure 6



Slope (E₀) = 2.00E+00 V cm
 Intercept (pre-exponential) = -4.38E+00 A V²
 Coefficient of linear correlation = 0.9900, 25 degrees of freedom

Figure 7

Capacitor slice Map

Data from 2988#3TR, examined on 07/08/85

Initial characteristics:

oxide thickness 375 Angstroms, gate area $1.03E-02$ cm²
p-type, doping density approximately $+1.50E+15$ cm⁻³
(convergence not obtained)
Flatband capacitance of $+4.90E-10$ F, obtained at
flatband voltage of -0.68 V
Slope (dC/dV) at flatband of $+8.03E-10$ F/V
workfunction difference of -0.86 V
Total flatband shift of $+0.17$ V
Total charge density of $-9.92E+10$ cm⁻²

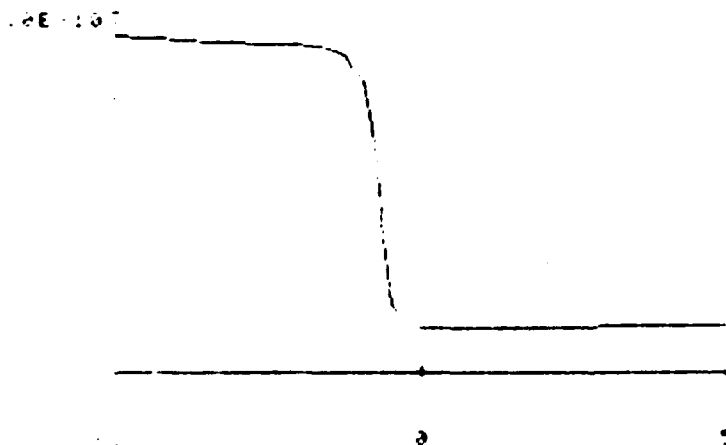


Figure 8

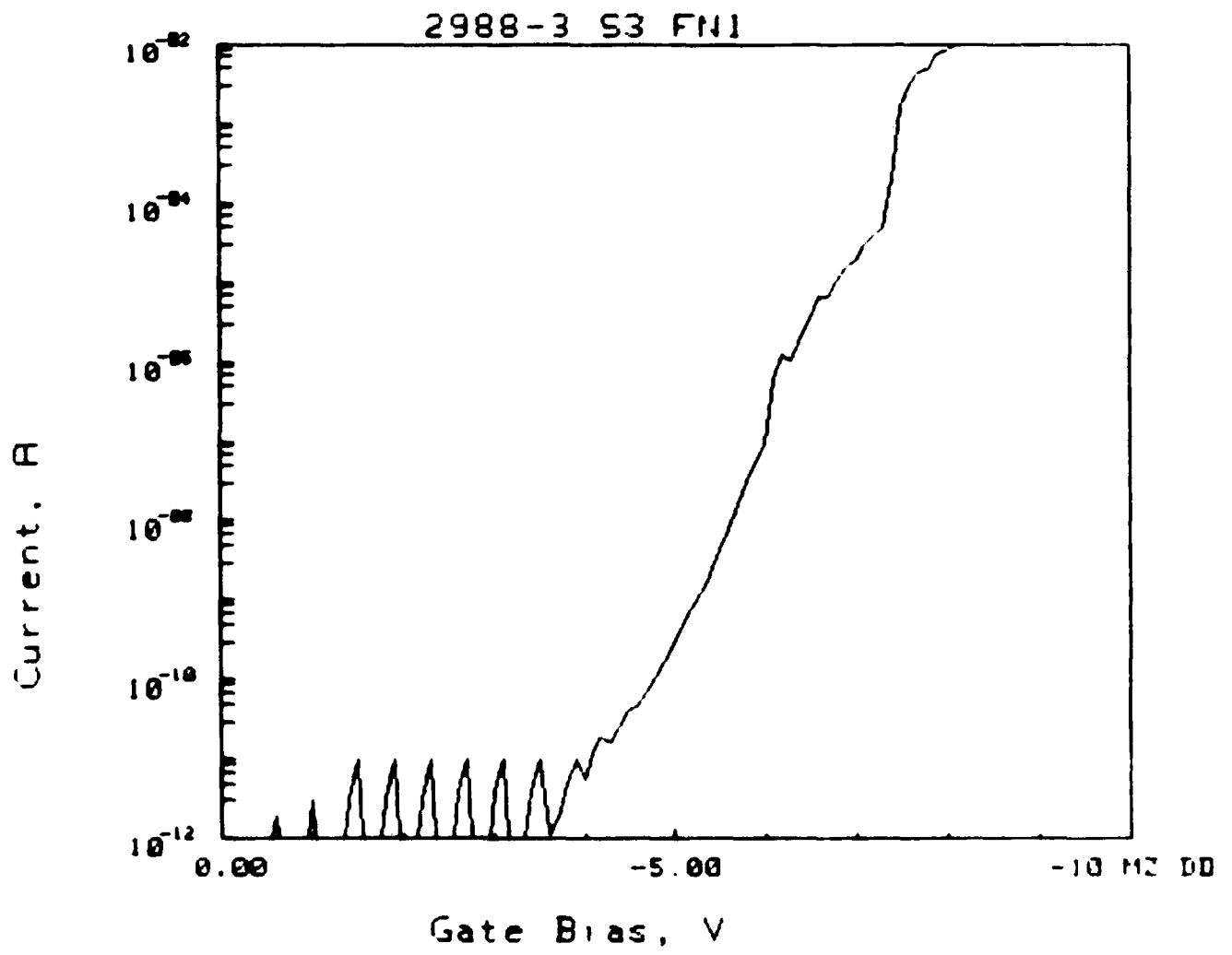
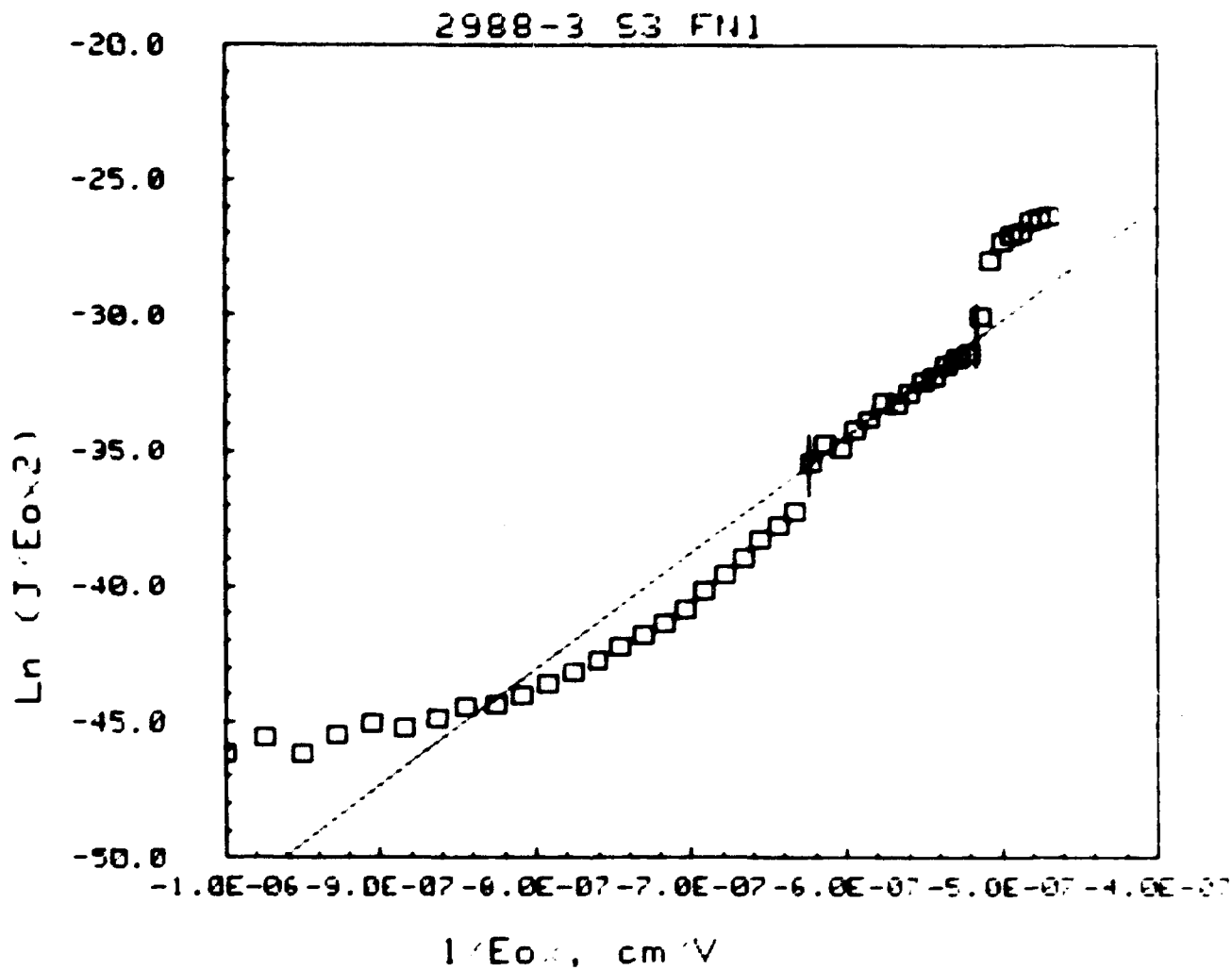
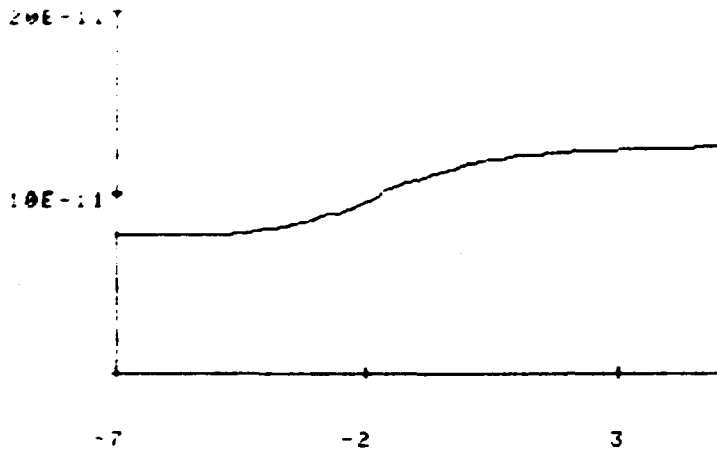


Figure 9



Slope (E_0) = $4.28E+07 \text{ V/cm}$
 Intercept (pre-exponential) = $-8.81E+00 \text{ A/V}^2$
 Coefficient of linear correlation = 0.9821 , 12 degrees of freedom

Figure 10



Capacitor Slice Map

Data from 3303 1 B. examined on 06/26/85

Initial characteristics:

Oxide thickness 154 Angstroms, gate area $5.78E-04 \text{ cm}^2$
 n-type, doping density approximately $+1.07E+18 \text{ cm}^{-3}$
 (convergence obtained in 5 iterations)
 Flatband capacitance of $+1.18E-10 \text{ F}$, obtained at
 Flatband voltage of $+0.16 \text{ V}$
 Slope (dC/dV) at flatband of $+5.92E-12 \text{ F/V}$
 Workfunction difference of -0.14 V
 Total flatband shift of $+0.30 \text{ V}$
 Total charge density of $-4.08E+11 \text{ cm}^{-2}$

Figure 11

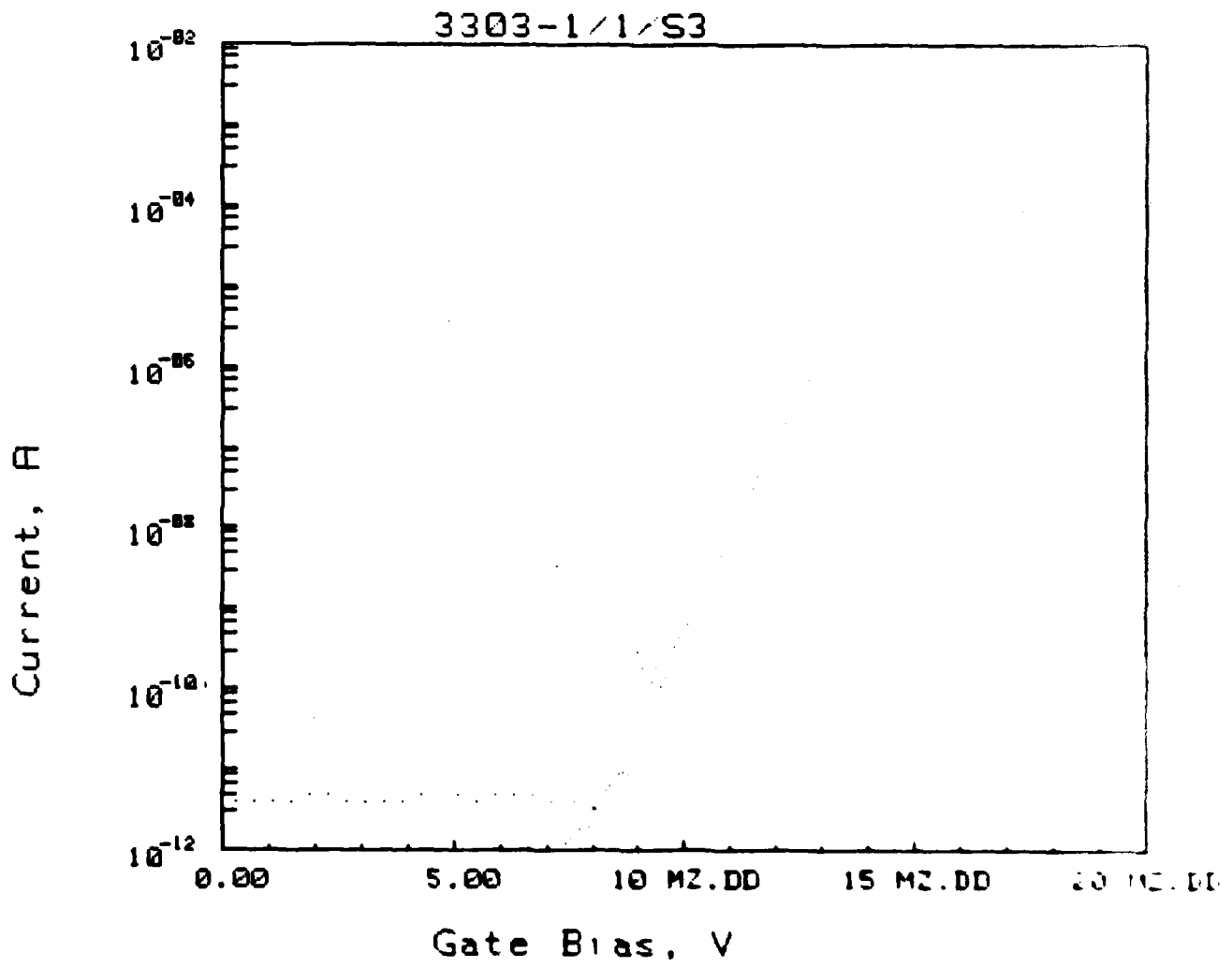
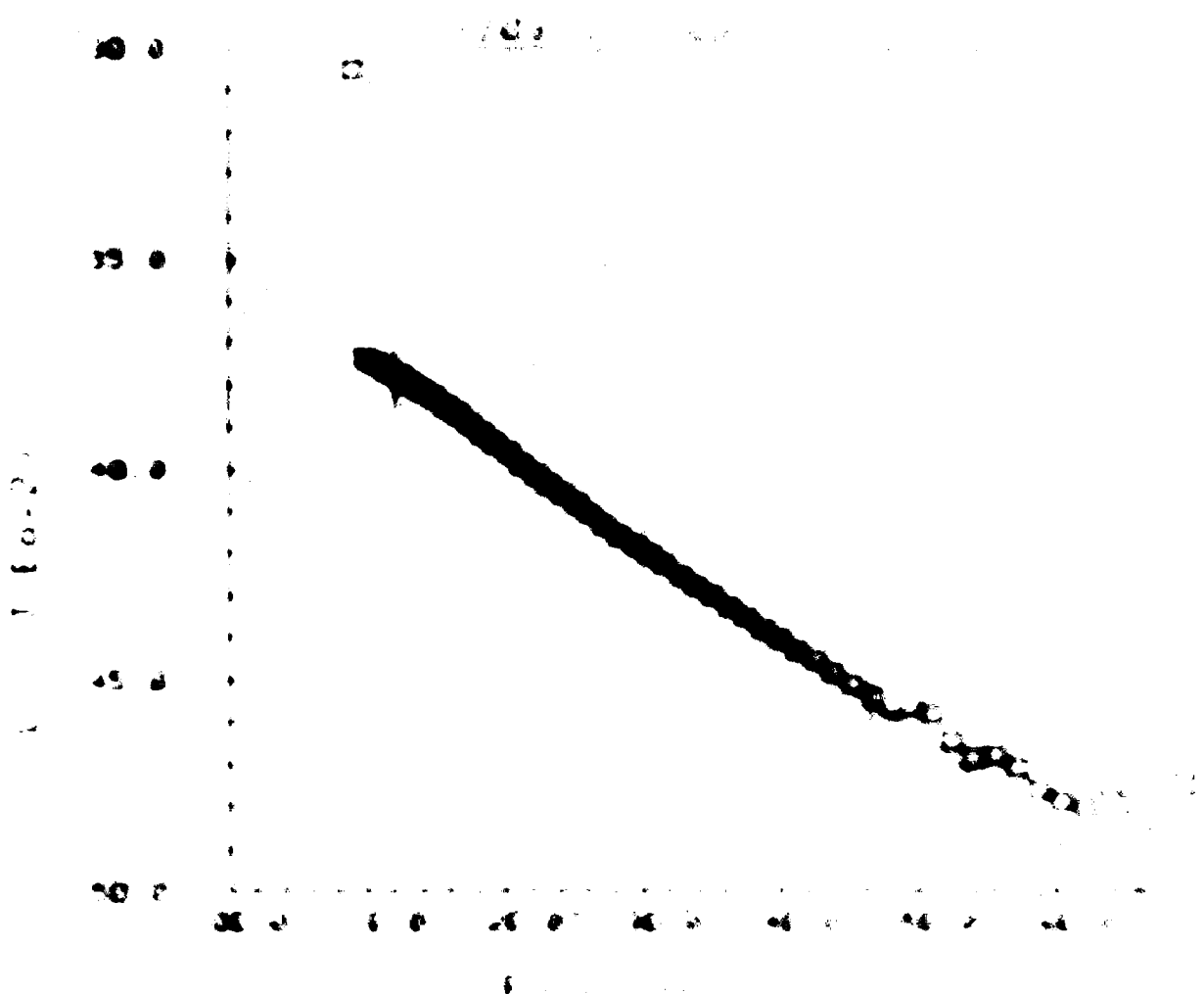


Figure 12



Intercept: 75
 Slope: -0.35

...

...

...

... on 2/25/65 ...

... characteristics

... of ... gate area ...
 ... approximately ...
 ... obtained ...
 ... obtained at
 ... voltage of ...
 ... of ...
 ... difference ...
 ...
 ...

Figure 18

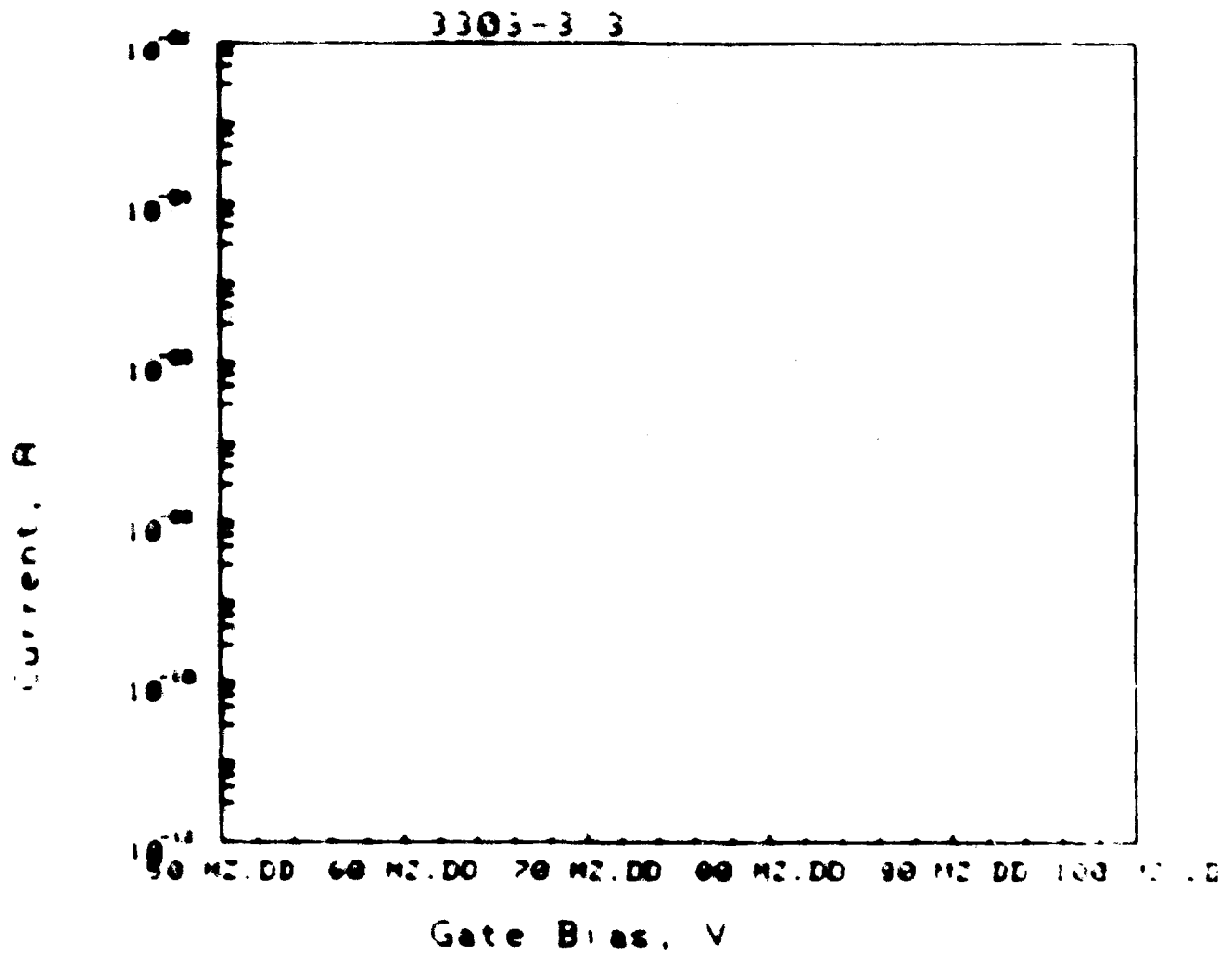
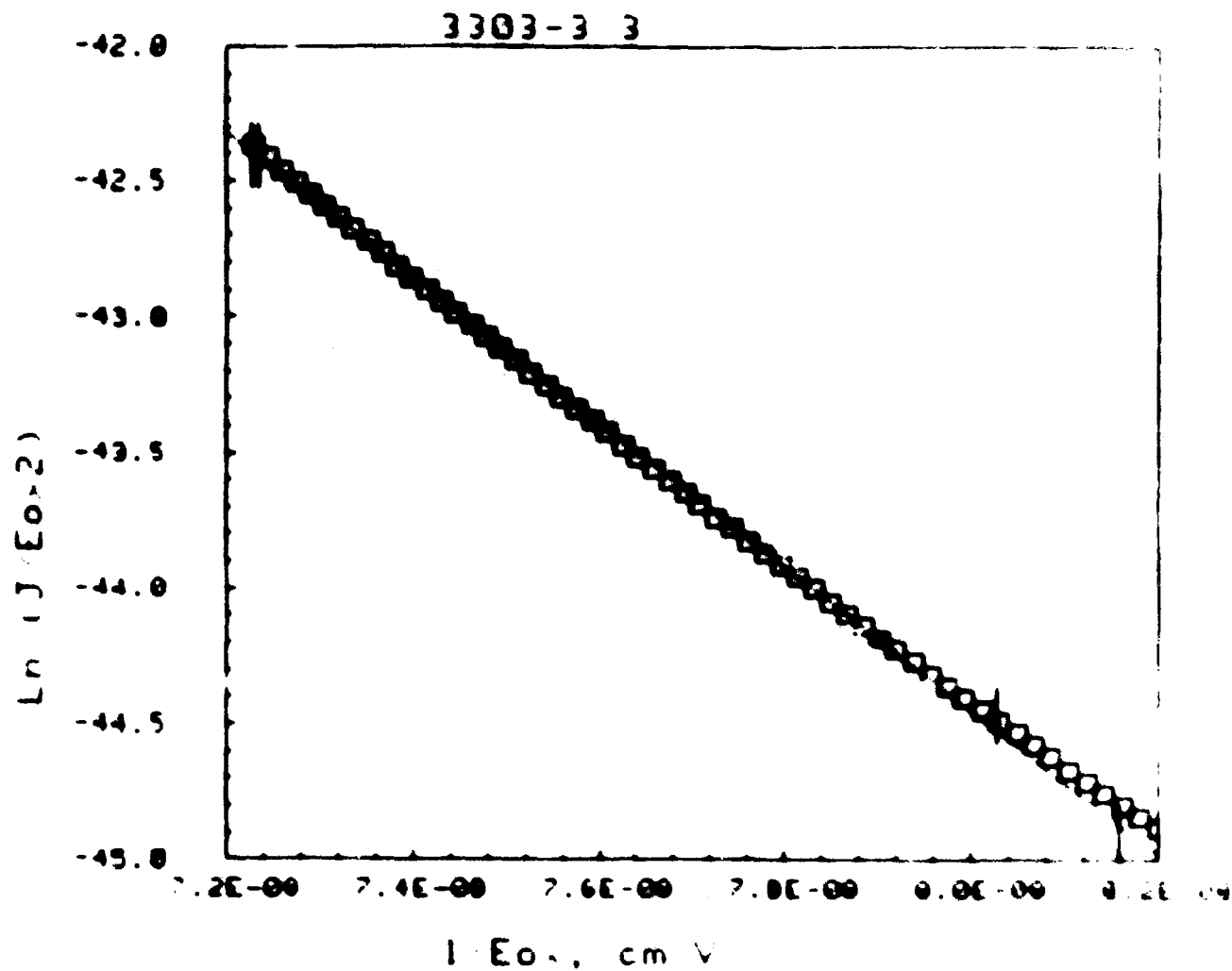
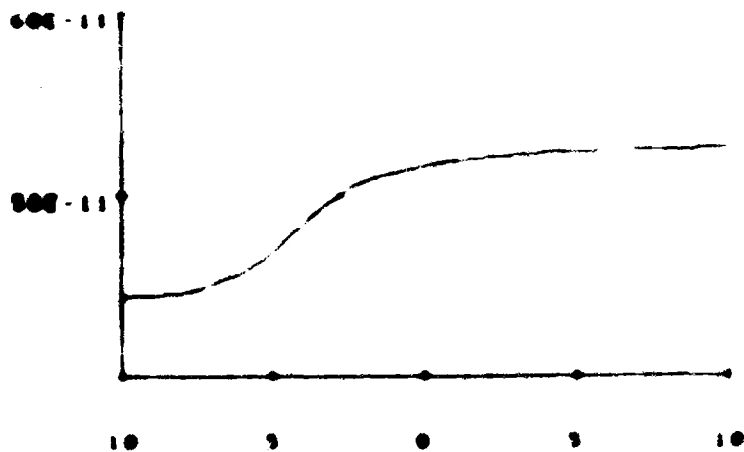


Figure 15



Slope (E_o) = $-2.66E+00 \text{ V cm}^{-1}$
 Intercept (pre-exponential) = $-2.32E+01 \text{ A V}^2$
 Coefficient of linear correlation = 0.9997, 46 degrees of freedom

Figure 16



Capacitor Slice Map

Data from 3303 5 right, examined on 06/26/85

Initial characteristics:

Oxide thickness 719 Angstroms, gate area 1.00E-02 cm²
 n-type, doping density approximately $9.03E+17$ cm⁻³
 (convergence obtained in 3 iterations)
 Flatband capacitance of $4.64E-10$ F, obtained at
 Flatband voltage of -0.14 V
 Slope (dC/dV) at flatband of $2.56E-12$ F/V
 Workfunction difference of 0.14 V
 Total flatband shift of 0.00 V
 Total charge density of $3.44E+08$ cm⁻²

Figure 17

3303-5 2

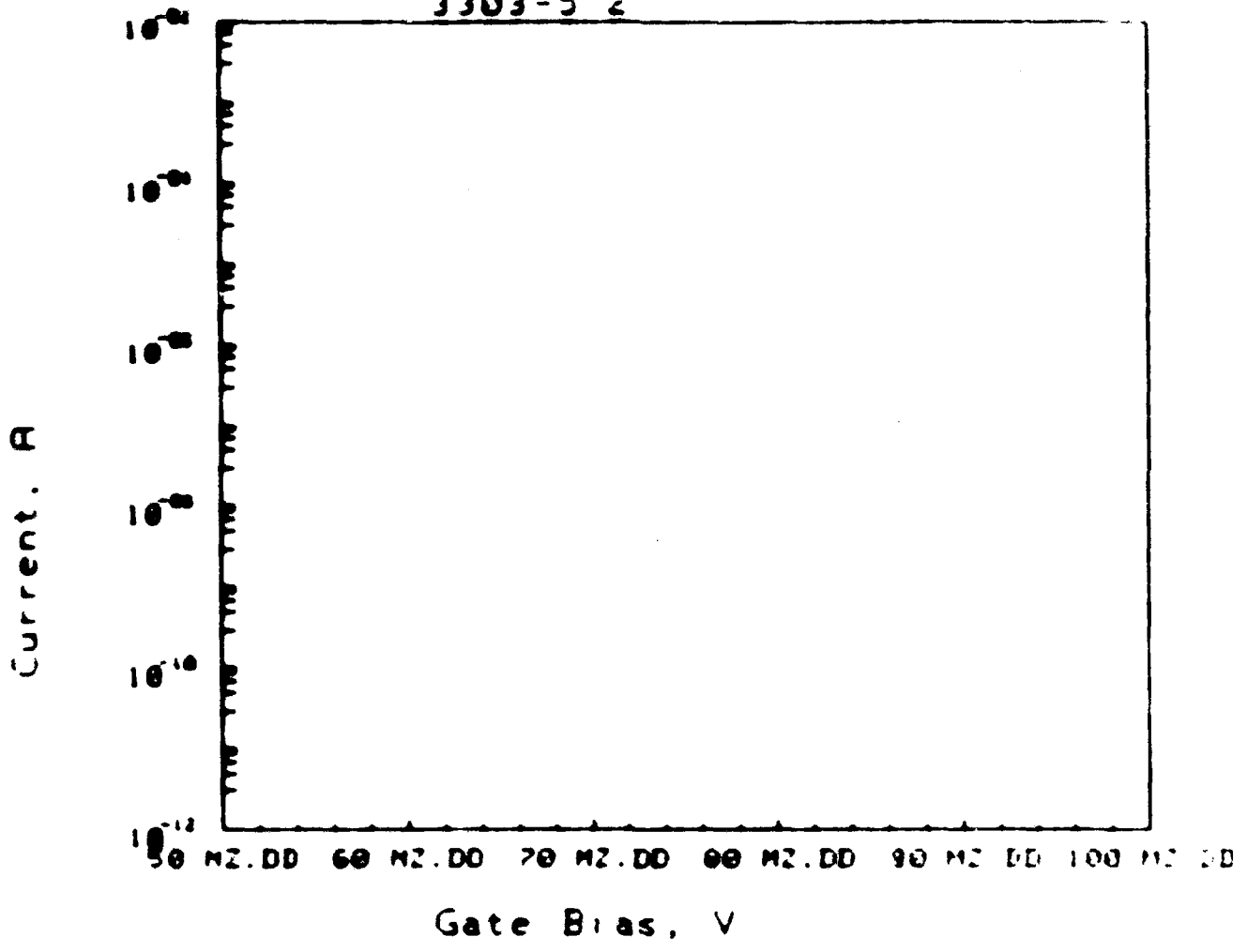
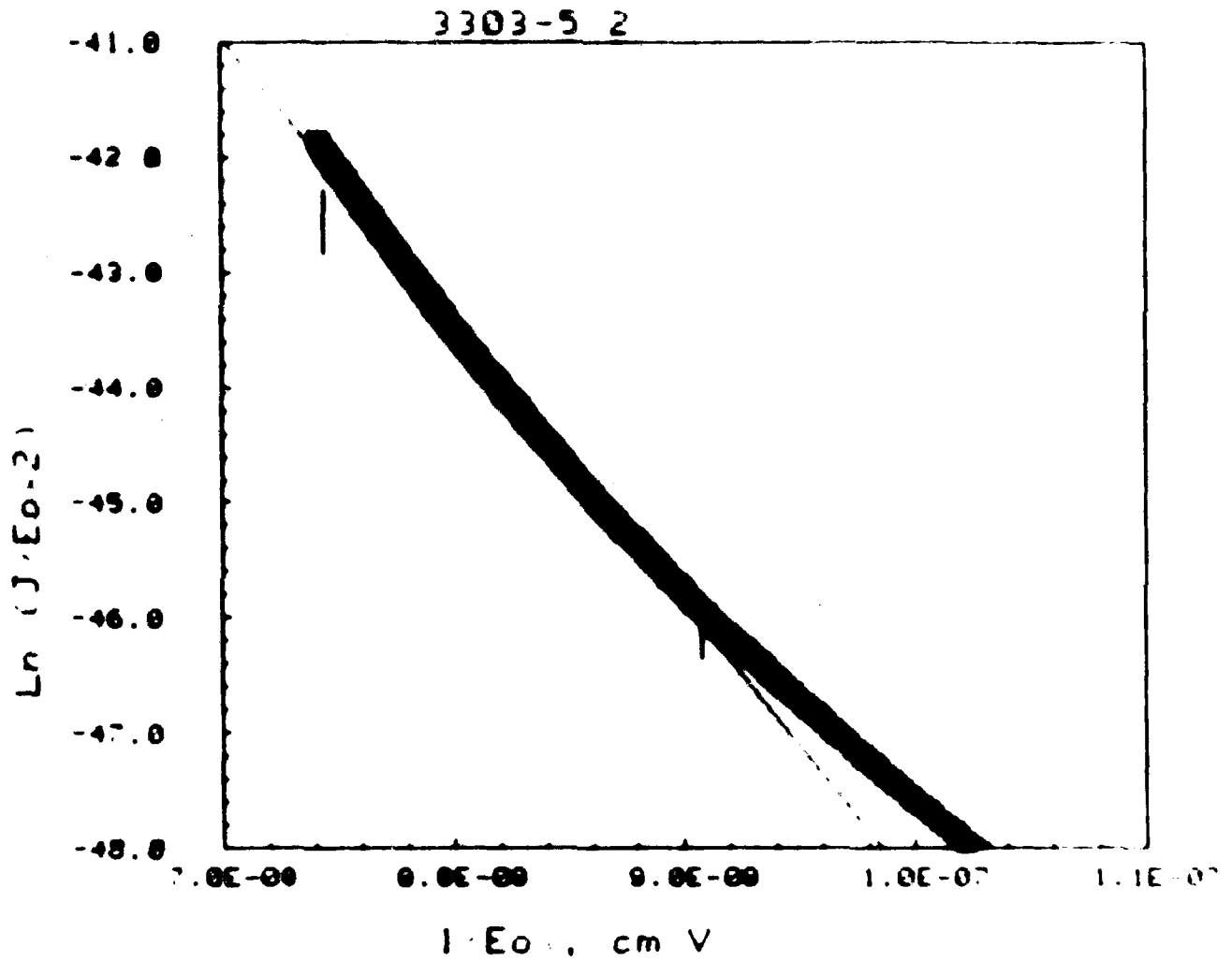


Figure 18



Slope $\cdot E_o = -2.47E+08 \text{ V cm}$
 Intercept $\cdot \text{pre-exponential} = -2.37E+01 \text{ A V}^2$
 Coefficient of linear correlation = 0.9985, 89 degrees of freedom

Figure 19

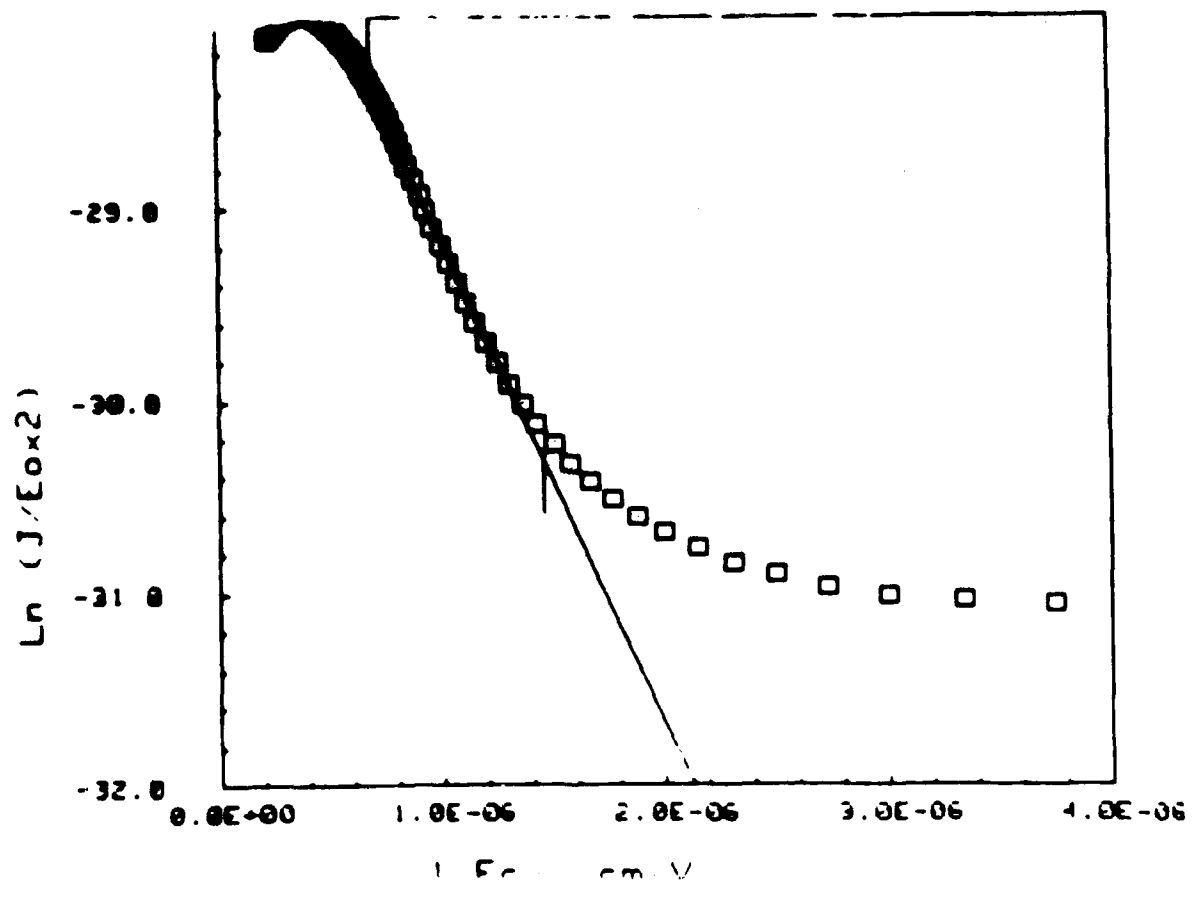
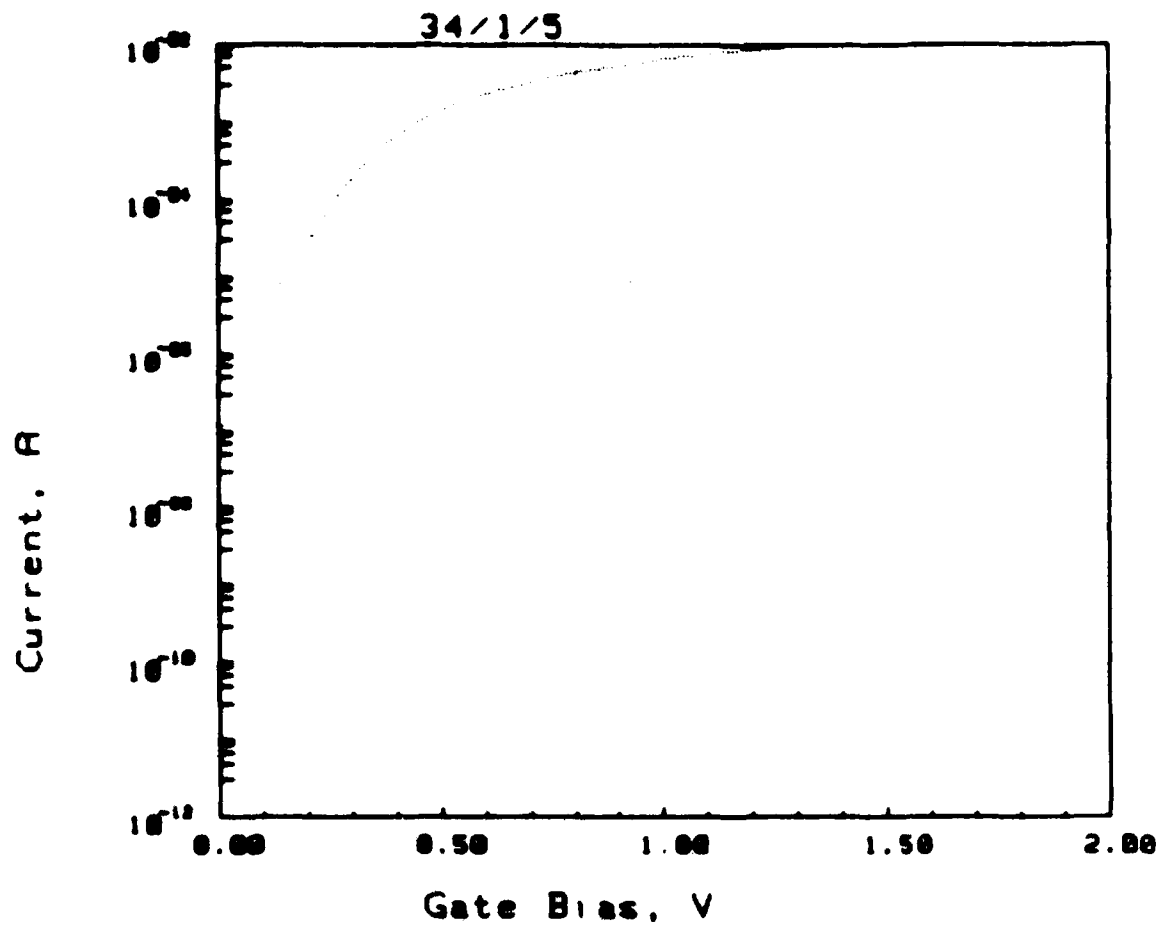
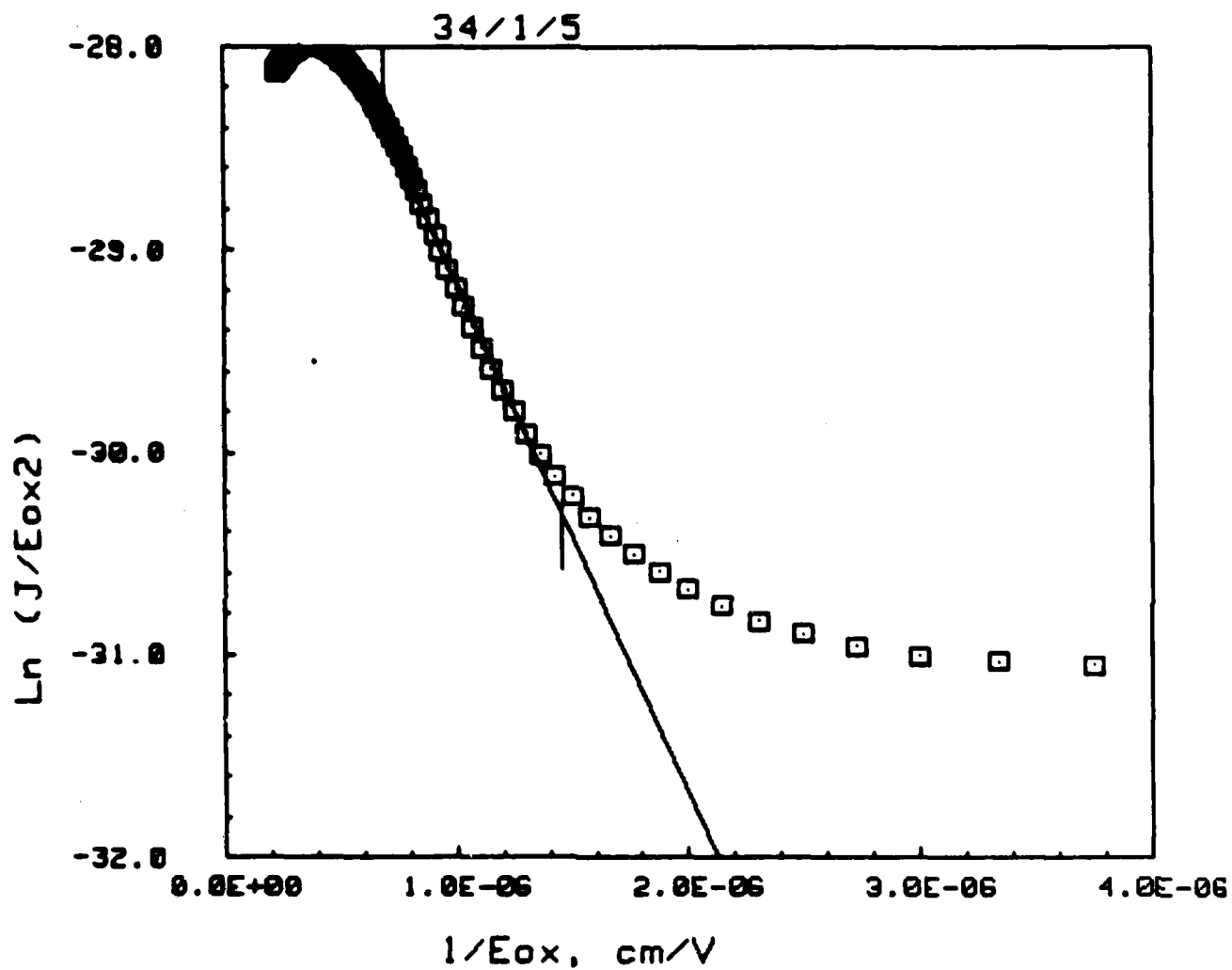


Figure 20



Slope (E_0) = $-2.53E+06 \text{ V/cm}$
 Intercept (pre-exponential) = $-2.66E+01 \text{ A/V}^2$
 Coefficient of linear correlation = 0.9976 , 22 degrees of freedom

Figure 21

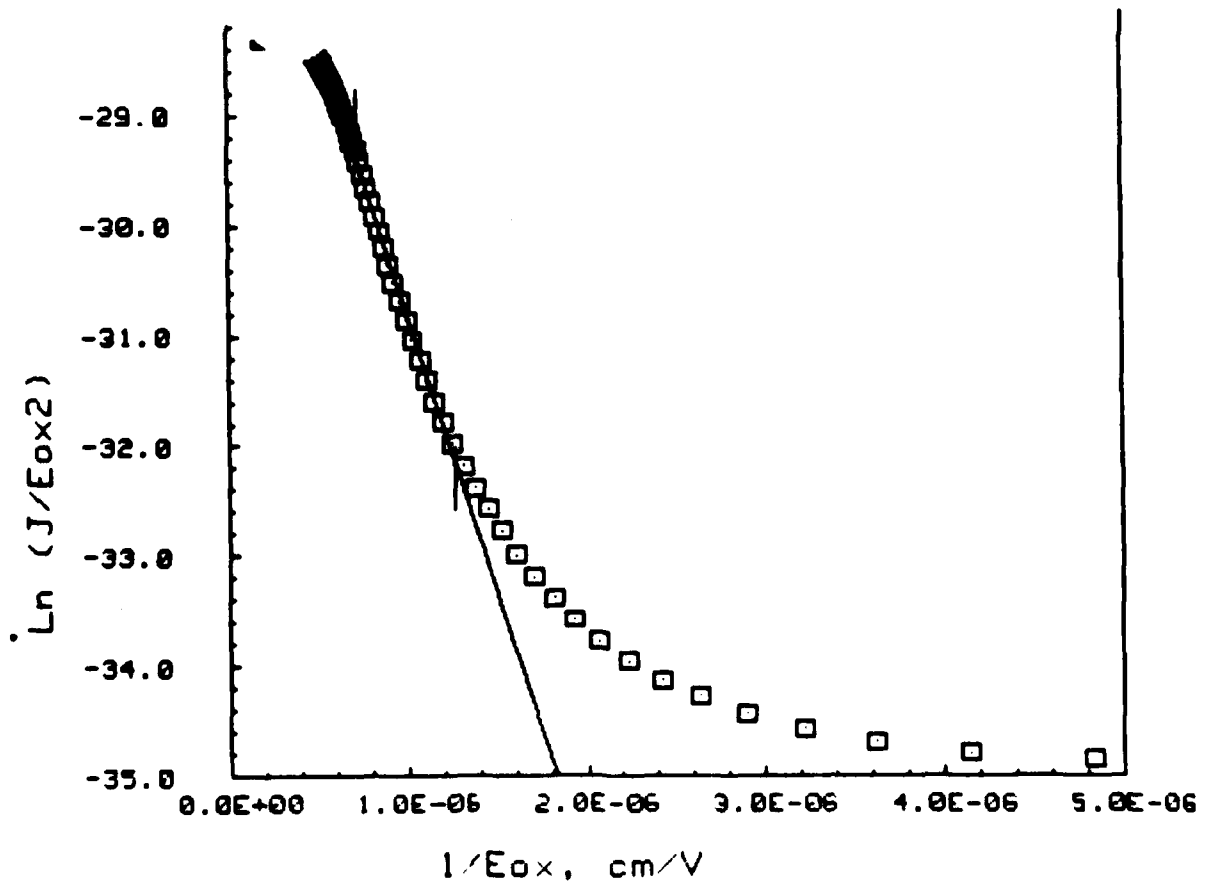
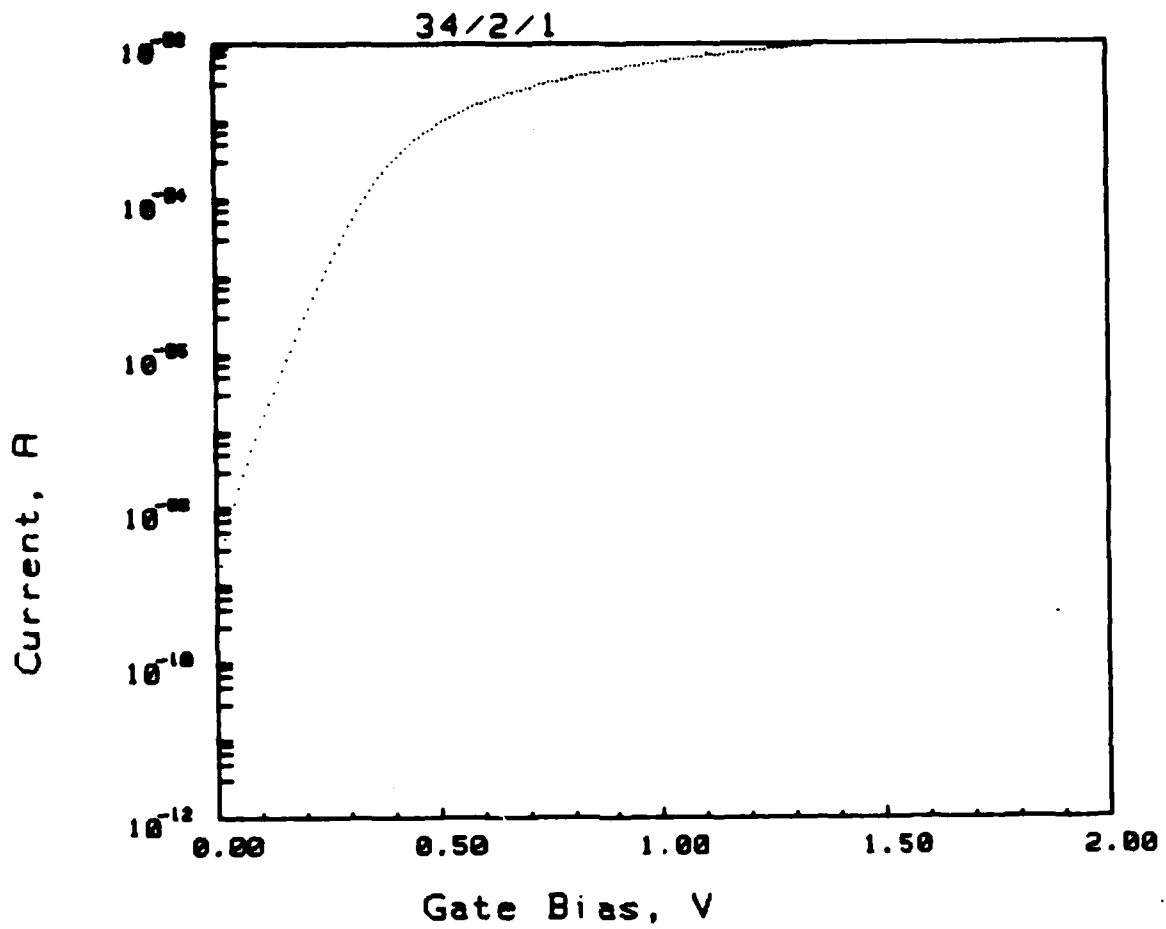
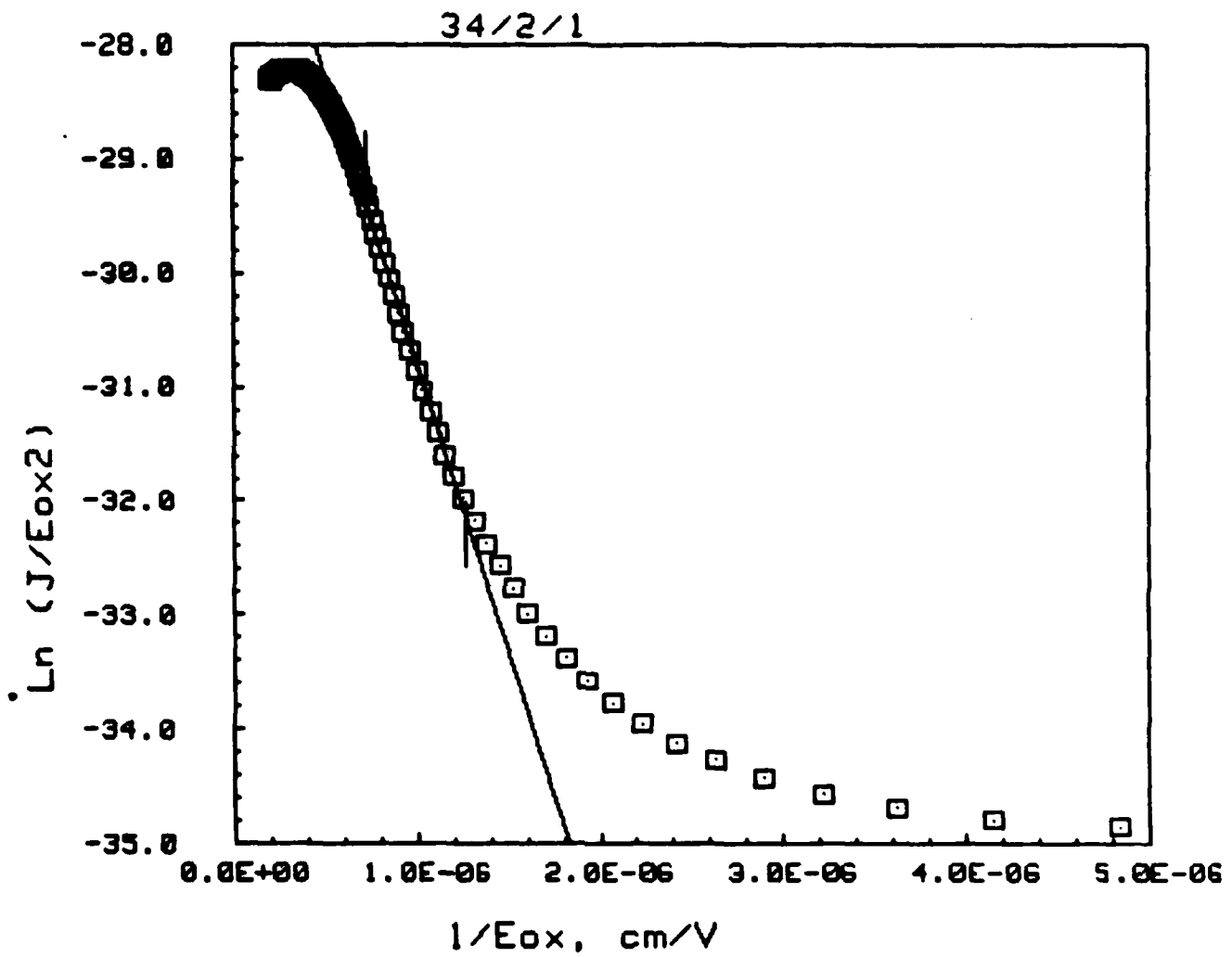


Figure 22



Slope (E_0) = $-5.09E+06 \text{ V/cm}$
 Intercept (pre-exponential) = $-2.57E+01 \text{ A/V}^2$
 Coefficient of linear correlation = 0.9977 , 16 degrees of freedom

Figure 23

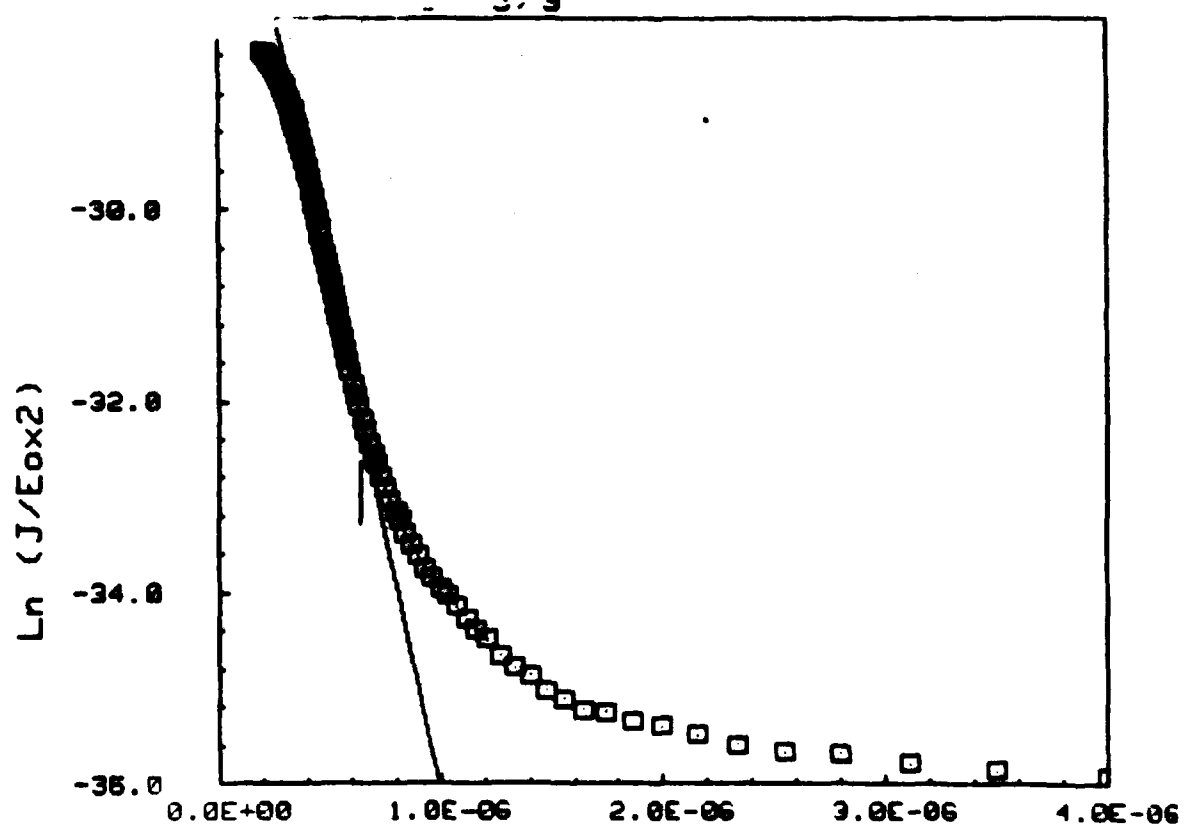
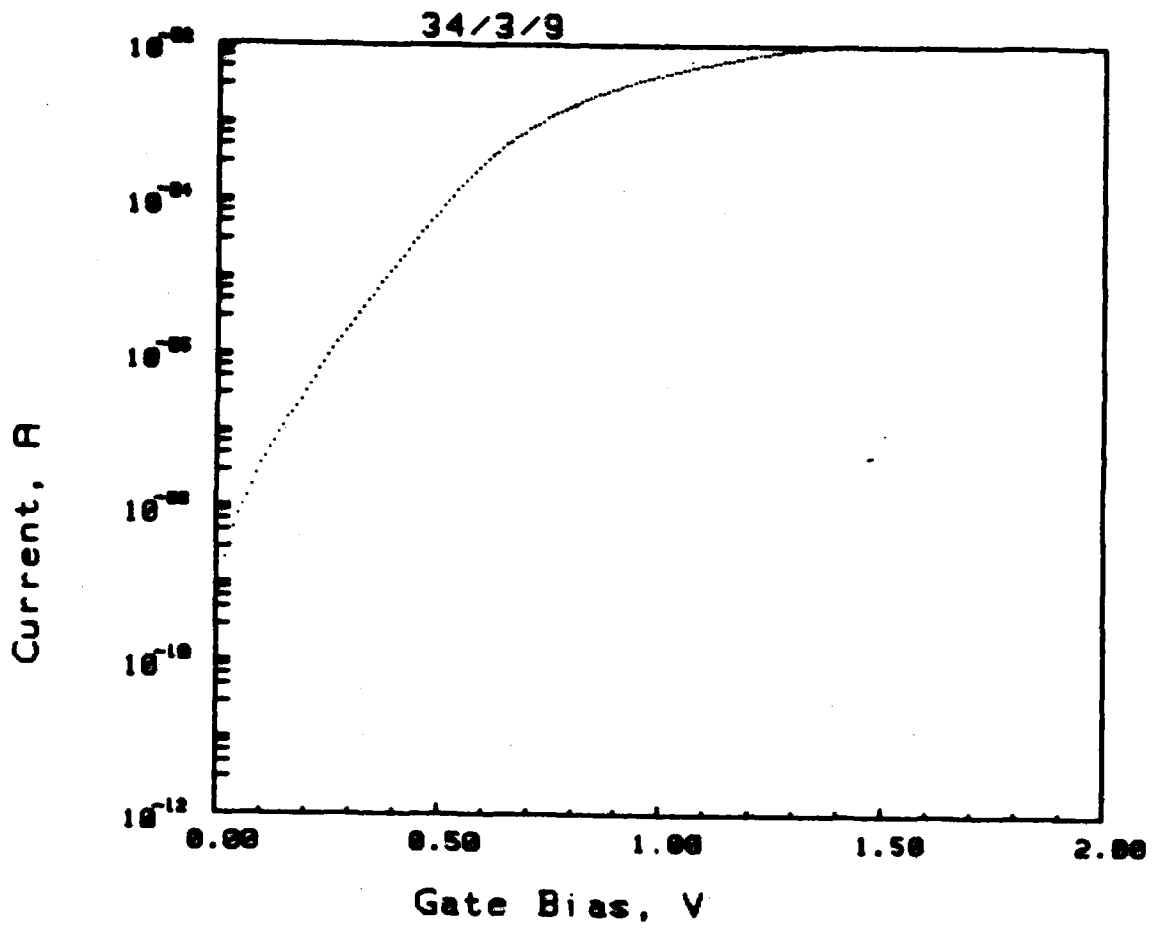
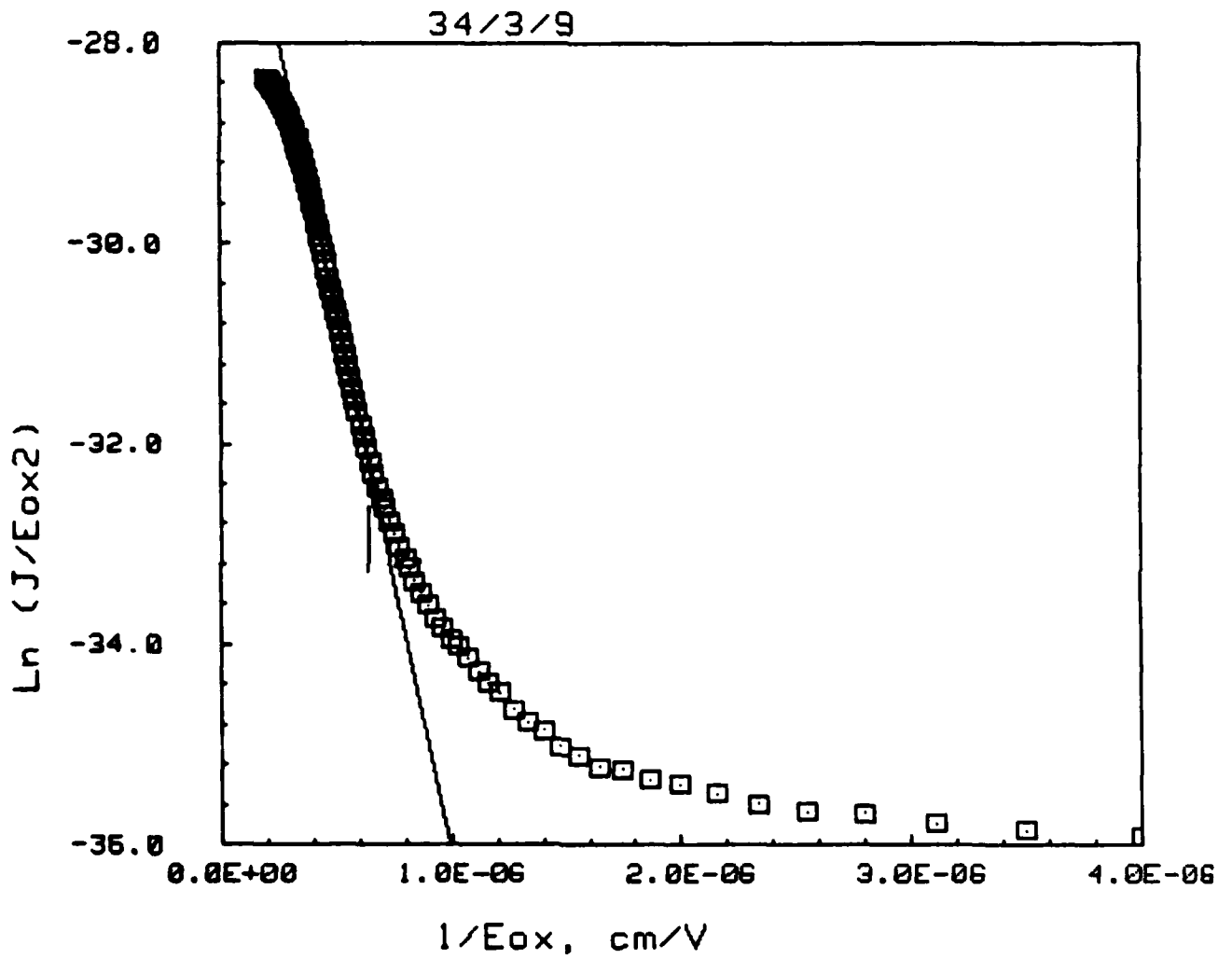


Figure 24



Slope (E_0) = $-1.09E+07 \text{ V/cm}$
 Intercept (pre-exponential) = $-2.52E+01 \text{ A/V}^2$
 Coefficient of linear correlation = 0.9995 , 29 degrees of freedom

Figure 25

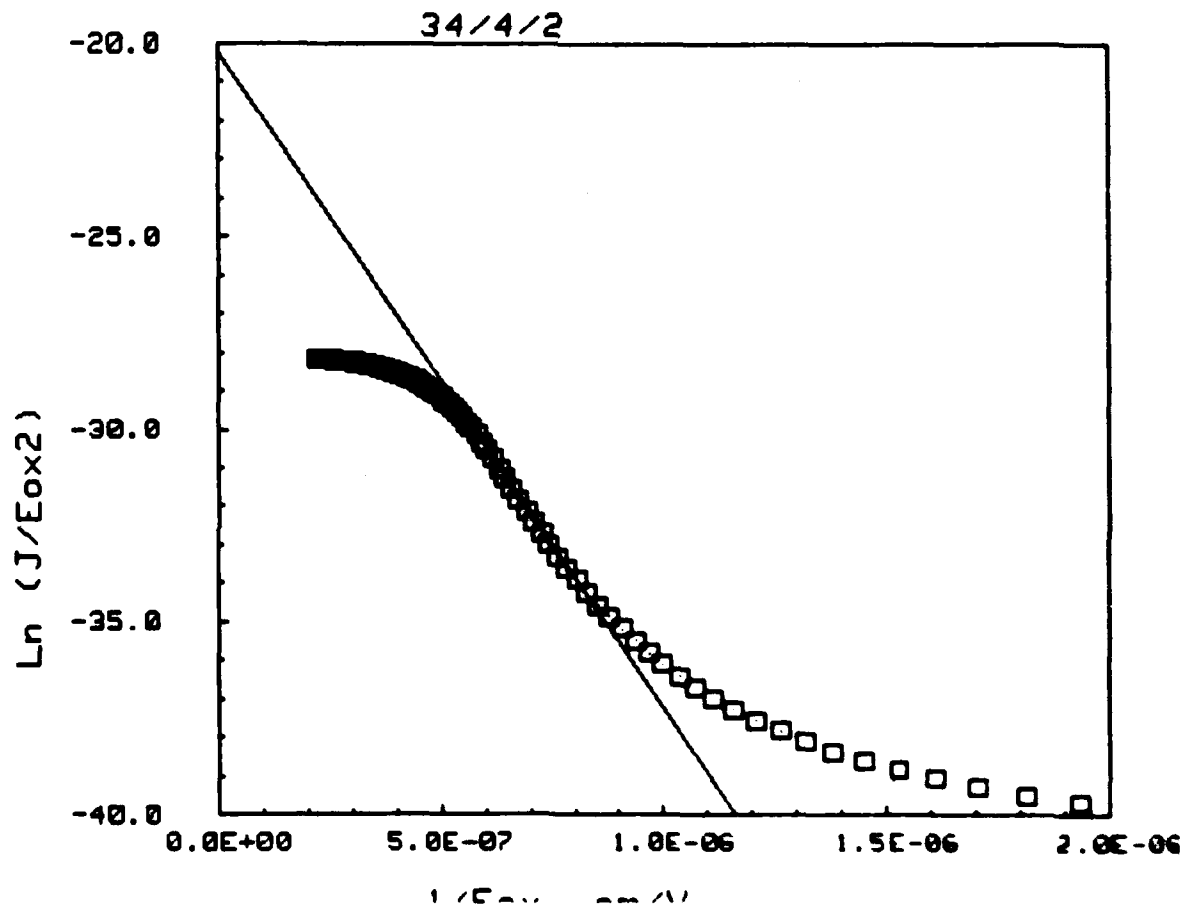
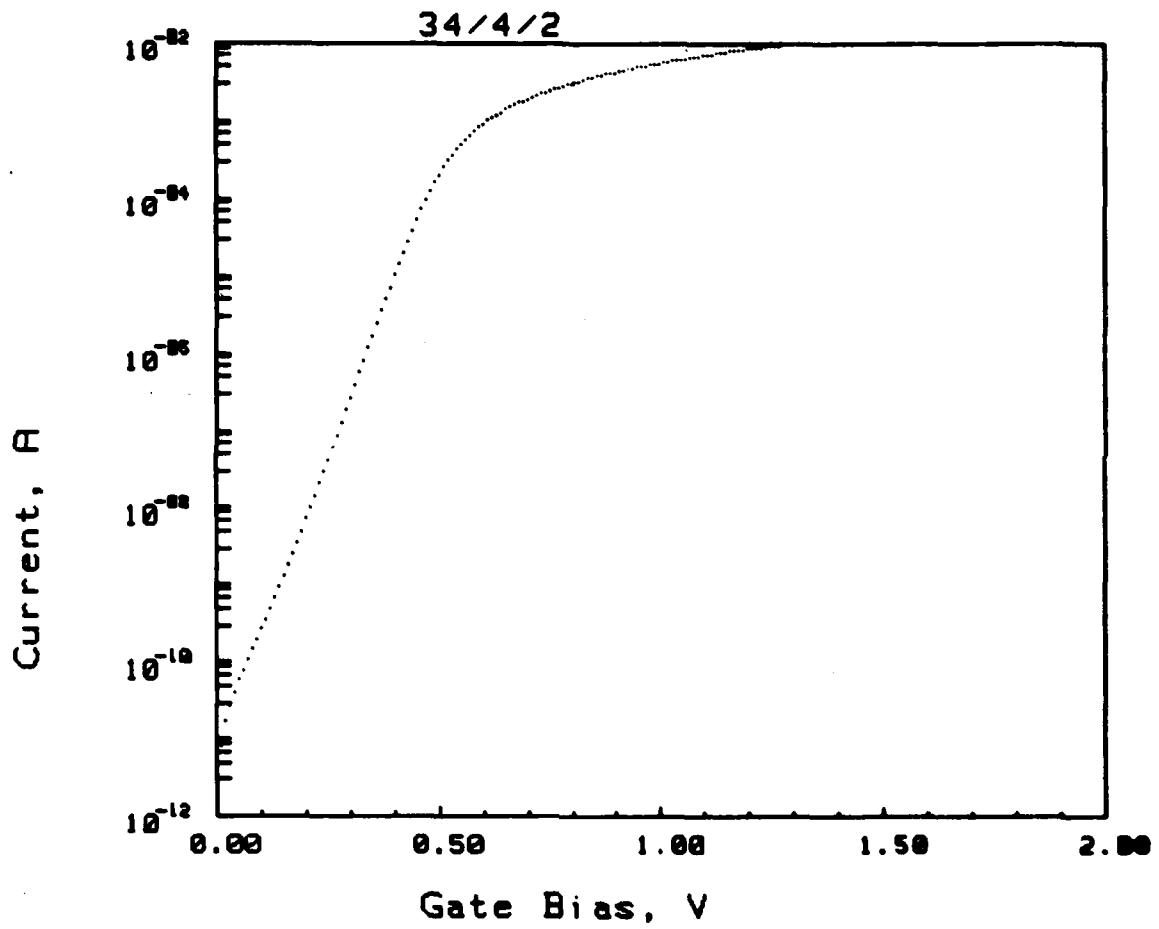
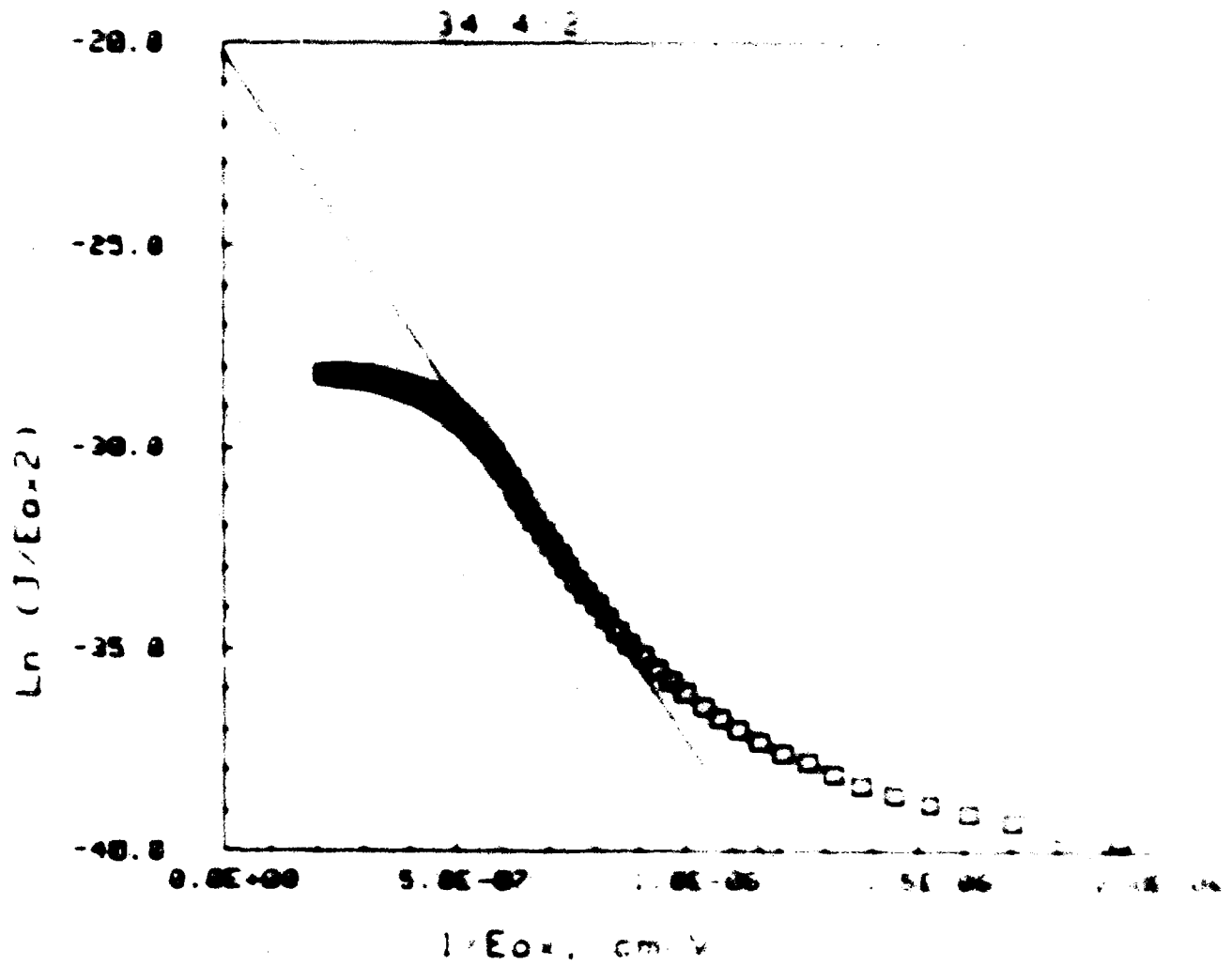


Figure 26



Slope (E_0) = $-1.70E+07 \text{ v/cm}$
 Intercept (pre-exponential) = $-2.02E+01 \text{ A/V}^2$

Figure 27

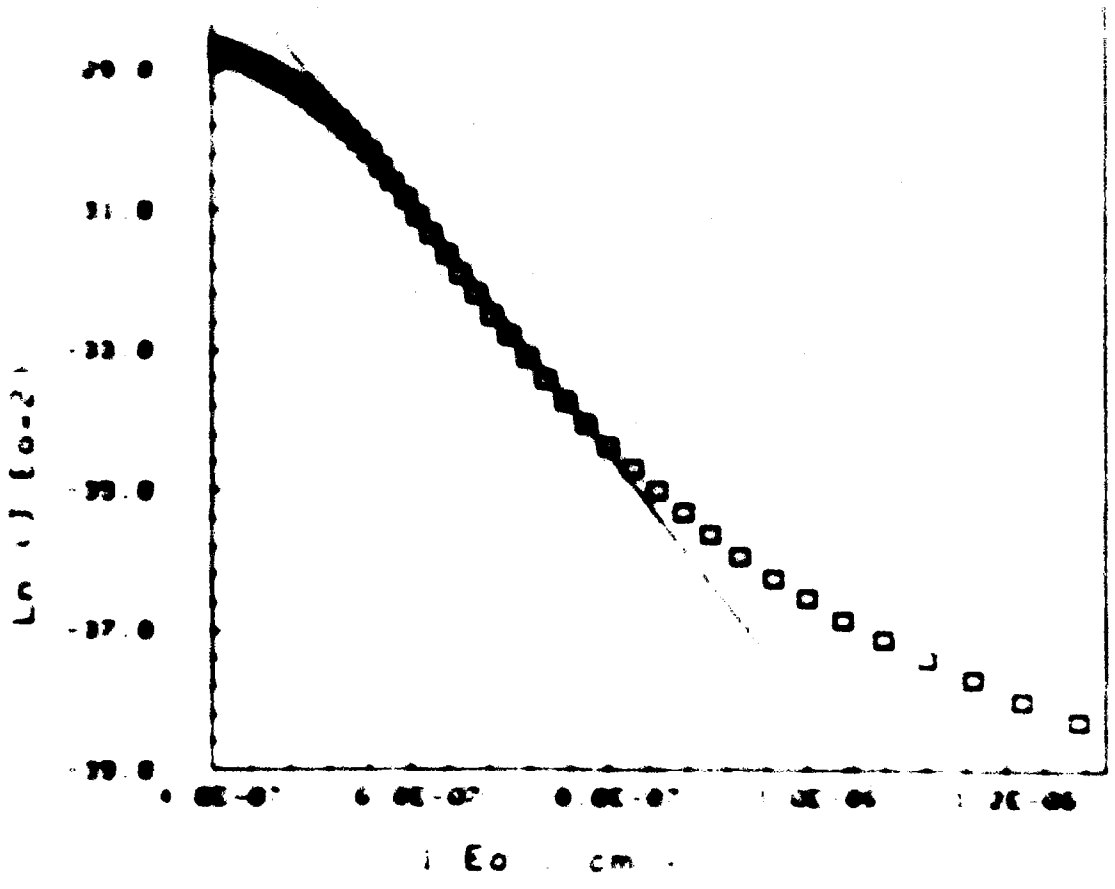
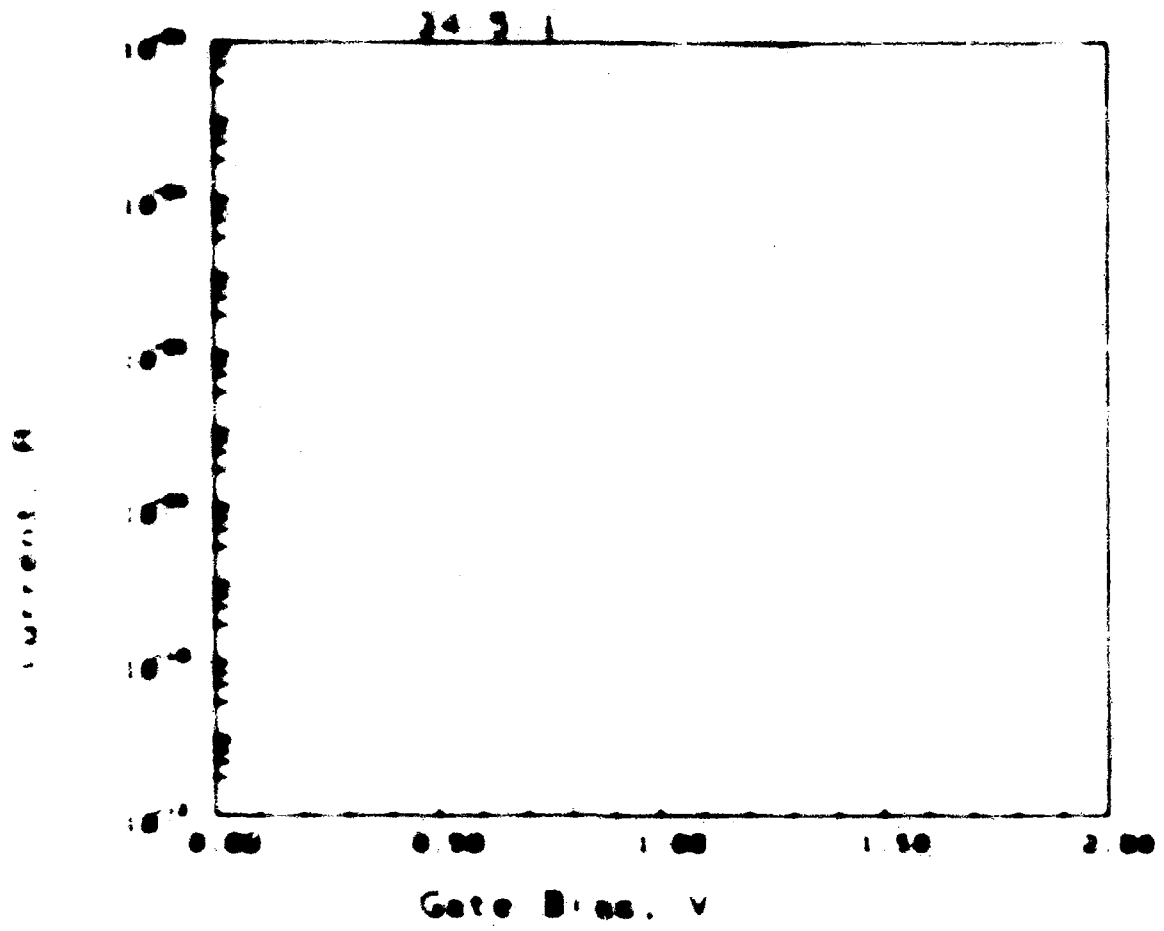
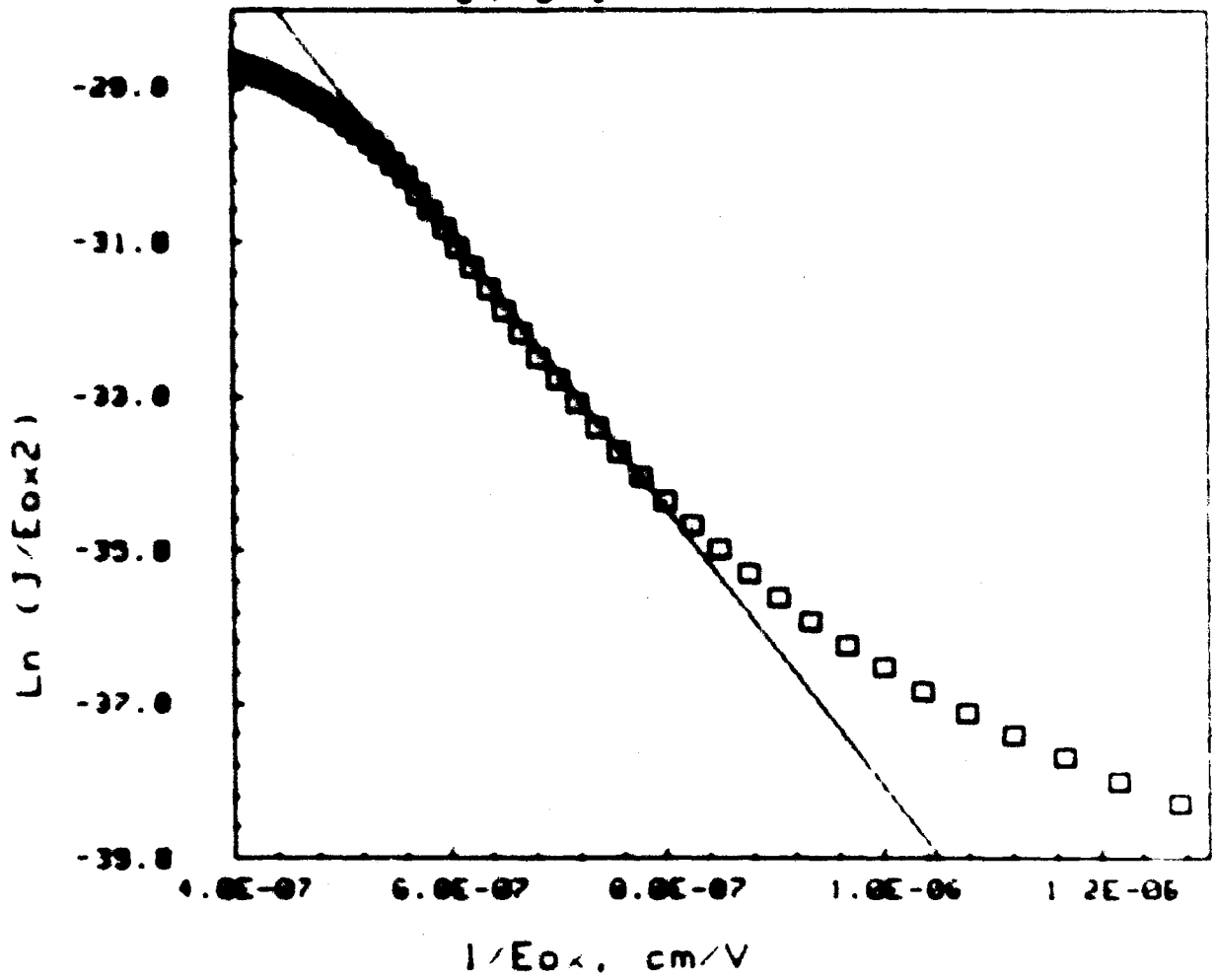


Figure 20

34 5 1



Slope (E_0) = $-1.00E+07$ V/cm
Intercept (pre-exponential) = $-2.01E+01$ A/V²

Figure 29

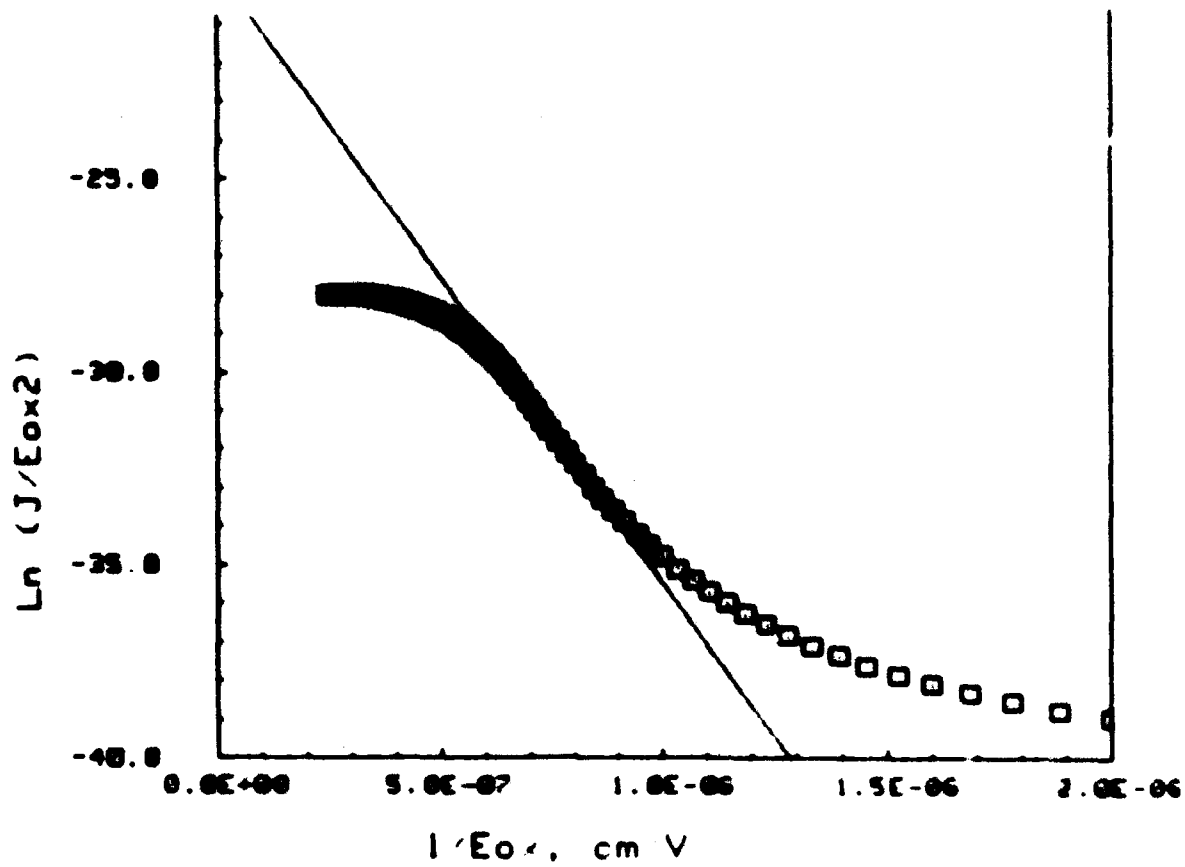
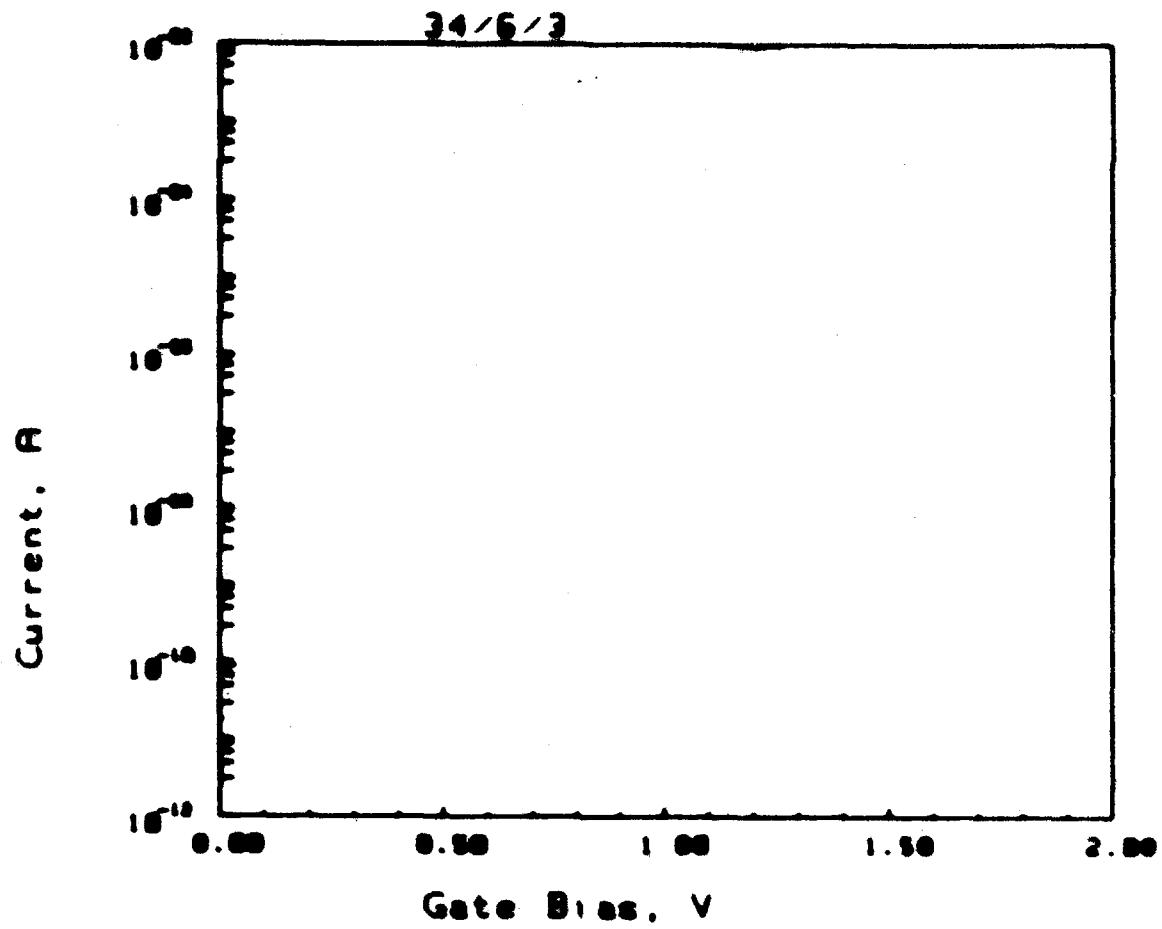
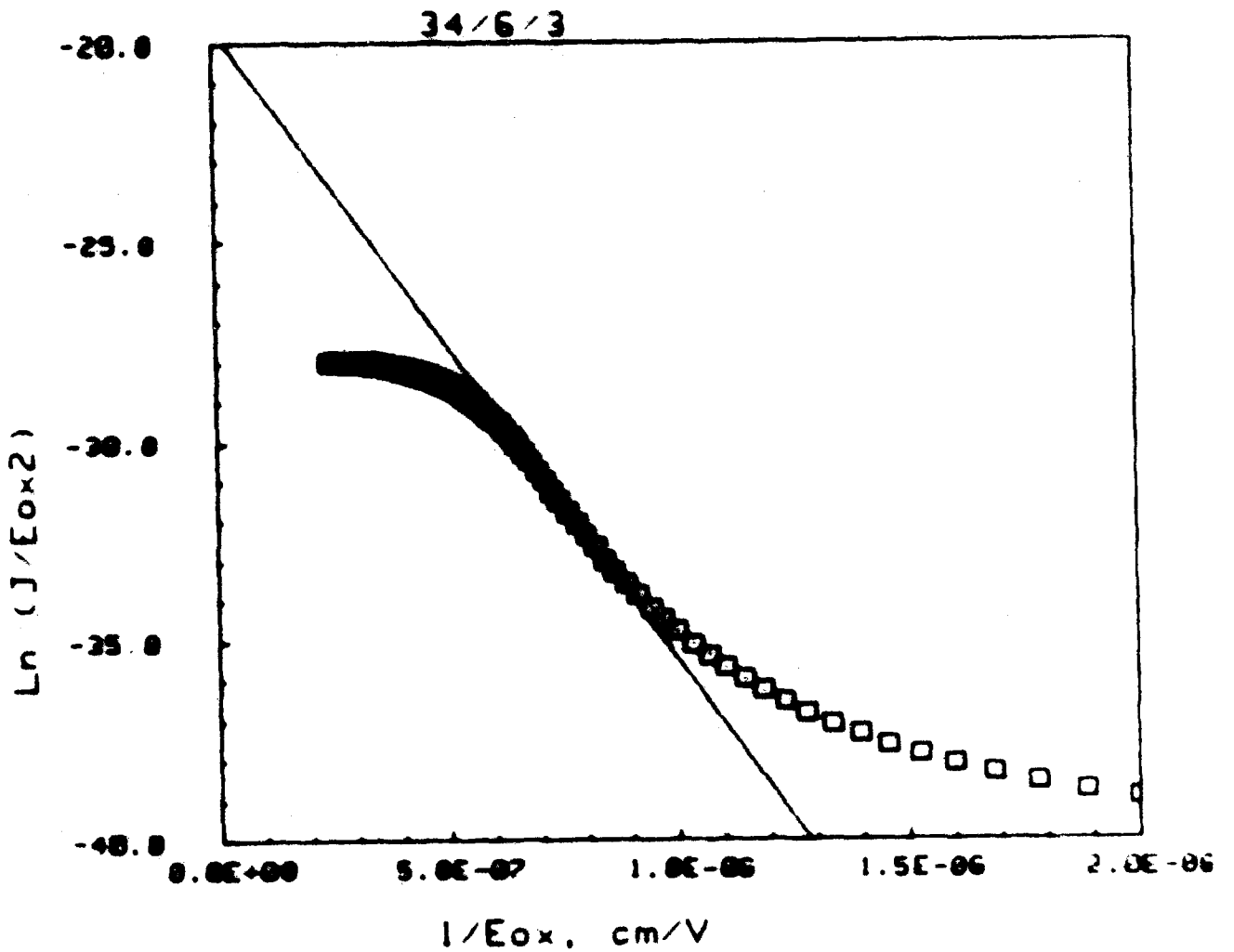


Figure 30



Slope (E_0) = $-1.99E+07 \text{ V/cm}$
 Intercept (pre-exponential) = $-1.96E+01 \text{ A}\cdot\text{V}^2$

Figure 31

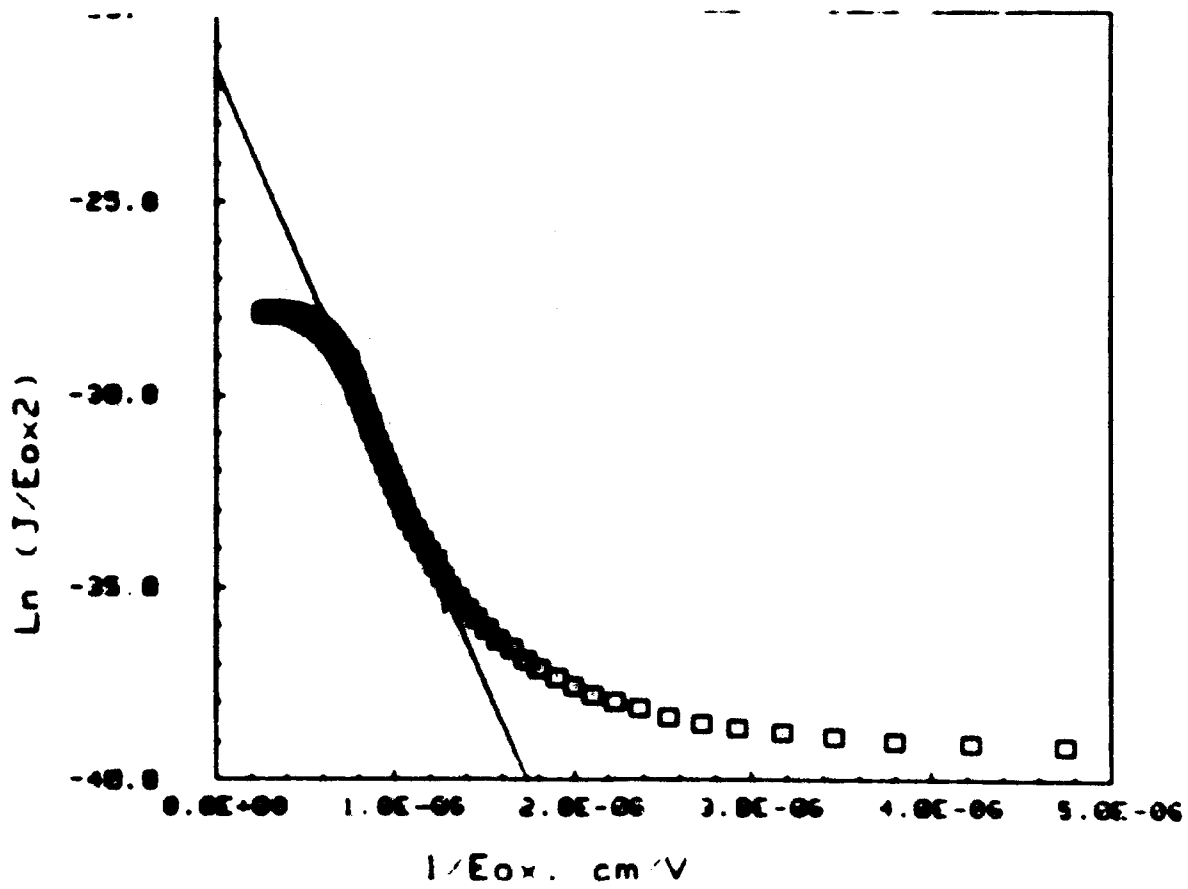
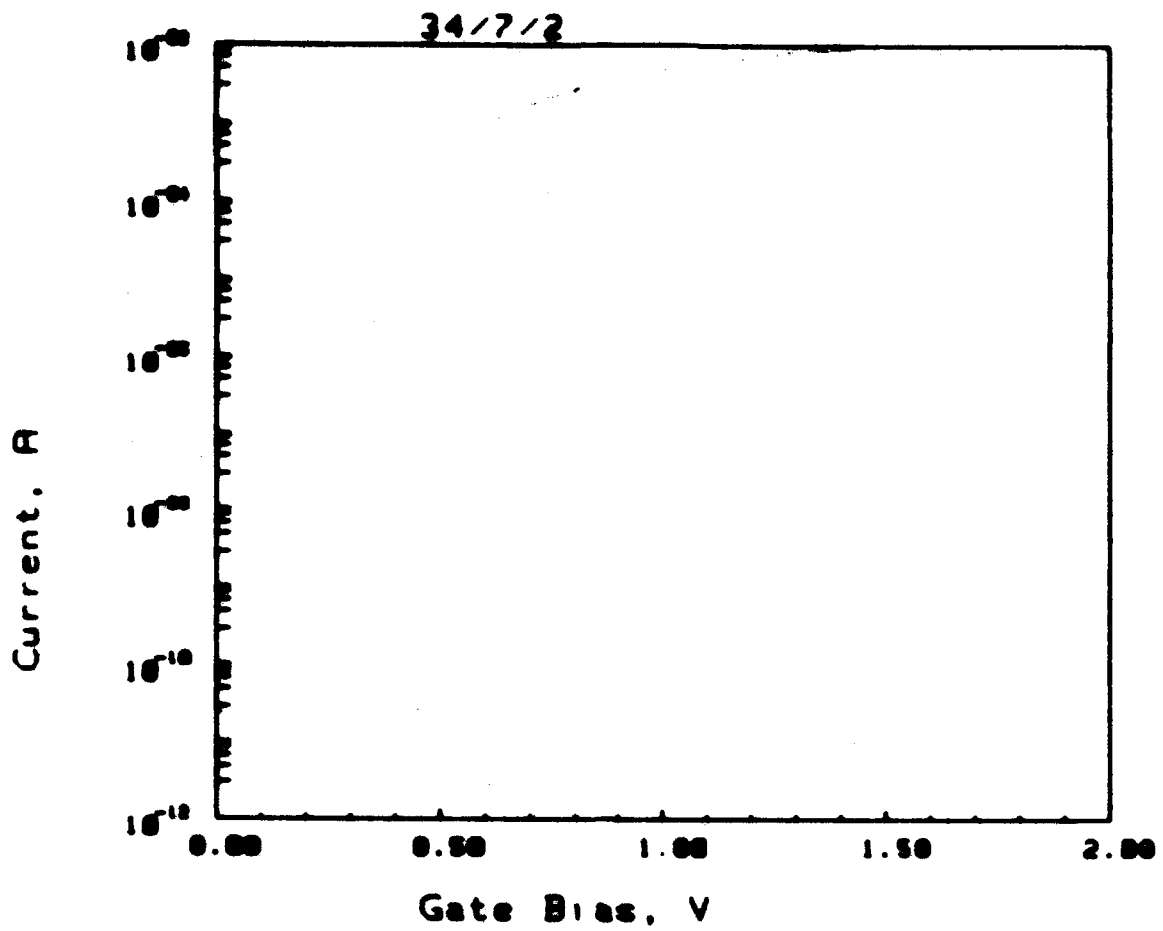
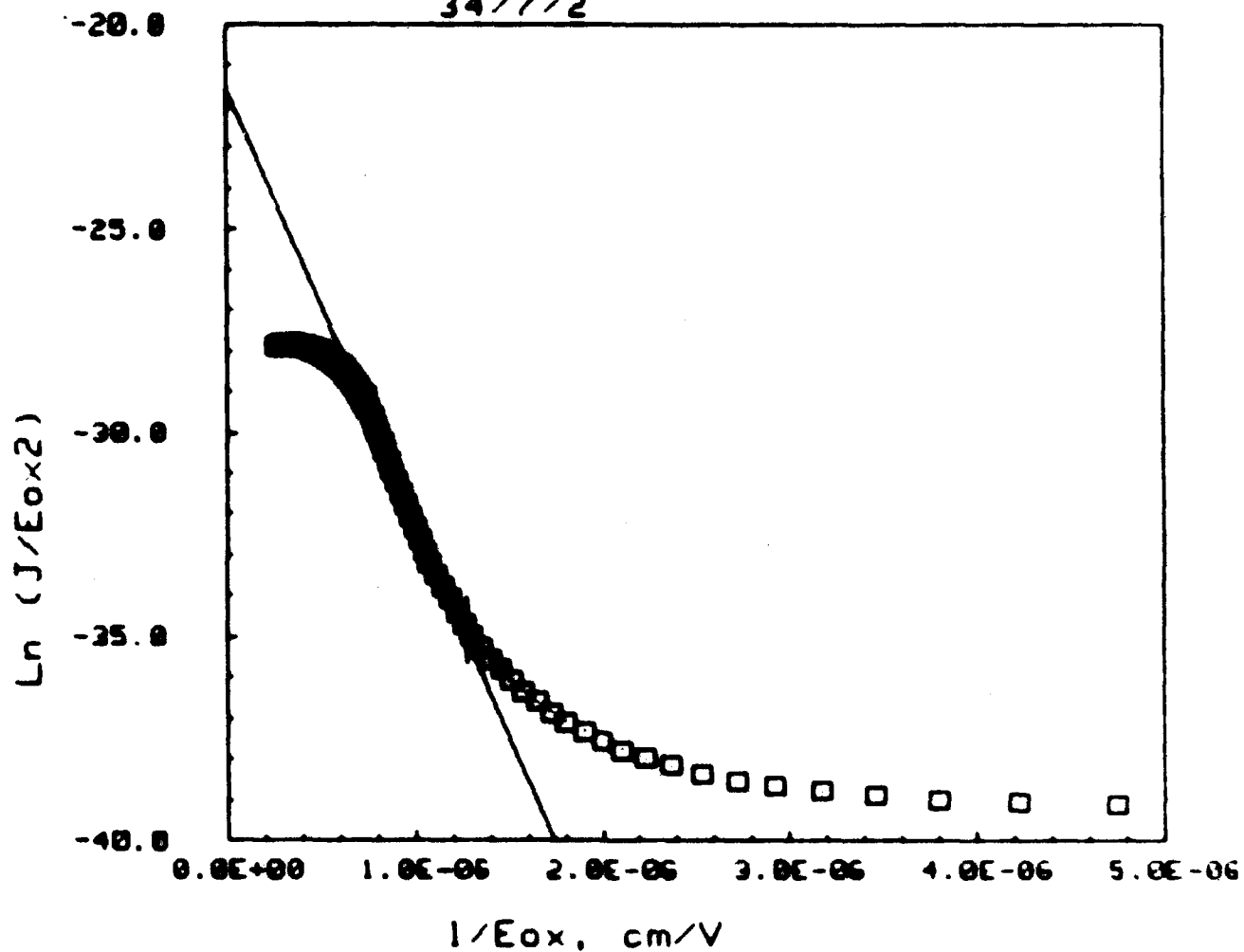


Figure 32

34/7/2



Slope (E_0) = $-1.06E+07$ V/cm
Intercept (pre-exponential) = $-2.15E+01$ A/V²
Coefficient of linear correlation = 0.9963

Figure 33

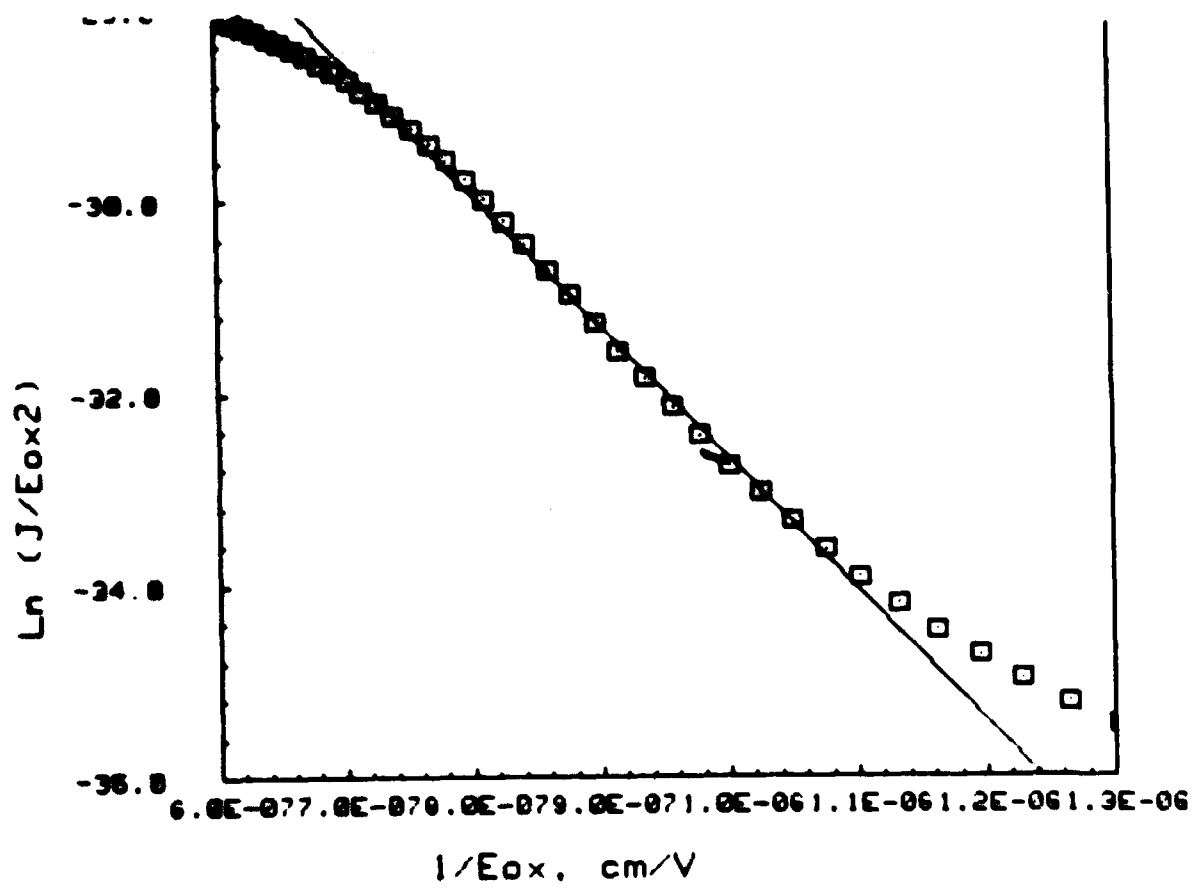
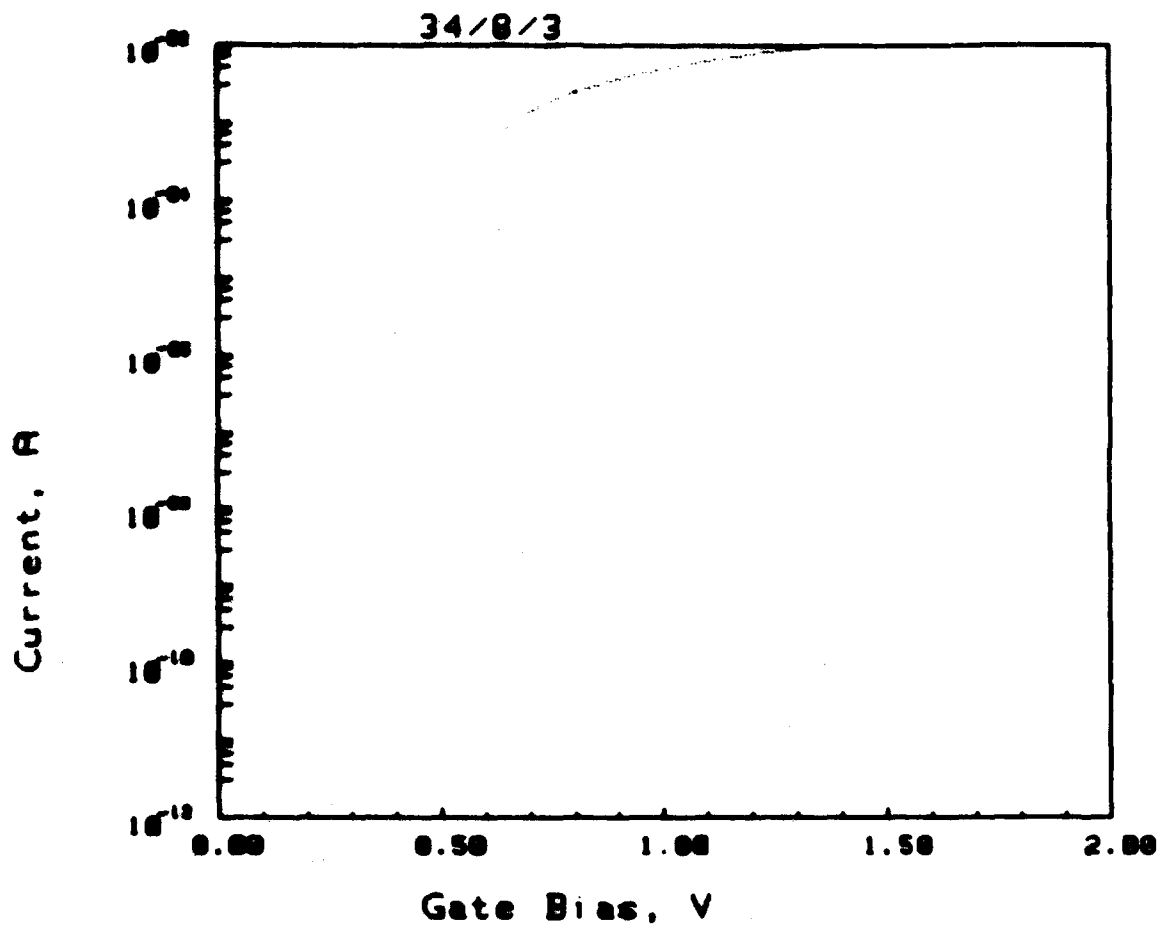
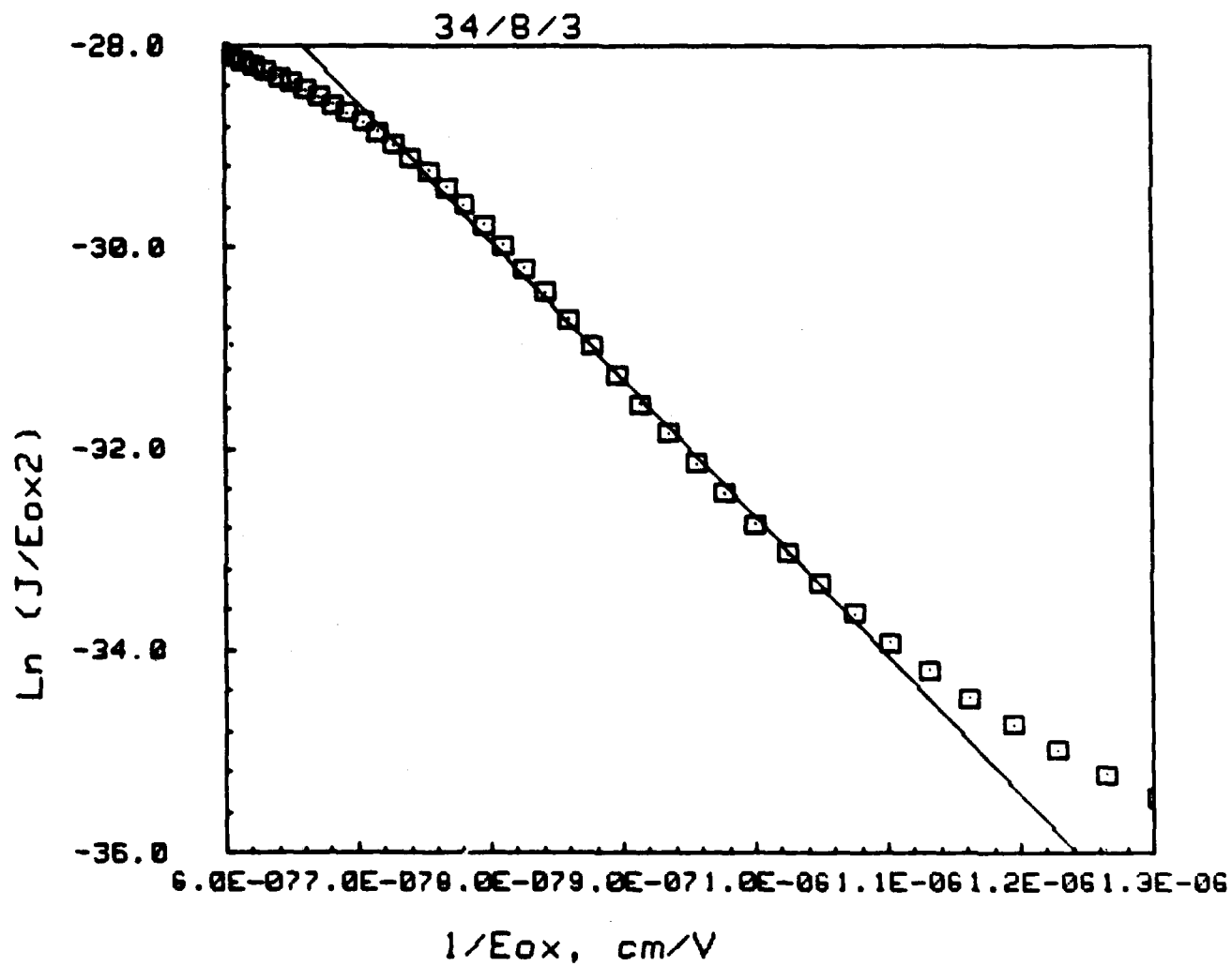


Figure 34



Slope (E_0) = $-1.38E+07 \text{ V/cm}$
 Intercept (pre-exponential) = $-1.89E+01 \text{ A/V}^2$

Figure 35

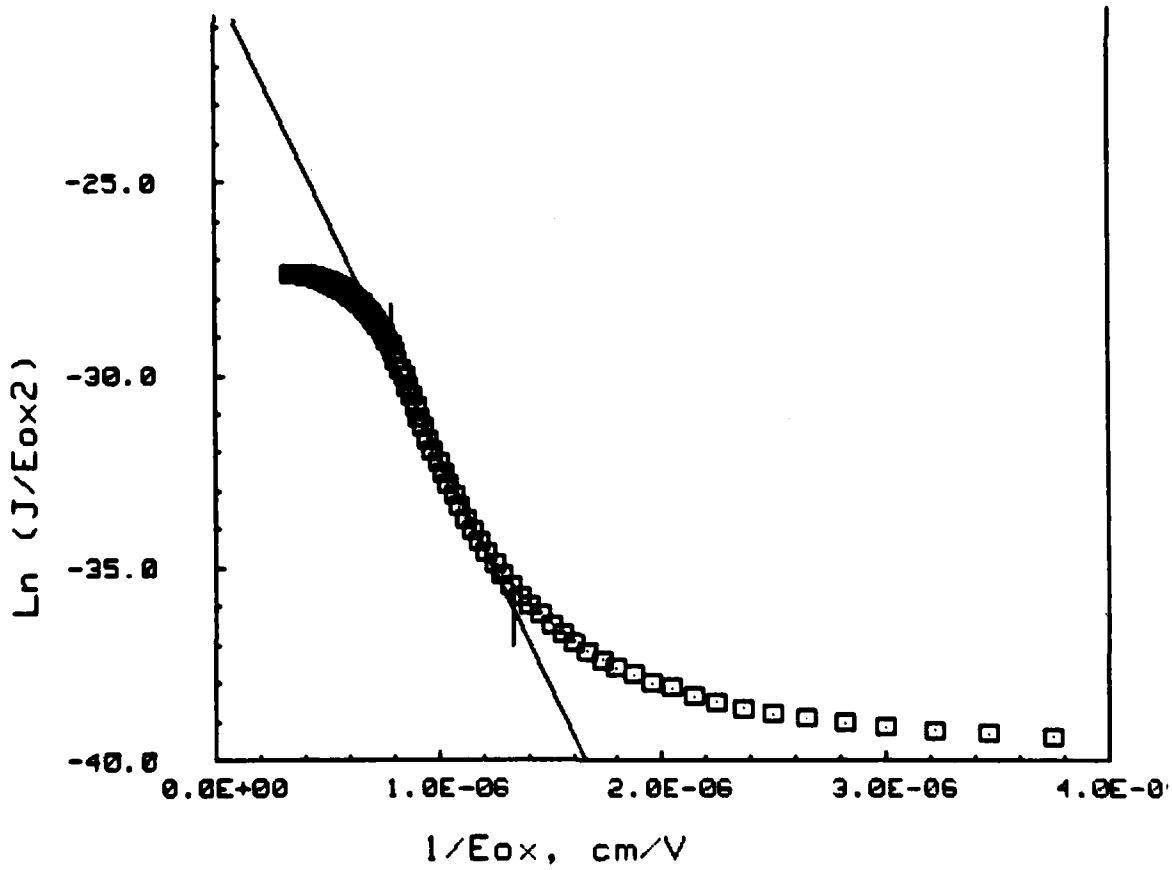
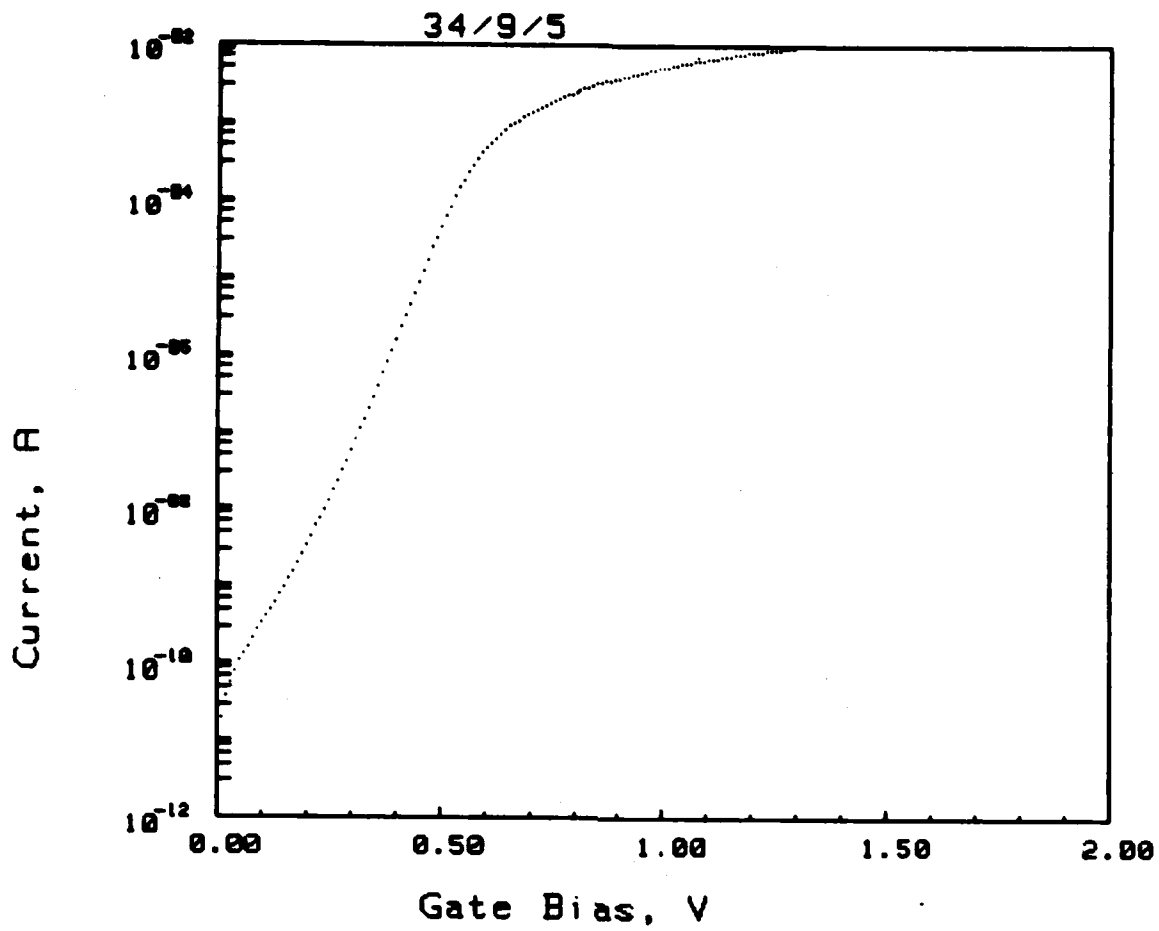
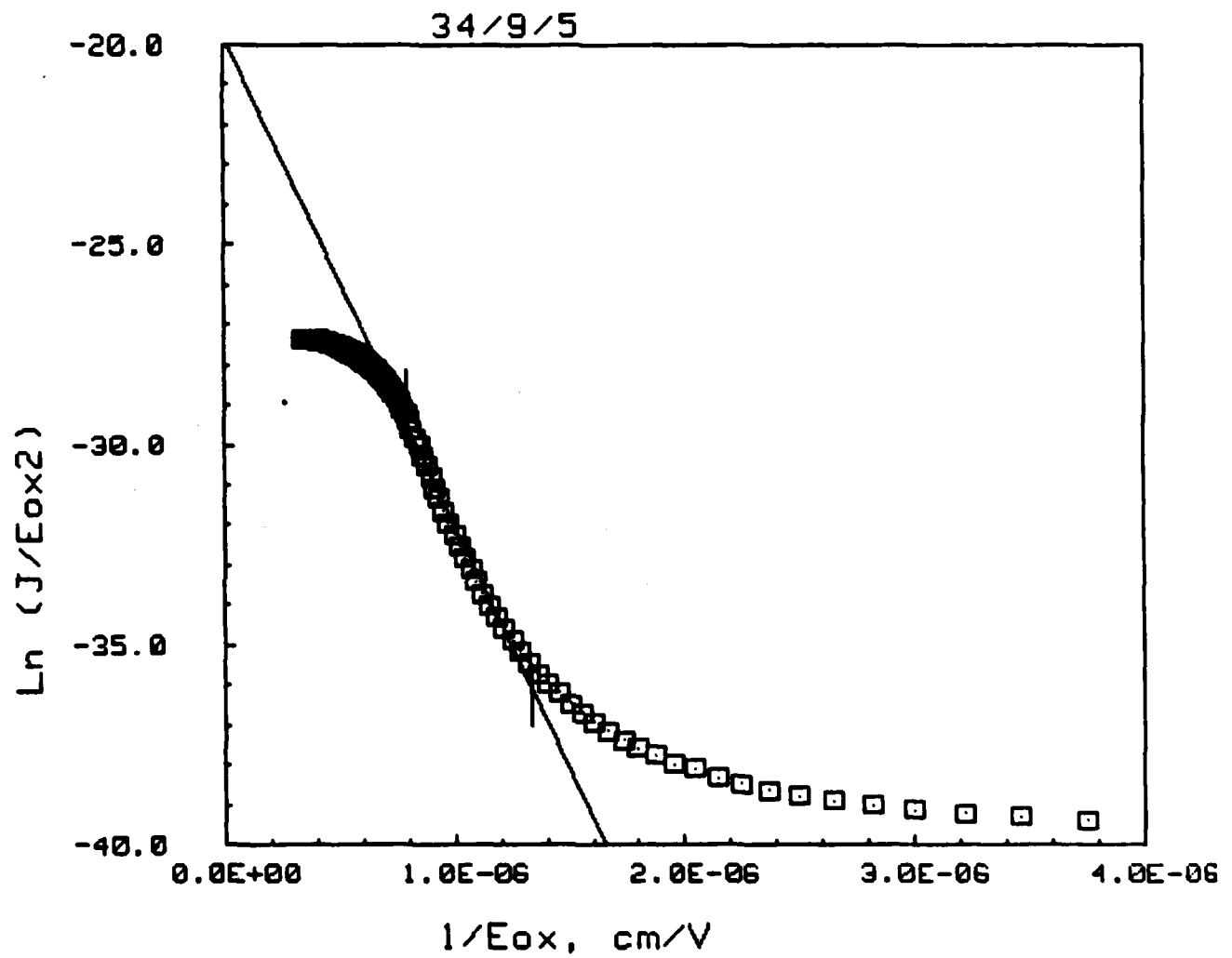


Figure 36



Slope (E_0) = $-1.22\text{E}+07$ V/cm
 Intercept (pre-exponential) = $-1.98\text{E}+01$ A/V²
 Coefficient of linear correlation = 0.9948, 23 degrees of freedom

Figure 37

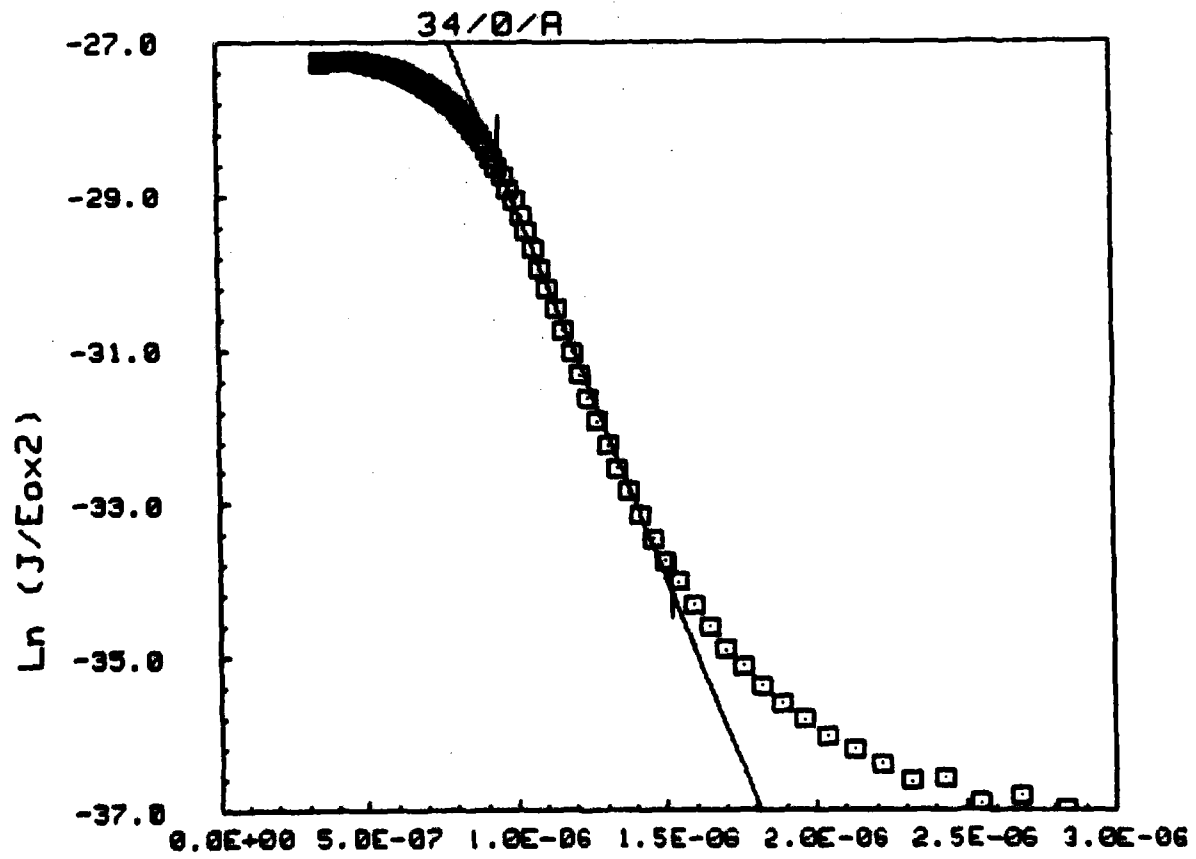
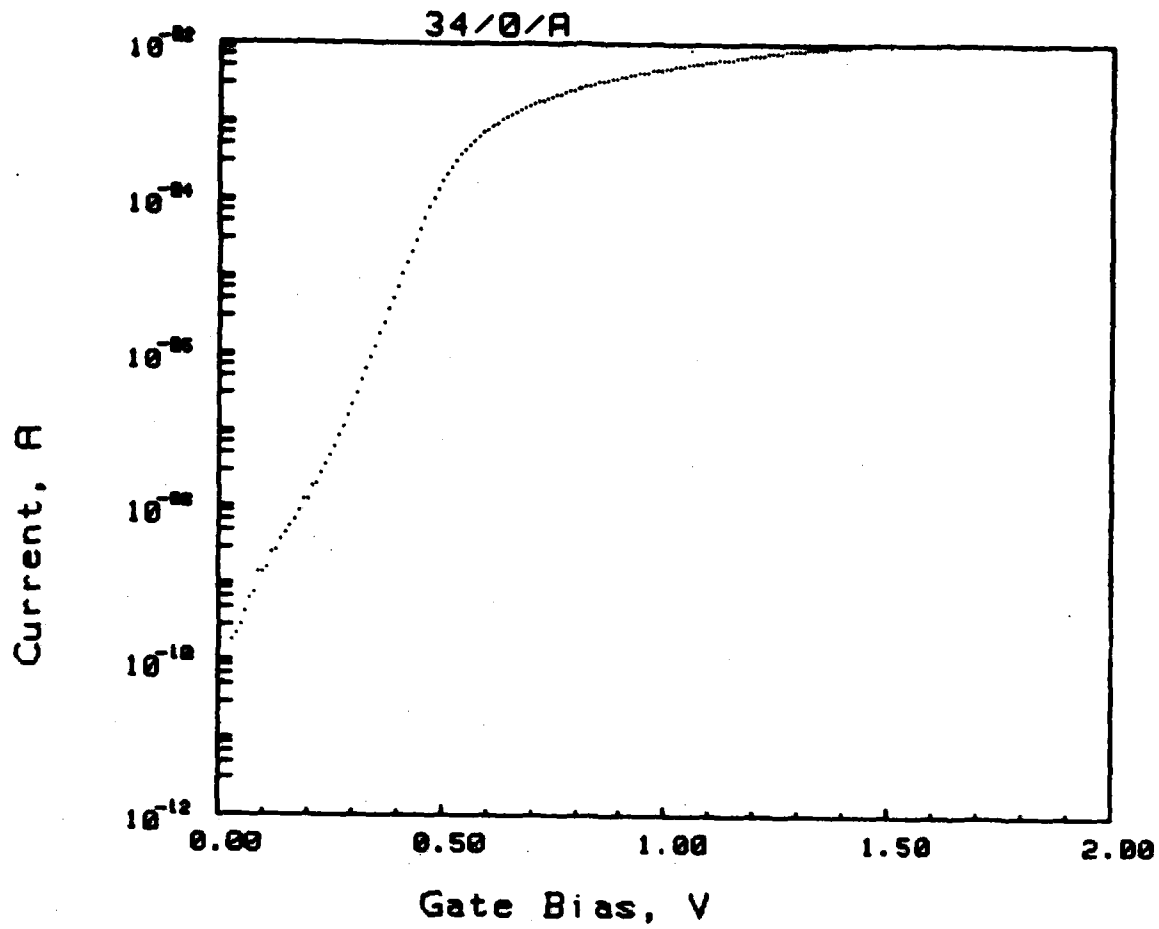
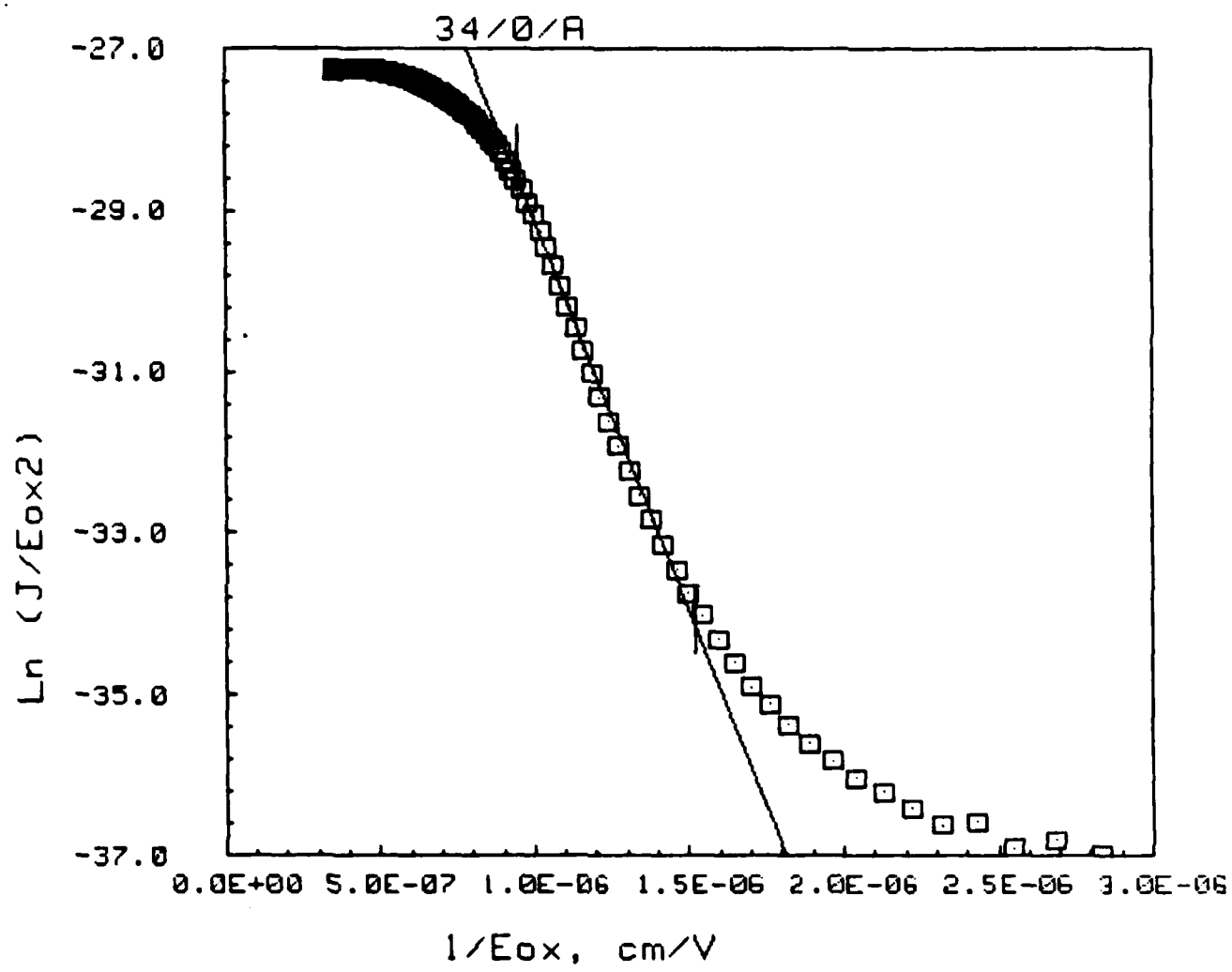


Figure 38



Slope (E_0) = $-9.69E+06$ V/cm
 Intercept (pre-exponential) = $-1.94E+01$ A/V²
 Coefficient of linear correlation = 0.9985, 19 degrees of freedom

Figure 39

END

FEB.

1988

DTIC